# CARDIOVASCULAR COMPLICATIONS FOLLOWING TRANSCATHETER AORTIC VALVE REPLACEMENT: QUANTIFICATION AND SYSTEMATIC DIFFERENTIATION USING CLINICAL MEASUREMENTS AND IMAGE-BASED PATIENT-SPECIFIC IN SILICO MODELING

# CARDIOVASCULAR COMPLICATIONS FOLLOWING TRANSCATHETER AORTIC VALVE REPLACEMENT: QUANTIFICATION AND SYSTEMATIC DIFFERENTIATION USING CLINICAL MEASUREMENTS AND IMAGE-BASED PATIENT-SPECIFIC IN SILICO MODELING

BY

SEYEDVAHID KHODAEI, M.Sc.

A Thesis Submitted to the Department of Mechanical Engineering and School of Graduate Studies in Partial Fulfilment of the Requirements for the Degree Doctor of Philosophy

McMaster University © Copyright by Seyedvahid Khodaei, September 2022

Doctor of Philosophy (2022), Department of Mechanical Engineering, McMaster University, Hamilton, Ontario

**TITLE**: Cardiovascular complications following transcatheter aortic valve replacement: quantification and systematic differentiation using clinical measurements and image-based patient-specific in silico modeling

**AUTHOR**: Seyedvahid Khodaei, M.Sc.

**SUPERVISOR**: Professor Zahra K. Motamed

**CO-SUPERVISOR**: Professor Ali Emadi

**PAGES**: xxv, 272

# Lay Abstract

Transcatheter aortic valve replacement is an emerging less invasive intervention for patients with aortic stenosis. Although hemodynamics quantification is critical for accurate and early diagnosis of aortic stenosis, proper diagnostic methods for these diseases are still lacking because fluid-dynamics methods, that can be used as engines of new diagnostic tools, are not well developed yet. We developed an image-based patient-specific computational framework that can quantify hemodynamics in patients with aortic stenosis who received transcatheter aortic valve replacement. We also used its diagnostic abilities by providing novel analyses and interpretations of clinical data to answer clinical questions.

# Abstract

The success of TAVR procedure hinges on quantifications of the global hemodynamics (heart function metrics and workload), and the local hemodynamics (3-dimensional flow dynamics in left ventricle, aortic root, and coronary arteries). In this study, we developed an image-based framework that can quantify local and global hemodynamics for TAVR assessment. The proposed framework uses fluid-structure interaction method and lumped-parameter modeling that only needs routine non-invasive clinical patient data. The computational framework was validated against clinical cardiac catheterization data and Doppler echocardiographic measurements.

One of the challenging aspects of TAVR is its common association with complex valvular, ventricular, and vascular diseases (C3VD). Treatment strategies for these patients are quite uncertain and, on a case-by-case basis. In order to examine long term risk factors and create guidelines for intervention aimed at minimizing the progression of cardiovascular disease, the impact of C3VD on ventricle fluid dynamics in patients who underwent TAVR was investigated in this thesis. Our results showed that interactions of C3VD with TAVR fluid dynamics may amplify adverse hemodynamic effects that limit the benefits of TAVR and might contribute to speed up disease progression. The results suggest that some other interventions in addition to TAVR, such as mitral valve intervention and percutaneous coronary intervention, might be required as regularly chosen current surgical techniques might not be optimal for patients with C3VD who undergo TAVR.

Post-TAVR complications including paravalvular leakage, thrombosis and coronary obstruction remain as the main Achilles heels of TAVR. While coronary artery disease (CAD) is present in approximately half of TAVR candidates, correlation of post-TAVR complications such as

paravalvular leakage (PVL) or misalignment with CAD are not fully understood. To effectively evaluate risk status and create guidelines for intervention, precise quantification of aortic root and coronary artery hemodynamics is required. We used a patient-specific multiscale computational-mechanics framework in both pre and post TAVR states to investigate the effect of TAVR complications such as PVL and misalignments on the coronary arteries and aortic root hemodynamics. The proposed framework could provide a platform for testing the intervention scenarios and evaluating their influences on the hemodynamics.

# Acknowledgements

I would like to acknowledge first and foremost Prof. Zahra K. Motamed for her boundless support, continues guidance and continued dedication from the first day and during the course of my PhD. I am also thankful to my co-supervisor Prof. Ali Emadi for his support and precious feedbacks and suggestions during my PhD. I had the best supervisor and co-supervisor, and this work could not have been accomplished without their continues and endless motivation, professional supervision, and encouragement. Their precious advice guided me throughout my research and prepared me for the next chapter of my life.

I had the privilege to have the distinguished researchers with different backgrounds in my PhD defence committee. I would like to thank Prof. Juan C. del Alamo for accepting to be the external member of my PhD defense committee and for his valuable comments. I sincerely appreciate my supervisory committee members Prof. Stephen Tullis and Dr. Javier Ganame for their time and constructive comments during my PhD. I would like to give special thanks to Prof. Jonathon Leipsic, Dr. Philipp Blanke, and Dr. Stephanie Sellers from University of British Colombia to provide us clinical data and to assist us to analyze them.

In my entire PhD study, I would like to appreciate the valuable assistance of my colleagues and friends in Motamed Lab, Dr. Reza Sadeghi, Louis Garber, Alison Henstock, Melissa Baiocchi, Julia Bauer, Mohamed Abdelkhalek whose inputs helped me to fulfill the goals of my project. I also thank all the faculty, staff, and graduate students at the department of mechanical engineering for all their help and support.

This work was supported by NSERC Discovery Grant (RGPIN-2017-05349) and NSERC CRD Grant (CRDPJ 537352 - 18) which I am very thankful.

Beyond everything, I would like to thank my parents and my wife, Clara, for the unconditional love and support. I would not be who I am today without their unwavering love and kindness. The generosity, patience and support they have provided me through so many challenges are immeasurable.

# Contents

# List of Figures

# List of Tables

# Nomenclatures

| | | | |
|---|---|---|---|
| Vs | Velocity of the surface | $R_{SV}$ | Systemic vein resistance |
| F | Deformation gradient tensor | $C_{SAC}$ | Systemic arteries and veins compliance |
| τ | Relaxation time | $R_{SA}$ | systemic arteries resistance (including arteries, arterioles, and capillaries) |
| ∀ | Volume | $R_{PDA}$ | Proximal descending aorta resistance |
| I | Identity tensor | $R_{ub}$ | Upper body resistance |
| ∑ | Piola-Kirchhoff stress tensor | $P_{CV0}$ | Central venous pressure |
| $\rho$ | Density | $Q_{mv}$ | Mitral valves mean flow rate |
| u | Velocity | E | Elastance |
| σ | Cauchy stress tensor | $A_{LVOT}$ | LVOT area |
| λ | Lame's constants | $PG_{net}$ | pressure gradient formulation |
| E | Green-Lagrangian strain tensor | $t_{ee}$ | End-ejection time |
| $\rho_s$ | Density of the LV structure | $T_{EJ}$ | ejection time |
| Ω | Vorticity tensor | ΔP | Pressure gradient |
| $S$ | Rate of strain tensor | $m_1$ | Elastance ascending gradient |
| Q | Q-criterion | $m_2$ | Elastance descending gradient |
| $T_{EJ}$ | Ejection time | $L_{PV}$ | Pulmonary Vein Inertance |
| δij | Kronecker delta | $R_{PV}$ | Pulmonary Vein Resistance |
| p | Pressure | $R_{PVC}$ | Pulmonary Vein and capillary Resistance |
| $\vec{\tau}$ | Wall stress vector | $C_{PVC}$ | Pulmonary Vein and Capillary Compliance |
| $\vec{n}$ | Normal vector | $L_{PC}$ | Pulmonary Capillary Inertance |
| Re | Reynolds number | $R_{PC}$ | Pulmonary Capillary Resistance |
| μ | Dynamic Viscosity | $R_{PA}$ | Pulmonary Arterial Resistance |
| $R_{ao}$ | Aortic resistance | $C_{PA}$ | Pulmonary Arterial Compliance |
| $C_{ao}$ | Aortic compliance | $Q_{MPV}$ | Mean Flow Rate of Pulmonary Valve |
| T | Duration of cardiac cycle | $P_{CV0}$ | Central venous pressure |
| R | Coefficient of determination | $\tau_1$ | Ascending time translation |

| | | | |
|---|---|---|---|
| N | Elastance normalization | $\tau_2$ | Descending time translation |
| $R_{cor,p}$ | Proximal Coronary Resistance | $R_{cor,d}$ | Distal Coronary Resistance |
| $R_{cor,m}$ | Medial Coronary Resistance | $C_{cor,p}$ | Proximal Coronary Compliance |
| $C_{cor,m}$ | Medial Coronary Compliance | MAP | Mean arterial pressure |

# Abbreviations

| | | | |
|---|---|---|---|
| FSI | Fluid structure interaction | BAV | Bicuspid aortic valve |
| CFD | Computational fluid dynamics | CMR | Cardiac magnetic resonance |
| VFM | Vector flow mapping | IVUS | Intravascular ultrasound |
| ALE | Arbitrary Lagrangian–Eulerian | LVH | Left ventricular hypertrophy |
| FVM | Finite volume method | ASE | American Society of Echocardiography |
| SAVR | Surgical replacement of the aortic valve | AS | Aortic stenosis |
| CAD | Coronary artery disease | AR | Aortic regurgitation |
| LPM | Lumped parameter modelling | MS | Mitral stenosis |
| BC | Boundary conditions | MR | Mitral regurgitation |
| PVL | Paravalvular leakage | LVOT | Left ventricular outflow tract |
| STL | Stereolithography | SAC | Systemic arterial compliance |
| CT | Computed Tomography | EOA | Effective orifice area |
| CTA | Computed tomographic angiography | TAVR | Transcatheter aortic valve replacement |
| DE | Doppler Echocardiography | TPG | Transvalvular pressure gradient |
| MRI | Magnetic Resonance Imaging | EDV | End diastolic volume |
| PC | Phase contrast | ESV | End systolic volume |
| VFM | Colour-Doppler vector flow mapping | HR | Heart rate |
| Ao | Ascending aorta | LA | Left Atrium |
| LMCA | Left main coronary artery | SD | Standard deviations |
| LAD | Left anterior descending | PP | pulse pressure |
| LCX | Left Circumflex | SV | stroke volume |
| RCA | Right coronary artery | SAC | stroke volume/pulse pressure |

| | | | |
|---|---|---|---|
| OCT | Optical coherence tomography | WSS | Wall shear stress |
| LCC | Left coronary cusp | TAWSS | Time averaged wall shear stress |
| RCC | Right coronary cusp | SI | Sphericity index |
| COA | Coarctation of aorta | VFT | Vortex formation time |
| NCC | Non-coronary cusp | VD | Viscous dissipation |
| MVD | Mixed valvular diseases | KE | kinetic energy |

# Declaration of Academic Achievement

- Chapter 1, “Introduction and literature review”, was drafted by Seyedvahid Khodaei.
- Chapter 2, “Towards a non-invasive computational diagnostic framework for personalized cardiology of transcatheter aortic valve replacement in interactions with complex valvular, ventricular and vascular disease”, Seyedvahid Khodaei performed computational modeling, data collection and analysis, interpretation of data and manuscript writing; Reza Sadeghi, Dr. Philipp Blanke and Dr. Jonathon Leipsic performed data analysis and interpretation of data; Dr. Ali Emadi performed interpretation of data and critical revision of the manuscript; Dr. Zahra Keshavarz-Motamed performed conception and design, data analysis, algorithm development (LPM), interpretation of data, manuscript writing, critical revision, final approval of the manuscript and supervised this research.
- Chapter 3, “Personalized intervention cardiology with transcatheter aortic valve replacement made possible with a non-invasive monitoring and diagnostic framework”, Seyedvahid Khodaei performed Fluid–structure interaction and computational framework development, data collection and analysis, interpretation of data and manuscript writing; Alison Henstock performed interpretation of data and manuscript writing; Reza Sadeghi performed data analysis; Dr. Stephanie Sellers, Dr. Philipp Blanke and Dr. Jonathon Leipsic performed data collection and analysis; Dr. Ali Emadi performed data analysis, interpretation of data and critical revision of the manuscript; Dr. Zahra Keshavarz-Motamed performed conception and design, data analysis, algorithm development (LPM), interpretation of data, manuscript writing, critical revision, final approval of the manuscript and supervised this research.

- Chapter 4, “The interplay between paravalvular leakage and coronary arteries following TAVR: quantification and systematic differentiation using clinical measurements and image-based patient-specific in silico modeling”, Seyedvahid Khodaei performed conception and design, FSI development, data collection and analysis , interpretation of data, manuscript writing and critical revision; Louis Garber performed data analysis, algorithm development (LPM) and manuscript writing; Julia Bauer performed Interpretation of data and manuscript writing; Dr. Ali Emadi performed data analysis, interpretation of data, and supervision; Dr. Zahra Keshavarz-Motamed performed conception and design, data analysis, algorithm development (LPM), interpretation of data, manuscript writing, critical revision, final approval of the manuscript and supervised this research.
- Chapter 5, “Reducing long-term mortality post-TAVR requires systemic differentiation of patient-specific coronary hemodynamics”. Seyedvahid Khodaei performed conception and design, FSI development, data collection and analysis , interpretation of data, manuscript writing and critical revision; Louis Garber performed data analysis, algorithm development (LPM) and manuscript writing; Mohamed Abdelkhalek performed statistical analysis and interpretation of data; Dr. Ali Emadi performed data analysis, interpretation of data, and supervision; Dr. Zahra Keshavarz-Motamed performed conception and design, data analysis, algorithm development (LPM), interpretation of data, manuscript writing, critical revision, final approval
- Chapter 6, “Conclusions and Future Direction” was drafted by Seyedvahid Khodaei.

# Chapter 1: Introduction and literature review

## 1.1 Aortic valve stenosis

Aortic stenosis (AS), mainly caused by progressive calcification of aortic valve, is one of the most common chronic cardiovascular diseases in the world [1]. AS is specified by reduced aortic valve opening area, following which the valve cannot fully open and has restricted motion [2]. Calcific degeneration is the most common etiology for AS with an increased prevalence with age [2]. Among all heart valve disease, AS is the most prevalent of all and occurs in up to 7% of individuals older than 65 and up to 10% of patients over the age of 80 [1–3]. Heart failure is the primary cause of death for AS patients, and if aortic valve disease is left untreated , 50% of the patients with AS will die within two years of symptom onset [4].

AS can be asymptomatic (i.e., patient has a good outlook even with severe complications) or symptomatic with angina, syncope and heart failure [3]. In most cases, AS is associated with other cardiovascular defects, including left ventricle hypertrophy [5], diastolic dysfunction [6], coronary artery disease [7], arrhythmia [8], atrial fibrillation [9] and stroke [10].

Aortic valve replacement is now a routine clinical procedure for patients suffering from AS and transcatheter interventions are exponentially growing [11]. Nevertheless, despite the advancements in interventional and surgical techniques, large-scale data on long-term outcomes of surgical or transcatheter interventions are scarce and patients with aortic valve interventions and surgeries require close monitoring because of acute post-surgical complications, including hypertension, structural valve deterioration, valve thrombosis, cerebrovascular events, and prosthetic valve endocarditis [11]. In addition, in some cases, the situation worsens or the pre-existing cardiovascular disease changes to another form of cardiovascular disease [12–15].

## 1.2 Associated cardiovascular complications with aortic stenosis

Patients with severe AS are referred to valve replacement, only if they are symptomatic [16]. However, prior to the onset of severe symptoms, the left ventricle is under continues pressure overload and afterload due to the left-ventricular outflow obstruction, which subsequently lead to other complications such as hypertrophy, impaired ejection fraction, systolic and diastolic dysfunction, impaired coronary blood-flow reserve and mitral regurgitation [3,16]. Some of these complications can irreversibly damage the cardiac tissue and preclude an optimal postoperative outcome [16]. Therefore, pre-existing complication that coexist with AS would accelerate the heart failure after the onset of severe symptoms [3,17].

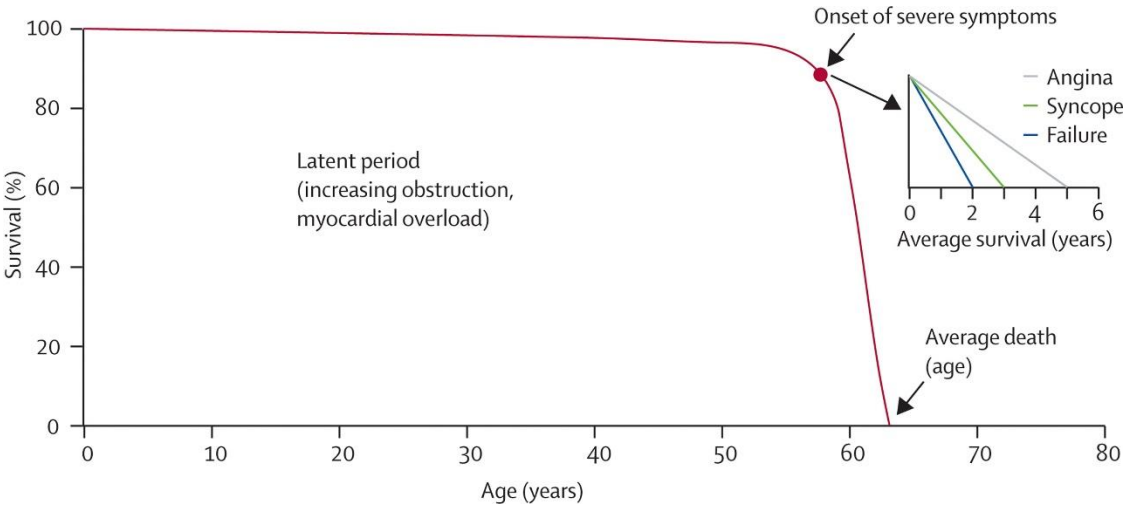


Figure 1-1. Survival of patients with aortic stenosis over time[3,17]

### 1.2.1 Left ventricular hypertrophy

Left ventricular (LV) hypertrophy is a condition in which the muscle wall of heart's left pumping chamber becomes thickened. LV hypertrophy is a response to increased afterload caused by of AS,

in order to maintain wall stress and cardiac function [5]. By the time AS becomes severe, LV hypertrophy is present in up to 2/3 of AS patients [18].

Although this process seems to be a compensatory mechanism, hypertrophy is a double-edge sword, helping to preserve ejection fraction but impairing coronary flow and diastolic function [5] . The LV hypertrophy in the long term decompensates with progressive cell death and fibrosis which is associated with heart failure and sudden death [5,19].

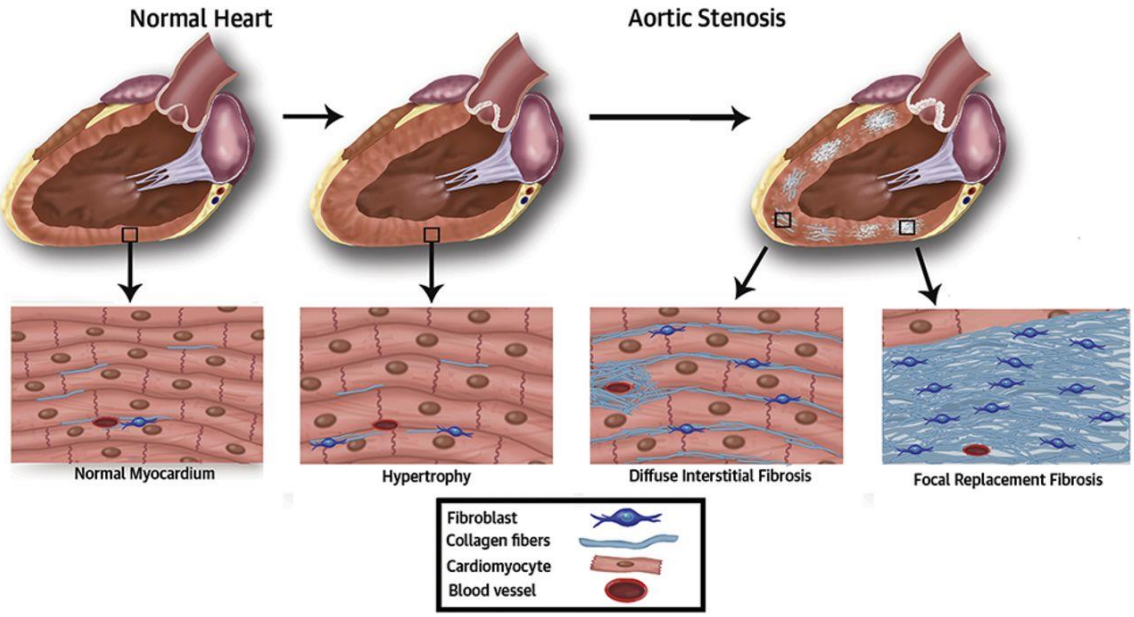


Figure 1-2. LV hypertrophy and myocardial fibrosis in AS patients [20]

### 1.2.2 Diastolic dysfunction

Diastolic dysfunction refers to the impaired LV relaxation caused by stiffening of LV tissue [21]. Commonly, LV hypertrophy leads to increased stiffness of the LV chamber and diastolic dysfunction [22]. Impaired diastolic function in patients with AS is present in up to 50 percent of patients [23].

There is growing attention towards the importance of diastolic dysfunction influence on the outcomes of aortic valve replacement for AS patients [6]. It has been shown that advanced stages of

diastolic dysfunction is associated with an incremental risk of mortality in AS patients [24]. Therefore, diastolic function assessment before intervention might translate into better clinical out-comes for AS patients [6].

The severity of diastolic dysfunction can be assessed through transmittal filling pattern (early filling velocity ratio to late filling velocity, known as E/A ratio) and tissue doppler imaging of mitral annulus(e` and a`)[21,25,26].

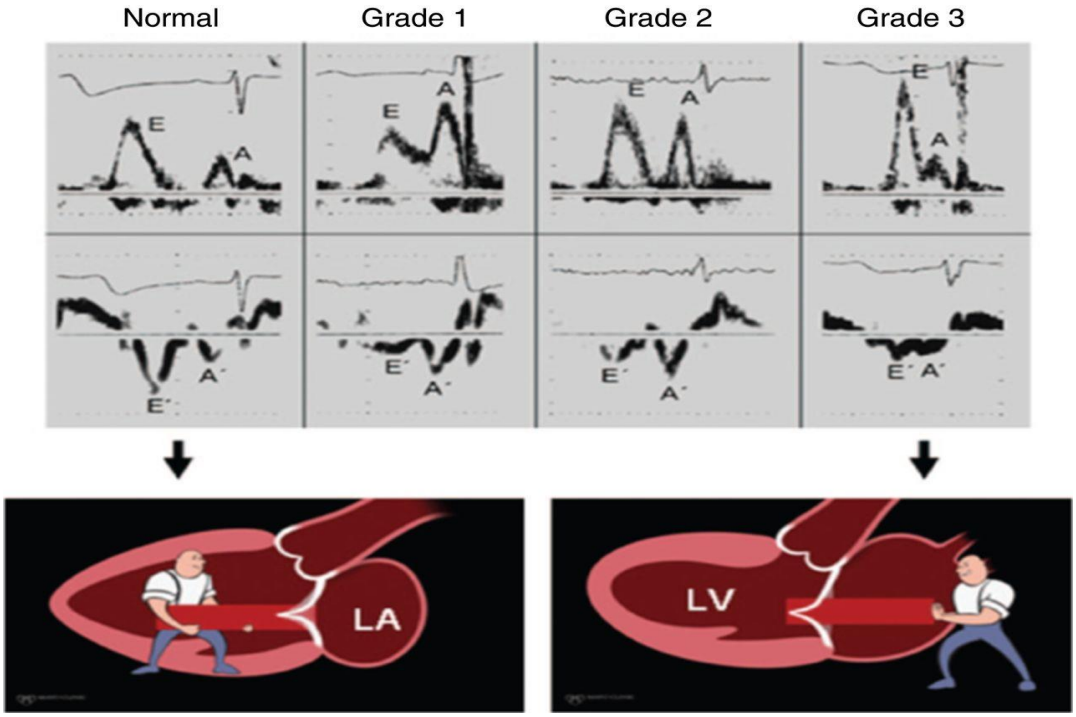


Figure 1-3. Grades of diastolic dysfunction: mild (grade 1), moderate (grade 2) and severe (grade 3) [26]

### 1.2.3 Coronary artery disease

The progression mechanism of AS is very similar to that of atherosclerosis in coronary artery disease (CAD) and there is a high coincidence of both disease in the same patient [3]. AS and CAD share several important cellular mechanisms including lipid deposition, inflammatory cell infiltration, cytokine release, and calcification [27] and CAD is present in approximately 50% of the AS patients [28]. The question, however, of if CAD should be treated or reduced in severity prior to valve intervention is still a topic for debate [28]. Patients suffering from CAD would typically undergo percutaneous coronary intervention (PCI) prior to aortic valve replacement, but some research suggests there may be less associated mortality if PCI is performed parallel to aortic valve intervention [28].

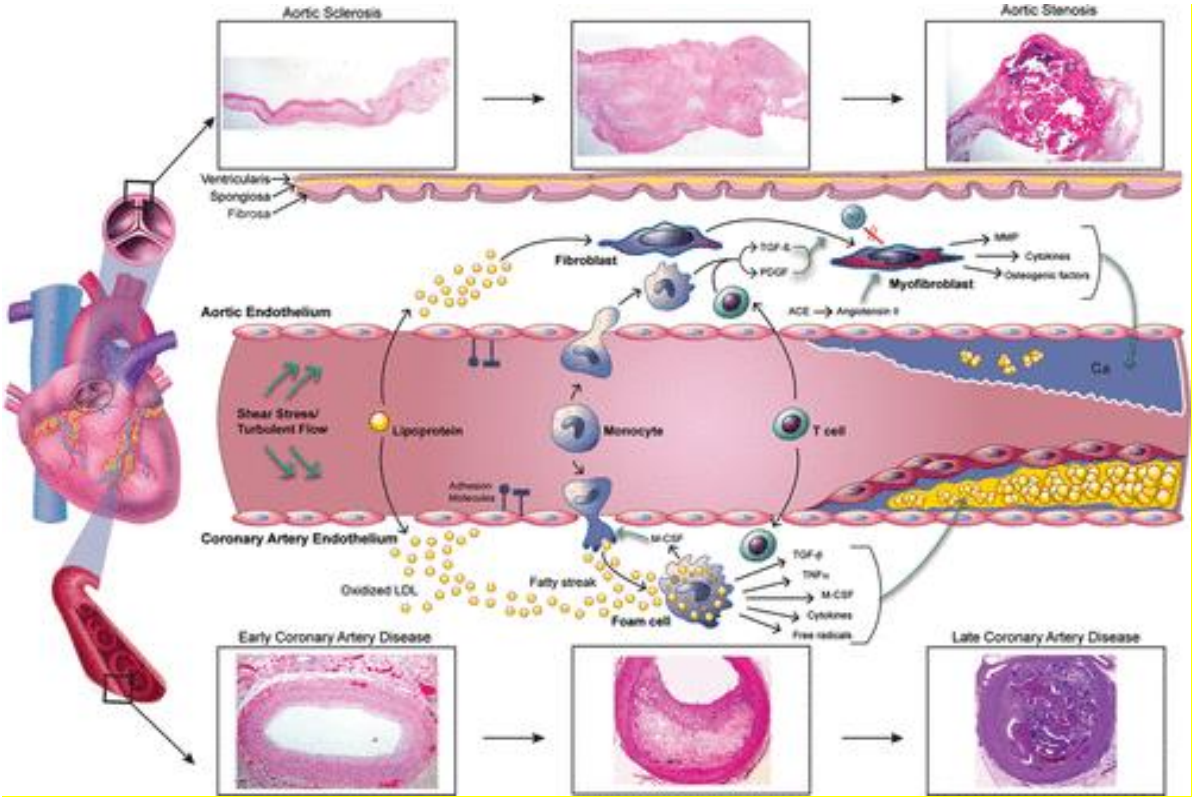


Figure 1-4. The evolution of coronary artery disease in parallel to aortic stenosis [27]

### 1.2.4 Arrhythmia and atrial fibrillation

Arrhythmia is a condition in which the heart beats with an irregular pattern. The most common arrhythmia is atrial fibrillation (AF) and is characterized by uncoordinated activation of the atria [29]. Like AS, the prevalence of AF Increases significantly with age (from 0.1% in patients<55 years to 9% in patients aged > 80 years ) [9]. Because of the overlapping risk factors for AF and AS, both of these complications may coexist in up to 50% of the patients [9].

Arrhythmia and AF attribute to the loss of atrioventricular synchrony which will lead to reduced ejected flow and increased ventricle filling pressure [9]. Moreover, new conduction abnormalities and the need for permanent pacemaker are frequent in patients with AS who receive aortic valve intervention [8]. AF is associated with a 1.5 to 1.9 fold mortality risk [9,30].

### 1.2.5 Stroke

Calcified aortic valve increases the risk of spontaneous cerebral embolism and stroke. It has been shown that AS attributes to thrombus formation, increase platelet activation and reduce fibrinolysis around the valve region [10]. Therefore, patients with AS are at significantly higher risk of cardioembolic stroke and thromboembolic events compared to background population [10].

## 1.3 Diagnostic imaging techniques

### 1.3.1 Echocardiogram

Transthoracic echocardiography is the gold standard non-invasive imaging modality for initial assessment of patients with AS [31]. As severity can be examined with the use of Doppler echocardiography by measuring hemodynamic and anatomical parameters [32]. The AS jet velocity waveform during ejection can be measured from continuous wave doppler across the aortic valve.

Afterwards, the simplified Bernoulli equation can be used to estimate the pressure gradient across the aortic valve [31]. Finally, based on the maximum velocity and pressure gradient, a decision will be made on the severity of AS.

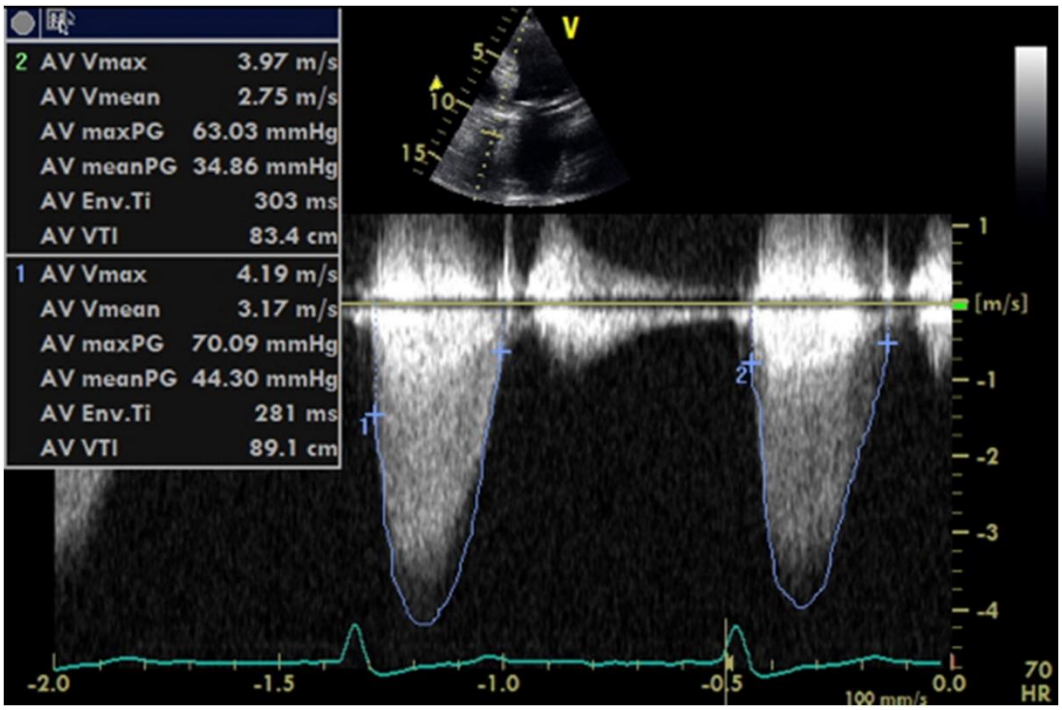


Figure 1-5. Example of aortic valve assessment using Doppler echocardiography[33]

Echocardiography is currently preferred over any other imaging modalities for assessment of patients with cardiovascular disease, thanks to its non-invasive and radiation-free nature that allows to be used for a broad spectrum of patients. However, some theoretical and technical limitations of echocardiography might attribute to some inaccuracies. The main sources of inaccuracies include (1) Improper use of Bernoulli equation for the non-steady flow which results in overestimation of peak pressure drops [34] and lower spatial resolution for accurate assessment of calcium score [35].

### 1.3.2 Cardiac catheterization

Cardiac catheterization is an invasive hemodynamic assessment tool for examining the pressure and pressure gradient. Although the usage of cardiac catheterization has become limited with the advent of echocardiography, it is still used for the patients with complicated hemodynamic conditions such as patients with low-flow low-gradient AS or patients with LV dysfunction [31]. Moreover, it is used for diagnosis and interventional planning of coronary artery disease, which is highly prevalent in patients with AS [31]. However, it is an invasive procedure and is associated with multiple risk factors including vascular bleeding, arteriovenous fistula, dissection and pseudoaneurysm [36].

### 1.3.3 Computed tomography

Computed tomography (CT) provides high resolution 3D imaging of the aortic valve, aortic root, LVOT and LV, using ionizing radiation and intravenous contrast [37]. The high-resolution CT images can contribute to accurate quantification of calcification severity and distribution which will improve diagnosis and surgical planning for patients with AS [37].

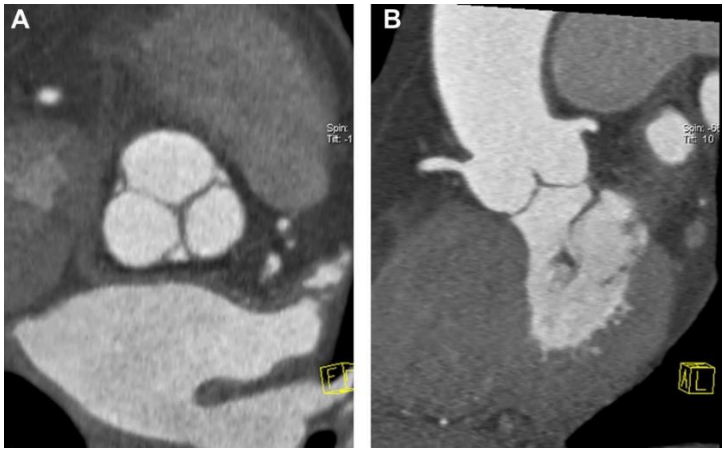


Figure 1-6. CT provides 3D high spatial resolution images: aortic valve (A) and aortic root (B) [37].

However, there are drawbacks for CT imaging which makes it a tool that should be used with caution. The primary drawbacks for CT imaging include the ionizing radiation and increased risk of cancer [38], inability to provide hemodynamic information (velocity and pressure) and low temporal resolutions [39].

### 1.3.4 Magnetic resonance imaging

Magnetic resonance imaging (MRI) is a non-invasive imaging modality that produces detailed images of the heart structures by employing a magnetic field and computer-generated radio waves. Also, 4D flow MRI provides a sophisticated tool for quantifying blood flow velocities inside the heart chambers and large vessels with reasonable temporal and spatial resolution [40]. 4D flow MRI provides tridirectional blood flow velocities, which makes it a more accurate tool for eccentric blood flow jets [40]. As mentioned previously, transthoracic echocardiography is, and will most likely remain the gold standard technique for AS evaluation. However, MRI could be a good alternative to invasive methods such as cardiac catheterization or transesophageal echocardiography [40]. It is important to note that MRI technique is susceptible to metallic artifacts. Therefore, it is not a promising imaging modality for patients who receive metallic stents and pacemaker [41]

## 1.4 Current treatments for aortic stenosis

Although there are some medical limited treatment options for moderate AS patients, such as 3-hydroxy-3-methylglutaryl-coa reductase inhibitors (statins), no medical treatment option is currently available for chronic patients with severe AS [3]. Therefore, aortic valve replacement is the clearest choice for those patients [3]. Upon referral to aortic valve replacement, there are two

general options available for patients: surgical aortic valve replacement (SAVR) and transcatheter aortic valve implantation (TAVI) (or transcatheter aortic valve replacement (TAVR)). Unlike invasive SAVR with high risk in older adults, TAVR is a minimally invasive procedure that is not inferior to SAVR[42] and might become the superior treatment modality for the whole risk spectrum [43], including younger population and low-risk patients [44].

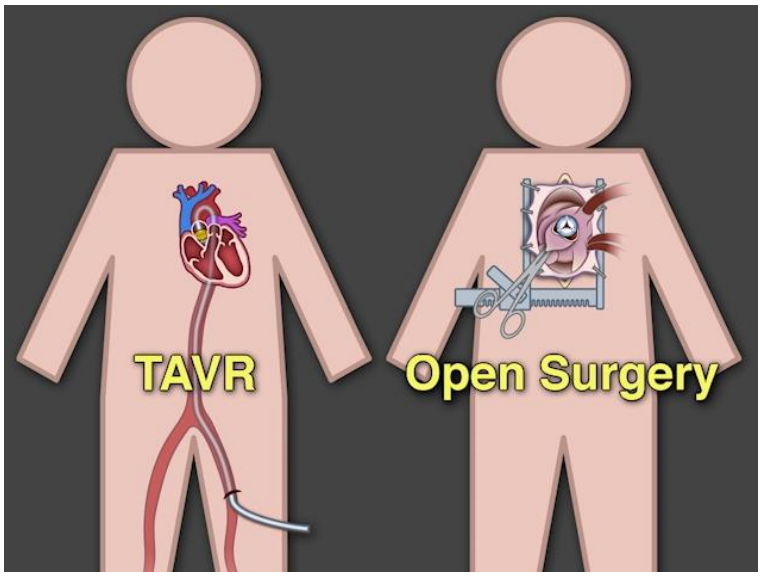


Figure 1-7. TAVR vs SAVR (open heart surgery)[45]

### 1.4.1 Surgical aortic valve replacement

The standard treatment for AS that has been used for years is surgical aortic valve replacement (SAVR) or aortic valve replacement (AVR). The prosthetic valve options for SAVR are mechanic valve and biological valve, each of which comes with some advantages and disadvantages. The decision for the best choice for each patient should be made considering all future complications such as the need for anticoagulation and valve-in-valve insertion in case of prosthetic failure[46]. Although SAVR has been the first choice of surgery for decades, its procedure is life threatening for elderly patients since it requires thoracotomy to access the heart and valve position as well as

cardiopulmonary bypass [47,48]. Observational studies have shown different subgroups of patients with advanced age or other diseases such as left ventricle dysfunction would be at high risk of death once receive AVR. A less invasive approach may be a good alternative for such patients to decrease the possibility of death [49].

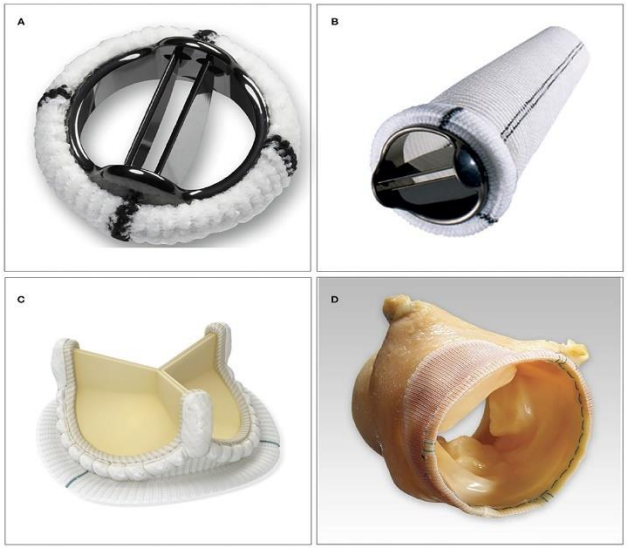


Figure 1-8. Examples of SAVR valve options: A) and B) mechanical heart valve, C) and D) bioprosthetic valves[50]

### 1.4.2 Transcatheter aortic valve replacement

As the risk-benefit ratio of invasive interventions increases with age, for older patients, non-invasive or minimally invasive interventions are preferred as they confer reduced risk of hospitalization and future complications [51]. Transcatheter Aortic Valve Replacement (TAVR) or Transcatheter Aortic Valve Implantation (TAVI) is a novel solution for the patients who are not eligible to receive invasive open-heart surgery (SAVR). This novel technique has been known as a promising solution to replace SAVR due to its most minimal invasive procedure [45,47]. However, the decision upon the type of surgery is highly dependent to many factors and conditions that must be taken into the account by the surgery team. That means an approach by the heart valve surgery

team should be examined carefully in patients who are candidates for TAVR or high risk SAVR, since TAVR outcomes are highly dependent to the improvement of patient selection by surgery team [52].

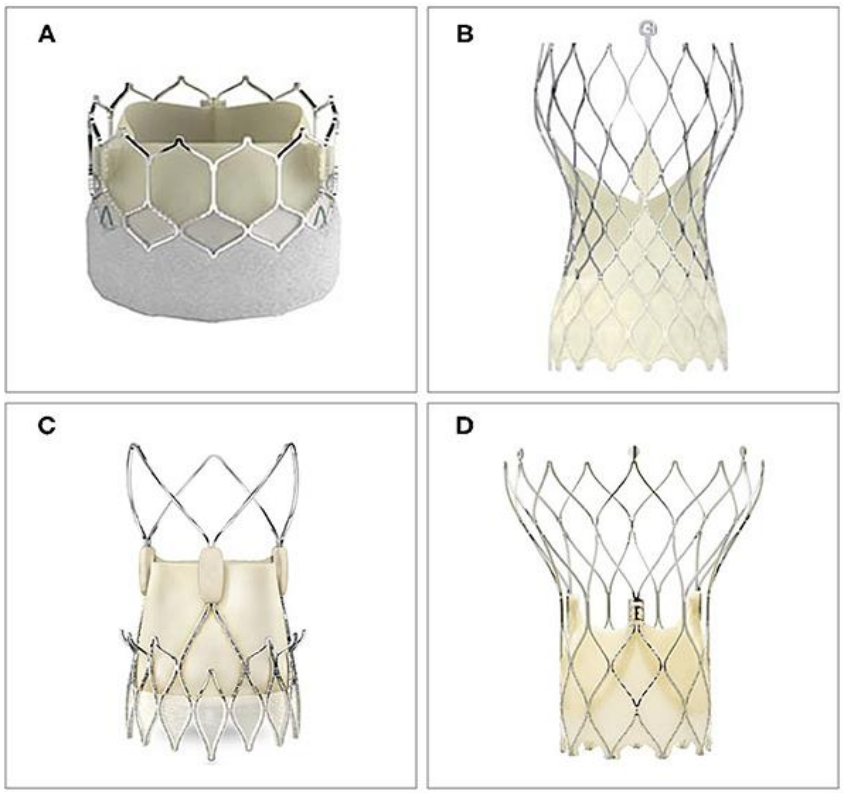


Figure 1-9. Commercially available transcatheter aortic bioprosthesis. (A) SAPIEN 3 (Ultra), (B) Evolut R/PRO, (C) ACURATE Neo (2), and (D) Portico TAVI System[50]

## 1.5 Complications of Transcatheter aortic valve replacement

After the TAVR, careful monitoring of patient condition is essential to make sure the surgery has been successful. Predicting the patient condition in the long term is the major concern that needs to be addressed carefully. Although TAVR has been proven to be a good replacement for SAVR, still some complications remain after surgery. These complications may happen during any stage of TAVR procedure and can cause irreversible problems that can lead to death. At the vascular level, toward reaching the position of aortic valve, guiding the catheter can cause vascular injury

and perforation. At the heart level, several other complications might occur. If the valve is deployed in the wrong angle or wrong position with respect to the original valve, it can cause positional shift of valve or leakage. Also, if the valve is deployed very close to the coronary arteries, which are only around 10 mm above the aortic valve, it may block the coronary inlet [53]. Choosing the size of prosthesis is a critical decision; if the size is smaller than the available space, that leads to positional shift or paravalvular leakage and if the size is bigger than a specific value, that can lead to aortic root rupture or deformation of valve (that can cause transvalvular leakage) [53]. Paravalvular leakage is a very common complication after TAVR and can affect the flow and pressure of left ventricle [54]. Either together with the above-mentioned complications or separately, thrombosis around TAVR or on the leaflets and leaflet thickening are other important complications [55].

### 1.5.1 Paravalvular leakage

Paravalvular leakage (PVL) has been known to be the most common drawback of TAVR [56]. Since the TAVR procedure is sutureless, paravalvular leakage occurs more than surgical aortic valve replacement, affecting 26% to 67% of patients [45,57]. In general, leakage in valve can be central (transvalvular), between prosthesis and deployment zone (PVL) or supra-skirtal. Therefore, PVL can occur if a TAVR is implanted too low within the annulus or if the valve does not fit completely inside the annulus. Leakage can specifically affect left ventricle (LV) and lead to changes in LV diameter, volume, and mass due to the available preload in diastole phase.

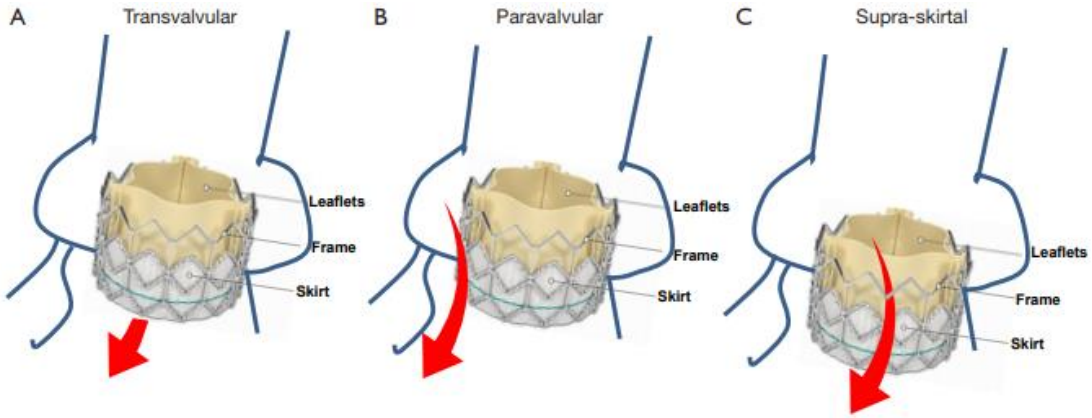


Figure 1-10. Aortic regurgitation (AR) after TAVR [54]

Prosthetsis-patient mismatch occurs when the effective orifice area (EOA) of the vale is smaller than that of a normal valve [58,59]. Prosthetic mismatches are more prevalent in female patients and will cause ventricular outflow obstruction and increased LV pressure [60]. While finding the optimum size of the valve and exact deployment location for each patient with unique anatomical and physiological characteristics is challenging, surgeons must consider the risk-benefit ratio of implantation depth and potential risks for device migration, conduction disturbance and thrombosis on a case by case basis [61].

### 1.5.2 Valve leaflet thrombosis

Most recently, clinical, or sub-clinical valve thrombosis (detected by hypo-attenuating leaflet thickening or HALT) has shown to restrict valve leaflet mobility and increase the risk of early valve deterioration or consequent embolic stroke [62–64]. The prevalence of leaflet thrombosis and subclinical HALT is uncertain with reported frequencies up to 30% for leaflet thrombosis [65] and up to 40% for HALT [66] in the literature. Despite those unfavorable trends, there is still no clear understanding of hemodynamic details correlations with clinical outcomes [67–69]. Among the

previously reported potential causes of post-TAVR thrombosis including THV metallic frame material, incomplete valve expansion, patients coexisting prothrombotic conditions and diminished blood flow and stagnation [70,71], most recent studies have shown a strong correlation between blood stasis in sinus and neo-sinus region and thrombus formation [72].

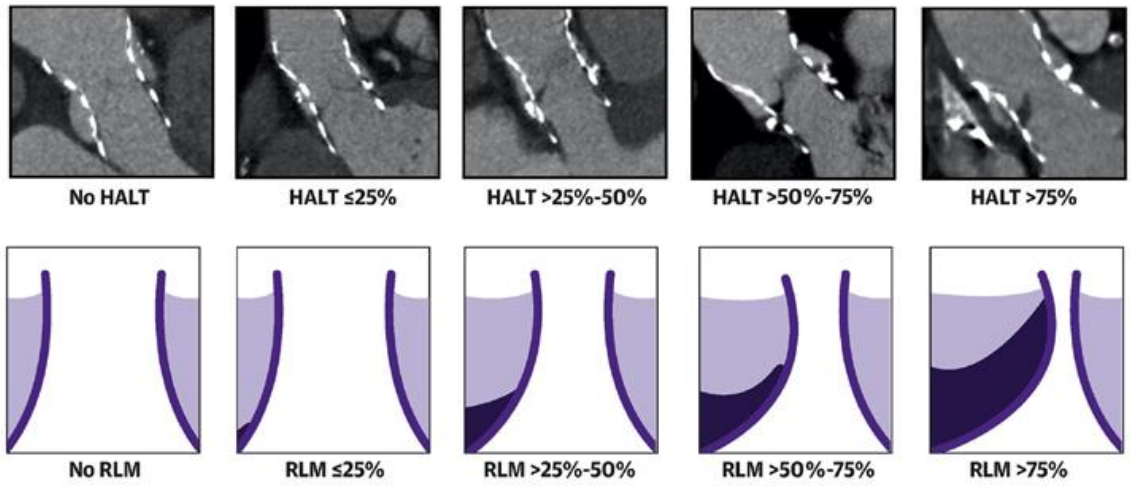


Figure 1-11. The Frequency and Extent of Hypoattenuated Leaflet Thickening (HALT) [69]

Obstruction to the coronary arteries is caused by several factors, including but not limited to, calcification of the leaflets which become displaced into the coronary ostia, the coronary ostia being anatomically lower, and incorrect placement of the transcatheter heart valve (THV) [73,74]. This event may immediately follow TAVR or can be delayed especially in self-expanding TAVR cases [75]. A patient suffering with coronary artery obstruction will typically present with severe hypertension and ventricular arrhythmias[75]. Revascularization and the use of stents may be necessary, but it is more important to thoroughly assess a patient's risk prior to the procedure [75].

## 1.6 Computational modelling

### 1.6.1 Numerical modelling of the Cardiovascular System

Over the recent years, high fidelity multiscale patient-specific cardiovascular simulations have proven their capability to become a powerful tool for improving cardiovascular research, medical device optimization and interventional planning [76,77]. While medical imaging techniques have revolutionized the non-invasive diagnostic capabilities of clinicians, areas of uncertainty remain in understanding patient's condition. In addition to traditional echocardiography, modern imaging modalities such as CT, 3D MRI and 4D-MRI provide an appreciable amount of information on the morphology of cardiovascular organs including LV, aortic valve, mitral valve, atrium, aorta, etc. as well as measurement of velocity field. However, none of the current imaging modalities is currently able to provide the precise pressure of atrium, LV, aorta and across the heart valves (aortic valve and mitral valve). In addition, the important hemodynamic parameters such as wall shear stress cannot be accurately obtained by low spatial resolution flow measurement from medical imaging (including echo and 4D flow MRI), as this parameter is very sensitive to accurate quantification of blood flow (with high spatial resolution) near the tissue wall [78]. It is important to note that inaccurate quantification of such important hemodynamic parameters might result in incorrect interpretation of data [79].

With the rapid progress in the field of computational fluid dynamics (CFD) and modern 3D imaging techniques over the recent years, it is now possible to simulate velocity and pressure filed in virtual models of cardiovascular system in a patients-specific manner. The fusion of CFD with subject-specific input parameters (e.g., flow measurement and anatomical geometries) can provide a powerful tool with high spatial and temporal resolution data for diagnosis, prediction and surgical planning [78,80–82].

### 1.6.2 Computational modelling of transcatheter aortic valve replacement

During last decade, there has been an emerging interest in numerical simulation of TAVR. The first computational fluid dynamics (CFD) modelling of TAVR was performed by Dwyer et al. [83] in 2009 to calculate the migration force of prosthesis. Also, the first effort towards patient-specific simulation was done in 2011 by Sirois et al. [84]. Since then, there have been multiple studies with a focus on prosthesis deployment, as it could predict the final position of valve at the aortic root and also can provide the induced stress at the aortic wall [85–87]. Also several studies have been performed to understand the interactions of blood flow across the heart valves [88] and within the left ventricle [89–91]. However, there is still a scarcity of a quantitative understanding of the interplay between pre-existing pathologies and post-TAVR recovery. Further studies are needed to elucidate the relationship between valvular diseases, left ventricle remodeling and TAVR. Effective quantification hinges on quantification of the local and global blood flow dynamics. With the ongoing developments and enhancement of computational resources, the combination of high-fidelity personalized numerical simulation and in vivo data could provide an ideal diagnostic and predictive tool for a complete virtual model of TAVR procedure.

### 1.6.3 Fluid-structure interaction modelling

Different numerical techniques including computational fluid dynamics (CFD), finite element analysis (FEM) and fluid-solid interaction (FSI) have been used recently to simulate structural and local hemodynamics of aortic valve leaflets [92]. Among all those numerical methods, FSI can overcome the limitations of rigid tissue assumption, by coupling the fluid model with a structure solver. Since the traditional Lagrangian-Eulerian method with the comprehensive description of fluid and solid domain is challenging for heart valve simulation, other simplified FSI formulations

such as immersed boundary method and smoothed particles hydrodynamics (SPH) are preferred in recent years [92]. The immersed boundary method assumes that the valve is a thin elastic structure embedded inside the fluid domain, making it suitable for overcoming the challenges of large deformation of solid domain [93,94]. Therefore, the numerical simulation of heart valve is achieved by simplifying the structural solver. However, the validation and agreement between immersed boundary simulations and experimental tests are not satisfying yet [94]. On the other hand, SPH method uses a simplified meshless analysis for the fluid domain to overcome the numerical challenges [91,95]. However, SPH method suffers from accuracy in the computational domain [96] and there is still no rigorous validations in the previous studies [91,95]. Therefore, more work is needed to prepare the heart valve FSI simulation as a reliable tool to be used in regulatory process [92].

Regarding left ventricle flow, because there is no inlets and outlets at the same time during cardiac cycle (inlet only during diastole and outlet only during systole) the FSI modelling is necessary to achieve mass conservation. Left ventricles tissue is a complex multilayer structure and several empirical models have been designed to describe its behaviour [97–100]. These models are based on ex-vivo experimental results from animal hearts, with considerable structural differences from human hearts [101]. Due to the complexities of in-vivo quantification of LV tissue behaviour, several studies focused on the blood flow simulation assuming that the LV tissue is a moving surface with extracted motions from MRI images [102–104] . In other words, the effect of LV tissue is excluded, and tissue is treated as a moving wall. Other studies have tried to obtain patient-specific simulations of the LV tissue by calibrating material properties with the displacement fields obtained from patients MRI data[105,106]. In addition to 3D MRI imaging, tensor diffusive MRI is required for accurate quantification of myocardial fibers and anisotropic characteristics of LV

tissue [107–109]. While most of the studies included MRI data into the FSI model for blood flow simulation inside the ventricle, it is not a practical imaging modality for patients with TAVR [110,111].

### 1.6.4 Critical role of lumped parameter model-based boundary conditions

Given the complexity of cardiovascular system and the outrageous computational cost of modelling hemodynamics in the entire circulatory system, computational fluid dynamic models are limited to only a specific region of cardiovascular system and boundary conditions are applied to account for downstream and upstream. The accuracy of computational models are, therefore, very dependent to the accuracy of boundary condition. With the advances in precision medicine for valvular and ventricular diseases, proper application of personalized boundary conditions for computational models of TAVR is crucial for translating numerical models into clinical practice [39,112]. Unfortunately, accurate hemodynamic clinical data in all the domains is often unavailable, and several current studies use non-patient specific boundary conditions for their computational simulations [91,113–115].

Currently only lumped parameter models (LPM) are capable of quantifying the global hemodynamics and to overcome the difficulties of providing accurate boundary conditions for computational models [116,117]. LPM models can provide patient-specific boundary conditions for all different parts of cardiovascular system from aorta[118] , to ventricle [119], valves [120][ and coronary arteries [121]. Such LPM models though, must be patient-specific and developed based on case by case clinical data [116]. In addition, the LPM models should be based on non-invasive input parameters such as routine echocardiography or sphygmomanometer [122]. The combination of accurate boundary conditions and exponential growth of computational capabilities, makes the future of personalized cardiovascular simulation (including TAVR) very promising.

## 1.7 Objectives of the thesis

The present research's aims and objectives are as follows:

**Aim 1:** To develop an innovative imaged-based patient-specific computational fluid dynamics framework for patients with C3VD who undergo TAVR that uses fluid-structure interactions method and lumped-parameter modeling that is solely based on routine non-invasive clinical patient data.

**Aim 2:** To validate the proposed framework against clinical Doppler echocardiographic measurements.

**Aim 3:** To investigate the interplay between paravalvular leakage and coronary arteries following TAVR to evaluate risk status of future coronary artery stenosis.

**Aim 4**: To investigate the impact of TAVR deployment characteristic and anatomical parameters on coronary hemodynamics to provide novel hemodynamic analysis and interpretation of clinical data to predict coronary artery disease progression.

## 1.8 Thesis organization

**Chapter 1:** "Introduction and literature review". This chapter provides a general introduction to the research by describing aortic stenosis and transcatheter aortic valve replacement. Moreover, different relevant clinical imaging modalities, invasive diagnostic methods, and heart valve treatment options are also discussed in terms of their advantages and drawbacks. This chapter also provides the background and state of the art literature on computational modelling with a focus on TAVR.

**Chapter 2:** "Towards a non-invasive computational diagnostic framework for personalized cardiology of transcatheter aortic valve replacement in interactions with complex valvular, ventricular and vascular disease". This chapter covers the development of a novel non-invasive method that can quantify local and global hemodynamics for patients who undergo TAVR. This computational framework uses fluid-structure interactions method and lumped-parameter modelling that only rely on routine non-invasive clinical patient data. Our findings proved the capability of this framework to be used as a promising new non-invasive diagnostic tool that can provide diagnostic analyses not possible with conventional diagnostic methods. The proposed framework was validated against clinical Doppler echocardiographic measurements. It is shown that the framework can provide diagnostic information that is needed to assess the efficacy of TAVR, patient risk and clinical outcomes.

**Chapter 3:** "Personalized intervention cardiology with transcatheter aortic valve replacement made possible with a non-invasive monitoring and diagnostic framework". In this chapter, we used our developed framework to investigate the impact of pre-existing complex vascular, ventricular, and valvular diseases on the outcomes of TAVR. The proposed patient-specific computational-mechanics framework combines the local hemodynamics with the global circulatory cardiovascular system using the fluid-structure interaction method along with lumped parameter modeling. The computational framework was also validated against clinical Doppler echocardiographic measurements data for both pre- and post-TAVR states.

**Chapter 4:** "The interplay between paravalvular leakage and coronary arteries following TAVR: quantification and systematic differentiation using clinical measurements and image-based patient-specific in silico modeling". In this chapter, we developed a new non-invasive method that can quantify local and global hemodynamics of aortic root and coronary arteries for patients with TAVR to investigate post-TAVR complications such as PVL. It was shown that PVL after TAVR might disturb the flow patterns of neo-sinus region and aortic root which would contribute to increased blood stagnation at the neo-sinus region and irregular flow inside coronary artery vessels. Since treatment strategies for patients with PVL and CAD are quite unclear and differ on an individualized basis, we used our patient-specific numerical framework to investigate the effects of PVL on coronary artery hemodynamics in terms of both local and global hemodynamic.

**Chapter 5: "**Reducing long-term mortality post-TAVR requires systemic differentiation of patient-specific coronary hemodynamics". In this chapter, we investigated the impact of TAVR characteristics and aortic sinus variations on the coronary hemodynamics in 31 patients who received TAVR. Our non-invasive patient-specific framework was used to quantify blood flow through aortic root and coronary arteries. As majority of the patients who receive TAVR end up with CAD in the long run, our results can provide insights into possible reasons for CAD and heart failure after TAVR.

**Chapter 6:** "Conclusion and future works". This chapter puts the important findings from each of the previous chapters together. Moreover, some new exploratory research directions for future work were proposed.

# Chapter 2: Towards a non-invasive computational diagnostic framework for personalized cardiology of transcatheter aortic valve replacement in interactions with complex valvular, ventricular, and vascular disease

Seyedvahid Khodaei[1], Reza Sadeghi[1], Philipp Blanke[2,3], Jonathon Leipsic[2,3], Ali Emadi [1,4], Zahra Keshavarz-Motamed*[1,5,6]

1. Department of Mechanical Engineering, McMaster University, Hamilton, ON, Canada
2. St. Paul's Hospital, Vancouver, British Columbia, Canada
3. Department of Radiology, University of British Columbia, Vancouver, British Columbia, Canada
4. Department of Electrical and Computer Engineering, McMaster University, Hamilton, ON, Canada
5. School of Biomedical Engineering, McMaster University, Hamilton, ON, Canada
6. School of Computational Science and Engineering, McMaster University, Hamilton, ON, Canada

*International Journal of Mechanical Sciences*, 202, 106506 (2021).
https://doi.org/10.1016/j.ijmecsci.2021.106506

* Correspondence author

## 2.1 Abstract

Aortic stenosis is an acute and chronic cardiovascular disease that often coexists with other complex valvular, ventricular and vascular diseases (C3VD). Transcatheter aortic valve replacement is an emerging less invasive intervention for patients with aortic stenosis. Although hemodynamics quantification is critical for accurate and early diagnosis of aortic stenosis and C3VD, proper diagnostic methods for these diseases are still lacking because fluid-dynamics methods, that can be used as engines of new diagnostic tools, are not well developed yet. As the heart resides in a sophisticated vascular network which imposes a load on the heart, effective diagnosis requires quantifications of the global hemodynamics (metrics of circulatory function and metrics of cardiac function), and of the local hemodynamics (cardiac fluid dynamics). To enable the development of new non-invasive diagnostic methods that can quantify local and global hemodynamics, we developed an innovative computational-mechanics and imaging-based framework that only needs patient data routinely and non-invasively measured in clinics. We not only validated the framework against clinical cardiac catheterization and Doppler echocardiographic measurements but also, we demonstrated its diagnostic utility in providing novel analyses and interpretations of clinical data.

## 2.2 Introduction

Aortic stenosis is an acute and chronic cardiovascular disease. In this disease, the aortic valve is damaged and no longer works properly. This condition can rapidly affect the pumping action of the heart and can progress to heart failure. Heart failure is a deadly disease affecting at least 26 million people worldwide with high mortality and morbidity [1]. If aortic valve disease is left untreated in these patients, 50% of them will die within two years of developing symptoms. Most importantly, in many patients, aortic valve disease coexists with other diseases making the most general and fundamentally challenging condition: complex valvular, ventricular, and vascular diseases (C3VD). In C3VD, multiple valvular, ventricular and vascular pathologies interact with one another mechanically wherein physical phenomena associated with each pathology magnify the impact of others on the cardiovascular system [2–8].

Until recently, the only possible choice for high-risk patients with aortic stenosis was surgical replacement of the valve. Transcatheter aortic valve replacement (TAVR) is an emerging less invasive intervention and is a growing alternative for patients with aortic stenosis which is *increasingly used in lower-risk (moderate valvular disease and/or young)* patients as well. Although TAVR has had notable success, there are risks associated with TAVR procedures. It was shown that many patients experience a significant improvement after TAVR intervention but in many others, the situation worsens or the pre existed valvular disease changes to other forms of cardiovascular diseases [2–4,6]. One example of such major complications, with significant impacts on mortality, after TVR is heart failure [2–4,6]. The risk of congestive heart failure can be substantially increased due to worsening the valvular disease that may lead to left-ventricle volume overload and an increase in the left-ventricle load. Another example of such major complications after TVR is a back flow from the aorta to the left ventricle known as paravalvular leak. Paravalvular leak is

an independent predictor of mortality following TVR. Paravalvular leak may result in hemolytic anemia [9] and severe anemia may even manifest itself as heart failure, and may contribute to bacteremia which results in developing infective endocarditis that can destroy heart valves [9]. To safely use TAVR in patients, it is imperative to answer a series of questions: Who will benefit from costly TAVR? If performed, what impacts will there be on the heart mechanics and function? What is the best timing for intervention? Is there a means to assess which patients will do worse and which better? A tool that can answer these questions in each patient considering his/her specific conditions is highly needed.

*"Cardiology is flow"* [10]. Fluid mechanics plays a vital role in the development, progression, diagnosis, and treatment of cardiovascular disease [11–16]. Indeed, the essential sources of cardiovascular mortality and morbidity can be explained on the basis of adverse hemodynamics: abnormal biomechanical forces and flow patterns, leading to the development and progression of cardiovascular disease [14,15,17–19]. Despite its importance and advances in medical imaging, as described in the following, the current clinical diagnostic tools cannot sufficiently quantify flow conditions in patients with many cardiovascular diseases, including in patient with C3VD who undergo TAVR. Cardiac catheterization is used as the clinical gold standard for evaluating heart function and metrics but it is invasive and carries high risk [20] and therefore not practical for diagnosis in routine clinical practice. Phase-contrast magnetic resonance imaging can provide 3-D flow field (local hemodynamics) but it has a low temporal resolution [21,22] and it cannot be used for patients with most implanted medical devices except safely for MRI-conditional devices. Doppler echocardiography (DE) is potentially the most versatile tool to quantify blood flow (local hemodynamics). While 3-D DE suffers from a low temporal resolution, 2-D colour DE is low-cost and risk-free, and has high temporal resolution. Recent advances in DE velocity measurements

are: (1) Echo-PIV is an adaptation of Particle Image Velocimetry (PIV) for computing flow velocity by tracking speckles often enhanced with contrast agents (microbubbles) [23–25]. Echo-PIV is promising but depending on the acquisition frame rate, high velocities can be underestimated [26], which has implications for diagnosis. In addition, the contrast agent must constantly and homogeneously fill the field to avoid both saturated and dark areas. These may hinder routine clinical application of the method [27]; (2) Colour-Doppler vector flow mapping (VFM) permits calculation of the velocity field without contrast agents through colour DE [28]. Despite all potentials that DE has and the progresses that were made, there is no DE method to date to evaluate local hemodynamics comprehensively in the LV, valves, ascending aorta and left atrium in terms of 3-D flow, vortical structures and their temporal evolutions (local hemodynamics). There is also no DE method to evaluate global hemodynamics and to breakdown contributions of each component of the cardiovascular diseases.

There has been an emerging conclusion by many researchers that valvular disease is a complex disease that also depends on the dictates of the ventricle and the vascular system [29–39]. Indeed, the quantitative investigations of hemodynamics in patients with C3VD who undergo TAVR should take the interactive coupling of the valve, ventricle, and the vascular system into account [29–39]. The following three hemodynamics quantification capabilities are required to enable clinically-useful computational diagnostic frameworks for patients with C3VD who undergo TAVR. The required quantities are: **global** hemodynamics metrics advocated by [39–49] as follows: **(1)** ***Metrics of circulatory function,*** e.g., detailed information of the dynamics of the circulatory system, and **(2)** ***Metrics of cardiac function***, e.g., heart workload and its contribution breakdown of each component of the cardiovascular diseases; **local** hemodynamics metrics advocated by [8,13,50–54]: **(3)**

***Cardiac fluid dynamics***, e.g., details of the instantaneous 3-D flow, vortex formation, growth, eventual shedding, and their effects on fluid transport and stirring inside the heart.

The recent advances in fluid dynamics can enable the development of novel fluid-dynamics methods that can be used as engines of new patient-specific diagnostic tools to sufficiently quantify flow conditions and satisfy the three requirements described above. In patients with C3VD who undergo TAVR, analysis of blood flow using these fluid-dynamics methods necessitate a combination of image analysis and 3-D model reconstruction, imposing boundary conditions, identification of material properties, and accurate solution of the governing equations. Several studies quantified blood flow (local hemodynamics) inside the LV using computational fluid dynamics (CFD) based on the discretization of Navier-Stokes equations (finite volume method, finite element method, etc.) with moving boundaries [55–64]. However, these studies did not consider the LV tissue characteristics (e.g., tissue thickness) and did not model the interactions of LV's wall deformation with the fluid domain. Recently, several researchers [65–84] used fluid-solid interaction (FSI) models of the LV to couple the solid deformation of the heart wall and blood flow as a promising tool for computational cardiology. However, most of these studies [67–69,71,74,75,79,82–84] do not satisfy Requirement #1 described above (for patients suffering from C3VD who undergo TAVR) and none of them [65–84] satisfy Requirement 2 and 3 above. The methodological reasons for not satisfying these requirements were one or a combination of these shortcomings: (1) did not use patient-specific boundary conditions; (2) did not model C3VD instead they modeled normal valves and ventricles; (3) did not use patient-specific geometries. Among all, five studies [65,66,72,74,77] coupled fluid-structure modeling calculations with lumped parameter modelling (LPM) to impose boundary conditions on the calculations. However, the lumped parameter models either were not patient specific and/or needed information from blood-flow and geometrical measurements using

MRI, that is not feasible in patient with most implanted medical devices and is not available in all clinics. Moreover, some of these studies [59,60,62,67,74,75,77] used idealized geometries that could significantly affect the flow and vortex structures. Most of these studies were not validated while some were only partially validated using DE [75,82] or MRI [65] data.

In this study, we developed a highly innovative computational-mechanics framework that, upon further development and validation, can eventually function as a diagnostic tool for patients with C3VD who undergo TAVR. Currently only lumped-parameter models have the capabilities to quantify global hemodynamics due to the complexity of the cardiovascular system and the unmanageable computational cost of 3-D models of hemodynamics in the entire cardiovascular system. Our diagnostic framework, therefore, uses an innovative Doppler-based patient-specific lumped-parameter algorithm and a 3-D strongly-coupled FSI model to quantify both local and global hemodynamics in patients with C3VD who underwent TAVR. It provides a platform for testing the intervention scenarios and evaluating their effects on the global (Requirements #1 and #2) and local hemodynamics (Requirement #3). Our lumped parameter algorithm allows analysis of combinations of valvular, vascular and ventricular diseases for C3VD patients and only uses a limited number of parameters that can be reliably and non-invasively measured using DE and sphygmomanometer and calculates patient-specific global hemodynamics quantities (Requirements #1 and #2). We used clinical cardiac catheterization data [85] and clinical DE measurements in 3 patients with C3VD in both pre and post TAVR (6 cases) to validate our proposed framework and to demonstrate its diagnostic abilities by providing novel analyses and interpretations of clinical data.

## 2.3 Materials and Methods

We developed an innovative image-based computational fluid dynamics framework (Figures 1 to 4) to quantify: (1) metrics of circulatory function (global hemodynamics); (2) metrics of cardiac function (global hemodynamics) as well as (3) cardiac fluid dynamics (local hemodynamics) in patients with C3VD who underwent TAVR (Table 1: Baseline patient characteristics). This framework is based on a non-invasive Doppler-based patient-specific lumped-parameter algorithm that allows for the analysis of any combination of mixed and complex valvular, vascular and ventricular diseases [85] and 3-D strongly-coupled FSI designed using FOAM-Extend [86] with additional supplements as explained below (Figures 1 and 4: schematic diagram; Figure 5: algorithm flow chart). Our lumped-parameter algorithm allows patient-specific hemodynamic quantities to be continuously calculated with the use of reliable, non-invasive input parameters from Doppler echocardiography (DE) and sphygmomanometers. DE parameters were measured in the parasternal long axis, parasternal short axis, apical two-chamber, apical four-chamber and apical five-chamber views of the heart (see Figure 1 and Table 2 for details). Other input parameters of the model were systolic and diastolic blood pressures measured using a sphygmomanometer. Note that the proposed computational framework does not need catheter data to quantify local and global hemodynamics. Because CT images have higher resolution than Doppler echocardiography data, they were used for 3-D reconstruction of the LV for fluid-solid interaction calculations. Clinical cardiac catheterization data [85] and clinical Doppler echocardiographic measurements (Figure 7) were used to validate the calculations of this computational fluid dynamics framework [85].

Table 2-1. Baseline patient characteristics.

| | **C3VD Patients (n=3, mean ± SD)** |
|---|---|
| **Patient description** | |
| Mean age (years) | 83 ± 2.16 |
| Gender | (Male: 2; Female: 1) |
| Mean weight (kg) | 67.5 ± 14.23 |
| Mean height (cm) | 166.56 ± 12.5 |
| Body surface area ($m^2$) | 1.74 ± 0.13 |
| Body mass index ($kg/m^2$) | 31.8 ± 25.2 |
| EuroScore II | 7.17 ± 6.94 |
| STS Mortality Rate | 7.1 ± 4.8 |
| NYHA classifications | |
| • Patient No. 1 | Pre-TAVR: Grade 3; Post-TAVR: Grade 3 |
| • Patient No. 2 | Pre-TAVR: Grade 3; Post-TAVR: Grade 3 |
| • Patient No. 3 | Pre-TAVR: Grade 4; Post-TAVR: Grade 4 |
| **Arterial hemodynamics** | |
| Systolic arterial pressure (mmHg) | Pre-TAVR: 144 ± 19.43; Post-TAVR: 122 ± 20.61 |
| Diastolic arterial pressure (mmHg) | Pre-TAVR: 76 ± 9.88; Post-TAVR: 57.67 ± 10.87 |
| **Aortic valve hemodynamics** | |
| Stenotic aortic valve effective orifice area ($cm^2$) | 0.8 ± 0.08 |
| Stenotic aortic valve type | Tricuspid: 3; Bicuspid: 0 |
| Prosthetic size (mm) | 25 ± 2.83 |
| Prosthetic type | |
| • Edwards SAPIEN | n= 3 |
| Maximum aortic valve pressure gradient (mmHg) | Pre-TAVR: 56 ± 23.4; Post-TAVR: 18.7 ± 4.49 |
| Mean aortic valve pressure gradient (mmHg) | Pre-TAVR: 30 ± 25.3; Post-TAVR: 11.3 ± 3.4 |
| **Left ventricle hemodynamics** | |
| Ejection fraction (%) | |
| • Patient No. 1 | Pre-TAVR: 18; Post-TAVR: 20 |
| • Patient No. 2 | Pre-TAVR: 8; Post-TAVR: 10 |
| • Patient No. 3 | Pre-TAVR: 28; Post-TAVR: 32 |
| Stroke volume index ($ml/m^2$) | Pre-TAVR: 23.3 ± 12.35; Post-TAVR: 29.8 ± 17.46 |
| Heart rate (bpm) | Pre-TAVR: 52 ±1.5; Post-TAVR: 60.7 ± 7.9 |
| LV thickness, averaged (mm) | Pre-TAVR: 16 ± 0.8; Post-TAVR: 16 ± 0.8 |

Table 2-2. **Cardiovascular parameters**. Summarized parameters used in the lumped parameter modeling to simulate all patient-specific cases.

| Description | Abbreviation | Value |
|---|---|---|
| **Valve parameters** | | |
| Effective orifice area | EOA | Measured using DE |
| Inertance (mitral valve) | $M_{MV}$ | Constant value: 0.53 $gcm^{-2}$ [87] |
| **Systematic circulation parameters** | | |
| Aortic resistance | $R_{ao}$ | Constant value: 0.05 $mmHg.s.mL^{-1}$ [35,85,88–90] |
| Aortic compliance | $C_{ao}$ | Initial value: 0.5 mL/mmHg<br>Optimized based on brachial pressures<br>*(Systolic and diastolic brachial pressures are optimization constraints)* |
| Systemic vein resistance | $R_{SV}$ | 0.05 $mmHg.s.mL^{-1}$ [35,85,88–90] |
| Systemic arteries and veins compliance | $C_{SAC}$ | Initial value: 2 mL/mmHg<br>Optimized based on brachial pressures<br>*(Systolic and diastolic brachial pressures are optimization constraints)* |
| systemic arteries resistance (including arteries, arterioles and capillaries) | $R_{SA}$ | Initial value: 0.8 $mmHg.s.mL^{-1}$<br>Optimized based on brachial pressures<br>*(Systolic and diastolic brachial pressures are optimization constraints)* |
| Upper body resistance | $R_{ub}$ | Adjusted to have 15% of total flow rate in healthy case [35,85,88–90] |
| Proximal descending aorta resistance | $R_{pda}$ | Constant value: 0.05 $mmHg.s.mL^{-1}$ [35,85,88–90] |
| **Elastance Function*** | | |
| Maximum Elastance | $E_{max}$ | 2.1 (LV)<br>0.17 (LA) [91,92] |
| Minimum Elastance | $E_{min}$ | 0.06 (LV, LA) [91,92] |
| Elastance ascending gradient | $m_1$ | 1.32 (LV, LA) [91,92] |
| Elastance descending gradient | $m_2$ | 27.4 (LV)<br>13.1 (LA) [91,92] |
| Elastance ascending time translation | $\tau_1$ | 0.269 T (LV)<br>0.110 T (LA) [91,92] |
| Elastance descending time translation | $\tau_2$ | 0.452 T (LV)<br>0.18 T (LA) [91,92] |
| **Pulmonary circulation parameters** | | |
| Pulmonary Vein Inertance | $L_{PV}$ | Constant value:0.0005 $mmHg{\cdot}s^2{\cdot}mL^{-1}$ [87] |
| Pulmonary Vein Resistance | $R_{PV}$ | Constant value: 0.002 $mmHg{\cdot}s{\cdot}mL^{-1}$ [87] |
| Pulmonary Vein and capillary Resistance | $R_{PVC}$ | Constant value: 0.001 $mmHg{\cdot}s{\cdot}mL^{-1}$ [87] |
| Pulmonary Vein and Capillary Compliance | $C_{PVC}$ | Constant value: 40 mL/mmHg [87] |
| Pulmonary Capillary Inertance | $L_{PC}$ | Constant value: 0.0003 $mmHg{\cdot}s^2{\cdot}mL^{-1}$ [87] |
| Pulmonary Capillary Resistance | $R_{PC}$ | Constant value: 0.21 $mmHg{\cdot}s{\cdot}mL^{-1}$ [87] |
| Pulmonary Arterial Resistance | $R_{PA}$ | Constant value: 0.01 $mmHg{\cdot}s{\cdot}mL^{-1}$ [87] |
| Pulmonary Arterial Compliance | $C_{PA}$ | Constant value: 4 mL/mmHg [87] |
| Mean Flow Rate of Pulmonary Valve | $Q_{MPV}$ | *Forward LVOT-SV* is the only input flow condition (measured using DE)<br>*$Q_{MPV}$ is a flow parameter that was optimized so that the lump-parameter model could reproduce the desirable DE-measured Forward LVOT-SV.* |
| **Input flow condition** | | |
| Forward left ventricular outflow tract stroke volume | Forward LVOT-SV | Measured using DE |
| **Output condition** | | |
| Central venous pressure | $P_{CV0}$ | Constant value: 4 mmHg [35,85,88–90] |
| **Other** | | |
| Constant blood density | $\rho$ | Constant value: 1050 $kg/m^3$ [35,85,88–90] |
| Heart rate | HR | Measured using DE |
| Duration of cardiac cycle | T | Measured using DE |
| Systolic End Ejection time | $T_{EJ}$ | Measured using DE |
| End diastolic volume | EDV | Measured using DE |
| End systolic volume | ESV | Measured using DE |

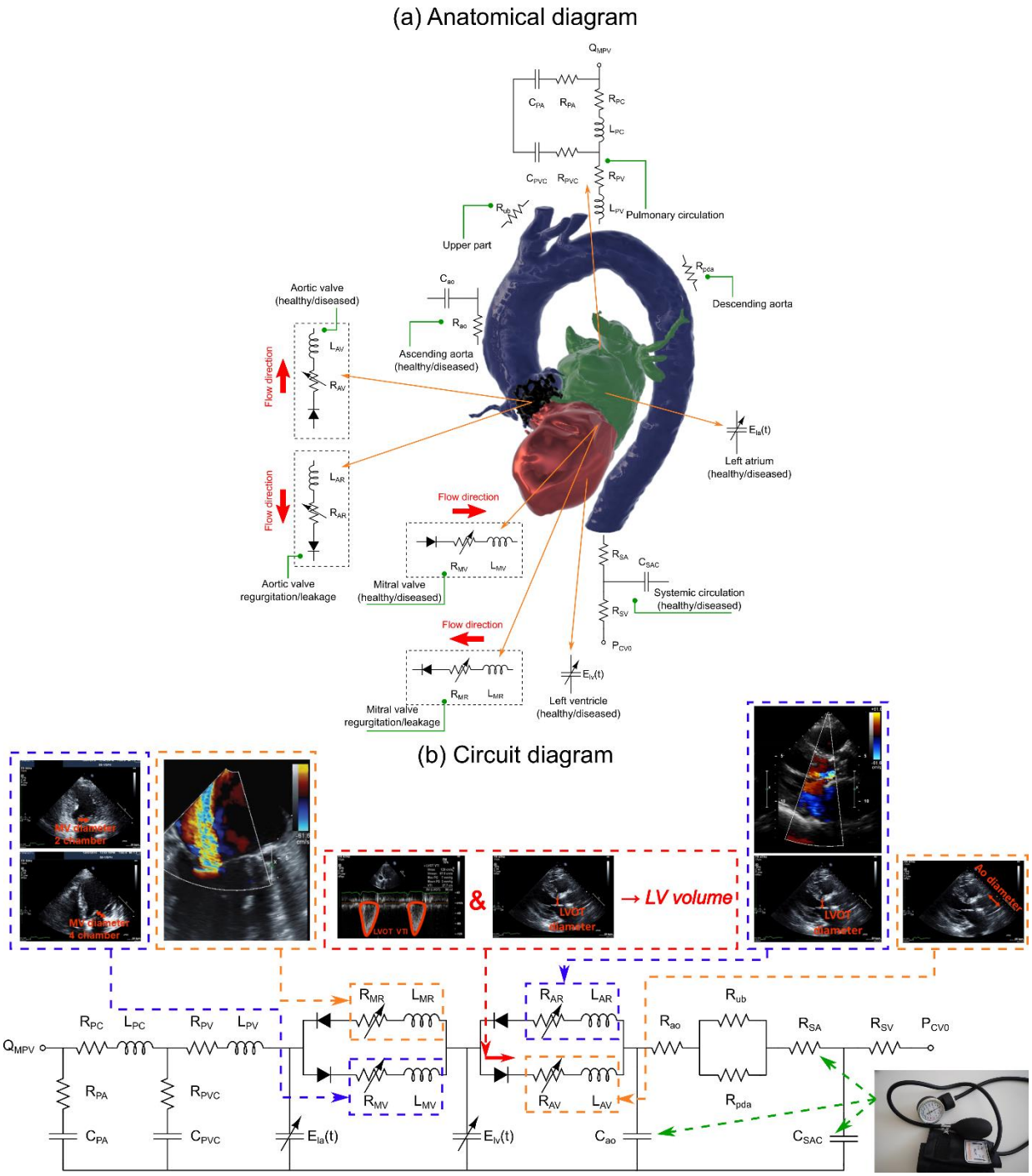


Figure 2-1. **Anatomical and electrical schematic diagrams of the lumped parameter modeling.** This model includes the following sub-models: left atrium, left ventricle, aortic valve, aortic valve regurgitation, mitral valve, mitral valve regurgitation, systemic circulation, and pulmonary circulation.

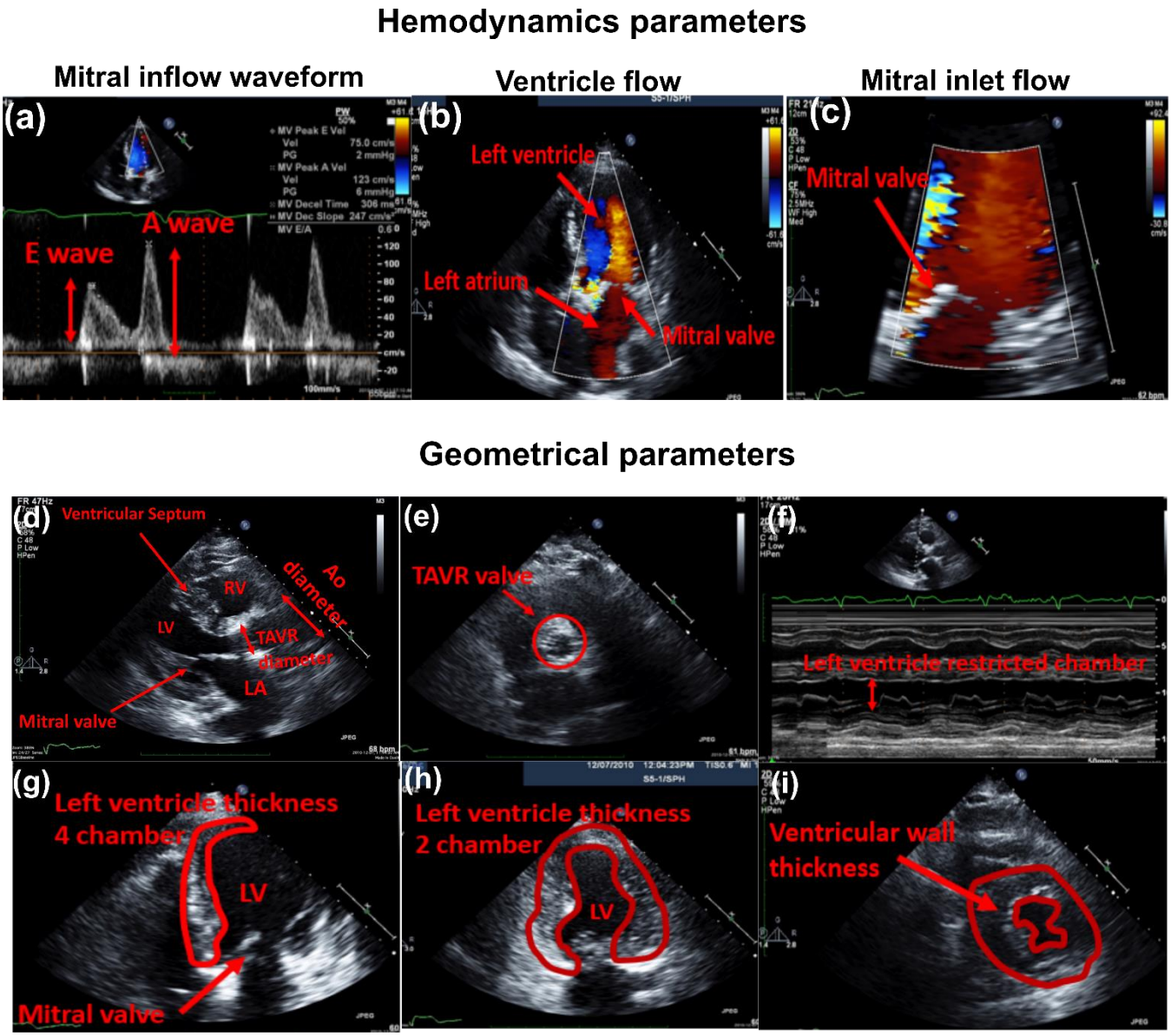


Figure 2-2. **Hemodynamics parameter**: (a) mitral inflow velocity (E/A= 0.6), showing grade I diastolic dysfunction, impaired relaxation); (b) 4 chamber view and color doppler echo of the LV during diastolic phase; (c) 4 chamber view and color doppler echo of the mitral valve during diastolic phase. **Geometrical parameters**: (d) Parasternal long-axis view associated with different parts of the LV; (e) Parasternal short-axis view of TAVR. (f) M-Mode measurement showing restricted LV chamber; (g) Apical 4 chamber view showing LV thickness and mitral valve dimensions; (h) Apical 2 chamber view showing LV thickness; (i) Parasternal short-axis view of the LV tissue showing the hypertrophic cardiomyopathy as well as the restricted chamber.

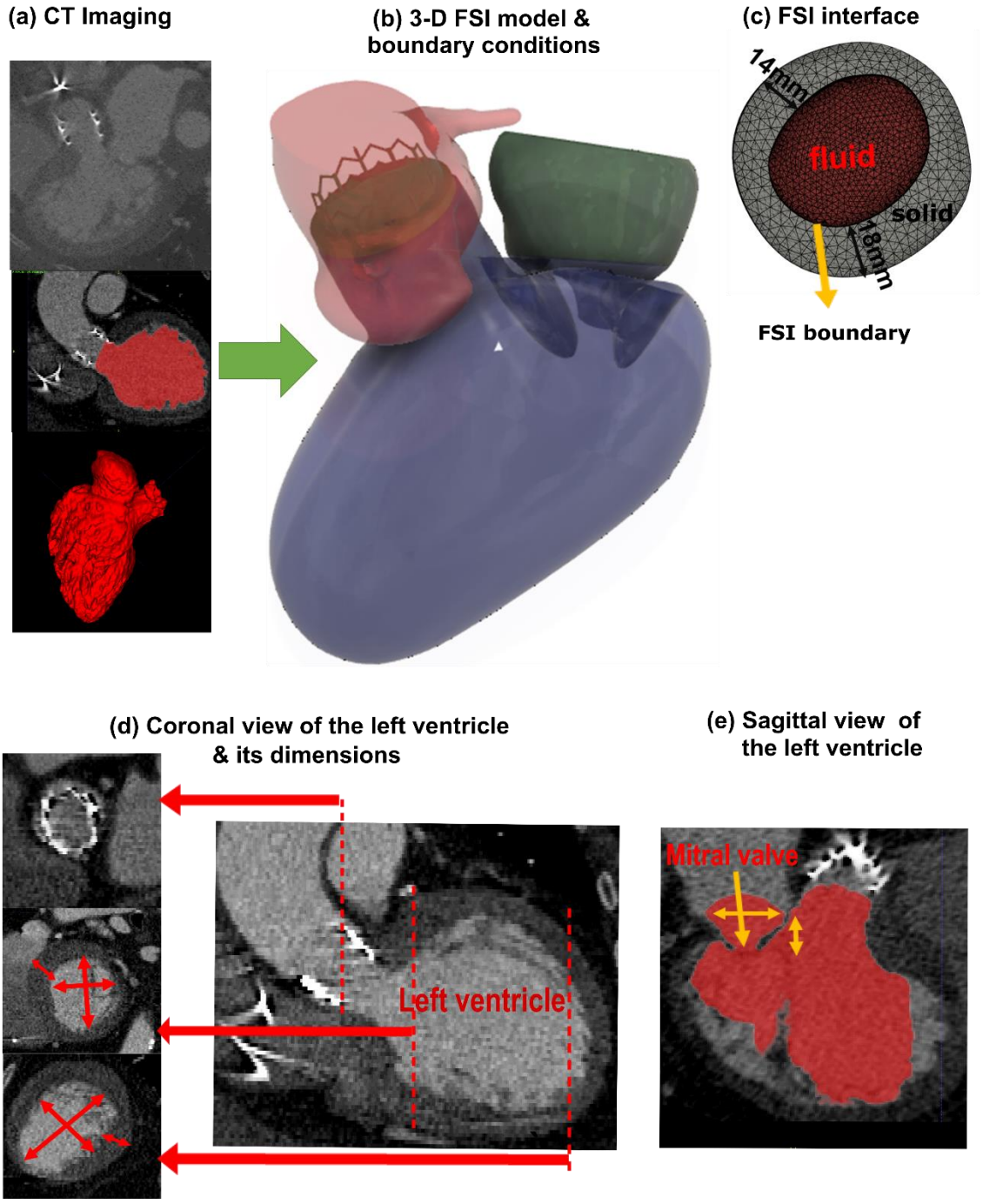


Figure 2-3. **Reconstructed 3-dimensional geometry in a patient with AS who received TAVR using computed tomography**. (a) Geometries were used for investigating hemodynamics using FSI and LPM; (b) and (c) Simulation domain and multi-thickness solid and fluid domain separated by FSI interface boundary; (d) CT Coronal view of the left ventricle showing its dimension at different sections (e.g., at the bases and apex) as well as transcatheter aortic valve position; (e) CT sagittal view of the left ventricle showing mitral valve annulus and anterior and posterior leaflets.

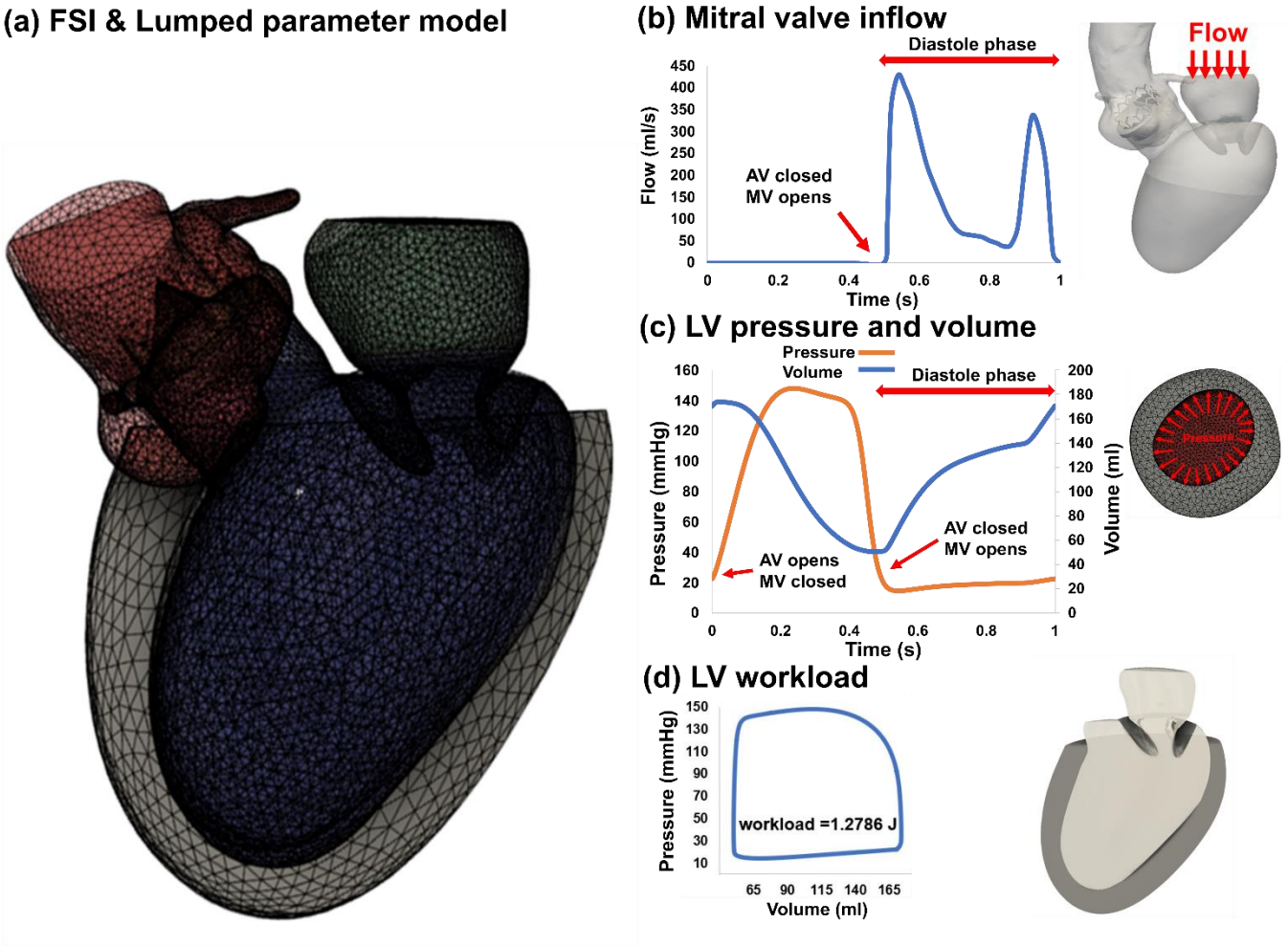


Figure 2-4. **Schematic diagram of LPM and FSI.** (a) computational domain. FSI simulations performed during diastole. Imposing correct boundary conditions to the flow model is critical because the local flow dynamics is influenced by downstream and upstream conditions. Patient-specific LPM simulating the function of the left side of the heart was coupled to the inlet of the mitral valve model. This data was obtained from patient-specific imaged based lumped parameter model (Figure 1); (b) mitral valve inflow during cardiac cycle; (c) left ventricle pressure and volume during cardiac cycle; (d) left ventricle (LV) workload. The workload is the integral of LV pressure and its volume change and was computed as the area encompassed by the LV pressure and LV volume loop.

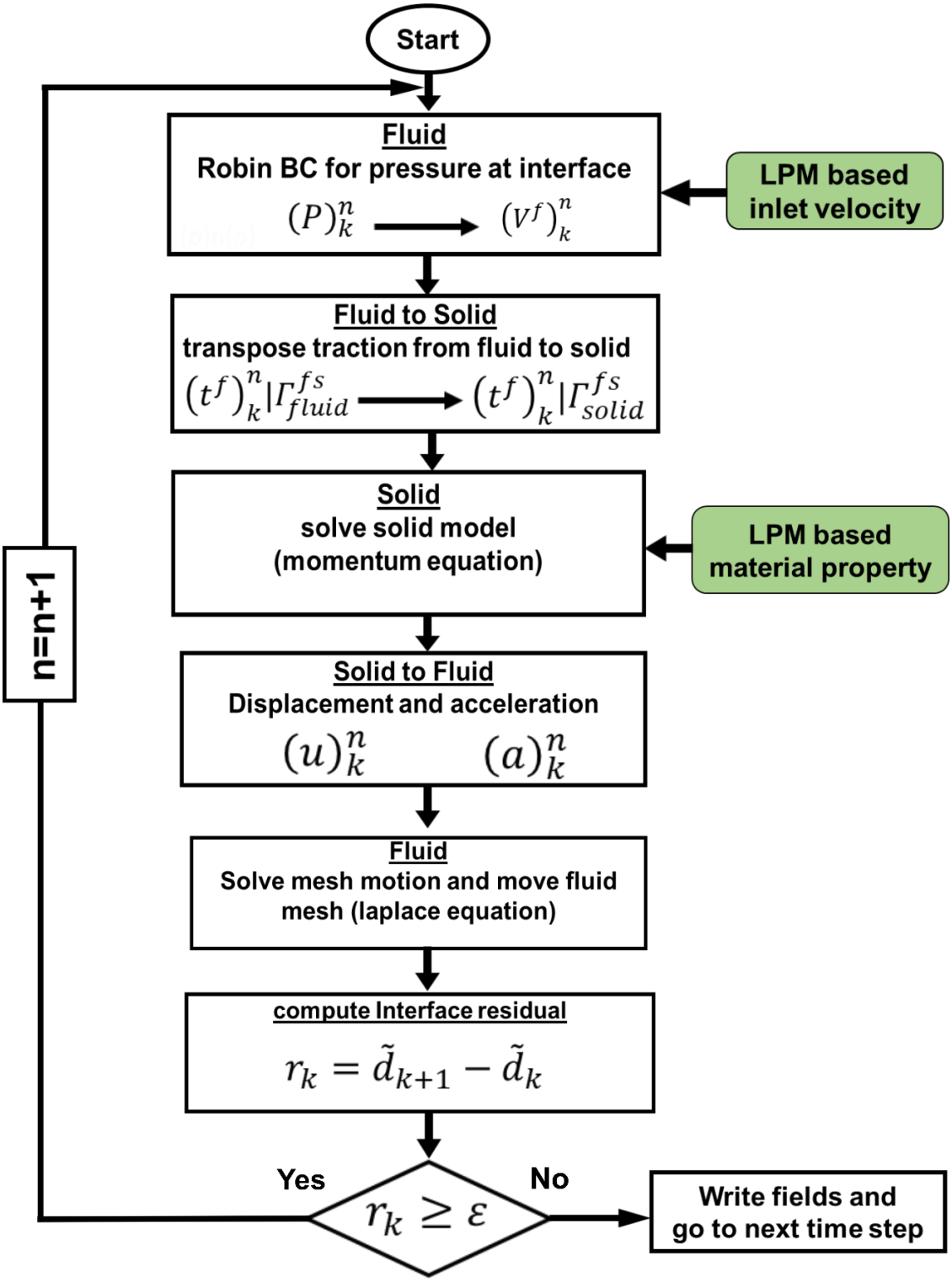


Figure 2-5. Patient-specific lumped parameter algorithm and strongly coupled FSI model flow chart.

### 2.3.1 Clinical medical imaging

#### 2.3.1.1 Study population & Data acquisition

Three patients with severe aortic valve stenosis who underwent TAVR procedure (Table 1; patients characteristics) between 2013 and 2017 at St. Paul's Hospital (Vancouver, Canada; N=3) were selected. The protocols were reviewed and approved by the Institutional Review Boards of the institution (the Clinical Research Ethics Board; CREB) and informed (written) consents were obtained from all human participants. The data were transferred as the de-identified & anonymized data from St. Paul's Hospital [5] and the approval was granted by the CREB. All methods and measurements were performed in accordance with the relevant guidelines and regulations including guidelines of the American College of Cardiology and American Heart Association. The patient medical records were used to collect demographic and procedural data (see Table 1 for details). Data was acquired at two time points: pre-procedure and 90-days post-procedure. The medical records, in combination with the New York Heart Association (NYHA) functional class, measured at each time point, allowed for the evaluation of the clinical outcome. All patients have left ventricle diastolic dysfunction, assessed according to the American Society of Echocardiography (ASE) guidelines [93]. Although there were no signs of malpositioning or transvalvular or paravalvular leakage following the TAVR procedure in any of the patients, they all had severe heart failure. The post-TAVR NYHA classifications for patients #1, #2 and #3 were 3, 3 and 4, respectively, with left ventricles exhibiting symptoms of hypertrophy and restrictive cardiomyopathy. The protocol was reviewed and approved by the Ethics Committee of the institutions. Pre-procedural echocardiographic, computed tomographic and angiographic imaging and data enabled the local clinical team to decide upon the required valve type and size prior to

the procedure. Results were expressed as mean ± standard deviations (SD) (Table 1: Baseline patient characteristics).

### 2.3.1.2 Doppler echocardiography (DE)

Doppler echocardiography (DE) data was collected at baseline and at 90-days post-procedure, including raw images and documented reports. Senior cardiologists reviewed and analyzed the echocardiograms and reports using OsiriX imaging software (version 8.0.2; Pixmeo, Switzerland). The following metrics were measured:

***Input parameters of the LPM algorithm***: DE can reliably measure several metrics; the algorithm included the following as input parameters: forward left ventricular outflow tract (LVOT) stroke volume, heart rate, ejection time, ascending aorta area, LVOT area, aortic valve effective orifice area, mitral valve effective orifice area and grading of aortic and mitral valve regurgitation severity (see Figure 1 and Table 2 for details).

***Clinical hemodynamics parameters:*** Severe diastolic dysfunction was present in all three patients investigated in this study. Following the ASE guidelines [94], dysfunction was classified from Grade I to III based on the E wave to A wave ratio (E/A) from mitral inflow (See Figure 2(a), Patient No. 1, E/A=0.6 for an example). In addition, Doppler echocardiogram measurements taken in the apical four-chamber view show the velocity and direction of blood flow during the diastolic phase (Figures 2(b) and 2(c)).

***Geometrical parameters*:** A number of parameters were measured using the parasternal long axis, parasternal short axis, M-Mode, apical two-chamber and apical four-chamber views of the heart. We assessed the height, diameter and wall thickness of the LV as well as the leaflet and annulus sizes of the aortic and mitral valves (Figure 2(d) to 2(i)). We used 3-D reconstructed models, based on CT data, for fluid-structure interaction simulations. However, the collected DE measurements

were extremely helpful to verify the corresponding features in the 3-D models reconstructed using CT data, in addition to providing us with indispensable insights about the patients' state.

#### 2.3.1.3 Computed tomography (CT)

CT data was collected at baseline and at 90-days post-procedure, including images and documented reports. We used the data for the following:

***Model reconstruction:*** We segmented and reconstructed the 3-D geometries of the complete ventricle in patients with TAVR using CT images and ITK-SNAP (version 3.8.0-BETA) [95], a 3-D image processing and model generation software package (Figure 3). These 3-D reconstructions of the model (including the ventricle, TAVR, ascending aorta, mitral valve and left atrium) were performed based on using images taken at the beginning of diastole. The reconstructed 3-D models were then used for FSI simulations during diastole. We used smoothing procedure for the surfaces to overcome the challenges of computational convergence and stability. The smoothing procedure mainly removed the effect of trabeculae and papillary muscles, which has been shown to have negligible influence on the ventricle hemodynamics [96]. Change in the volume due to smoothing was less than 3% in all three patients.

***Geometrical parameters:*** We measured dimensions at various sections of the LV using an assortment of different views. For example, we evaluated the tissue thickness and the differentiation between the fluid and solid domains (Figure 3(b)) using a coronal view of the LV (Figure 3(d)) that displays its dimensions and wall thickness at the base and apex cross sections. In addition, this view provides essential information about the transcatheter valve shape and positioning. It is evident from Figure 3(d) that, following the procedure, the transcatheter valve maintained its initial circular shape and is positioned correctly, without being too close to the LV or too high to block the coronary inlets. Furthermore, the sagittal view of the heart describes

features including the mitral valve location, its dimensions and annulus size in addition to the various thicknesses of the anterior and posterior leaflets, as shown in Figure 3(e). These details were essential in the reconstruction of the complete model (LV, mitral valve, aortic valve, etc.).

### 2.3.2 Lumped parameter model

We developed a non-invasive Doppler-based diagnostic, monitoring and predictive computational-mechanics framework for complex valvular-vascular-ventricular interactions (C3VD) [85], called C3VD-CMF for simplicity. The method was described in details elsewhere [85]. We provide a succinct description herein that will help in understanding the new computational framework investigated in this study based on the Doppler-based lumped-parameter algorithm and a 3-D strongly-coupled FSI model. C3VD-CMF enables the quantification of (1) local hemodynamics through details of the physiological pulsatile flow and pressures through the heart and circulatory system; (2) global hemodynamics through heart function metrics such as left ventricle workload and instantaneous left-ventricular pressure. Currently, the above measures can only be obtained through invasive methods in patients, and when these procedures are undertaken, the collected metrics cannot be as complete as the results that the non-invasive C3VD-CMF provides [85]. uses limited input parameters that all can be reliably measured using DE and a sphygmomanometer. C3VD-CMF was validated against clinical catheterization data in forty-nine C3VD patients with a substantial inter- and intra-patient variability with a wide range of disease [85]. In addition, some of the sub-models of C3VD-CMF have been used previously [5,33,88,97–100], with validation against *in vivo* C3VD-CMF cardiac catheterization (N=34) [89] and *in vivo* MRI data (N=57) [35].

### 2.3.2.1 Heart-arterial model

#### 2.3.2.1.1 Left Ventricle

A time-varying elastance, E(t), is a measure of the ventricle muscle stiffness and couples the LV pressure and volume:

$$E(t) = \frac{P_{LV}(t)}{V(t) - V_0} \quad (1)$$

where $P_{LV}(t)$, $V(t)$ and $V_0$ are the LV time-varying pressure, time-varying volume and unloaded volume, respectively. The double Hill function proposed by Stergiopulos et al. [91] is widely used to describe the elastance function. Mynard et al. [92] expanded this function to other heart chambers than the LV. The double Hill function is a cooperative process, as physiologically expected from myocyte recruitment during preload and is modeled by a sigmoidal Hill function:

$$E(t) = N\left(\frac{\left(\frac{t}{\tau_1}\right)^{m_1}}{1+\left(\frac{t}{\tau_1}\right)^{m_1}}\right)\left(\frac{1}{1+\left(\frac{t}{\tau_2}\right)^{m_2}}\right) + E_{min} \quad (2)$$

$$N = \frac{E_{max} - E_{min}}{2} \quad (3)$$

where $\tau_1$ , $\tau_2$, $m_1$, $m_2$, $E_{max}$ and $E_{min}$ are ascending time translation, descending time translation, ascending gradient, descending gradient, maximum elastance and minimum elastance, respectively (see Table 2). A double Hill function was deemed necessary to model the contraction and relaxation in the heart chambers in Equation 2, the first term in brackets corresponds to the contraction of the chamber and the second term in brackets corresponds to the relaxation of the chamber. As detailed in Table 2 $\tau_1$ , $\tau_2$, $m_1$, $m_2$ govern the time translation and gradient of the elastance function, respectively: (1) $\tau_1$ and $\tau_2$ are parameters that are functions of the cardiac cycle duration (T) and are calculated in each patient using the equations provided in Table 2; (2) $m_1$, $m_2$ are constant for all patients (Stergiopulos et al. [91], Mynard et al. [92], Seemann et al. 2019 [41] ).

Parameter values used for the elastance function were adapted to obtain physiological waveforms for pressure, volume and flow that can be found in Table 2 [91,101–109].

#### 2.3.2.1.2 Left Atrium

The procedure outlined for the LV was also employed to couple the LA pressure and volume, making use of a time varying elastance, E(t), a measure of cardiac muscle stiffness. The parameter values used for the LA are found in Table 2, while the elastance function is defined by Equations (2) and (3) [85].

#### 2.3.2.1.3 Modeling heart valves

***Aortic valve***. Aortic valve was modeled using the net pressure gradient formulation ($PG_{net}$) across the aortic valve during LV ejection:

$$PG_{net}|_{AV} = \frac{2\pi\rho}{\sqrt{E_L Co|_{AV}}}\frac{\partial Q(t)}{\partial t} + \frac{\rho}{2E_L Co|_{AV}^2}Q^2(t) \quad (4)$$

and

$$E_L Co|_{AV} = \frac{(EOA|_{AV})A_{AO}}{A - EOA|_{AV}} \quad (5)$$

where $E_L Co|_{AV}$, $EOA|_{AV}$, $A_{AO}$, $\rho$ and $Q$ are the valvular energy loss coefficient, the effective orifice area, ascending aorta cross sectional area, blood density and transvalvular flow rate, respectively.

***Aortic regurgitation***. Aortic regurgitation (AR) was modeled using the same analytical formulation as aortic stenosis as the following. AR pressure gradient is the difference between aortic pressure and LV pressure during diastole.

$$PG_{net}|_{AR} = \frac{2\pi\rho}{\sqrt{E_L Co|_{AR}}}\frac{\partial Q(t)}{\partial t} + \frac{\rho}{2E_L Co|_{AR}^2}Q^2(t) \quad (6)$$

and

$$E_L Co|_{AR} = \frac{EOA_{AR}\, A_{LVOT}}{A_{LVOT} - EOA_{AR}} \quad (7)$$

where $E_L Co|_{AR}$ , $EOA_{AR}$ and $A_{LVOT}$ are the regurgitation energy loss coefficient, regurgitant effective orifice area and LVOT area, respectively.

***Mitral valve***. We modeled the mitral valve (MV) using the analytical formulation for the net pressure gradient ($PG_{net}|_{MV}$) across the MV during LA ejection. $PG_{net}|_{MV}$ is expressed as a function of $\rho$, $Q_{MV}$, $EOA_{MV}$ and $M_{MV}$, where these quantities describe the density of the fluid, the transvalvular flow rate, effective orifice area and inertance, respectively.

$$PG_{net}|_{MV} = \frac{M_{MV}}{EOA_{M_V}}\frac{\partial Q_{MV}(t)}{\partial t} + \frac{\rho}{2EOA|_{MV}^2}{Q_{MV}}^2(t) \quad (8)$$

***Mitral regurgitation***. Mitral regurgitation (MR) was modeled using Equation (9). The difference between mitral pressure and LA pressure during systole is known as the MR pressure gradient.

$$PG_{net}|_{MR} = \frac{M_{MV}}{EOA_{MR}}\frac{\partial Q(t)}{\partial t} + \frac{\rho}{2EOA|_{MR}^2}Q^2(t) \quad (9)$$

where $EOA|_{MR}$ is the MR effective orifice area.

## 2.3.2.1.4 Pulmonary flow

A rectified sine curve with duration $t_{ee}$ and amplitude $Q_{MPV}$ simulated the pulmonary valve flow waveform as follows:

$$Q_{PV}(t) = Q_{MPV}\, sin\left(\frac{\pi t}{t_{ee}}\right),\ t \le t_{ee};\quad Q_{PV}(t) = 0,\ t_{ee} < t \le T \tag{10}$$

where $Q_{MPV}$, $t_{ee}$ and T are the mean flow rate of the pulmonary valve, end-ejection time and cardiac cycle time period, respectively. It is important to note that the only input flow condition that can be reliably measured using DE in this study is the forward left ventricular outflow tract stroke volume (*Forward LVOT-SV*). The lumped-parameter model could reproduce this DE-measured Forward LVOT-SV when $Q_{MPV}$, the mean flow rate of the pulmonary valve, was optimized.

#### 2.3.2.2 Input parameters

The following patient-specific parameters were inputs for the lumped-parameter model: forward left ventricular outflow tract stroke volume (*Forward LVOT-SV*), cardiac cycle time (T), ejection time ($T_{EJ}$), $EOA_{AV}$, $EOA_{MV}$, $A_{AO}$, $A_{LVOT}$, $EOA_{AR}$, $EOA_{MR}$ measured by DE as well as brachial systolic and diastolic pressures measured by sphygmomanometer. All details about patient-specific parameter estimation were described in [85].

#### 2.3.2.3 Computational algorithm

A system of ordinary differential equations was formed and solved in Matlab Simscape (MathWorks, Inc.) to numerically analyse the lumped-parameter model. This process was augmented with the inclusion of supplemental functions written in Matlab and Simscape. The system of differential equations was solved using Matlab's ode23t trapezoidal rule variable-step solver with an initial time step of 0.1 milliseconds. The convergence residual criterion was set to $10^{-6}$, with the initial voltages and currents of the capacitors and inductors set to zero. The model was run for several cycles (around 50 cycles) to reach steady state before starting the response optimization process (described below). We generated a signal to model LV elastance using a

double Hill function representation of a normalized elastance curve for human adults [85]. The LV pressure, $P_{LV}$, calculated using the initial values of the model input parameters from Table 2, and the time-varying elastance (Equation 1) were used to compute the instantaneous LV volume, V(t). Subsequently, the time derivative of the instantaneous LV volume was calculated to find the LV flow rate. This approach was also applied to obtain the left-atrium volume, pressure and flow rate. As detailed below, by optimizing $Q_{MPV}$, the *Forward LVOT-SV* calculated using the lumped-parameter model was fitted to the one measured using DE. Finally, for each patient, the aortic pressure from the model was fit to the patient systolic and diastolic pressures measured using sphygmomanometer through the optimization of $R_{SA}$, $C_{SAC}$ and $C_{ao}$.

#### 2.3.2.4 Patient-specific response optimization

The parameters of the model are listed in Table 2. Some of the parameters were considered constant based on the previous studies in the literature or based on the rationale given below and their values are reported in Table 2. Additionally, the parameters that were measured in each patient are indicated in that table. In order to correctly simulate the conditions of the body of each patient, as described below, four parameters of the model were optimized so that the lumped-parameter model reproduced the physiological measurements performed in the patient. Simulink Design Optimization toolbox was used to optimize the response of the lumped-parameter model using the trust region reflective algorithm implemented in Matlab fmincon function. The response optimization was performed in two sequential steps with tolerances of $10^{-6}$.

The mean flow rate of the pulmonary valve, $Q_{MPV}$, cannot be reliably measured using DE. However, because *Forward LVOT-SV* can be measured reliably using DE, in the first step of optimization, $Q_{MPV}$ was optimized to minimize the error between the *Forward LVOT-SV* calculated by the lumped-parameter model and the one measured by DE in each patient (Equation 11):

$$Forward\ LVOT\text{-}SV = A_{LVOT}\ VTI_{LVOT} = \frac{\pi(D_{LVOT})^2}{4} VTI_{LVOT} \quad (11)$$

where $D_{LVOT}$, $A_{LVOT}$, and $VTI_{LVOT}$ are LVOT diameter, LVOT area, and LVOT velocity-time integral, respectively [85].

In the second step, $R_{SA}$, $C_{SAC}$, and $C_{ao}$ were optimized so that maximum and minimum of the aorta pressure were respectively equal to the systolic and diastolic pressures measured using a sphygmomanometer in each patient. Because the left ventricle faces the total systemic resistance and not the individual resistances, and the systemic arteries resistance, $R_{SA}$, is one order of magnitude greater than both the aortic resistance, $R_{ao}$, and systemic vein resistance, $R_{SV}$, for the sake of simplicity we considered $R_{ao}$ and $R_{SV}$ as constants and optimized $R_{SA}$ as the main contributor of the total systemic resistance. $C_{ao}$ was considered to be 0.6 of $C_{SAC}$ because 60% of the total arterial compliance resides in the proximal aorta [110].

End systolic volume (ESV) or end diastolic volume (EDV) measured by DE was fed to the lumped-parameter model to adjust only starting and ending volumes in the P-V loop diagram. For this purpose, the Biplane Ellipsoid model was used to calculate the instantaneous LV volume at the end of diastole or the end of systole as follows [85]:

$$\forall = \frac{A_1\ A_2}{(L_1 + L_2)/2} \quad (12)$$

where $A_1$, $A_2$, $L_1$ and $L_2$ are LV area measured in the apical four-chamber view, LV area measured in the apical two-chamber view, LV length measured in the apical four-chamber view and LV length measured in the apical two-chamber view, respectively.

In addition, we conducted an extensive parameter sensitivity analysis that revealed negligible effects of changes in the pulmonary parameters (e.g., $C_{PVC}$) on the model

output variables. We, therefore, did not include these pulmonary parameters in the parameter-optimization process and considered them as constants given in Table 1.

### 2.3.3 Fluid solid interaction simulation study

In this study, blood flow simulations rely on 3-D FSI computational fluid dynamics. The system of equations governing the FSI problem for both fluid and solid domains are formulated using the finite volume method in FOAM-Extend [86].

#### 2.3.3.1 Governing equations for fluid domain

The 3-D incompressible Navier-Stokes equations governed the blood flow [111]. Blood was assumed to be an incompressible, Newtonian fluid with a dynamic viscosity of 0.004 Pa·s and a density of 1060 kg/m$^3$ [55]. In a LV that is free from valvular diseases (e.g. aortic valve regurgitation or mitral valve insufficiency), the blood flow is laminar and does not experience turbulence during the diastolic phase [56,112]. In this study, for all 3 patients, we considered the blood flow to be laminar [82,113,114]. The following continuity and momentum equations were employed [115]:

$$\oint_s (n.V)ds = 0 \tag{13}$$

$$\int_\forall \frac{\partial V}{\partial t} d\forall + \oint_s V[n.V]ds = \frac{1}{\rho}\oint_s n.[\mu \nabla V]ds - \frac{1}{\rho}\int_\forall \nabla p d\forall \tag{14}$$

where $n$, $\forall$ , $V$, $\mu$, $P$ and $\rho$ are the normal vector to the surface $S$, the volume, fluid velocity, fluid dynamic viscosity, blood pressure and fluid density, respectively. In all equations "." represents the dot product. Due to the deformation of the fluid-solid interface, momentum Equation (14) was considered in the Arbitrary Lagrangian-Eulerian (ALE) form as follows [115]:

$$\int_{\forall} \frac{\partial V}{\partial t} d\forall + \oint_s n.(V - V_s)Vds = \frac{1}{\rho}\oint_s n.[\mu \nabla V]ds - \frac{1}{\rho}\int_{\forall} \nabla p d\forall \quad (15)$$

$$\frac{d}{dt}\int_{\forall} d\forall = \oint_s n.V_S\, ds \quad (16)$$

where $V_s$ is the velocity of the surface. Conservation law governed the relationship between the rates of change of the cell volume and the mesh motion flux [116]. The rates of change of the volume and velocity of the surface are in equilibrium, as indicated by Equation (16) [116].

### 2.3.3.2 Governing equations for solid domain

The LV is passive during diastole, which means that the tissue structure and the blood pressure inside the chamber are responsible for its deformation [117]. The heart wall comprises three layers, the endocardium, myocardium and epicardium, with the center layer, the myocardium, constituting the majority of the LV tissue thickness. Thus, the mechanical behaviour of the LV wall is primarily governed by the myocardium [118]. Creating an empirical model to describe the passive behaviour of the myocardial layer has been of great interest, with several previous designs [119–122], of which the most notable is the Holzapfel and Ogden model [122]. This model, although proven to be reliable, is based on experimental results from canine or porcine hearts, and is therefore restricted in its applicability due to the significant structural differences from human hearts [123]. There are several limitations with models based on animal testing, including the animal's environment, morphology and physiology. These factors may prevent the model from accurately simulating human physiology and pathophysiology in a clinical setting [124,125]. There are several studies that optimized the parameters of the Holzapfel and Ogden model to obtain patient-specific simulations of the LV tissue using displacement fields acquired from human 3-D Magnetic Resonance Imaging (MRI) data [126,127]. However, in those studies, the models and parameters were developed for non-pulsatile blood flow of healthy LVs, and additional imaging data was required. For instance, in these

models, imaging methods such as tensor diffusive MRI are required to characterize the direction of myocardial fibers [128–132]. While other studies have tailored their models to pulsatile blood flow, the tissue parameters were not optimized to be patient-specific [56–59,65,113,133,134]. The thickness of the LV was usually excluded from these models, with the primary focus being the simulation of the moving boundary of the LV wall, which relied upon high-resolution MRI data. In addition, the combination of LPM and MRI data has been performed in several recent studies to obtain anisotropic material properties of the LV for electro-mechanical models [129,130,132,135,136]. However, there are some disadvantages with the use of MRI; MRI cannot be used for patients with most implanted medical devices except safely for MRI-conditional devices. Indeed, its use is limited in patients with implanted medical devices as they remain a major risk during the examination [21,22].

In this study, a method to adjust patient-specific passive material properties of the LV for patients who undergo TAVR was developed, based on our patient-specific Doppler-based LPM algorithm [85]. The algorithm decisively uses reliable non-invasive input parameters acquired with DE. We assumed the LV tissue to be an isotropic Saint Venant-Kirchhoff solid [59,137–141] and used the time varying pressure and volumed obtained from our LPM algorithm, to adjust the non-linear material properties of the ventricle during diastole in each patient. The LV diastolic pressure and the LV pressure-volume (P-V) diagram obtained from the LPM were used to produce a series of LV P-V diagrams by applying the diastolic pressure as the boundary condition on the inner wall of the LV for different values for the material parameters. We then interpolated the material parameters to find the best values that could reproduce the LV P-V results obtained using the LPM.

According to the total Lagrangian form of the law of conservation of linear momentum, the deformation of the elastic and compressible solid were considered as follows [142]:

$$\int_{V_0} \rho_0 \frac{\partial}{\partial t}(\frac{\partial u}{\partial t})dV = \oint_{s_0} n.(\sum.F^T)ds + \int_{V_0} \rho_0 b dV \quad (17)$$

where the subscript 0 denotes the undeformed configuration and u is the displacement vector. F is the deformation gradient tensor, described by $F = I + (\nabla u)^T$, where $I$ is the second order identity tensor.

In Equation (17), Σ is the second Piola-Kirchhoff stress tensor, described through the Cauchy stress tensor (σ) as follows:

$$\sigma = \frac{1}{det\, F} F.\Sigma.F^T \quad (18)$$

Using the St. Venant-Kirchhoff constitutive material model, Σ was explained through isotropic Hooke's law:

$$\Sigma = \lambda tr(E)I + 2\mu E \quad (19)$$

where μ and λ are the Lame's constants (related to the Young's modulus and Poisson's ratio of material). E is the Green-Lagrangian strain tensor and is defined as follows:

$$E = \frac{1}{2}[\nabla u + (\nabla u)^T + \nabla u.(\nabla u)^T] \quad (20)$$

By substituting Equations (19) and (20) into Equation (17), the governing equation for the St. Venant-Kirchhoff hyperelastic solid in the total Lagrangian form can be obtained as follows [142]:

$$\int_{V_0} \rho_0 \frac{\partial}{\partial t}(\frac{\partial u}{\partial t})dV - \oint_{s_0} n.(2\mu + \lambda)\nabla u ds = \rho_0 \int_{V_0} b dV + \quad (21)$$

$$\oint_{s_0} n.[\mu(\nabla u)^T + \lambda tr(\nabla u)I - (\mu + \lambda)\nabla u + \mu \nabla u.(\nabla u)^T + \frac{1}{2}\lambda tr[\nabla u.(\nabla u)^T]I + \sum.\nabla u]ds$$

#### 2.3.3.3 Fluid-solid interaction (FSI)

The LV was simulated under pathophysiological flow and pressure conditions with the strong coupling of the fluid and solid solvers. The system of equations of the fluid and solid domains were solved separately using the partitioned approach while the data was transferred at the interface. In order to reduce the cost of transferring information between the two domains, both the solid and fluid were modeled using a finite-volume approach [143]. Coupling of the fluid and solid solvers was achieved by satisfying the kinematic and dynamic conditions of the LV. The velocity and displacement must be continuous across the interface to satisfy the kinematic condition [142]:

$$u_{f,i} = u_{s,i} \tag{22}$$

$$V_{f,i} = V_{s,i} \tag{23}$$

where subscripts *i, s* and *f* indicate the interface, solid and fluid regions, respectively. To satisfy the dynamic condition, the forces at the interface must be in equilibrium:

$$n_i . \sigma_{f,i} = n_i . \sigma_{s,i} \tag{24}$$

The Dirichlet-Neumann procedure at the interface indicates that the fluid domain is solved for a given velocity/displacement while the solid domain is solved for a given traction [142].

##### 2.3.3.3.1 Grid Study

For FSI simulations in cardiovascular system, different studies in the literature reported different acceptable error values between medium and refined mesh for the mesh independency. Several studies attained a reasonable accuracy once the variation of the peak transvalvular velocity was less than 5%, e.g., [144,145]. Several other studies considered the flow results to be acceptable with variations of lower than 2% in the average of velocity, flow rate [146–149] and cardiac output [75] for

mesh independency. More specifically regarding the ventricular flow, there are studies that considered 5% variation of the average velocity inside the LV [150], 2% variation of the average of outflow velocity [148] or 2% variation at the peak transmitral velocity [151] to be acceptable for mesh independency. In addition, regarding the mesh independency with respect to WSS, previous studies considered either less than 3% variation in peak (maximum) WSS [152] or less than 2% variation in the average WSS [149,153].

We used an open-source mesh generation software, SALOME, to produce the mesh for all models [154]. The number of elements for FSI simulation was optimized through the examination of spatial mesh resolution. We had performed a grid convergence analysis and the spatial resolution for our models was ranged between 0.2 mm to 1.4 mm (unstructured tetrahedral elements with refined mesh near walls) (See Figure 6 for a sample of our grid convergence study). With optimized non-orthogonality and skewness values, the mesh definition for both the fluid and solid domains was considered acceptable when the velocity profiles in successive meshes showed a variation of less than 2%, such that this difference was not significant. The fluid dynamic mesh was controlled by Laplace mesh motion, which was subsequently influenced by variable diffusivity, to ensure the initial quality of the cells was maintained [115,155]. Mesh at the interface of the fluid and solid domains was not conformal. Consequently, following the face-interpolation and vertex-interpolation procedures, interpolation could be performed between the fluid and solid boundaries [115]. Indeed, we observed 2% variation is the maximum error in our mesh independency study in the entire velocity domain. This 2% maximum variation occurs only at the mitral valve orifice cross-section area and only at the peak transmitral velocity instance. At any other point in the domain and at any instance during diastole, the maximum error was less than 1% and the variation of average of velocity was less than 0.5%. In our study, the maximum WSS variations occurred at the mitral

valve and was less than 3% while the variation of the average WSS at the mitral valve was less than 2%. Also, the variation of the maximum value of WSS for the LV and TAVR was less than 2% and the variation of the average of WSS was less than 1%. Moreover, the maximum variation of the surface-averaged WSS ($(wss)_s = \frac{1}{A_s}\left\|\int_S (wss)ds\right\|_2$) for the entire geometry surface [156] was less than 1.5%. In addition, the maximum variation of the transmitral pressure gradient was lower than 2% in our study, which is consistent with previous studies on transvalvular pressure gradients [144,146,147,151].

Moreover, time step independency had been studied for all models. We found that a maximum Courant number of 0.2 was yielded as the solution marched in time with a time step of 0.0001s. For all simulations investigated in this study, the Courant number was lower than 0.25. This limit improved the accuracy of the numerical solution and reduced numerical dispersion. Convergence was obtained when all residuals reached a value lower than $10^{-6}$. Temporal discretization and spatial discretization were performed using a second-order Euler backward scheme and a second-order accurate scheme, respectively.

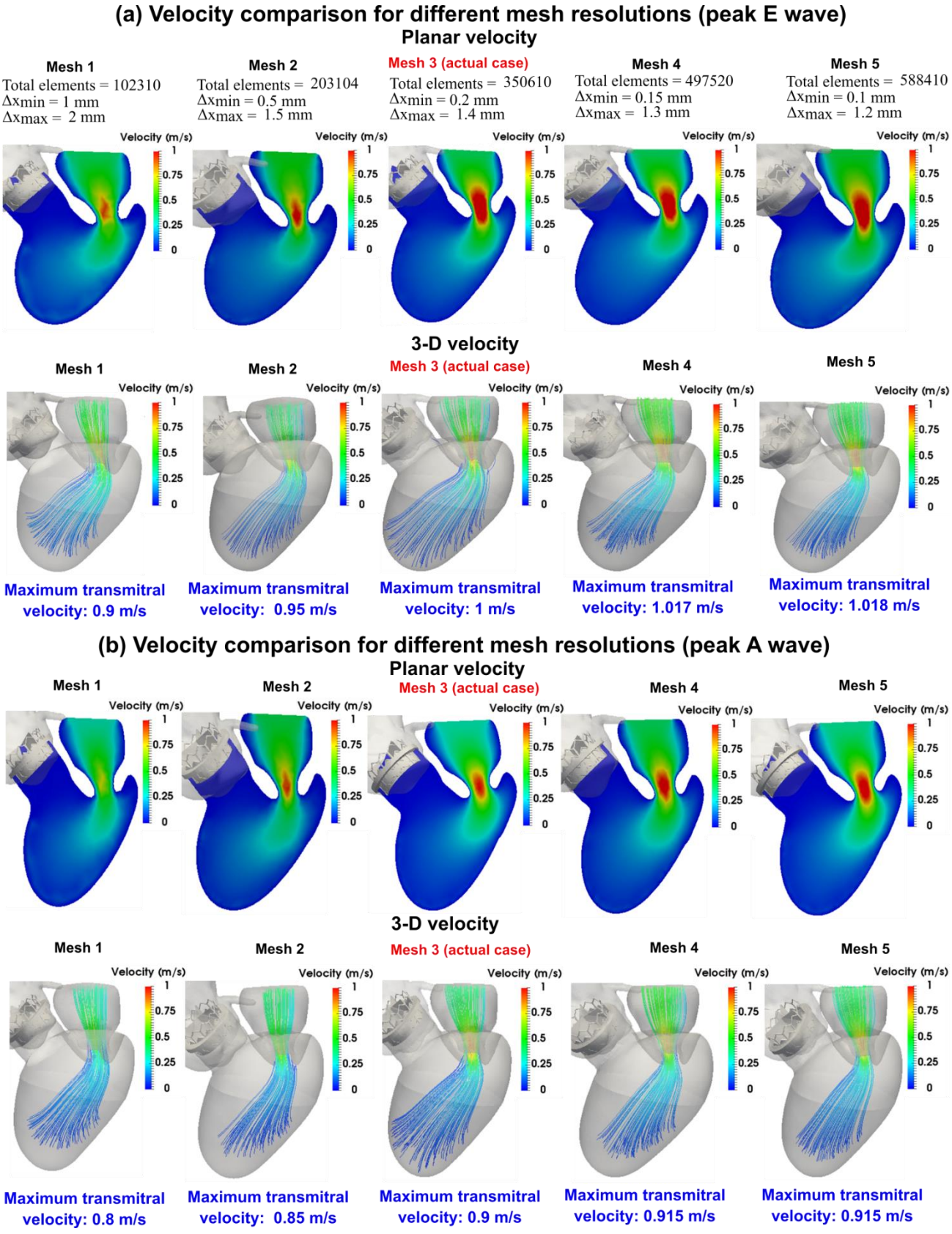
(a) Velocity comparison for different mesh resolutions (peak E wave)
Planar velocity
Mesh 1
Total elements = 102310
Δxmin = 1 mm
Δxmax = 2 mm
Mesh 2
Total elements = 203104
Δxmin = 0.5 mm
Δxmax = 1.5 mm
Mesh 3 (actual case)
Total elements = 350610
Δxmin = 0.2 mm
Δxmax = 1.4 mm
Mesh 4
Total elements = 497520
Δxmin = 0.15 mm
Δxmax = 1.3 mm
Mesh 5
Total elements = 588410
Δxmin = 0.1 mm
Δxmax = 1.2 mm
Velocity (m/s)
1
0.75
0.5
0.25
0
3-D velocity
Mesh 1
Mesh 2
Mesh 3 (actual case)
Mesh 4
Mesh 5
Maximum transmitral velocity: 0.9 m/s
Maximum transmitral velocity: 0.95 m/s
Maximum transmitral velocity: 1 m/s
Maximum transmitral velocity: 1.017 m/s
Maximum transmitral velocity: 1.018 m/s
(b) Velocity comparison for different mesh resolutions (peak A wave)
Planar velocity
Mesh 1
Mesh 2
Mesh 3 (actual case)
Mesh 4
Mesh 5
3-D velocity
Mesh 1
Mesh 2
Mesh 3 (actual case)
Mesh 4
Mesh 5
Maximum transmitral velocity: 0.8 m/s
Maximum transmitral velocity: 0.85 m/s
Maximum transmitral velocity: 0.9 m/s
Maximum transmitral velocity: 0.915 m/s
Maximum transmitral velocity: 0.915 m/s

Figure 2-6. **Grid convergence analysis.** (a) velocity comparisons for different mesh resolutions at the peak of E wave; (b) velocity comparisons for different mesh resolutions at the peak of A wave. In a LV that is free from valvular diseases (e.g. aortic valve regurgitation), the blood flow is laminar and does not experience turbulence during the diastolic phase. In this study, for all 3 patients, we considered the blood flow to be laminar.

### 2.3.3.4 Boundary conditions & material properties

Local flow dynamics are influenced by both downstream and upstream conditions, and therefore, it is critical to impose correct boundary conditions to the flow model. Our patient-specific image-based lumped-parameter algorithm provided boundary conditions (Figure 1) [85]: (1) to provide the time-dependent trans-mitral blood flow rate with the physiologic E and A waveforms (Figure 4); (2) to calculate material properties (Young modulus: Patient #1: 65 kpa, Patient #2: 50 kpa, Patient #3: 40 kpa; Poisson's ratio for all 3 patients: 0.4; density for all 3 patients: 1000 $kg/m^3$; see section Solid domain for details); (3) to provide the reference pressure, set inside the LV. Since LV diastolic dysfunction occurs during the left ventricular filling phase, all geometries were reconstructed based on images taken at the beginning of diastole, with all simulations performed during diastole. Therefore, the model was designed to show a rigidly closed TAVR and a fully open mitral valve. Neither mitral valve opening nor diastolic fluid dynamics are significantly influenced by the chordae tendineae, so the effect of the chordae tendineae was not considered [59]. A moving wall boundary condition was applied at the fluid-solid boundary inside the LV [59,113]. During diastole, the LV receives an inflow from the atrium but does not experience outflow due to the closed aortic valve. In order to ensure that mass is conserved, the interactions between the fluid and solid domains should be considered. Since blood is incompressible [111], we understand that the blood expands and contracts the LV wall. The no-slip boundary condition was applied to the fluid-solid interface while the Robin boundary condition for pressure, based on the approach

proposed by Tukovic et al., was used to solve the FSI problem inside the nonlinearly deforming LV [157]. The boundary condition for pressure was obtained from the following momentum equation [157]:

$$\frac{\partial V}{\partial t} + (V - V_s).\nabla V = \nabla.(v\nabla V) - \frac{1}{\rho}\nabla p \tag{25}$$

At the non-permeable moving LV wall, the following equation holds [157]:

$$n.\nabla p = -\rho\frac{\partial V_n}{\partial t} \tag{26}$$

where $V_n$ is the normal component of the LV wall fluid velocity.

Fluid pressure at the interface was estimated by solid inertia as follows:

$$p \approx \rho_s h_s \frac{\partial V_n}{\partial t} \tag{27}$$

where $\rho_s$ is the density of the LV structure and $h_s$ is the LV thickness calculated as [157]:

$$h_s = \Delta t\sqrt{\frac{\lambda + 2\mu}{\rho_s}} \tag{28}$$

where $\lambda$ and $\mu$ are Lame constants of the LV and $\Delta t$ is the time step size. Finally, the Robin boundary condition for pressure was obtained by combining Equations (26) and (27) [157]:

$$p + \frac{\rho_s h_s}{\rho}\frac{\partial p}{\partial n} = 0 \tag{29}$$

Therefore, the coupled FSI problem employed the Robin-Neumann approach. The fluid component used the Robin boundary condition for pressure from which the velocity was subsequently calculated.

#### 2.3.3.5 FSI solution and strategy

Our FSI simulations relied on FOAM-Extend [86] to formulate the system of equations governing the FSI problem using the finite volume method (See Figure 5 for FSI algorithm flowchart). The cell-centered finite volume method, frequently used in CFD and increasingly used for solid modeling, was employed to solve this system of equations [158].

Discretization in space was performed for the fluid model using the second-order accurate cell-centered finite volume method while the second-order backward Euler scheme allowed for numerical integration in time. The coupling between pressure and velocity was performed using the segregated PISO algorithm [155,159]. The system of discretized equations was solved with a preconditioned Bi-Conjugate Gradient method [160].

A second-order accurate backward scheme was used to discretize the second-order derivative of the solid model. This method is proven to stabilize the numerical model [161], and was performed to unify the discretization of the temporal terms between the fluid and solid discretization methods. A preconditioned Conjugate Gradient method was applied with a linear solver to then solve the system of discretized equations [142].

The dynamic mesh methodology controlled the moving boundary (interface) of the LV, and was updated with the movement of the solid boundary. This method, based on the Laplace equation, was discretized with the cell-centered finite-volume method, and was used to update the computational and geometric nodes of the fluid mesh [155]. The systems of discretized equations were solved by a geometric agglomerated algebraic multi-grid solver.

Coupling of the discretized governing equations of the fluid and solid domains was performed using the interface Quasi-Newton-Implicit Jacobian Least-Squares (IQN-ILS) algorithm [162].

Although this method has been compared with the monolithic method and other partitioned methods such as Aitken's dynamic relaxation, IQN-ILS is more stable, with better performance [162,163]. With this partitioned approach, a traction boundary condition at the solid side of the interface was provided through the calculation of traction at the fluid side of the interface.

### 2.3.4 Validation: Doppler-based LPM and FSI framework vs. clinical Doppler echocardiography data

#### 2.3.4.1 Trans-mitral velocity

Figure 7(a) to 7(f) compare the peak trans-mitral velocity simulated using our computational framework and Doppler echocardiography data in patients No. 1 to 3. The simulated peak velocities correlated well with the ones measured by Doppler echocardiographic in all 3 patients with a maximum relative error of 8.3% for E-waves and 9.2% for A-waves.

#### 2.3.4.2 Left ventricle flow (apical view)

The DE velocity measurement is based on direction of blood flow toward or away from the transducer (red and blue colors, respectively). Therefore, there are positive and negative values for velocity depending on the direction of the flow. As shown in figure 7(g) to 7(i), both magnitude and direction of flow show a good qualitative and quantitative agreements between our computational results and DE data.

#### 2.3.4.3 Mitral valve flow (parasternal short axis & apical views)

Figure 7(k) to 7(m) investigated mitral valve inflow computed with computational framework and measured by DE (7(k) and 7(i): parasternal short axis; 7(m): apical view). The results show good

agreements between velocity calculated using the computational framework and the ones measured using DE in all 3 cases investigated in this study.

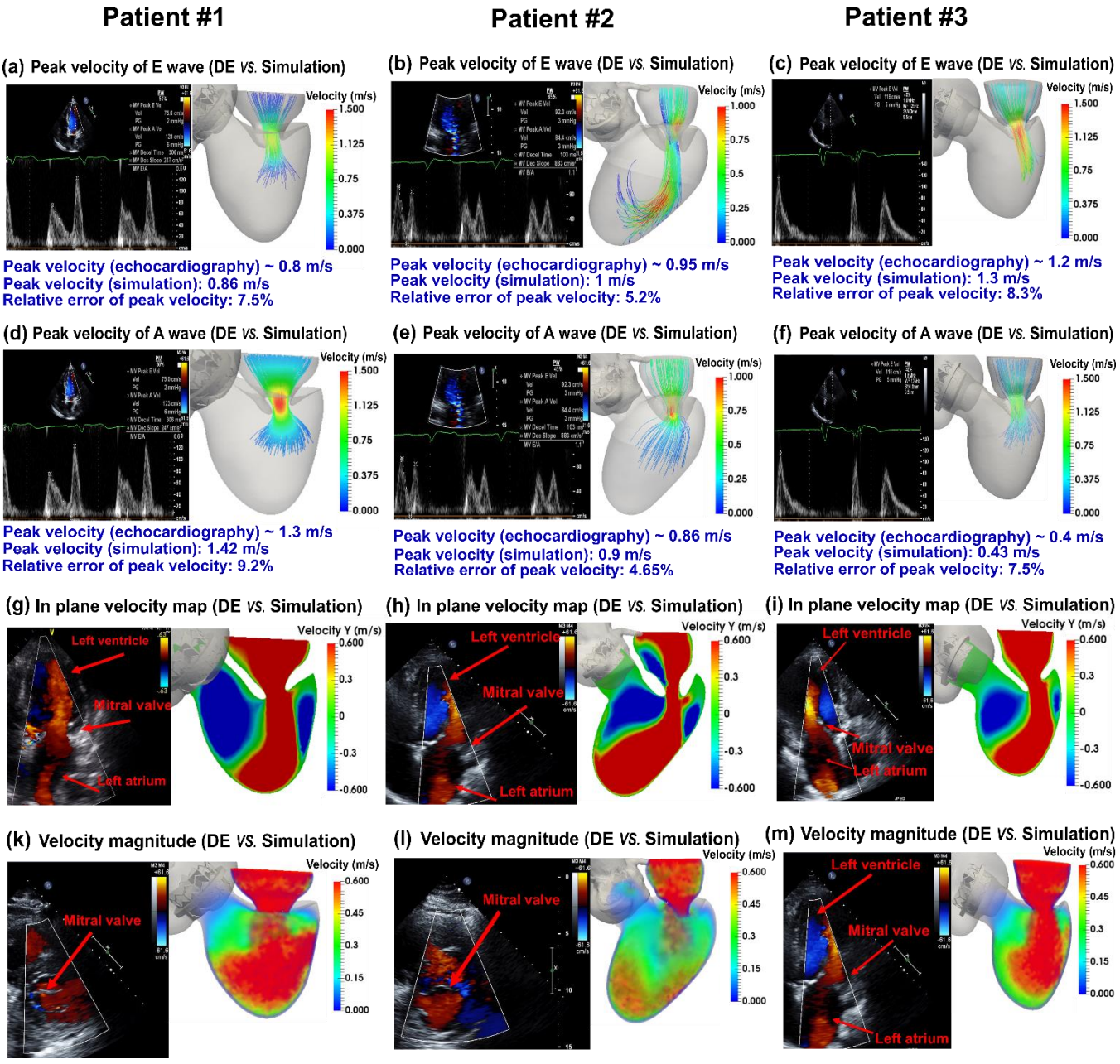


Figure 2-7. **Validation: Doppler-based LPM and FSI framework vs. patients Doppler echocardiography data.** (a) to (f) Trans-mitral velocity during diastole in patients #1 to #3; (g) to (i) Left ventricle flow (apical view) during diastole in patients #1 to #3; (k) & (m) Mitral valve flow (parasternal short axis view) during diastole in patients #1 and #2; (i) Mitral valve flow (apical view) in patient #3.

## 2.4 Results

LV dynamics during diastolic filling could play a crucial role in overall cardiac health. The persistence of abnormal intraventricular fluid dynamics after intervention may lead to blood clots, hypertrophy, heart failure, thrombus formation and other major heart-related complications. To show the utility of our computational-mechanics framework, described above, we investigate the LV dynamics during diastolic filling in terms of global and local hemodynamics in 3 patients with C3VD who underwent TAVR as follows.

### 2.4.1 Computed global hemodynamics (metrics of circulatory function and cardiac function)

#### 2.4.1.1 Circulatory function

The Doppler-based lumped-parameter algorithm quantifies hemodynamics metrics of circulatory system such as left-ventricle pressure, left-atrium pressure, aorta pressure, mitral and left-ventricle flow, left ventricle and left atrium volumes, etc. (Figure 8). This algorithm tracks changes in both cardiac and vascular states in terms of both shape of the waveform, and specific wave features such as the amplitude and the timing of the peak of the waveforms (see Figure 8 for details). Moreover, systemic arterial compliance ($C_{SAC}$ = stroke volume (SV)/pulse pressure (PP)) can be obtained as an index of arterial hemodynamics. It is important to note that a low $C_{SAC}$ (lower than 0.64 ml/m$^2$/mmHg) is associated with an increased risk of morbidity for patients with AS [164]. For all 3 C3VD patients after TAVR, $C_{SAC}$ was greater than 1 (ml/mmHg). Moreover, the maximum LA pressure was still greater than 18 mmHg for 3 C3VD patients following TAVR (compared with normal LA pressure defined as < 15 mmHg [165]).

#### 2.4.1.2 Cardiac function

The lumped parameter algorithm also quantifies hemodynamics metrics of cardiac function, e.g., the LV workload (patient #1: 1.9576 J, patient #2: 1.2786 J and patient #3: 1.2172 J; Figure 8). The LV workload are still greater than 1 J for all 3 patients after TAVR (compared with normal LV workload (in average) < 1 J [5,35,41,88,166]. LV workload has been shown to be effective in characterizing patient's outcome and in assessing the inotropic state in patients with C3VD and its quantifications is vital to guide prioritizing interventions [5,33,35,85]. Some patients with C3VD who underwent TAVR, experienced a significant improvement in terms of pronounced reverse LV remodeling and less congestive heart failure symptoms while the situation worsened in the others. While all theses information is vitally needed for effectively using advanced therapies to improve clinical outcomes and guiding interventions in C3VD patients, they are not currently accessible in clinic.

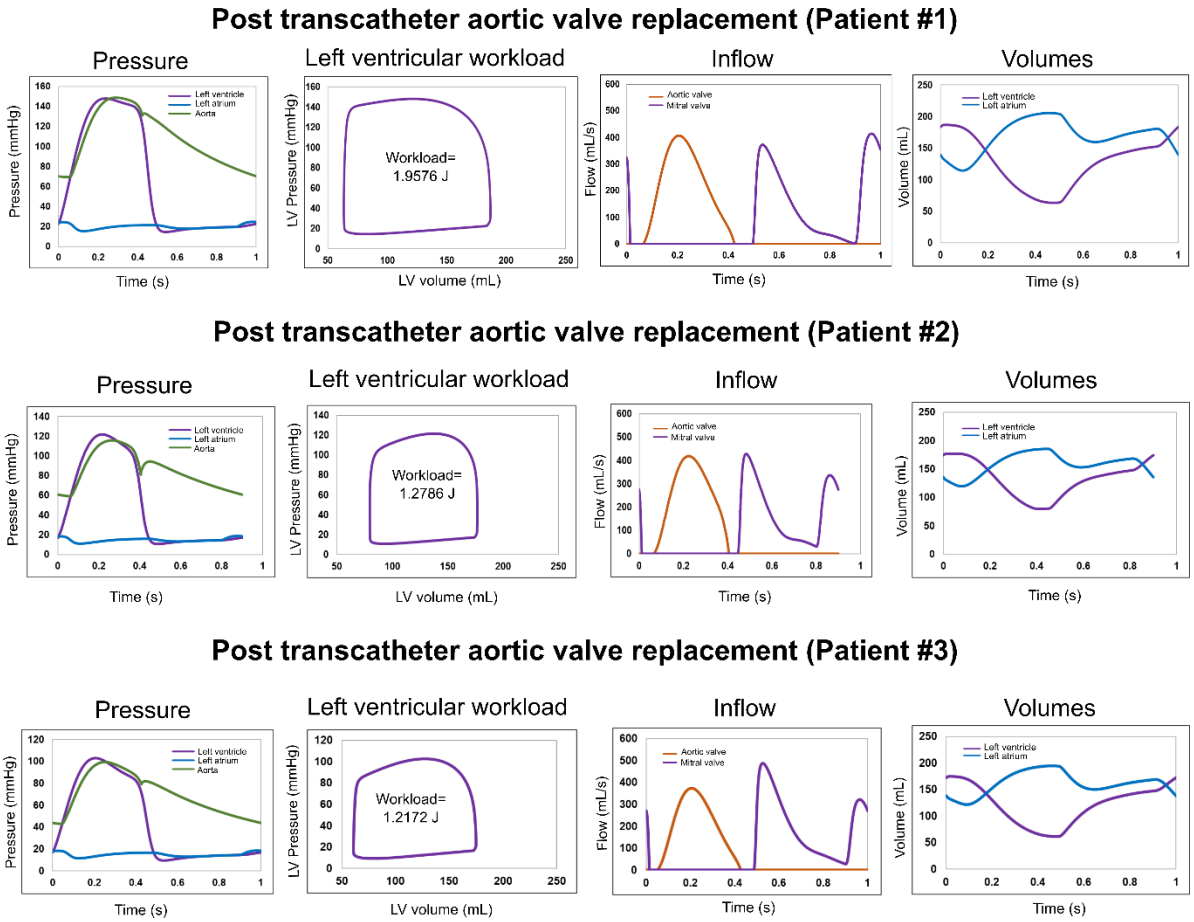


Figure 2-8. **Examples of global hemodynamics in C3VD patients post-TAVR.** Details of the physiological pulsatile flow and pressures throughout the heart and the circulatory system as well as the heart workload in patients with C3VD who underwent TAVR (Edwards biological prosthesis) and had the following conditions: ***Patient #1***: *Pre-TAVR*: severe aortic stenosis (EOA=0.9 $cm^2$), coronary artery disease and hypertension, moderate to severe concentric hypertrophy, ejection fraction: 18%, brachial pressures: 85 and 170 mmHg, forward LV stroke volume: 78 mL; *Post-TAVR*: aortic valve (EOA=1.8 $cm^2$), hypertension, moderate to severe concentric hypertrophy, ejection fraction: 20%, brachial pressures: 69 and 150 mmHg, forward LV stroke volume: 82 mL; ***Patient #2***: *Pre-TAVR*: severe aortic stenosis (EOA=0.7 $cm^2$), coronary artery disease severe asymmetric septal hypertrophy, ejection fraction: 8%, brachial pressures: 80 and 140 mmHg, forward LV stroke volume: 74 mL; *Post-TAVR*: aortic valve (EOA=1.74 $cm^2$), severe asymmetric septal hypertrophy, ejection fraction: 10%, brachial pressures: 61 and 115 mmHg, forward LV stroke volume: 72 mL; ***Patient #3***: *Pre-TAVR*: severe aortic stenosis (EOA=0.8 $cm^2$), moderate to severe concentric hypertrophy, coronary artery disease, chronic atrial fibrillation, ejection fraction: 28%, brachial pressures: 62 and 123 mmHg, forward LV stroke volume: 89 mL; *Post-TAVR*: aortic valve (EOA=1.7 $cm^2$), moderate to severe concentric hypertrophy, coronary artery disease, chronic atrial fibrillation, ejection fraction: 32%, brachial pressures: 43 and 101 mmHg, forward LV stroke volume: 92 mL.

### 2.4.2 Computed local hemodynamics (cardiac fluid dynamics)

#### 2.4.2.1 Evolution of vortical structure

The flow vortical structure inside the LV depends on the atrioventricular pressure, LV geometry, LV wall stiffness and mitral valve geometry. LV dynamics during diastolic filling, in particular, could play a crucial role in overall cardiac health [8,51]. The Doppler-based lumped-parameter algorithm and a 3-D strongly-coupled FSI model quantify local hemodynamics in the 3 patients with C3VD who underwent TAVR. Figures 9(a), 10(a) and 11(a) show the selected time-evolving flow patterns in the parasternal long axis view of the heart during diastole: early diastole (the E wave) to late diastole (the A wave) in the 3 patients. For patients #1 and #3, the maximum transmitral velocity are higher than a healthy LV ($0.79 \pm 0.18$ m/s) [167]. In all 3 patients, during the rapid filling phase (early E wave), blood enters through the mitral valve and develops a shear layer at the edges of anterior and posterior mitral valve leaflets, particularly at the anterior valve leaflets. The shear layer separates two regions with different velocities and forms a vortex ring that is seen as a vortex pair in the cross section of Figures 9(a), 10(a) and 11(a). The vortex ring pinches off from mitral valve leaflets and propagates toward the LV apex (peak E wave to late A wave). For all 3 patients, the vortex ring is larger close to the anterior valve leaflet and this large portion chiefly determines the blood flow pattern inside the LV – it occupies the LV cavity towards the apex and expands both laterally and longitudinally. The vortex is smaller close to the posterior valve leaflets and its size in this region was larger in patients #1 and #3 than it was in patient #2.

To better explore the vortex interactions, the velocity distributions in the short-axis view are shown in Figures 9(b), 10(b) and 11(b) for patients #1 to #3, respectively. In Patient #1 (Figure 9(b)), the

flow in the short-axis plane shows maxima near the center of the LV (0.3 m/s and 0.25m/s at the peak of E wave and A wave, respectively) consistent with the flow observations in the long-axis plane shown in Figure 9(a). In Patient #2 (Figure 10(b)), regions of high velocity magnitudes are near the LV lateral and septal walls (0.5 m/s and 0.4 m/s at the peak of E wave and A wave, respectively). In Patient #3 (Figure 11(b)), the fluid moves towards the center of LV, but close to the lateral wall (with a maximum velocity magnitude of 0.4 m/s at the peak of E wave). The short-axis cross view of the vortex ring shows the time-dependent evolution of the vortex ring and its motion during diastole. Although all these patients received TAVR, the complexity and evolution of the vortex ring are different among individuals. The region of high velocity (as detailed above) remains almost at the same position during the diastole and does not move toward the LVOT. In fact, specifically for patients #2 and #3, the vortex does not aid the redirection of the flow from the mitral valve towards the LVOT once compared with a normal LV [56,148]; instead the flow is redirected away from the LVOT. Such spatial alterations of the vortex ring in the short axis view lead to a low-velocity region close to LVOT at the end of diastole in comparison to a normal LV [56,148].

We characterized 3-D vortical structure in the LV using Q-criterion iso-surface (threshold 200 $s^{-1}$; Figures 9(c), 10(c) and 11(c)). The Q-criterion looks at the second invariant of the velocity gradient tensor and is defined as [168]:

$$Q = \frac{1}{2}[|\Omega|^2 - |S|^2] \tag{30}$$

where $\Omega = \frac{1}{2}\left[\nabla v - (\nabla v)^T\right]$ is the vorticity tensor and $S = \frac{1}{2}\left[\nabla v + (\nabla v)^T\right]$ is the rate of strain tensor. Indeed, the Q criterion represents the local balance between shear strain rate and vortices magnitude. The coherent vortex and eddy cores are distinguished as the regions characterized by

a positive value of Q, which indicates regions where vorticity overcomes strain in the flow. It allows, therefore, a better description of vortical structures and gives a better vision on flow irregularities occurring inside the LV. In all three patients, during the E wave, a vortex ring is formed distal to the mitral valve leaflets during the rapid filling phase (early E wave). For patients #1 and #3, the vortex ring is tilted towards the septum (close to the LVOT) with a more acute angle between the normal vector to the fitted vortex plane (vortex axis) and the normal vector to the LV short-axis plane (patient #1: 72º; patient #3: 68º) than the ones in healthy cases (82º ± 4) [169]. Due to the restricted motion of LVs and increased thickness of their tissue, this vortex ring impinge the wall soon after early E wave that leads to form a complex vortex structure at the peak of E wave. Therefore, for all 3 patients investigated in this study, the vortex break down occurs before reaching the apex, while for a normal LV this vortex penetrates further into the LV [58,170,171]. During very early A wave, the vortex ring already dissipates its energy and evolves into an asymmetrically shaped vortex, located at the LV basal position, close to the lateral wall from one side and to the septum from the other side. However, because all three patients have severe hypertrophic and restrictive cardiomyopathy LVs, the short period of diastasis does not permit the vortex ring to penetrate further into the LV chamber adversely affecting the LV wash out ability in the apex. In all three patients, the vortex enlarges longitudinally toward the LV apex direction, expands circumferentially at the peak of A wave and persists with a complex structure until the end of diastole without a major dissipation.

In order to explore the vortex morphology more precisely, the vortex sphericity index is calculated by dividing the vortex length to the vortex width ($D_2/D_1$; Figures 9(d), 10(d) and 11(d)) [172,173]. Vortex sphericity indices ($D_2/D_1$) are as follows: patient #1: 1.66 and 1.46; patient #2: 1.07 and 1.07; patient #3: 1.57 and 1.36 at the peak of E wave and A wave, in each patient, respectively.

The vortex in the diseased LVs is consistently more spherical than the ones in the healthy LVs [52,173,174]. The vortex sphericity indices in patients #1 to #3 is even lower than the previously reported values of 2.13 – 2.32 in patients with acute myocardial infarction [173]. In addition, patient #2 has a circular shape vortex (vortex sphericity index is 1.07 for both E and A waves). This may be interpreted as the risk of thrombus formation in patient #2 (with asymmetric septal hypertrophy) is more than the ones in patients #1 and #3 (with concentric hypertrophy with uniform increase in the LV tissue). In fact, when the elongated shape of vortex turns into a more circular shape, the apex of the LV is not exposed to a fast-moving blood flow and thus, the flow separated from the vortex in the mainstream could lead to the development of a LV thrombus at the apex. This is an established complication in many cardiac conditions with the highest rate detected in myocardial infarction and congestive heart failure [175]. Moreover, it has been shown that asymmetric septal myocardial thickening adjacent to LVOT (such as the one in patient #2) is associated with aortic stenosis [176,177]. Therefore, our results for patient #2 also suggest that, for patients with septal myocardial thickening, a more circular vortex (instead of elongated vortex) is associated with low velocity regions at the upper septum (close to LVOT). This complication could potentially limit the beneficial outcome of TAVR since the redirection of flow from the mitral valve towards the LVOT does not happen as it occurs in a normal LV.

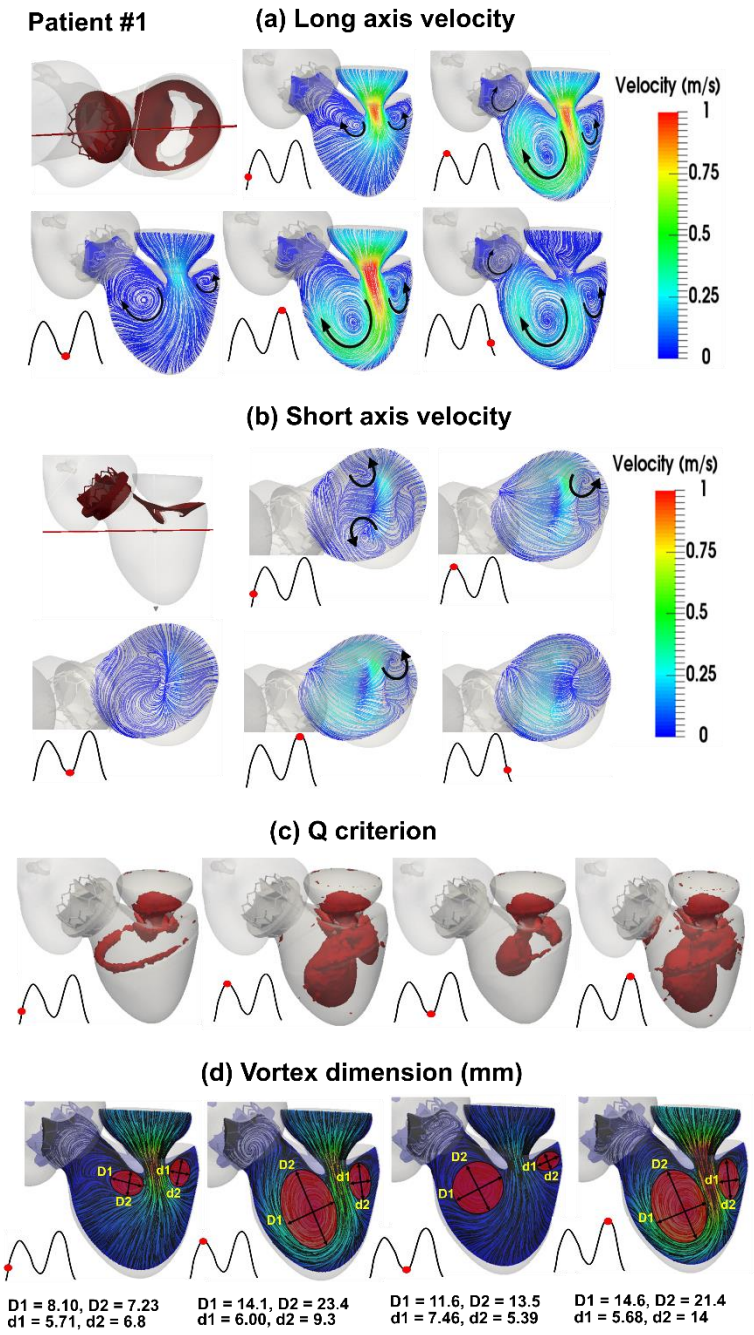


Figure 2-9. **Evolution of vortical structure following TAVR in patient #1 during diastole.** (a) Velocity in long-axis view; (b) Velocity in short-axis view; (c) Q-criterion iso-surface; (d) Vortex dimension. *Pre-TAVR*: severe aortic stenosis (EOA=0.9 $cm^2$), coronary artery disease and hypertension, moderate to severe concentric hypertrophy, ejection fraction: 18%, brachial pressures: 85 and 170 mmHg, forward LV stroke volume: 78 mL; *Post-TAVR*: aortic valve (EOA=1.8 $cm^2$), hypertension, moderate to severe concentric hypertrophy, ejection fraction: 20%, brachial pressures: 69 and 150 mmHg, forward LV stroke volume: 82 mL

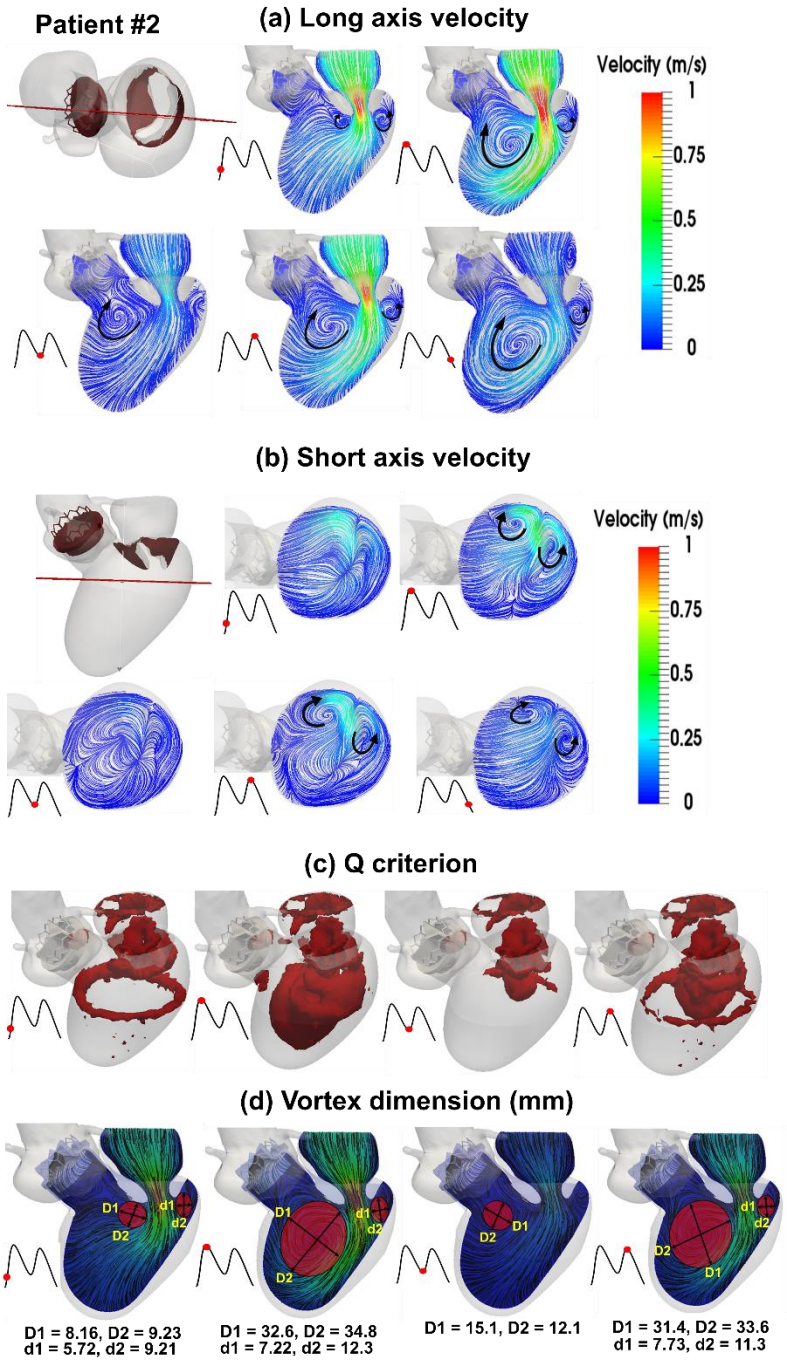


Figure 2-10. **Evolution of vortical structure following TAVR in patient #2 during diastole.** (a) Velocity in long-axis view; (b) Velocity in short-axis view; (c) Q-criterion iso-surface; (d) Vortex dimension. *Pre-TAVR*: severe aortic stenosis (EOA=0.7 $cm^2$), coronary artery disease severe asymmetric septal hypertrophy, ejection fraction: 8%, brachial pressures: 80 and 140 mmHg, forward LV stroke volume: 74 mL; *Post-TAVR*: aortic valve (EOA=1.74 $cm^2$), severe asymmetric septal hypertrophy, ejection fraction: 10%, brachial pressures: 61 and 115 mmHg, forward LV stroke volume: 72 mL

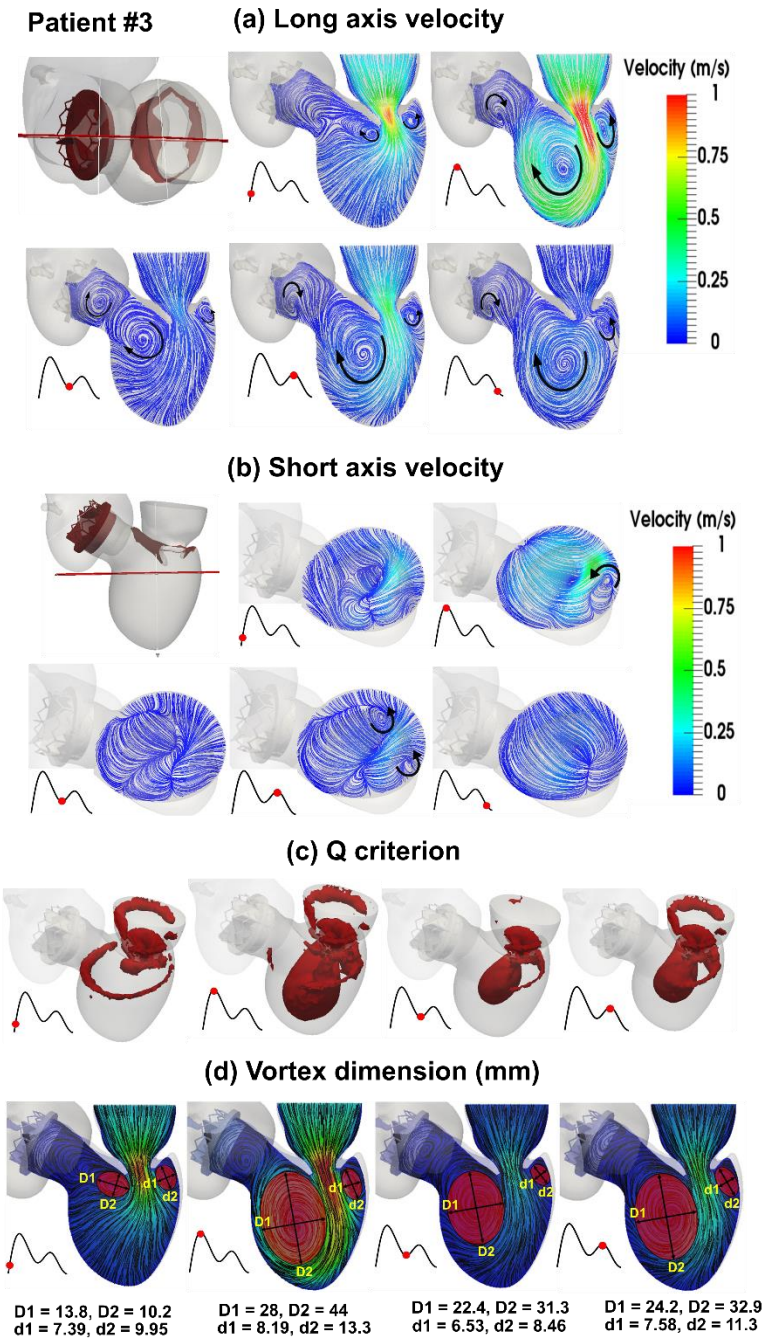


Figure 2-11. **Evolution of vortical structure following TAVR in patient #3 during diastole.** (a) Velocity in long-axis view; (b) Velocity in short-axis view; (c) Q-criterion iso-surface; (d) Vortex dimension. *Pre-TAVR*: severe aortic stenosis (EOA=0.8 $cm^2$), moderate to severe concentric hypertrophy, coronary artery disease, chronic atrial fibrillation, ejection fraction: 28%, brachial pressures: 62 and 123 mmHg, forward LV stroke volume: 89 mL; *Post-TAVR*: aortic valve (EOA=1.7 $cm^2$), moderate to severe concentric hypertrophy, coronary artery disease, chronic atrial fibrillation , ejection fraction: 32%, brachial pressures: 43 and 101 mmHg, forward LV stroke volume: 92 mL

#### 2.4.2.2 Stagnant and low-velocity flow

During filling of the normal heart, the blood entering the left ventricle through the mitral valve forms a vortex that minimizes energy dissipation while prevents blood stagnation. In the presence of C3VD and TAVR, the vortical structure in the LV and its valves' regions is altered, leading to intraventricular stagnant flow which is one of the most important factors for thrombus formation [178–181].

*Stagnant flow.* Figure 12 shows the regions of stagnation flow (velocity is lower than 0.001 m/s [150,182–184]) where thrombi can potentially form. In all 3 patients, due to the LV hypertrophy, the gap between the posterior leaflet of the mitral valve and the lateral wall of the LV is reduced. Our findings show these regions are at a high risk of thrombus formation as the stagnant flow persists until the end of diastole (Figure 12). Additionally, in patient #2, stagnation regions are formed at the lateral and septum walls of the LV during diastasis and stay there even at the peak of A wave (Figure 12(b)). Most importantly, stagnant flow dominates a substantial portion of the transcatheter aortic valve and LVOT regions which are consistent with the vortex morphology and sphericity results. This is a very important finding as this outcome limits the benefit of TAVR: may potentially worsen thrombus formation at this region. This possible exacerbation by stagnant and low flow will likely play an important hindering role in success of TAVR. This presents an important finding especially considering the expansion of TAVR candidacy to lower-risk and/or young patients.

*Low-velocity flow.* Although patient #1 has lower transmitral velocity magnitude at the peak of E wave compared to patient #2 (0.86 m/s *vs*. 1 m/s; respectively), the blood flow reaches the septum wall in patient #1, while this is not the case in patient #2: peak velocity near septum wall is 0.35

m/s and 0.1 m/s in patients #1 and #2, respectively (Figure 9(a), 10(a) and 11(a)). This situation becomes worse at the peak of A wave: peak velocity near septum wall is 0.3 m/s and 0.05 m/s for patients #1 and #2, respectively. This could describe the reason of having septum hypertrophy in patient #2. In addition, in patient #3, the higher transmitral velocity at the peak of E wave (1.3 m/s) facilitates the transport mechanism such that the velocity increases to 0.4 m/s near the septum wall. However, the blood flow cannot reach to the septum wall at the peak A wave: peak velocity near septum wall is 0.03 m/s.

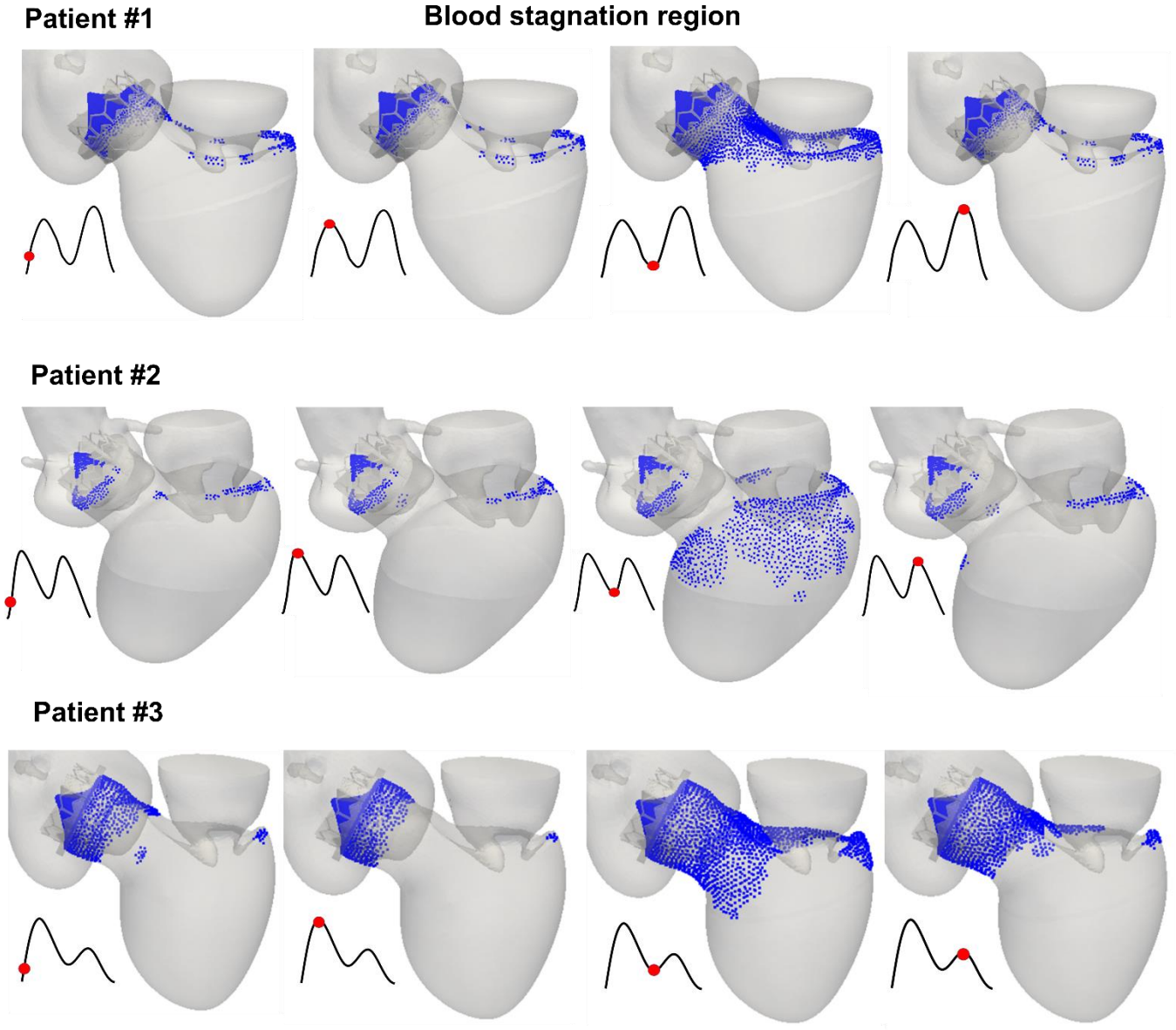


Figure 2-12. Stagnant and low-velocity flow region for patients #1 to #3.

### 2.4.2.3 Vortex formation time (VFT)

We quantify the process of vortex formation and progression during early filling using vortex formation time (VFT). VFT is a dimensionless index of optimal conditions for vortex formation, defined as follows [51,185]:

$$VFT = \frac{V_{ave} \times E_{duration}}{D} \quad (31)$$

where $V_{ave}$, $E_{duration}$ and $D$ are the average velocity during early filling, duration of E wave and diameter of mitral valve opening in its fully open state, respectively. Calculated VFTs for these 3 patients with cardiomyopathy, who received TAVR, is between 2.30 and 2.85 (Table 3) which is less than the optimal VFT of between 3.3 and 5.5 reported for the normal LV function [51]. Moreover, our results show that, in these 3 patients, the sphericity index has a linear relation with VFT (i.e. the lower value of sphericity index for patient #2 than patients #1 and 3 is associated with lower VFT as well) which is in agreement with a previous study [172].

Table 2-3. Vortex formation time (VFT)

| Patient # | Vortex formation time |
|---|---|
| **Patient#1** | 2.726696 |
| **Patient#2** | 2.290076 |
| **Patient#3** | 2.850877 |

### 2.4.2.4 LV kinetic energy and its association with viscous dissipation rate

In a normal LV, vortical flow in the LV provides the required kinetic energy to redirect mitral inflow toward the aortic valve while minimizing the energy dissipation rate [50,186]. In this study, we introduce normalized kinetic energy (N-KE; mJ/ml) as the computed kinetic energy normalized by stroke volume. In each patient, N-KE represents the kinetic energy of the intra-LV flow for each unit volume of the ejected blood (Figure 13(a)). Similarly, we introduce normalized viscous dissipation (N-VD; mW/ml) as the computed viscous dissipation normalized by stroke volume,

representing the intra-LV viscous dissipation for each unit volume of flow redirected from mitral valve toward the aortic valve (Figure 13(b)).

The kinetic energy (KE) [60] and the viscous dissipation rate (VD) [60,186] were calculated as follows:

$$KE = \frac{1}{2}(\rho)\left(u^2 + v^2 + w^2\right) \tag{32}$$

$$VD = \int (\tau : \nabla v) dV \tag{33}$$

where $\rho$ is the density and $u$, $v$ and $w$ are velocity components. The total kinetic energy is obtained by integrating the KE over the LV volume. Moreover, $\tau$ , $\nabla v$ and V are the viscous stress, the deformation tensor and volume, respectively.

Two separate peaks for both N-KE and N-VD during diastole are discriminated: the first during early filling, associated with E-wave, and the second during late filling, associated with A-wave. All three patients have considerably higher N-KE (> 0.05 mJ/ml) than healthy controls [187]. It is remarkable that, as Figure 13 shows, in each patient N-KE and N-VD are in phase. In addition to dependency to the geometrical features of the valves and the LV, N-KE and N-VD magnitudes depend on the vortical structures of the blood flow and their interactions with surrounding tissue. Therefore, inter-patient variability causes that the time waveforms for these two variables to be different across patients. Although all three patients are clinically classified to have the same diseases (pre-intervention: sever aortic stenosis and cardiomyopathy) and they received the same intervention (TAVR), their N-KE and N-VD waveforms are very different. As one example, Patient #1 shows a much different waveforms in both E-wave and A-wave regions: unlike two other patients, the peaks of A-wave regions are much higher than the ones in the E-wave regions (N-KE: E-wave region: 0.15 mJ/ml & A wave region: 0.19 mJ/ml; N-VD: E-wave region: 0.02 mW/ml & A wave region: 0.036 mW/ml). Our results also show that viscous dissipation rates are

about 15%, 11% and 9% of the kinetic energy for patients #1, #2 and #3, respectively, which are substantially higher than the one in a normal LV (2%) [188].

*Pressure gradient.* Pressure gradient from the center of mitral orifice at the left atrium side to the apex is calculated as shown in Figure 13(c). All three patients have higher pressure gradient than the one in a normal heart [189–191]. Patient #2 has moderate pressure gradients of 7 and 4 (mmHg) at the peak of E wave and A wave, respectively. Patient #3 has considerably higher pressure-gradient at the peak of E wave (9 mmHg) than the other two patients. However, following deceleration of the E wave, negative pressure gradient (-2 mmHg) is observed before diastasis, preventing more flow to get into the LV with a following low pressure gradient (2.5 mmHg) at the peak of A wave. Although Patient #1 has a low peak value of 6 (mmHg) at the peak of E wave, considerable higher atrial contraction leads to a high pressure-gradient at the peak of A wave (9 mmHg). Due to hypertension in patients #1 and #3, the increased left atrium pressure and/or irregular pressure gradient could be expected in these patients [192].

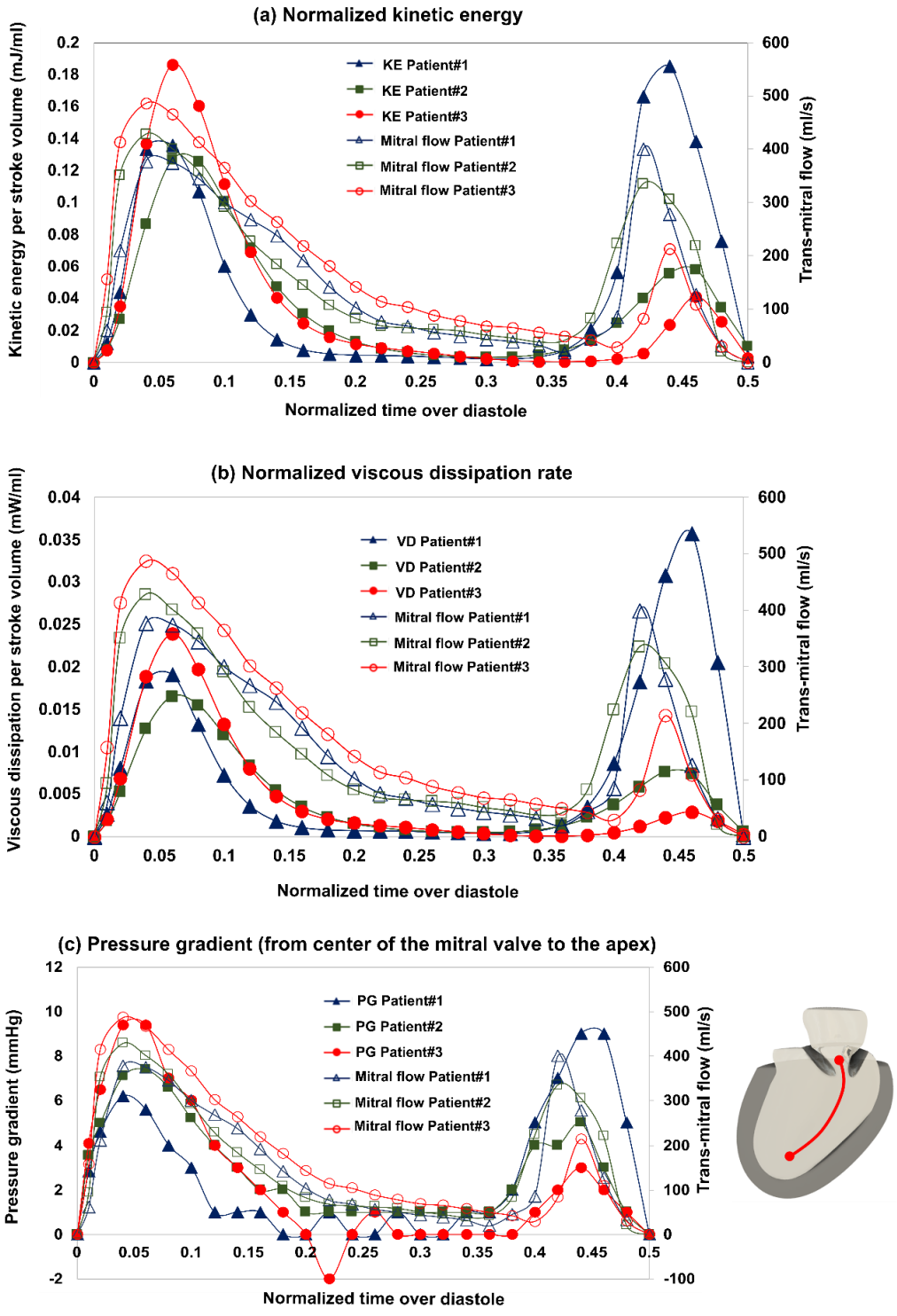


Figure 2-13. **Kinetic energy and its association with viscous dissipation rate.** (a) Normalized kinetic energy (computed kinetic energy per stroke volume) in patients #1 to 3; (b) Normalized viscous dissipation (computed viscous dissipation per stroke volume) in patients #1 to 3; (c) Pressure gradient (from center of the mitral valve to the apex) in patients #1 to 3.

## 2.5 Discussions

Quantification of the complex flow plays an essential role in accurate and early diagnosis in C3VD patients [11,12] and can be used for planning interventions and making critical clinical decisions with life-threatening risks. A clinically useful computational diagnostic framework should quantify the following 3 requirements:

### 2.5.1 Metrics of circulatory function (global hemodynamics)

The heart resides in a sophisticated vascular network whose loads interact with the function of the heart [5,11,13,33,89]. As the local flow dynamics are influenced by downstream and upstream conditions, replicating correct flow and pressure conditions is critical in developing a patient-specific cardiovascular simulator. This not only gives patient-specific flow and pressure conditions to the local flow but also enables investigation of effects of local hemodynamics on the global circulatory physiology. Complex valvular, ventricular and vascular diseases (C3VD) is the most fundamentally challenging cardiovascular pathology, in which several pathologies have mechanical interactions with one another wherein adverse physical phenomena associated with each pathology amplify the effects of others on the cardiovascular system [2–7,33]. TAVR often coexists with C3VD, thus making the investigation of flow and pressure details in the presence of TAVR very challenging. It is important to note that in clinics, *cardiac catheterization* is the gold standard to evaluate pressure and flow through heart and circulatory system *(global function)* but it is invasive, expensive, and high risk [20] and therefore not practical for diagnosis in routine daily clinical practice or serial follow-up examinations. Most importantly, cardiac catheterization only provides access to the blood pressure in very limited regions rather than details of the physiological pulsatile flow and pressures throughout the heart and the circulatory system.

### 2.5.2 Metrics of cardiac function (global hemodynamics)

In the presence of TAVR and/or C3VD, the heart is overloaded since the healthy instantaneous left-ventricle pressure and/or left-ventricle flow are altered [5,33]. In clinics, *cardiac catheterization* is the gold standard for evaluating heart function in terms of the heart workload obtained from the instantaneous left-ventricle pressure and/or left-ventricle flow. However, there is no method to invasively or non-invasively quantify the heart workload (global function) that can provide contribution breakdown of each component of the cardiovascular system. This is especially crucial in C3VD and TAVR because quantification of the left-ventricle workload and its breakdown are vital to guide prioritizing interventions and to sufficiently validate devices in regulatory testing machines. Moreover, there is no non-invasive method for determining left-ventricular end-diastolic pressure, instantaneous left-ventricular pressure, and contractility – all of which provide valuable information about the patient's state of cardiac deterioration and heart recovery.

### 2.5.3 Cardiac fluid dynamics (local hemodynamics)

Chirality of the human heart causes the complex pulsatile flow in the left ventricle and its valves to be strongly three dimensional, and with C3VD, this flow becomes even more complicated [8,51]. Moreover, as a result of TAVR, new interactions occur between the artificial implant and the native valve geometry, thus altering the fluid dynamics [193]. During normal filling of the left ventricle, a vortex is formed by the blood entering the chamber through the mitral valve; the vortex minimizes energy dissipation, prevents blood stagnation and optimizes pumping efficiency [8,51]. This optimized flow is altered by C3VD and TAVR [5], causing vortex dynamics to become less synchronized with heart contraction. Additional vortices apart from the healthy vortex ring may also emerge and interact with one another. Details of the instantaneous 3-D flow, vortex formation,

growth and eventual shedding must be known in addition to their effects on fluid transport and stirring both inside the left ventricle and in the vicinity of the valves after deployment [8,51,194].

In this study, we developed an innovative computational diagnostic framework for complex diseases like C3VD and TAVR that dynamically couple the local hemodynamics (using 3-D strongly-coupled FSI) with the global circulatory cardiovascular system (using lumped parameter modeling, LPM) and satisfies the 3 requirements. This computational diagnostic framework is promising for future clinical adoption and can quantify: (1) metrics of circulatory function (global hemodynamics); (2) metrics of cardiac function (global hemodynamics) as well as (3) cardiac fluid dynamics (local hemodynamics) in patients with C3VD in both pre and post intervention states. These metrics are not currently accessible in clinics, but with our framework, they can be quantified in patients with C3VD in both pre- and post-intervention states. This information is essential for the effective use of advanced therapies in Complex 3VD patients to improve clinical outcomes and to guide interventions.

### 2.5.4 Patients with C3VD who benefited from TAVR

Recent data show that 54.9% of patients who received TAVR had heart failure prior to intervention [195], and approximately 60% of aortic stenosis patients undergoing TAVR have a hypertrophic LV [196]. Commonly, LV hypertrophy leads to increased stiffness of the LV chamber and diastolic dysfunction [196], with 50 percent of patients found to have impaired diastolic function prior to TAVR in one recent study [197]. Although TAVR has proven to be a reliable replacement for surgical aortic valve replacement due to its minimally invasive approach, there is still significant risk of adverse events [198,199]. Some patients, who underwent TAVR, experienced a significant improvement in terms of pronounced reverse LV remodeling and less congestive heart failure symptoms. However, the situation in some other patients worsened; e.g., the long-term morbidity

of patients with prior diastolic dysfunction who received TAVR remains high in comparison to the general population [197]. Figure 14 shows examples of changes in the local and global hemodynamics in patient #3 between baseline and 90-day post-TAVR. This figure shows that patient #3 benefited from TAVR intervention: (1) *Global hemodynamics* (Figure 14(a)): TAVR leads to a reduction in transvalvular pressure gradient and significant improvement in the LV workload in patient #3 (pre-TAVR: 2.508 J and post-TAVR: 1.2172 J; 51% reduction), leading to experiencing an improvement in terms of pronounced reverse LV remodeling and less congestive heart failure symptoms [5,33]; (2) *Local hemodynamics* (Figure 14(b)): TAVR modifies the flow dynamics and vortical structure in the LV. Following intervention, the flow pattern is relatively smoother with a lower velocity magnitude. Such flow alterations contribute to a substantial reduction of stress and wear on the mitral valve leaflets and the left ventricle. Vortical structure in particular is crucial to the balance of fluid dynamics between blood and myocardial tissue [8] and can be used as an indicator of overall cardiac health [51].

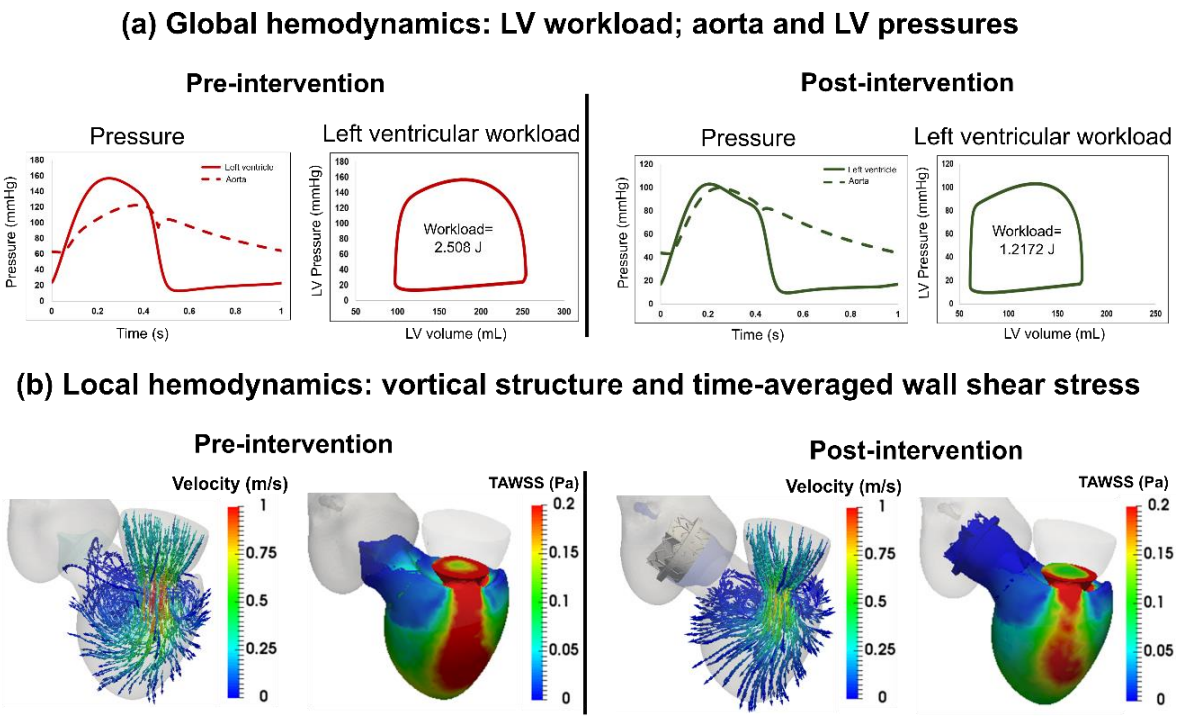


Figure 2-14. **Changes in local and global hemodynamics in patient #3 between baseline and 90-day post-TAVR.** (a) *Global hemodynamics*: LV workload; aorta and LV pressures; (b) *Local hemodynamics*: vortical structure and time-averaged wall shear stress.

## 2.6 Limitations

There have been several studies that optimized the parameters of the anisotropic Holzapfel and Ogden model to obtain patient-specific simulations of the LV tissue using displacement fields acquired from human 3-D Magnetic Resonance Imaging (MRI) data [126,127]. Such models require tensor diffusive MRI data to characterize the direction of myocardial fibers [128–132]. However, as mentioned before, MRI cannot be used for patients with most implanted medical devices including TAVR except safely for MRI-conditional devices [21,22]. In this study, we assumed the LV tissue to be an isotropic Saint Venant-Kirchhoff solid model [59,137–141] in patients with C3VD who underwent TAVR (see Governing equations for solid domain section for more details). Future studies should explore anisotropy of the LV tissue. This study was performed and validated on 3 patients with C3VD who undergo TAVR using a 3-D strongly-coupled fluid-solid interaction and lumped

parameter modeling framework in both pre and post intervention states (6 cases). Future studies must consider further validation of the computational framework in a large population of C3VD patients in both pre and post intervention states. However, our results in this study demonstrate the ability of the framework to track changes in both cardiac, and vascular states. However, it is important to note that our LPM algorithm, allowing analysis of any combination of complex valvular, vascular and ventricular diseases in both pre and post intervention conditions, was validated against clinical catheterization data in forty-nine C3VD patients with a substantial inter- and intra-patient variability with a wide range of disease [85]. These observations made us more confident that the limitation in the number of patients in this study does not affect our conclusions. One limitation that may be associated with our simulations is modeling the transcatheter aortic valve leaflets to be rigidly close and mitral valve leaflets to be rigidly open throughout the diastolic phase. It is important to note that this study focuses on diastole and the left ventricular filling phase. However, the good agreement between the numerical simulations and Doppler echocardiography velocity measurements, which include moving valve leaflets, shows that this limitation does not affect the conclusions of this study. Future numerical studies will consider the interactions between the fluid and deforming valve-leaflet structure during the entire cardiac cycle and will investigate the effects of dynamical opening and closing of the aortic and mitral valve leaflets on vortex dynamics in the LV.

## *Acknowledgments*

This work was supported by NSERC Discovery Grant (RGPIN-2017-05349). The funders had no role in study design, data collection and analysis, decision to publish, or preparation of the manuscript. We are thankful of great comments of two anonymous reviewers that helped us to improve the quality of this manuscript.

## *Competing interests*

Drs. Blanke and Leipsic provide CT core lab services for makers of transcatheter heart valves (Edwards Lifesciences, Medtronic, Neovasc, Aegis and Tendyne Holdings), for which no direct compensation is received. Dr. Leipsic is a consultant to Edwards Lifesciences and has received institutional research support from Edwards Lifesciences.

## *Author contributions*

S.K. FSI development, data collection and analysis (FSI), interpretation of data and manuscript writing; R.S. Data analysis; P.B., and J.L. Data analysis and interpretation of data; A.M. Interpretation of data and critical revision of the manuscript; Z.K.M. Conception and design, data analysis, algorithm development (LPM), interpretation of data, manuscript writing, critical revision, final approval of the manuscript and supervised this research. All authors read and approved the final manuscript.

## *Data availability*

The codes and the optimization algorithm are available from the author upon request.

## 2.7 References


1. Savarese, G. & Lund, L. H. Global Public Health Burden of Heart Failure. *Card. Fail. Rev.* **3**, 7–11 (2017).
2. Généreux, P. *et al.* Paravalvular Leak After Transcatheter Aortic Valve Replacement: The New Achilles' Heel? A Comprehensive Review of the Literature. *J. Am. Coll. Cardiol.* **61**, 1125–1136 (2013).
3. Nombela-Franco, L. *et al.* Significant Mitral Regurgitation Left Untreated at the Time of Aortic Valve Replacement: A Comprehensive Review of a Frequent Entity in the Transcatheter Aortic Valve Replacement Era. *J. Am. Coll. Cardiol.* **63**, 2643–2658 (2014).
4. Blanke, P. *et al.* Predicting LVOT Obstruction in Transcatheter Mitral Valve Implantation: Concept of the Neo-LVOT. *JACC Cardiovasc. Imaging* **10**, 482–485 (2017).
5. Keshavarz-Motamed Zahra *et al.* Mixed Valvular Disease Following Transcatheter Aortic Valve Replacement: Quantification and Systematic Differentiation Using Clinical Measurements and Image-Based Patient-Specific In Silico Modeling. *J. Am. Heart Assoc.* **9**, e015063 (2020).
6. Elmariah Sammy *et al.* Outcomes of Transcatheter and Surgical Aortic Valve Replacement in High-Risk Patients With Aortic Stenosis and Left Ventricular Dysfunction. *Circ. Cardiovasc. Interv.* **6**, 604–614 (2013).
7. Sotiropoulos, F., Le, T. B. & Gilmanov, A. Fluid Mechanics of Heart Valves and Their Replacements. *Annu. Rev. Fluid Mech.* **48**, 259–283 (2016).
8. Pedrizzetti, G., La Canna, G., Alfieri, O. & Tonti, G. The vortex—an early predictor of cardiovascular outcome? *Nat. Rev. Cardiol.* **11**, 545–553 (2014).
9. Kliger, C. *et al.* Review of surgical prosthetic paravalvular leaks: diagnosis and catheter-based closure. *Eur. Heart J.* **34**, 638–649 (2013).
10. Richter Yoram & Edelman Elazer R. Cardiology Is Flow. *Circulation* **113**, 2679–2682 (2006).
11. Marsden, A. L. Simulation based planning of surgical interventions in pediatric cardiology. *Phys. Fluids* **25**, 101303 (2013).
12. Di Carli Marcelo F., Geva Tal, & Davidoff Ravin. The Future of Cardiovascular Imaging. *Circulation* **133**, 2640–2661 (2016).
13. Taylor, C. A. & Steinman, D. A. Image-Based Modeling of Blood Flow and Vessel Wall Dynamics: Applications, Methods and Future Directions. *Ann. Biomed. Eng.* **38**, 1188–1203 (2010).
14. Siebes, M. & Ventikos, Y. The Role of Biofluid Mechanics in the Assessment of Clinical and Pathological Observations. *Ann. Biomed. Eng.* **38**, 1216–1224 (2010).
15. Lieber, B. B., Siebes, M. & Yamaguchi, T. Correlation of Hemodynamic Events with Clinical and Pathological Observations. *Ann. Biomed. Eng.* **33**, 1695–1703 (2005).
16. Ricotta, J. J. *et al.* Cardiovascular disease management: the need for better diagnostics. *Med. Biol. Eng. Comput.* **46**, 1059–1068 (2008).
17. Vlachopoulos, C., O'Rourke, M. & Nichols, W. W. *McDonald's Blood Flow in Arteries: Theoretical, Experimental and Clinical Principles*. (CRC Press, 2011).

18. Bermejo, J., Martínez-Legazpi, P. & del Álamo, J. C. The Clinical Assessment of Intraventricular Flows. *Annu. Rev. Fluid Mech.* **47**, 315–342 (2015).
19. Carlhäll, C. J. & Bolger, A. Passing Strange: Flow in the Failing Ventricle. *Circ. Heart Fail.* **3**, 326–331 (2010).
20. Omran, H. *et al.* Silent and apparent cerebral embolism after retrograde catheterisation of the aortic valve in valvular stenosis: a prospective, randomised study. *The Lancet* **361**, 1241–1246 (2003).
21. Elkins, C. J. & Alley, M. T. Magnetic resonance velocimetry: applications of magnetic resonance imaging in the measurement of fluid motion. *Exp. Fluids* **43**, 823–858 (2007).
22. Kilner, P. J., Gatehouse, P. D. & Firmin, D. N. Flow Measurement by Magnetic Resonance: A Unique Asset Worth Optimising. *J. Cardiovasc. Magn. Reson.* **9**, 723–728 (2007).
23. Trahey, G. E., Allison, J. W. & von Ramm, O. T. Angle Independent Ultrasonic Detection of Blood Flow. *IEEE Trans. Biomed. Eng.* **BME-34**, 965–967 (1987).
24. Kim, H. B., Hertzberg, J. R. & Shandas, R. Development and validation of echo PIV. *Exp. Fluids* **36**, 455–462 (2004).
25. Poelma, C. *et al.* 3D Flow reconstruction using ultrasound PIV. *Exp. Fluids* **50**, 777–785 (2011).
26. Sengupta, P. P. *et al.* Left Ventricular Isovolumic Flow Sequence During Sinus and Paced Rhythms: New Insights From Use of High-Resolution Doppler and Ultrasonic Digital Particle Imaging Velocimetry. *J. Am. Coll. Cardiol.* **49**, 899–908 (2007).
27. Jensen, J. A., Nikolov, S. I., Yu, A. C. H. & Garcia, D. Ultrasound Vector Flow Imaging—Part I: Sequential Systems. *IEEE Trans. Ultrason. Ferroelectr. Freq. Control* **63**, 1704–1721 (2016).
28. Garcia, D. *et al.* Two-Dimensional Intraventricular Flow Mapping by Digital Processing Conventional Color-Doppler Echocardiography Images. *IEEE Trans. Med. Imaging* **29**, 1701–1713 (2010).
29. Dweck, M. R., Boon, N. A. & Newby, D. E. Calcific Aortic Stenosis: A Disease of the Valve and the Myocardium. *J. Am. Coll. Cardiol.* **60**, 1854–1863 (2012).
30. Otto, C. M. Valvular Aortic Stenosis: Disease Severity and Timing of Intervention. *J. Am. Coll. Cardiol.* **47**, 2141–2151 (2006).
31. Pibarot, P. & Dumesnil, J. G. Improving Assessment of Aortic Stenosis. *J. Am. Coll. Cardiol.* **60**, 169–180 (2012).
32. Pibarot, P. & Dumesnil, J. G. Assessment of aortic stenosis severity: check the valve but don't forget the arteries! *Heart* **93**, 780–782 (2007).
33. Ben-Assa, E. *et al.* Ventricular stroke work and vascular impedance refine the characterization of patients with aortic stenosis. *Sci. Transl. Med.* **11**, (2019).
34. Garcia, D. *et al.* A ventricular-vascular coupling model in presence of aortic stenosis. *Am. J. Physiol.-Heart Circ. Physiol.* **288**, H1874–H1884 (2005).
35. Keshavarz-Motamed, Z. *et al.* Non-Invasive Determination of Left Ventricular Workload in Patients with Aortic Stenosis Using Magnetic Resonance Imaging and Doppler Echocardiography. *PLOS ONE* **9**, e86793 (2014).
36. Antonini-Canterin, F. *et al.* The Ventricular-Arterial Coupling: From Basic Pathophysiology to Clinical Application in the Echocardiography Laboratory. *J. Cardiovasc. Echography* **23**, 91–95 (2013).
37. Borlaug, B. A. & Kass, D. A. Ventricular-Vascular Interaction in Heart Failure. *Heart Fail. Clin.* **4**, 23–36 (2008).

38. Yin, F. C. P. *Ventricular/Vascular Coupling: Clinical, Physiological, and Engineering Aspects*. (Springer Science & Business Media, 2012).
39. Ikonomidis, I. *et al.* The role of ventricular–arterial coupling in cardiac disease and heart failure: assessment, clinical implications and therapeutic interventions. A consensus document of the European Society of Cardiology Working Group on Aorta & Peripheral Vascular Diseases, European Association of Cardiovascular Imaging, and Heart Failure Association. *Eur. J. Heart Fail.* **21**, 402–424 (2019).
40. Casas, B. *et al.* Bridging the gap between measurements and modelling: a cardiovascular functional avatar. *Sci. Rep.* **7**, 1–15 (2017).
41. Seemann, F. *et al.* Noninvasive Quantification of Pressure-Volume Loops From Brachial Pressure and Cardiovascular Magnetic Resonance. *Circ. Cardiovasc. Imaging* **12**, e008493 (2019).
42. Capoccia, M., Marconi, S., Singh, S. A., Pisanelli, D. M. & De Lazzari, C. Simulation as a preoperative planning approach in advanced heart failure patients. A retrospective clinical analysis. *Biomed. Eng. OnLine* **17**, 52 (2018).
43. Sughimoto, K. *et al.* Assessment of cardiovascular function by combining clinical data with a computational model of the cardiovascular system. *J. Thorac. Cardiovasc. Surg.* **145**, 1367–1372 (2013).
44. Cooper Leroy L. *et al.* Components of Hemodynamic Load and Cardiovascular Events. *Circulation* **131**, 354–361 (2015).
45. Burkhoff, D., Mirsky, I. & Suga, H. Assessment of systolic and diastolic ventricular properties via pressure-volume analysis: a guide for clinical, translational, and basic researchers. *Am. J. Physiol.-Heart Circ. Physiol.* **289**, H501–H512 (2005).
46. Welt, F. G. P. & Fang, J. C. Pressure Volume System for Management of Heart Failure and Valvular Heart Disease. *Curr. Cardiol. Rep.* **21**, 153 (2019).
47. Ky, B. *et al.* Ventricular-Arterial Coupling, Remodeling, and Prognosis in Chronic Heart Failure. *J. Am. Coll. Cardiol.* **62**, 1165–1172 (2013).
48. Mohananey, D. *et al.* Association of peripheral artery disease with in-hospital outcomes after endovascular transcatheter aortic valve replacement. *Catheter. Cardiovasc. Interv.* **94**, 249–255 (2019).
49. Philip, J. L. *et al.* Pulmonary vascular mechanical consequences of ischemic heart failure and implications for right ventricular function. *Am. J. Physiol.-Heart Circ. Physiol.* **316**, H1167–H1177 (2019).
50. Arvidsson, P. M. *et al.* Vortex ring behavior provides the epigenetic blueprint for the human heart. *Sci. Rep.* **6**, 22021 (2016).
51. Gharib, M., Rambod, E., Kheradvar, A., Sahn, D. J. & Dabiri, J. O. Optimal vortex formation as an index of cardiac health. *Proc. Natl. Acad. Sci.* **103**, 6305–6308 (2006).
52. Kim, I.-C. *et al.* Usefulness of Left Ventricular Vortex Flow Analysis for Predicting Clinical Outcomes in Patients with Chronic Heart Failure: A Quantitative Vorticity Imaging Study Using Contrast Echocardiography. *Ultrasound Med. Biol.* **44**, 1951–1959 (2018).
53. Martínez-Legazpi, P. *et al.* Contribution of the Diastolic Vortex Ring to Left Ventricular Filling. *J. Am. Coll. Cardiol.* **64**, 1711–1721 (2014).
54. Kheradvar, A. *et al.* Diagnostic and prognostic significance of cardiovascular vortex formation. *J. Cardiol.* **74**, 403–411 (2019).
55. Khodaei, S., Fatouraee, N. & Nabaei, M. Numerical simulation of mitral valve prolapse considering the effect of left ventricle. *Math. Biosci.* **285**, 75–80 (2017).

56. Khalafvand, S. S., Ng, E. Y.-K., Zhong, L. & Hung, T.-K. Three-dimensional diastolic blood flow in the left ventricle. *J. Biomech.* **50**, 71–76 (2017).
57. Le, T. B., Elbaz, M. S. M., Van Der Geest, R. J. & Sotiropoulos, F. High Resolution Simulation of Diastolic Left Ventricular Hemodynamics Guided by Four-Dimensional Flow Magnetic Resonance Imaging Data. *Flow Turbul. Combust.* **102**, 3–26 (2019).
58. Su, B. *et al.* Cardiac MRI based numerical modeling of left ventricular fluid dynamics with mitral valve incorporated. *J. Biomech.* **49**, 1199–1205 (2016).
59. Govindarajan, V. *et al.* Synergy between Diastolic Mitral Valve Function and Left Ventricular Flow Aids in Valve Closure and Blood Transport during Systole. *Sci. Rep.* **8**, 1–14 (2018).
60. Seo, J. H. & Mittal, R. Effect of diastolic flow patterns on the function of the left ventricle. *Phys. Fluids* **25**, 110801 (2013).
61. Khalafvand, S. S., Ng, E. Y. K., Zhong, L. & Hung, T. K. Fluid-dynamics modelling of the human left ventricle with dynamic mesh for normal and myocardial infarction: Preliminary study. *Comput. Biol. Med.* **42**, 863–870 (2012).
62. Domenichini, F., Pedrizzetti, G. & Baccani, B. Three-dimensional filling flow into a model left ventricle. *J. Fluid Mech.* **539**, 179–198 (2005).
63. Jahanzamin, J., Fatouraee, N. & Nasiraei-Moghaddam, A. Effect of turbulent models on left ventricle diastolic flow patterns simulation. *Comput. Methods Biomech. Biomed. Engin.* **0**, 1–10 (2019).
64. Mao, W., Caballero, A., McKay, R., Primiano, C. & Sun, W. Fully-coupled fluid-structure interaction simulation of the aortic and mitral valves in a realistic 3D left ventricle model. *PLOS ONE* **12**, e0184729 (2017).
65. Gao, H. *et al.* A coupled mitral valve—left ventricle model with fluid–structure interaction. *Med. Eng. Phys.* **47**, 128–136 (2017).
66. Cheng, Y., Oertel, H. & Schenkel, T. Fluid-structure coupled CFD simulation of the left ventricular flow during filling phase. *Ann. Biomed. Eng.* **33**, 567–576 (2005).
67. Arefin, Md. S. & Morsi, Y. S. Fluid structure interaction (FSI) simulation of the left ventricle (LV) during the early filling wave (E-wave), diastasis and atrial contraction wave (A-wave). *Australas. Phys. Eng. Sci. Med.* **37**, 413–423 (2014).
68. Krittian, S., Janoske, U., Oertel, H. & Böhlke, T. Partitioned Fluid–Solid Coupling for Cardiovascular Blood Flow. *Ann. Biomed. Eng.* **38**, 1426–1441 (2010).
69. Tang, D., Yang, C., Geva, T. & del Nido, P. J. Image-based patient-specific ventricle models with fluid–structure interaction for cardiac function assessment and surgical design optimization. *Prog. Pediatr. Cardiol.* **30**, 51–62 (2010).
70. Le, T. B. & Sotiropoulos, F. Fluid–structure interaction of an aortic heart valve prosthesis driven by an animated anatomic left ventricle. *J. Comput. Phys.* **244**, 41–62 (2013).
71. Nordsletten, D. *et al.* Fluid–solid coupling for the investigation of diastolic and systolic human left ventricular function. *Int. J. Numer. Methods Biomed. Eng.* **27**, 1017–1039 (2011).
72. Chen, W. W., Gao, H., Luo, X. Y. & Hill, N. A. Study of cardiovascular function using a coupled left ventricle and systemic circulation model. *J. Biomech.* **49**, 2445–2454 (2016).
73. Chen, W. W., Gao, H., Luo, X. Y. & Hill, N. A. Study of cardiovascular function using a coupled left ventricle and systemic circulation model. *J. Biomech.* **49**, 2445–2454 (2016).

74. Quarteroni, A., Lassila, T., Rossi, S. & Ruiz-Baier, R. Integrated Heart—Coupling multiscale and multiphysics models for the simulation of the cardiac function. *Comput. Methods Appl. Mech. Eng.* **314**, 345–407 (2017).
75. Viola, F., Meschini, V. & Verzicco, R. Fluid–Structure-Electrophysiology interaction (FSEI) in the left-heart: A multi-way coupled computational model. *Eur. J. Mech. - BFluids* **79**, 212–232 (2020).
76. A, T. L. *et al. ventricle fluid dynamics with fictitious elastic*.
77. Watanabe, H., Sugiura, S., Kafuku, H. & Hisada, T. Multiphysics simulation of left ventricular filling dynamics using fluid-structure interaction finite element method. *Biophys. J.* **87**, 2074–2085 (2004).
78. Watanabe, H., Hisada, T., Sugiura, S., Okada, J. & Fukunari, H. Computer Simulation of Blood Flow, Left Ventricular Wall Motion and Their Interrelationship by Fluid-Structure Interaction Finite Element Method. *JSME Int. J. Ser. C Mech. Syst. Mach. Elem. Manuf.* **45**, 1003–1012 (2002).
79. Baillargeon, B., Rebelo, N., Fox, D. D., Taylor, R. L. & Kuhl, E. The Living Heart Project: A robust and integrative simulator for human heart function. *Eur. J. Mech. - ASolids* **48**, 38–47 (2014).
80. Caballero Andrés, Mao Wenbin, McKay Raymond, & Sun Wei. The impact of balloon-expandable transcatheter aortic valve replacement on concomitant mitral regurgitation: a comprehensive computational analysis. *J. R. Soc. Interface* **16**, 20190355 (2019).
81. Santiago, A. *et al.* Fully coupled fluid-electro-mechanical model of the human heart for supercomputers. *Int. J. Numer. Methods Biomed. Eng.* **34**, e3140 (2018).
82. Biffi, B. *et al.* A workflow for patient-specific fluid–structure interaction analysis of the mitral valve: A proof of concept on a mitral regurgitation case. *Med. Eng. Phys.* **74**, 153–161 (2019).
83. Gao, H., Carrick, D., Berry, C., Griffith, B. E. & Luo, X. Dynamic finite-strain modelling of the human left ventricle in health and disease using an immersed boundary-finite element method. *IMA J. Appl. Math.* **79**, 978–1010 (2014).
84. Nordsletten, D. A., Niederer, S. A., Nash, M. P., Hunter, P. J. & Smith, N. P. Coupling multi-physics models to cardiac mechanics. *Prog. Biophys. Mol. Biol.* **104**, 77–88 (2011).
85. Keshavarz-Motamed, Z. A diagnostic, monitoring, and predictive tool for patients with complex valvular, vascular and ventricular diseases. *Sci. Rep.* **10**, 6905 (2020).
86. Weller, H. G., Tabor, G., Jasak, H. & Fureby, C. A tensorial approach to computational continuum mechanics using object-oriented techniques. *Comput. Phys.* **12**, 620–631 (1998).
87. Tanné, D., Kadem, L., Rieu, R. & Pibarot, P. Hemodynamic impact of mitral prosthesis-patient mismatch on pulmonary hypertension: an in silico study. *J. Appl. Physiol. Bethesda Md 1985* **105**, 1916–1926 (2008).
88. Keshavarz-Motamed, Z., Garcia, J., Pibarot, P., Larose, E. & Kadem, L. Modeling the impact of concomitant aortic stenosis and coarctation of the aorta on left ventricular workload. *J. Biomech.* **44**, 2817–2825 (2011).
89. Keshavarz-Motamed, Z. *et al.* Elimination of transcoarctation pressure gradients has no impact on left ventricular function or aortic shear stress after intervention in patients with mild coarctation. *JACC Cardiovasc. Interv.* **9**, 1953–1965 (2016).
90. Sadeghi, R., Khodaei, S., Ganame, J. & Keshavarz-Motamed, Z. Towards non-invasive computational-mechanics and imaging-based diagnostic framework for personalized cardiology for coarctation. *Sci. Rep.* **10**, 9048 (2020).

91. Stergiopulos, N., Meister, J. J. & Westerhof, N. Determinants of stroke volume and systolic and diastolic aortic pressure. *Am. J. Physiol.-Heart Circ. Physiol.* **270**, H2050–H2059 (1996).
92. Mynard, J. P., Davidson, M. R., Penny, D. J. & Smolich, J. J. A simple, versatile valve model for use in lumped parameter and one-dimensional cardiovascular models. *Int. J. Numer. Methods Biomed. Eng.* **28**, 626–641 (2012).
93. Nagueh, S. F. *et al.* American Society of Echocardiography Clinical Recommendations for Multimodality Cardiovascular Imaging of Patients with Hypertrophic Cardiomyopathy: Endorsed by the American Society of Nuclear Cardiology, Society for Cardiovascular Magnetic Resonance, and Society of Cardiovascular Computed Tomography. *J. Am. Soc. Echocardiogr.* **24**, 473–498 (2011).
94. Nagueh, S. F. *et al.* Recommendations for the Evaluation of Left Ventricular Diastolic Function by Echocardiography: An Update from the American Society of Echocardiography and the European Association of Cardiovascular Imaging. *J. Am. Soc. Echocardiogr.* **29**, 277–314 (2016).
95. Yushkevich, P. A. *et al.* User-guided 3D active contour segmentation of anatomical structures: significantly improved efficiency and reliability. *Neuroimage* **31**, 1116–1128 (2006).
96. Vedula, V., Seo, J.-H., Lardo, A. C. & Mittal, R. Effect of trabeculae and papillary muscles on the hemodynamics of the left ventricle. *Theor. Comput. Fluid Dyn.* **30**, 3–21 (2016).
97. Keshavarz-Motamed, Z. *et al.* The role of aortic compliance in determination of coarctation severity: Lumped parameter modeling, in vitro study and clinical evaluation. *J. Biomech.* **48**, 4229–4237 (2015).
98. Keshavarz-Motamed, Z. *et al.* Effect of coarctation of the aorta and bicuspid aortic valve on flow dynamics and turbulence in the aorta using particle image velocimetry. *Exp. Fluids* **55**, 1696 (2014).
99. Keshavarz-Motamed, Z. *et al.* A new approach for the evaluation of the severity of coarctation of the aorta using Doppler velocity index and effective orifice area: In vitro validation and clinical implications. *J. Biomech.* **45**, 1239–1245 (2012).
100. Benevento, E., Djebbari, A., Keshavarz-Motamed, Z., Cecere, R. & Kadem, L. Hemodynamic Changes following Aortic Valve Bypass: A Mathematical Approach. *PLOS ONE* **10**, e0123000 (2015).
101. Gleason, W. L. & Braunwald, E. Studies on the first derivative of the ventricular pressure pulse in man. *J. Clin. Invest.* **41**, 80–91 (1962).
102. Van de Werf F *et al.* Diastolic properties of the left ventricle in normal adults and in patients with third heart sounds. *Circulation* **69**, 1070–1078 (1984).
103. Kass, D. A., Midei, M., Graves, W., Brinker, J. A. & Maughan, W. L. Use of a conductance (volume) catheter and transient inferior vena caval occlusion for rapid determination of pressure-volume relationships in man. *Cathet. Cardiovasc. Diagn.* **15**, 192–202 (1988).
104. Takeuchi, M., Odake, M., Takaoka, H., Hayashi, Y. & Yokoyama, M. Comparison between preload recruitable stroke work and the end-systolic pressure-volume relationship in man. *Eur. Heart J.* **13 Suppl E**, 80–84 (1992).
105. Senzaki Hideaki, Chen Chen-Huan, & Kass David A. Single-Beat Estimation of End-Systolic Pressure-Volume Relation in Humans. *Circulation* **94**, 2497–2506 (1996).
106. Brown, K. A. & Ditchey, R. V. Human right ventricular end-systolic pressure-volume relation defined by maximal elastance. *Circulation* **78**, 81–91 (1988).

107. Dell'Italia, L. J. & Walsh, R. A. Application of a time varying elastance model to right ventricular performance in man. *Cardiovasc. Res.* **22**, 864–874 (1988).
108. Maniar, H. S. *et al.* Impact of pericardial restraint on right atrial mechanics during acute right ventricular pressure load. *Am. J. Physiol. Heart Circ. Physiol.* **284**, H350-357 (2003).
109. Liang, F., Takagi, S., Himeno, R. & Liu, H. Multi-scale modeling of the human cardiovascular system with applications to aortic valvular and arterial stenoses. *Med. Biol. Eng. Comput.* **47**, 743–755 (2009).
110. Stergiopulos, N., Segers, P. & Westerhof, N. Use of pulse pressure method for estimating total arterial compliance in vivo. *Am. J. Physiol.-Heart Circ. Physiol.* **276**, H424–H428 (1999).
111. Fung, Y. C. *Biomechanics: Circulation*. (Springer Science & Business Media, 2013).
112. Jahanzamin, J., Fatouraee, N. & Nasiraei-Moghaddam, A. Effect of turbulent models on left ventricle diastolic flow patterns simulation. *Comput. Methods Biomech. Biomed. Engin.* **22**, 1229–1238 (2019).
113. Moosavi, M.-H. *et al.* Numerical simulation of blood flow in the left ventricle and aortic sinus using magnetic resonance imaging and computational fluid dynamics. *Comput. Methods Biomech. Biomed. Engin.* **17**, 740–749 (2014).
114. Chan, B. T. *et al.* Impact of myocardial infarction on intraventricular vortex and flow energetics assessed using computational simulations. *Int. J. Numer. Methods Biomed. Eng.* **35**, e3204 (2019).
115. Jasak, H. & Tuković, Z. *Automatic Mesh Motion for the Unstructured Finite Volume Method*. (2004).
116. Demirdžić, I. & Perić, M. Space conservation law in finite volume calculations of fluid flow. *Int. J. Numer. Methods Fluids* **8**, 1037–1050 (1988).
117. Nikolić, S. *et al.* Passive properties of canine left ventricle: diastolic stiffness and restoring forces. *Circ. Res.* **62**, 1210–1222 (1988).
118. Sands, G. B. *et al.* Automated imaging of extended tissue volumes using confocal microscopy. *Microsc. Res. Tech.* **67**, 227–239 (2005).
119. Demiray, H. Stresses in Ventricular Wall. *J. Appl. Mech.* **43**, 194–197 (1976).
120. Humphrey, J. D., Strumpf, R. K. & Yin, F. C. P. Determination of a Constitutive Relation for Passive Myocardium: I. A New Functional Form. *J. Biomech. Eng.* **112**, 333–339 (1990).
121. Yin, F. C. P., Strumpf, R. K., Chew, P. H. & Zeger, S. L. Quantification of the mechanical properties of noncontracting canine myocardium under simultaneous biaxial loading. *J. Biomech.* **20**, 577–589 (1987).
122. Holzapfel, G. A. & Ogden, R. W. Constitutive modelling of passive myocardium: a structurally based framework for material characterization. *Philos. Trans. R. Soc. Math. Phys. Eng. Sci.* **367**, 3445–3475 (2009).
123. Lee J M & Boughner D R. Mechanical properties of human pericardium. Differences in viscoelastic response when compared with canine pericardium. *Circ. Res.* **57**, 475–481 (1985).
124. Kayvanpour, E. *et al.* Towards Personalized Cardiology: Multi-Scale Modeling of the Failing Heart. *PLOS ONE* **10**, e0134869 (2015).
125. Wang, V. Y. *et al.* Modelling passive diastolic mechanics with quantitative MRI of cardiac structure and function. *Med. Image Anal.* **13**, 773–784 (2009).

126. Palit, A., Bhudia, S. K., Arvanitis, T. N., Turley, G. A. & Williams, M. A. In vivo estimation of passive biomechanical properties of human myocardium. *Med. Biol. Eng. Comput.* **56**, 1615–1631 (2018).
127. Mojsejenko, D. *et al.* Estimating Passive Mechanical Properties in a Myocardial Infarction using MRI and Finite Element Simulations. *Biomech. Model. Mechanobiol.* **14**, 633–647 (2015).
128. Mekkaoui, C., Reese, T. G., Jackowski, M. P., Bhat, H. & Sosnovik, D. E. Diffusion MRI in the heart. *NMR Biomed.* **30**, e3426 (2017).
129. Hong, B. D., Moulton, M. J. & Secomb, T. W. Modeling left ventricular dynamics with characteristic deformation modes. *Biomech. Model. Mechanobiol.* **18**, 1683–1696 (2019).
130. Dusturia, N., Choi, S. W., Song, K. S. & Lim, K. M. Effect of myocardial heterogeneity on ventricular electro-mechanical responses: a computational study. *Biomed. Eng. OnLine* **18**, 23 (2019).
131. Kim, Y. S. *et al.* Computational analysis of the effect of mitral and aortic regurgitation on the function of ventricular assist devices using 3D cardiac electromechanical model. *Med. Biol. Eng. Comput.* **56**, 889–898 (2018).
132. Dabiri, Y. *et al.* Method for Calibration of Left Ventricle Material Properties using 3D Echocardiography Endocardial Strains. *J. Biomech. Eng.* (2019) doi:10.1115/1.4044215.
133. Mangion, K., Gao, H., Husmeier, D., Luo, X. & Berry, C. Advances in computational modelling for personalised medicine after myocardial infarction. *Heart* **104**, 550–557 (2018).
134. Miyauchi, S., Yamada, T., Hosoi, K., Hayase, T. & Funamoto, K. Numerical analysis of the blood flow in the left ventricle with internal structures: Effect of trabeculae carneae models and atrial fibrillation. *AIP Adv.* **9**, 105209 (2019).
135. Kim, C.-H., Song, K.-S., Trayanova, N. A. & Lim, K. M. Computational prediction of the effects of the intra-aortic balloon pump on heart failure with valvular regurgitation using a 3D cardiac electromechanical model. *Med. Biol. Eng. Comput.* **56**, 853–863 (2018).
136. Garrett, A. S., Pham, T., Loiselle, D., Han, J.-C. & Taberner, A. Mechanical loading of isolated cardiac muscle with a real-time computed Windkessel model of the vasculature impedance. *Physiol. Rep.* **7**, e14184 (2019).
137. Bagnoli, P. *et al.* Computational Finite Element Model of Cardiac Torsion. *Int. J. Artif. Organs* **34**, 44–53 (2011).
138. Hassaballah, A. I., Hassan, M. A., Mardi, A. N. & Hamdi, M. An Inverse Finite Element Method for Determining the Tissue Compressibility of Human Left Ventricular Wall during the Cardiac Cycle. *PLOS ONE* **8**, e82703 (2013).
139. Hassan, M. A., Hamdi, M. & Noma, A. The nonlinear elastic and viscoelastic passive properties of left ventricular papillary muscle of a Guinea pig heart. *J. Mech. Behav. Biomed. Mater.* **5**, 99–109 (2012).
140. Quaini, A. *et al.* Validation of a 3D computational fluid–structure interaction model simulating flow through an elastic aperture. *J. Biomech.* **45**, 310–318 (2012).
141. Lassila, T. *et al.* Simulation of left ventricle fluid dynamics with mitral regurgitation from magnetic resonance images with fictitious elastic structure regularization. *ArXiv E-Prints* **1707**, arXiv:1707.03998 (2017).
142. Tuković, Ž., Karač, A., Cardiff, P., Jasak, H. & Ivanković, A. OpenFOAM Finite Volume Solver for Fluid-Solid Interaction. *Trans. FAMENA* **42**, 1–31 (2018).

143. Rugonyi, S. & Bathe, K. J. On finite element analysis of fluid flows fully coupled with structural interactions. *CMES - Comput. Model. Eng. Sci.* **2**, 195–212 (2001).
144. Mao, W., Li, K. & Sun, W. Fluid–Structure Interaction Study of Transcatheter Aortic Valve Dynamics Using Smoothed Particle Hydrodynamics. *Cardiovasc. Eng. Technol.* **7**, 374–388 (2016).
145. Toma, M. *et al.* Fluid-Structure Interaction Analysis of Subject-Specific Mitral Valve Regurgitation Treatment with an Intra-Valvular Spacer. *Prosthesis* **2**, 65–75 (2020).
146. Kivi, A. R. *et al.* Hemodynamics of a stenosed aortic valve: effects of the geometry of the sinuses and the positions of the coronary ostia. *Int. J. Mech. Sci.* 106015 (2020) doi:10.1016/j.ijmecsci.2020.106015.
147. Salman, H. E. & Yalcin, H. C. Computational Modeling of Blood Flow Hemodynamics for Biomechanical Investigation of Cardiac Development and Disease. *J. Cardiovasc. Dev. Dis.* **8**, 14 (2021).
148. Larsson, D. *et al.* Patient-Specific Left Ventricular Flow Simulations From Transthoracic Echocardiography: Robustness Evaluation and Validation Against Ultrasound Doppler and Magnetic Resonance Imaging. *IEEE Trans. Med. Imaging* **36**, 2261–2275 (2017).
149. Kelsey, L. J., Powell, J. T., Norman, P. E., Miller, K. & Doyle, B. J. A comparison of hemodynamic metrics and intraluminal thrombus burden in a common iliac artery aneurysm. *Int. J. Numer. Methods Biomed. Eng.* **33**, e2821 (2017).
150. Liao, S. *et al.* Numerical prediction of thrombus risk in an anatomically dilated left ventricle: the effect of inflow cannula designs. *Biomed. Eng. OnLine* **15**, 136 (2016).
151. Kohli, K. *et al.* A Simplified In Silico Model of Left Ventricular Outflow in Patients After Transcatheter Mitral Valve Replacement with Anterior Leaflet Laceration. *Ann. Biomed. Eng.* (2021) doi:10.1007/s10439-021-02740-z.
152. Cao, K. & Sucosky, P. Computational comparison of regional stress and deformation characteristics in tricuspid and bicuspid aortic valve leaflets. *Int. J. Numer. Methods Biomed. Eng.* **33**, e02798 (2017).
153. Doyle, B. J., McGloughlin, T. M., Kavanagh, E. G. & Hoskins, P. R. From Detection to Rupture: A Serial Computational Fluid Dynamics Case Study of a Rapidly Expanding, Patient-Specific, Ruptured Abdominal Aortic Aneurysm. in *Computational Biomechanics for Medicine* (eds. Doyle, B., Miller, K., Wittek, A. & Nielsen, P. M. F.) 53–68 (Springer, 2014). doi:10.1007/978-1-4939-0745-8_5.
154. Ribes, A. & Caremoli, C. Salomé platform component model for numerical simulation. in *31st Annual International Computer Software and Applications Conference (COMPSAC 2007)* vol. 2 553–564 (2007).
155. Tuković, Ž. & Jasak, H. A moving mesh finite volume interface tracking method for surface tension dominated interfacial fluid flow. *Comput. Fluids* **55**, 70–84 (2012).
156. Oliveira, I., Santos, G. B., Gasche, J. L., Militzer, J. & Baccin, C. E. Non-Newtonian Blood Modeling in Intracranial Aneurysm Hemodynamics: Impact On the WSS and OSI Metrics for Ruptured and Unruptured Cases. *J. Biomech. Eng.* (2021) doi:10.1115/1.4050539.
157. Nóbrega, J. M. & Jasak, H. *OpenFOAM®: Selected Papers of the 11th Workshop*. (Springer, 2019).
158. Cardiff, P. & Demirdžić, I. Thirty years of the finite volume method for solid mechanics. *ArXiv Prepr. ArXiv181002105* (2018).
159. Issa, R. I. Solution of the implicitly discretised fluid flow equations by operator-splitting. *J. Comput. Phys.* **62**, 40–65 (1986).

160. Demmel, J. W. Matrix Computations (Gene H. Golub And Charles F. van Loan). *SIAM Rev.* **28**, 252–255 (1986).
161. Oliveira, I. L. [UNESP *et al.* Rupture risk prediction of intracranial aneurysms using open source CFD software. *Int. Symp. Adv. Comput. Heat Transf.* 351–366 (2017).
162. Degroote, J., Bathe, K.-J. & Vierendeels, J. Performance of a new partitioned procedure versus a monolithic procedure in fluid–structure interaction. *Comput. Struct.* **87**, 793–801 (2009).
163. Degroote, J., Bruggeman, P., Haelterman, R. & Vierendeels, J. Stability of a coupling technique for partitioned solvers in FSI applications. *Comput. Struct.* **86**, 2224–2234 (2008).
164. Bahlmann, E. *et al.* Low systemic arterial compliance is associated with increased cardiovascular morbidity and mortality in aortic valve stenosis. *Heart* **105**, 1507–1514 (2019).
165. Braunwald Eugene, Brockenbrough Edwin C., Frahm Charles J., & Ross John. Left Atrial and Left Ventricular Pressures in Subjects without Cardiovascular Disease. *Circulation* **24**, 267–269 (1961).
166. Arbab-Zadeh Armin *et al.* Effect of Aging and Physical Activity on Left Ventricular Compliance. *Circulation* **110**, 1799–1805 (2004).
167. Caballero, L. *et al.* Echocardiographic reference ranges for normal cardiac Doppler data: results from the NORRE Study. *Eur. Heart J. - Cardiovasc. Imaging* **16**, 1031–1041 (2015).
168. Haller, G. An objective definition of a vortex. *J. Fluid Mech.* **525**, 1–26 (2005).
169. Kräuter, C. *et al.* Automated mitral valve vortex ring extraction from 4D-flow MRI. *Magn. Reson. Med.* **84**, 3396–3408 (2020).
170. Khalafvand, S. S. *et al.* Assessment of human left ventricle flow using statistical shape modelling and computational fluid dynamics. *J. Biomech.* **74**, 116–125 (2018).
171. Hedayat, M. *et al.* A hybrid echocardiography-CFD framework for ventricular flow simulations. *Int. J. Numer. Methods Biomed. Eng.* **36**, e3352 (2020).
172. Nucifora, G. *et al.* Left ventricular muscle and fluid mechanics in acute myocardial infarction. *Am. J. Cardiol.* **106**, 1404–1409 (2010).
173. Son, J.-W. *et al.* Abnormal Left Ventricular Vortex Flow Patterns in Association With Left Ventricular Apical Thrombus Formation in Patients With Anterior Myocardial Infarction. *Circ. J.* **76**, 2640–2646 (2012).
174. Hong, G.-R. *et al.* Characterization and quantification of vortex flow in the human left ventricle by contrast echocardiography using vector particle image velocimetry. *JACC Cardiovasc. Imaging* **1**, 705–717 (2008).
175. Rossini, L. *et al.* A clinical method for mapping and quantifying blood stasis in the left ventricle. *J. Biomech.* **49**, 2152–2161 (2016).
176. Kwiecinski, J. *et al.* Adverse prognosis associated with asymmetric myocardial thickening in aortic stenosis. *Eur. Heart J. - Cardiovasc. Imaging* **19**, 347–356 (2018).
177. Katayama, M. *et al.* Left Ventricular Septal Hypertrophy in Elderly Patients With Aortic Stenosis. *J. Ultrasound Med.* **37**, 217–224 (2018).
178. Habash, F. & Vallurupalli, S. Challenges in management of left ventricular thrombus. *Ther. Adv. Cardiovasc. Dis.* **11**, 203–213 (2017).
179. Weinsaft Jonathan W. *et al.* Echocardiographic Algorithm for Post–Myocardial Infarction LV Thrombus. *JACC Cardiovasc. Imaging* **9**, 505–515 (2016).

180. Yanagisawa Ryo *et al.* Early and Late Leaflet Thrombosis After Transcatheter Aortic Valve Replacement. *Circ. Cardiovasc. Interv.* **12**, e007349 (2019).
181. Massussi, M., Scotti, A., Lip, G. Y. H. & Proietti, R. Left Ventricular Thrombosis: New Perspectives on an Old Problem. *Eur. Heart J. Cardiovasc. Pharmacother.* (2020) doi:10.1093/ehjcvp/pvaa066.
182. Fraser, K. H., Zhang, T., Taskin, M. E., Griffith, B. P. & Wu, Z. J. Computational fluid dynamics analysis of thrombosis potential in left ventricular assist device drainage cannulae. *ASAIO J. Am. Soc. Artif. Intern. Organs 1992* **56**, 157–163 (2010).
183. Aycock, K. I., Campbell, R. L., Lynch, F. C., Manning, K. B. & Craven, B. A. The Importance of Hemorheology and Patient Anatomy on the Hemodynamics in the Inferior Vena Cava. *Ann. Biomed. Eng.* **44**, 3568–3582 (2016).
184. Itatani, K. *et al.* Optimal Conduit Size of the Extracardiac Fontan Operation Based on Energy Loss and Flow Stagnation. *Ann. Thorac. Surg.* **88**, 565–573 (2009).
185. Elbaz, M. S. M. *et al.* Assessment of viscous energy loss and the association with three-dimensional vortex ring formation in left ventricular inflow: In vivo evaluation using four-dimensional flow MRI. *Magn. Reson. Med.* **77**, 794–805 (2017).
186. Pedrizzetti, G. & Domenichini, F. Nature Optimizes the Swirling Flow in the Human Left Ventricle. *Phys. Rev. Lett.* **95**, 108101 (2005).
187. Kanski, M. *et al.* Left ventricular fluid kinetic energy time curves in heart failure from cardiovascular magnetic resonance 4D flow data. *J. Cardiovasc. Magn. Reson.* **17**, 111 (2015).
188. Khalafvand, S. S., Hung, T.-K., Ng, E. Y.-K. & Zhong, L. Kinematic, Dynamic, and Energy Characteristics of Diastolic Flow in the Left Ventricle. *Comput. Math. Methods Med.* **2015**, 701945 (2015).
189. Jain, S. *et al.* MRI Assessment of Diastolic and Systolic Intraventricular Pressure Gradients in Heart Failure. *Curr. Heart Fail. Rep.* **13**, 37–46 (2016).
190. Londono-Hoyos, F. *et al.* Non-invasive intraventricular pressure differences estimated with cardiac MRI in subjects without heart failure and with heart failure with reduced and preserved ejection fraction. *Open Heart* **6**, e001088 (2019).
191. Firstenberg, M. S. *et al.* Noninvasive estimation of transmitral pressure drop across the normal mitral valve in humans: importance of convective and inertial forces during left ventricular filling. *J. Am. Coll. Cardiol.* **36**, 1942–1949 (2000).
192. Verdecchia Paolo, Angeli Fabio, & Reboldi Gianpaolo. Hypertension and Atrial Fibrillation. *Circ. Res.* **122**, 352–368 (2018).
193. Shuhaiber, J. Transcatheter aortic valve replacement and thrombus formation. *Eur. J. Cardiothorac. Surg.* **56**, 495–496 (2019).
194. Shadden, S. C., Katija, K., Rosenfeld, M., Marsden, J. E. & Dabiri, J. O. Transport and stirring induced by vortex formation. *J. Fluid Mech.* **593**, 315–331 (2007).
195. Krittanawong, C. *et al.* Predictors of In-Hospital Mortality after Transcatheter Aortic Valve Implantation. *Am. J. Cardiol.* **125**, 251–257 (2020).
196. Fukui, M., Généreux, P. & Cavalcante, J. L. Assessment of Cardiac Damage in Aortic Stenosis. *Cardiol. Clin.* **38**, 23–31 (2020).
197. Anantha-Narayanan, M. *et al.* Impact of diastolic dysfunction on long-term mortality and quality of life after transcatheter aortic valve replacement. *Catheter. Cardiovasc. Interv.* **95**, 1034–1041 (2020).

198. Kapadia, S. R. *et al.* 5-year outcomes of transcatheter aortic valve replacement compared with standard treatment for patients with inoperable aortic stenosis (PARTNER 1): a randomised controlled trial. *Lancet Lond. Engl.* **385**, 2485–2491 (2015).
199. Virtanen, M. P. O. *et al.* Comparison of Survival of Transfemoral Transcatheter Aortic Valve Implantation Versus Surgical Aortic Valve Replacement for Aortic Stenosis in Low-Risk Patients Without Coronary Artery Disease. *Am. J. Cardiol.* **125**, 589–596 (2020).

# Chapter 3: Personalized intervention cardiology with transcatheter aortic valve replacement made possible with a non-invasive monitoring and diagnostic framework

Seyedvahid Khodaei[1], Alison Henstock[1], Reza Sadeghi[1], Stephanie Sellers[2,3], Philipp Blanke[2,3], Jonathon Leipsic[2,3], Ali Emadi [1,4], Zahra Keshavarz-Motamed*[1,5,6]

1. Department of Mechanical Engineering, McMaster University, Hamilton, ON, Canada
2. St. Paul's Hospital, Vancouver, British Columbia, Canada
3. Department of Radiology, University of British Columbia, Vancouver, British Columbia, Canada
4. Department of Electrical and Computer Engineering, McMaster University, Hamilton, ON, Canada
5. School of Biomedical Engineering, McMaster University, Hamilton, ON, Canada
6. School of Computational Science and Engineering, McMaster University, Hamilton, ON, Canada

*Nature - Scientific Reports,* 11(1), 1-28. (2021). https://doi.org/10.1038/s41598-021-85500-2

* Correspondence author

## 3.1 Abstract

One of the most common acute and chronic cardiovascular disease conditions is aortic stenosis, a disease in which the aortic valve is damaged and can no longer function properly. Moreover, aortic stenosis commonly exists in combination with other conditions causing so many patients suffer from the most general and fundamentally challenging condition: complex valvular, ventricular and vascular disease (C3VD). Although blood flow quantification is critical for accurate and early diagnosis of aortic stenosis and C3VD, proper diagnostic methods are still lacking because the fluid-dynamics methods that can be used as engines of new diagnostic tools are not well developed yet. Despite remarkable advances in medical imaging, imaging on its own is not enough to quantify the blood flow effectively. Moreover, understanding of C3VD and its progression has been hindered by the absence of a proper non-invasive tool for the assessment of the cardiovascular function. To enable the development of new non-invasive diagnostic methods, we developed an innovative image-based computational fluid dynamics framework to quantify: (1) metrics of global circulatory function; (2) metrics of global cardiac function as well as (3) local cardiac fluid dynamics in patients with C3VD. This framework is based on an innovative non-invasive Doppler-based patient-specific computational engine. We validated the framework against clinical cardiac catheterization and Doppler echocardiographic measurements and demonstrated its diagnostic utility in providing novel analyses and interpretations of clinical data. Our findings position this framework as a promising new non-invasive diagnostic tool that can provide blood flow metrics while posing no risk to the patient. The diagnostic information, that the framework can provide, is vitally needed to improve clinical outcomes, to assess patient risk and to plan treatment.

## 3.2 Introduction

One of the most common acute and chronic cardiovascular disease conditions is aortic stenosis, a disease in which the aortic valve is damaged and can no longer function properly. This condition can progress to heart failure through the rapid deterioration of the pumping action of the heart. Heart failure is a disease associated with high mortality and morbidity rates that is increasing in prevalence, affecting at least 26 million people worldwide. It is responsible for about $108 billion per year, or 1-3%, of global health expenditures [1]. For aortic stenosis patients, heart failure is the primary cause of death, and half of them will die within two years of symptom onset if aortic valve disease is left untreated [2]. Prior hospitalization due to heart failure is associated with poor outcomes following aortic stenosis intervention; some research suggests that by performing an earlier treatment, before patients experience hospitalization for heart failure, outcomes may be improved [2,3]. It is important to note that aortic valve disease commonly exists in combination with other conditions, so many patients suffer from the most general and fundamentally challenging condition: complex valvular, ventricular and vascular diseases (C3VD). In C3VD, mechanical interactions occur between multiple valvular, ventricular and vascular pathologies wherein the physical phenomena associated with each pathology exhibit magnified effects on the cardiovascular system due to the presence of the other conditions [4–10].

Transcatheter aortic valve replacement (TAVR) is an emerging minimally invasive intervention for patients with aortic stenosis *across a broad risk spectrum*. Prior to the recent introduction of TAVR, the only possible choice for high-risk patients with aortic stenosis was surgical replacement of the aortic valve (SAVR). TAVR is a growing alternative to surgical intervention that has provided positive outcomes and has reduced the mortality rate, with many patients experiencing a significant improvement following intervention. TAVR is also increasingly being

used in lower-risk patients who may be younger and/or have moderate valvular disease. However, there are risks associated with TAVR, because in some cases, the situation worsens or the pre-existing cardiovascular disease changes to another form of cardiovascular disease [4–6,8]. The following series of questions must be answered before and after TAVR to ensure the procedure is completed safely and effectively: What impacts will the procedure have on the heart mechanics and function? When is the best time to perform the intervention? Is there a means to assess which patients will have a better or worse outcome? If performed, what impacts will there be on the cardiac function, circulatory mechanics and valve function? A tool that can answer these questions for each patient while considering their specific conditions is highly needed.

*"Cardiology is flow"* [11], and therefore, the essential sources of cardiovascular mortality and morbidity can be explained on the basis of adverse hemodynamics: abnormal biomechanical forces and flow patterns, leading to the development and progression of cardiovascular disease [12]. *Despite its importance, there exists no diagnostic tool that can quantify fluid dynamics* for many cardiovascular diseases, including C3VD and TAVR, in a patient-specific manner, because the fluid-dynamics methods that can be used as engines of new diagnostic tools are not yet well developed. Moreover, there are varying prognostic implications, so careful diagnosis is vital [13]. In this research, we contributed to advancing computational mechanics as a powerful means to enhance clinical measurements and medical imaging to make novel diagnostic methods for patients with C3VD and TAVR *that pose no risk to the patient.*

The heart resides in a sophisticated vascular network whose loads impose boundary conditions on the heart function. **Precise and effective diagnosis hinges on the quantification of the following three Requirements**: **global** hemodynamics: **(1)** ***Metrics of circulatory function,*** e.g., detailed information of the dynamics of the circulatory system, and **(2)** ***Metrics of cardiac function***, e.g.,

heart workload and the breakdown of workload contributions from each cardiovascular disease component, and of the **local** hemodynamics: **(3)** ***Cardiac fluid dynamics***, e.g., details of the instantaneous 3-D flow, vortex formation, growth, eventual shedding, and their effects on fluid transport and stirring inside the heart. Although all of these can provide valuable information about the patient's state of cardiac deterioration and heart recovery, currently, clinical decisions are chiefly made based on the anatomy alone. To supplement anatomical information, cardiac catheterization is used as the clinical gold standard for evaluating heart function and workload, but it is invasive, expensive, and high risk [14], and is therefore not practical for diagnosis in routine daily clinical practice or serial follow-up examinations. Phase-contrast magnetic resonance imaging can provide 3-D velocity fields, but it has poor temporal resolution [15,16], is costly, lengthy and not possible for many patients with implanted devices. Doppler echocardiography (DE) is potentially the most versatile tool for hemodynamics. While 3-D DE suffers from low temporal resolution, 2-D colour DE is low-cost and risk-free, and has high temporal resolution. Studies with 4-D phase-contrast magnetic resonance unveiled that the intraventricular flow is mainly parallel to the apical long-axis plane, and measurement of 2-D flow on this plane can provide a very good estimate of the 3-D flow [17]. This makes the apical long-axis plane, passing through the left ventricle (LV) apex and the centers of the mitral valve, aortic valve, left atrium and proximal ascending aorta, the optimal 2-D representation of the 3-D LV flow. Recent advances in DE velocity measurements are: (1) Echo-PIV is an adaptation of Particle Image Velocimetry (PIV) for computing flow velocity by tracking speckles that are often enhanced with contrast agents (microbubbles) [18–20]. Echo-PIV is promising, but depending on the acquisition frame rate, high velocities can be underestimated [21], which has implications for diagnosis. In addition, the contrast agent must constantly and homogeneously fill the field to avoid both saturated and dark areas.

These factors may hinder routine clinical application of the method [22]; (2) Colour-Doppler vector flow mapping (VFM) permits calculation of the velocity field without contrast agents through colour DE [23]. Colour DE is fast and routinely used in clinics [22], but it cannot measure velocity in the direction perpendicular to the beam. Despite all the potential that DE has and the progress made with VFM, there is no DE method to date that can comprehensively evaluate local hemodynamics in the LV, valves, ascending aorta and left atrium in terms of vortical structures, their temporal evolutions, fluid transport and mixing. There is also no DE method to evaluate global hemodynamics and to break down the contributions of each cardiovascular system component.

In this study, we developed a highly innovative computational-mechanics framework that can eventually, upon further development and validation, function as a diagnostic tool for the most general and fundamentally challenging condition, C3VD, in both pre and post intervention states. Such a diagnostic tool should dynamically couple the local hemodynamics with the global circulatory cardiovascular system to provide a framework to evaluate the effects of the global (Requirements #1 and #2) and local hemodynamics (Requirement #3) in a patient-specific manner. For this purpose, we developed a framework based on an innovative Doppler-based patient-specific lumped-parameter algorithm and a 3-D strongly-coupled fluid-solid interaction. It satisfies all three requirements for developing a clinically-effective computational diagnostic framework that can quantify local and global hemodynamics in patients who have C3VD in both pre and post intervention states. Our lumped-parameter algorithm allows for the analysis of any combination of complex valvular, vascular and ventricular diseases in C3VD patients by *purposefully using limited and reliable non-invasive input parameters acquired with Doppler echocardiography and sphygmomanometers to continuously calculate patient-specific global hemodynamics quantities*

(Requirements #1 and #2). We used the clinical data of eleven patients with C3VD in both pre and post TAVR conditions (twenty-two cases) not only to validate the proposed framework but also to demonstrate its diagnostic abilities by providing novel analyses and interpretations of clinical data. The validation was done against clinical cardiac catheterization data [24] and clinical Doppler echocardiographic measurements.

## 3.3 Methods

We developed an innovative image-based computational fluid dynamics framework to quantify: (1) metrics of circulatory function (global hemodynamics); (2) metrics of cardiac function (global hemodynamics) as well as (3) cardiac fluid dynamics (local hemodynamics) in patients with C3VD in both pre and post intervention states. This framework is based on an innovative non-invasive Doppler-based patient-specific lumped-parameter algorithm that allows for the analysis of any combination of complex valvular, vascular and ventricular diseases [24], and a 3-D strongly-coupled fluid-solid interaction (FSI) (Figure 1: schematic diagram; Figure 2: algorithm flow chart; Table 1). Calculations of this computational fluid dynamics framework were validated against clinical cardiac catheterization data [24] and Doppler echocardiographic measurements (Figures 3 and 4).

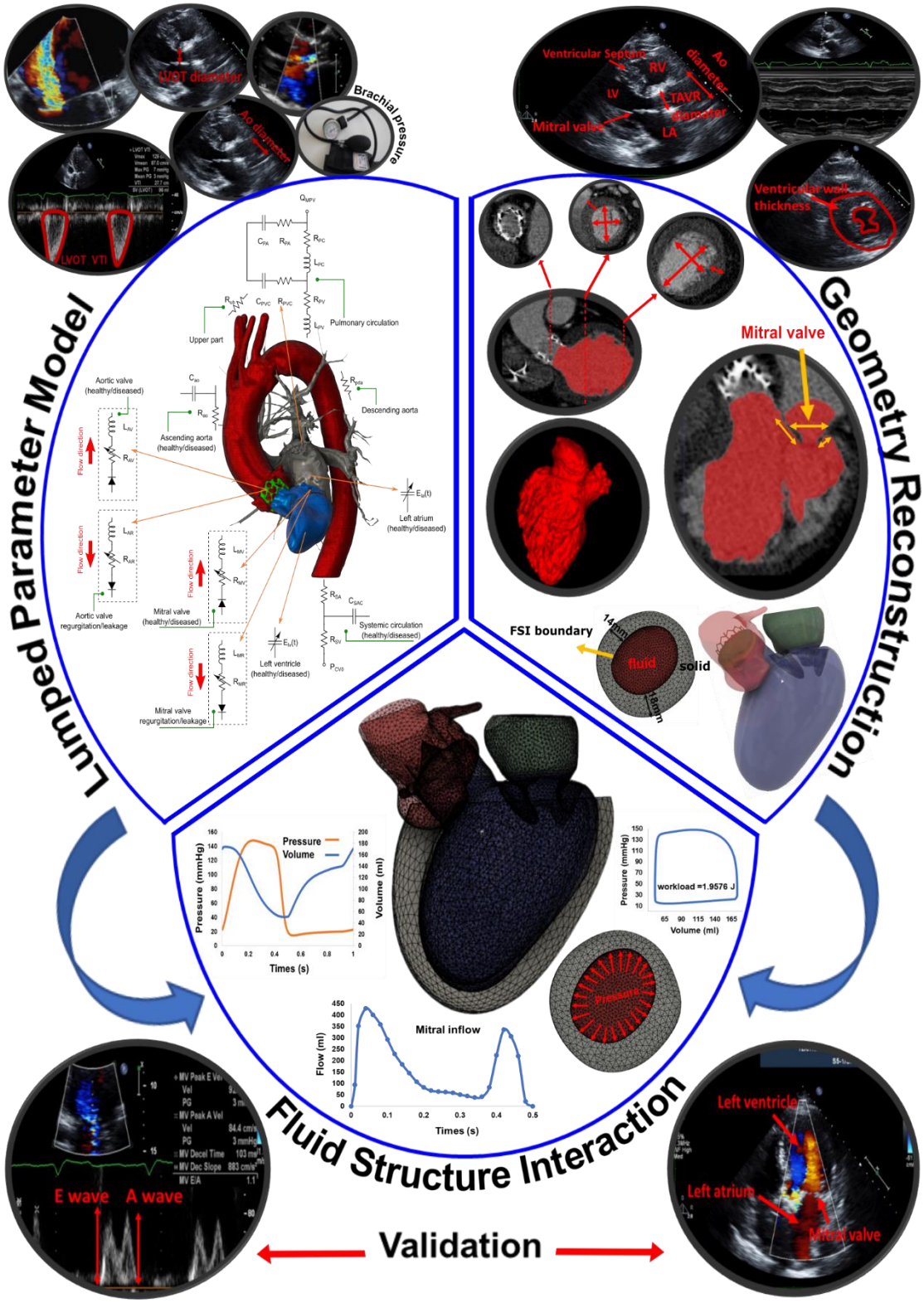


Figure 3-1. Schematic diagram of computational domain. Anatomical and electrical schematic diagrams of the lumped parameter modeling. This model includes the following sub-models. 1) left atrium, 2) left ventricle, 3) aortic valve, 4) mitral valve, 5) systemic circulation, and 6)

pulmonary circulation. Abbreviations are the same as in Table 1. Input parameters were measured using Doppler echocardiography and sphygmomanometer. Simulation domain and FSI modeling. Imposing correct boundary conditions to the flow model is critical because the local flow dynamics are influenced by downstream and upstream conditions. Patient-specific LPM simulating the function of the left side of the heart was coupled to the inlet of the mitral valve model. This data was obtained from the patient-specific image-based lumped parameter model. Reconstructed 3-dimensional geometry in a patient with AS who received TAVR using computed tomography. Geometries were used for investigating hemodynamics using FSI and LPM.

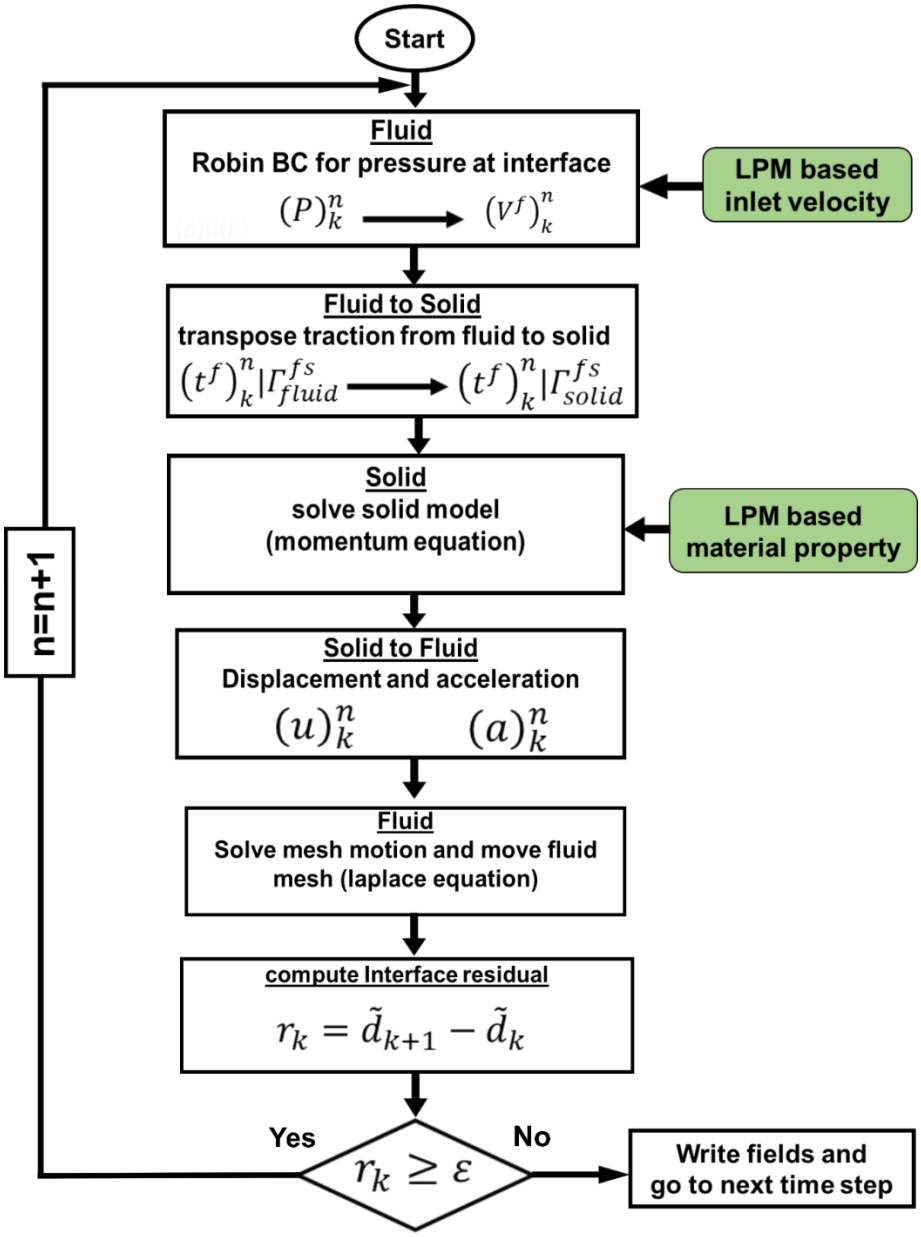


Figure 3-2. LPM and strongly coupled FSI algorithm flow chart.

Table 3-1. Cardiovascular parameters. Summarized parameters used in the lumped-parameter modeling to simulate all patient-specific cases.

| Description | Abbreviation | Value |
|---|---|---|
| **Valve parameters** | | |
| Effective orifice area | EOA | Measured using DE |
| Energy loss coefficient | $E_LCo$ | $\frac{(EOA)A}{A-EOA}$<br>EOA and A are measured using DE |
| Variable resistance | $R_{AV}$ & $R_{AR}$ | $\frac{\rho}{2E_LCo\|_{AV}^2}Q(t)$ & $\frac{\rho}{2E_LCo\|_{AR}^2}Q(t)$ |
| | $R_{MV}$ & $R_{MR}$ | $\frac{\rho}{2EOA\|_{MV}^2}Q_{MV}(t)$ & $\frac{\rho}{2EOA\|_{MR}^2}Q(t)$ |
| Inductance | $L_{AV}$ & $L_{AR}$ | $\frac{2\pi\rho}{\sqrt{E_LCo\|_{AV}}}$ & $\frac{2\pi\rho}{\sqrt{E_LCo\|_{AR}}}$ |
| | $L_{MV}$ & $L_{MR}$ | $\frac{M_{MV}}{EOA_{MV}}$ & $\frac{M_{MV}}{EOA_{MR}}$ |
| Inertance (mitral valve) | $M_{MV}$ | Constant value: 0.53 $gcm^{-2}$ |
| **Systematic circulation parameters** | | |
| Aortic resistance | $R_{ao}$ | Constant value: 0.05 $mmHg.s.mL^{-1}$ |
| Aortic compliance | $C_{ao}$ | Initial value: 0.5 mL/mmHg<br>Optimized based on brachial pressures<br>*(Systolic and diastolic brachial pressures are optimization constraints)* |
| Systemic vein resistance | $R_{SV}$ | 0.05 $mmHg.s.mL^{-1}$ |
| Systemic arteries and veins compliance | $C_{SAC}$ | Initial value: 2 mL/mmHg<br>Optimized based on brachial pressures<br>*(Systolic and diastolic brachial pressures are optimization constraints)* |
| systemic arteries resistance (including arteries, arterioles and capillaries) | $R_{SA}$ | Initial value: 0.8 $mmHg.s.mL^{-1}$<br>Optimized based on brachial pressures<br>*(Systolic and diastolic brachial pressures are optimization constraints)* |
| Upper body resistance | $R_{ub}$ | Adjusted to have 15% of total flow rate in healthy case[25] |
| Proximal descending aorta resistance | $R_{pda}$ | Constant value: 0.05 $mmHg.s.mL^{-1}$ |
| **Elastance Function*** | | |
| Maximum Elastance | $E_{max}$ | 2.1 (LV)<br>0.17 (LA) |
| Minimum Elastance | $E_{min}$ | 0.06 (LV, LA) |
| Elastance ascending gradient | $m_1$ | 1.32 (LV, LA) |
| Elastance descending gradient | $m_2$ | 27.4 (LV)<br>13.1 (LA) |
| Elastance ascending time translation | $\tau_1$ | 0.269 T (LV)<br>0.110 T (LA) |
| Elastance descending time translation | $\tau_2$ | 0.452 T (LV)<br>0.18 T (LA) |
| Elastance Normalization | N | $\frac{E_{MAX}-E_{MIN}}{2}$ |
| **Pulmonary circulation parameters** | | |
| Pulmonary Vein Inertance | $L_{PV}$ | Constant value:0.0005 $mmHg{\cdot}s^2{\cdot}mL^{-1}$ |
| Pulmonary Vein Resistance | $R_{PV}$ | Constant value: 0.002 $mmHg{\cdot}s{\cdot}mL^{-1}$ |
| Pulmonary Vein and capillary Resistance | $R_{PVC}$ | Constant value: 0.001 $mmHg{\cdot}s{\cdot}mL^{-1}$ |
| Pulmonary Vein and Capillary Compliance | $C_{PVC}$ | Constant value: 40 mL/mmHg |
| Pulmonary Capillary Inertance | $L_{PC}$ | Constant value: 0.0003 $mmHg{\cdot}s^2{\cdot}mL^{-1}$ |
| Pulmonary Capillary Resistance | $R_{PC}$ | Constant value: 0.21 $mmHg{\cdot}s{\cdot}mL^{-1}$ |
| Pulmonary Arterial Resistance | $R_{PA}$ | Constant value: 0.01 $mmHg{\cdot}s{\cdot}mL^{-1}$ |

| | | |
|---|---|---|
| Pulmonary Arterial Compliance | $C_{PA}$ | Constant value: 4 mL/mmHg |
| Mean Flow Rate of Pulmonary Valve | $Q_{MPV}$ | *Forward LVOT-SV* is the only input flow condition (measured using DE). *$Q_{MPV}$ is a flow parameter that was optimized so that the lump-parameter model could reproduce the desirable DE-measured Forward LVOT-SV*. |
| **Input flow condition** | | |
| Forward left ventricular outflow tract stroke volume | Forward LVOT-SV | Measured using DE |
| **Output condition** | | |
| Central venous pressure | $P_{CV0}$ | Constant value: 4 mmHg |
| **Other** | | |
| Constant blood density | $\rho$ | Constant value: 1050 kg/m$^3$ |
| Heart rate | HR | Measured using DE |
| Duration of cardiac cycle | T | Measured using DE |
| Systolic End Ejection time | $T_{EJ}$ | Measured using DE |
| End diastolic volume | EDV | Measured using DE |
| End systolic volume | ESV | Measured using DE |

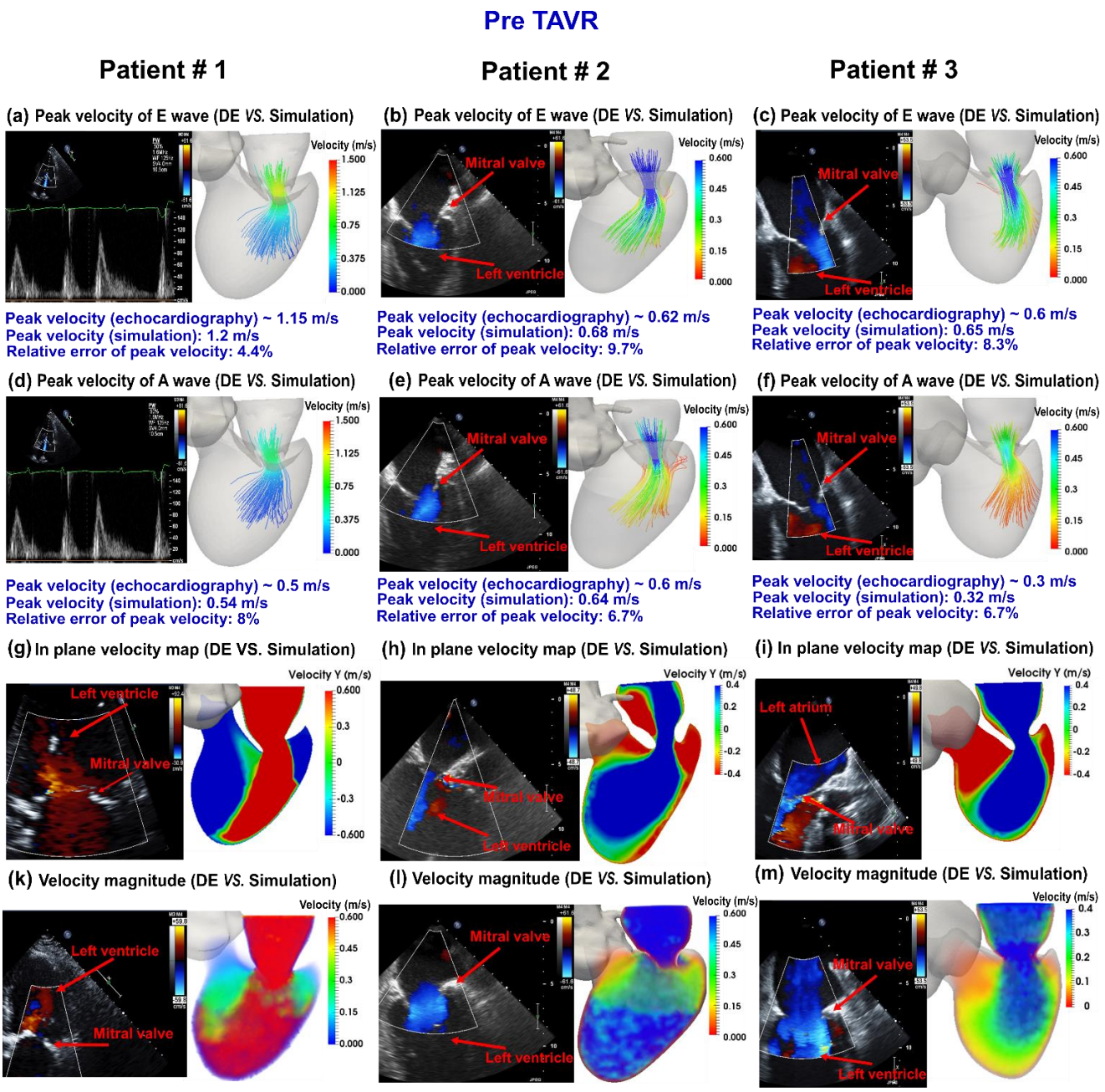


Figure 3-3. Validation: Doppler-based LPM and FSI framework vs. Clinical Doppler echocardiography data in pre-TAVR condition. (a) to (f) Trans-mitral velocity during diastole in patients #1 to #3; (g) to (i) Left ventricle flow (apical view) during diastole in patients #1 to #3; (j) to (l) Trans-mitral and left ventricle flow (apical view) in patients #1 to #3.

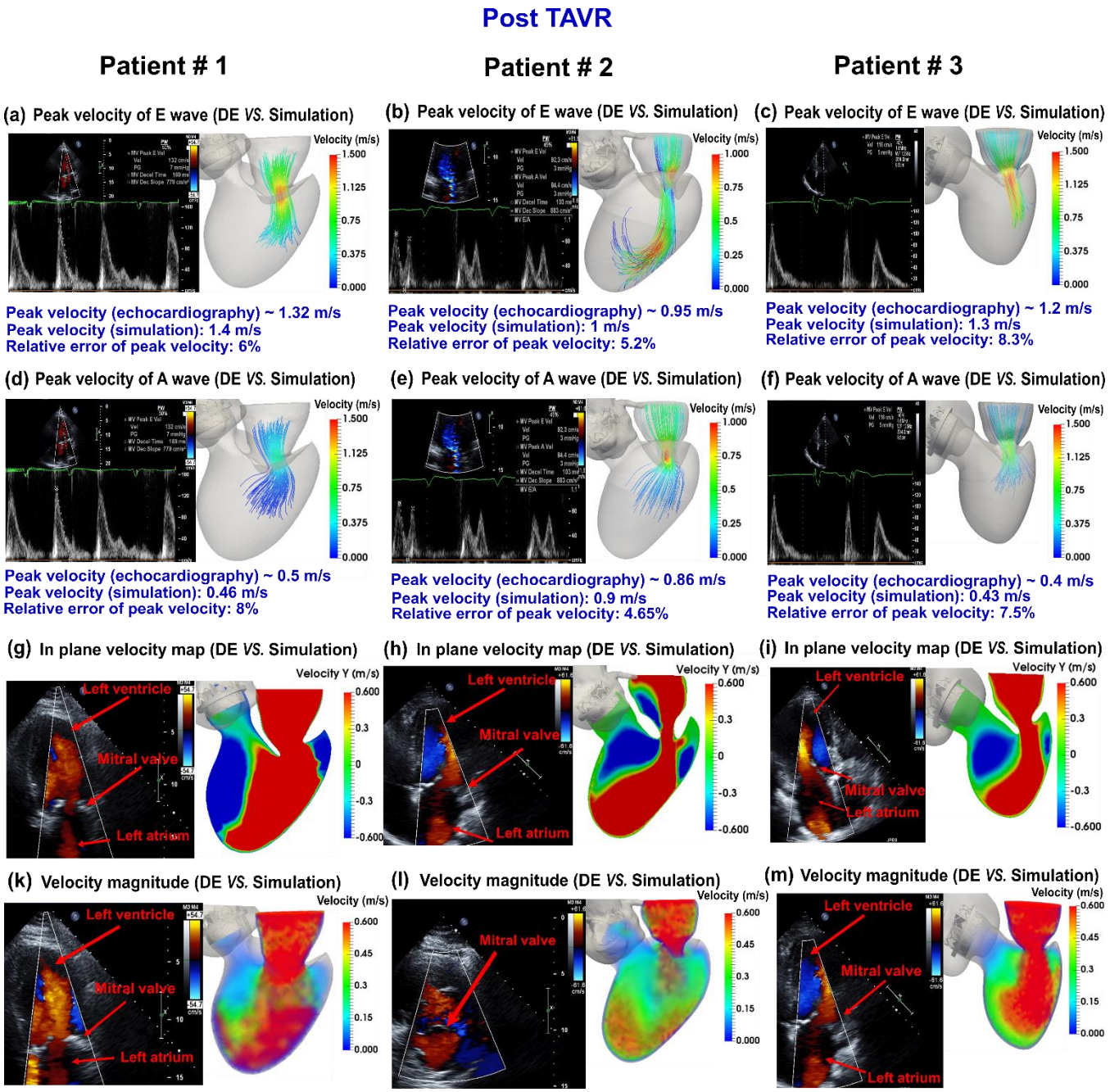


Figure 3-4. Validation: Doppler-based LPM and FSI framework vs. Clinical Doppler echocardiography data in post-TAVR condition. (a) to (f) Trans-mitral velocity during diastole in patients #1 to #3; (g) to (i) Left ventricle flow (apical view) during diastole in patients #1 to #3; (j) & (l) Trans-mitral and left ventricle flow (apical view) during diastole in patients #1 and #3; (k) Mitral valve flow (parasternal short axis view) in patient #2.

### 3.3.1 Clinical medical imaging

*Study population & Data acquisition*

We retrospectively selected 11 C3VD patients with severe aortic valve stenosis who underwent TAVR between 2013 and 2017 at St. Paul's Hospital (Vancouver, Canada; N=11). Demographic and procedural data were collected from the patient medical records. The clinical outcome was evaluated using medical records and the New York Heart Association (NYHA) functional class, assessed at baseline and at 90-days post-TAVR. The protocol was reviewed and approved by the Ethics Committee of the institutions. Data were acquired at two time points: pre-procedure and 90-days post-procedure. Valve type and size were decided prior to the procedure by the local clinical team based on pre-procedural echocardiographic, computed tomographic, and angiographic imaging and data.

*Doppler echocardiography (DE)*

Doppler echocardiography (DE) data included raw images and documented reports that were collected at baseline and at 90-days post-procedure. Echocardiograms and reports were reviewed and analyzed in a blinded fashion by three senior cardiologists using OsiriX imaging software (OsiriX version 8.0.2; Pixmeo, Switzerland) as recommended by the American Society of Echocardiography (ASE) [26]. The following metrics were measured:

***Input parameters of the LPM algorithm***: The algorithm used the following input parameters that all can be reliably measured using DE: forward left ventricular outflow tract stroke volume, heart rate, ejection time, ascending aorta area, left ventricular outflow tract area, aortic valve effective orifice area, mitral valve effective orifice area, and grading of aortic and mitral valves regurgitation severity. These parameters were measured in the parasternal long axis, parasternal short axis,

apical two-chamber, apical four-chamber and apical five-chamber views of the heart as recommended by the ASE [26] (see Figure 1 for details).

***Geometrical parameters*:** We used the parasternal long axis, parasternal short axis, M-Mode, apical two-chamber and apical four-chamber views of the heart to measure the following parameters: height, diameter and wall thickness of the LV; and leaflet and annulus sizes of the aortic and mitral valves. Such DE-based measurements give us indispensable insights about the patients' state, and they are extremely helpful to verify the same measurements made in reconstructed 3-D models based on CT data. These 3-D models will eventually be used in fluid-solid interaction (FSI) simulations.

*Computed tomography (CT)*

CT data included images and documented reports that were collected at baseline and at 90-days post-procedure. We used the data as follows:

***Model reconstruction:*** We used CT images from patients to segment and reconstruct the 3-D geometries of the complete ventricle (ventricle, TAVR, ascending aorta, mitral valve and left atrium) employing ITK-SNAP (version 3.8.0-BETA) [27], a 3-D image processing and model generation software package (Figure 1). These 3-D reconstructions were used for FSI simulations.

### 3.3.2 Lumped-parameter model

We have developed an innovative non-invasive image-based patient-specific diagnostic, monitoring and predictive computational-mechanics framework for *Complex valvular-vascular-ventricular diseases (C3VD)*. For simplicity, this C3VD computational mechanics framework is called C3VD-CMF, described in details elsewhere [24]. C3VD-CMF enables the quantification of (1) details of the physiological pulsatile flow and pressures throughout the heart and circulatory

system (local hemodynamics); (2) heart function metrics, e.g., left ventricle workload and instantaneous left ventricular pressure, etc. (global hemodynamics). C3VD-CMF also provides the breakdown of effects that each disease constituent imposes on the global function of the cardiovascular system. Currently, none of the above metrics can be obtained noninvasively in patients, and when invasive procedures are undertaken, the collected metrics cannot be as complete as the results that C3VD-CMF provides by any means [24].

The developed algorithm (C3VD-CMF) consists of a parameter estimation algorithm and a lumped-parameter model that includes several sub-models allowing analysis of any combination of complex valvular, vascular and ventricular diseases in both pre and post intervention conditions: 1) left atrium, 2) left ventricle, 3) aortic valve, 4) mitral valve, 5) systemic circulation and 6) pulmonary circulation (Figure 1; Table 1). The algorithm uses the following input parameters that can all be measured reliably using Doppler echocardiography: forward left ventricular outflow tract stroke volume (*Forward LVOT-SV*), heart rate, ejection time, ascending aorta area, left ventricular outflow tract area, aortic valve effective orifice area and mitral valve effective orifice area. Other input parameters of the model are systolic and diastolic blood pressures measured using sphygmomanometers. The innovative lumped-parameter model calculations were validated against cardiac catheterization data in forty-nine patients with C3VD [24]. Examples of C3VD components include: valvular disease (e.g., aortic valve stenosis, mitral valve stenosis, aortic valve regurgitation and mitral valve insufficiency), ventricular disease (e.g., left ventricle dysfunction and heart failure), vascular disease (e.g., hypertension), paravalvular leaks and LV outflow tract obstruction in patients with implanted cardiovascular devices such as transcatheter valve replacement (TVR), changes due to surgical procedures for C3VD (e.g., valve replacement and

left ventricular reconstructive surgery), etc. [4,6–8,28]. Some sub-models have already been used [7,28–33] and validated against *in vivo* cardiac catheterization (N=34) [25] and *in vivo* MRI data (N=57) [34].

*Heart-arterial model*

**Left Ventricle**

Coupling between LV pressure and volume was achieved through a time varying elastance E(t) as follows:

$$E(t) = \frac{dP_{LV}(t)}{V(t) - V_0} \tag{1}$$

where $P_{LV}(t)$, $V(t)$ and $V_0$ are LV time-varying pressure, time-varying volume and unloaded volume, respectively. The amplitude of E(t) can be normalized with respect to the maximal elastance $E_{max}$, *i.e.*, the slope of the end-systolic pressure-volume relation, giving $E_N(t_N)=E(t)/E_{max}$. Time can then be normalized with respect to the time to reach peak elastance, $T_{Emax}$ ($t_N=t/T_{Emax}$).

$$E_{\max} E_N(t / T_{E\max}) = \frac{dP_{LV}(t)}{V(t) - V_0} \tag{2}$$

To model the LV normalized elastance function ($E_N$), we used a double Hill function as follows [24]:

$$E_N(t) = N \left( \frac{\left(\frac{t}{\tau_1}\right)^{m1}}{1 + \left(\frac{t}{\tau_1}\right)^{m1}} \right) \left( \frac{1}{1 + \left(\frac{t}{\tau_2}\right)^{m2}} \right) + E_{\min} \tag{3}$$

where $N$, $\tau_1$, $\tau_2$, $m_1$, $m_2$, and $E_{\min}$ are elastane normalization, ascending time translation, descending time translation, ascending gradient, descending gradient and minimum elastance, respectively (see Table 1). A double Hill function was believed necessary to model the contraction

and relaxation in the heart chambers: in Equation 3, the first term in brackets corresponds to the contraction of the chamber, and the second term in brackets corresponds to the relaxation of the chamber. $\tau_1$ and $\tau_2$ govern the time translation, while $m_1$ and $m_2$ govern the gradient of the elastance function. Parameter values used for the elastance function were adapted to obtain physiological waveforms for pressure, volume and flow that can be found in Table 1 [1].

**Left Atrium**

Coupling between LA pressure and volume was done through a time varying elastance E(t), a measure of cardiac muscle stiffness, using the same procedure as outlined above for the LV. The elastance function used for the LA is defined in Equations 2 and 3 [24]; parameter values used can be found in Table 1.

*Modeling heart valves*

**Modeling the aortic valve**

***Aortic valve***. The aortic valve was modeled using the net pressure gradient formulation $(PG_{net})$ across the aortic valve during LV ejection. This formulation expresses the instantaneous net pressure gradient across the aortic valve as a function of the instantaneous flow rate and the energy loss coefficient. It also links the LV pressure to the ascending aorta pressure:

$$PG_{net}\big|_{AV} = \frac{2\pi\rho}{\sqrt{E_L Co\big|_{AV}}}\frac{\partial Q(t)}{\partial t} + \frac{\rho}{2E_L Co\big|_{AV}^2}Q^2(t) \tag{4}$$

and

$$E_L Co\big|_{AV} = \frac{(EOA\big|_{AV})A_{AO}}{A - EOA\big|_{AV}} \tag{5}$$

where $E_L Co|_{AV}$, $EOA|_{AV}$, $A_{AO}$, $\rho$ and $Q$ are the valvular energy loss coefficient, the effective orifice area, ascending aorta cross sectional area, blood density and transvalvular flow rate, respectively.

***Aortic regurgitation***. Aortic regurgitation (AR) was modeled using the same analytical formulation as aortic stenosis as follows. The AR pressure gradient is the difference between aortic pressure and LV pressure during diastole.

$$PG_{net}|_{AR} = \frac{2\pi\rho}{\sqrt{E_L Co|_{AR}}} \frac{\partial Q(t)}{\partial t} + \frac{\rho}{2E_L Co|_{AR}^2} Q^2(t) \tag{6A}$$

and

$$E_L Co|_{AR} = \frac{EOA_{AR} A_{LVOT}}{A_{LVOT} - EOA_{AR}} \tag{6B}$$

where $E_L Co|_{AR}$ , $EOA_{AR}$ and $A_{LVOT}$ are the regurgitation energy loss coefficient, regurgitant effective orifice area and LVOT area, respectively.

**Modeling the mitral valve**

***Mitral valve***. The mitral valve (MV) was modeled using the analytical formulation for the net pressure gradient ($PG_{net}|_{MV}$) across the MV during LA ejection. This formulation expresses the instantaneous net pressure gradient across the LA and vena contracta as an unsteady incompressible inviscid flow. $PG_{net}|_{MV}$ is expressed as a function of $\rho$ , $Q_{MV}$ , $EOA_{MV}$ and $M_{MV}$ , where these quantities represent the density of the fluid, the transvalvular flow rate, effective orifice area and inertance, respectively.

$$PG_{net}|_{MV} = \frac{M_{MV}}{EOA_{M_V}}\frac{\partial Q_{MV}(t)}{\partial t} + \frac{\rho}{2EOA|_{MV}^2}{Q_{MV}}^2(t) \quad (7)$$

***Mitral regurgitation***. Mitral regurgitation (MR) was modeled using Equation 8. The MR pressure gradient is the difference between mitral pressure and LA pressure during systole.

$$PG_{net}\big|_{MR} = \frac{M_{MV}}{EOA_{MR}}\frac{\partial Q(t)}{\partial t} + \frac{\rho}{2EOA\big|_{MR}^2}Q^2(t) \quad (8)$$

where $EOA\big|_{MR}$ is the MR effective orifice area.

**Pulmonary flow**

The pulmonary valve flow waveform was simulated by a rectified sine curve with duration $t_{ee}$ and amplitude $Q_{MPV}$ as follows.

$$Q_{PV}(t) = Q_{MPV}\, sin\left(\frac{\pi t}{t_{ee}}\right),\ t \le t_{ee};\quad Q_{PV}(t) = 0,\ t_{ee} < t \le T \quad (9)$$

where $Q_{MPV}$, $t_{ee}$ and T are the mean flow rate of the pulmonary valve, end-ejection time and cardiac cycle time period, respectively. In this study, it is very important to note that *Forward LVOT-SV* is the only input flow condition that can be reliably measured using DE. $Q_{MPV}$, the mean flow rate of the pulmonary valve, was optimized so that the lumped-parameter model could reproduce the desirable DE-measured *Forward LVOT-SV*.

*Determining arterial compliance and peripheral resistance*

The total systemic resistance was computed as the quotient of the average brachial pressure and the cardiac output (assuming a negligible peripheral venous pressure (mean ~ 5 mmHg) compared to aortic pressure (mean ~ 100 mmHg)). This total systemic resistance represents the equivalent electrical resistance for all resistances in the current model. Because the LV faces the total systemic

resistance as opposed to the individual resistances, we considered the aortic resistance, $R_{ao}$, and systemic vein resistance, $R_{SV}$, as constants and adjusted the systemic artery resistance, $R_{SA}$, according to the acquired total systemic resistance. Systemic artery resistance was assessed using an optimization scheme outlined in the patient-specific parameter estimation section.

For each degree of hypertension, we fit the predicted pulse pressure to the actual pulse pressure (measured by arm cuff sphygmomanometer) obtained from clinical study by adjusting the compliances (aorta ($C_{ao}$) and systemic ($C_{SAC}$)). Therefore, for each degree of arterial hypertension, the compliance was evaluated using an optimization scheme outlined in the patient-specific parameter estimation section [24].

*Patient-specific parameter estimation*

The lumped-parameter model took the following patient-specific parameters as its inputs: forward left ventricular outflow tract stroke volume (*Forward LVOT-SV*), cardiac cycle time (T), ejection time ($T_{EJ}$), $EOA_{AV}$, $EOA_{MV}$, $A_{AO}$, $A_{LVOT}$, $EOA_{AR}$, $EOA_{MR}$ and brachial systolic and diastolic pressures measured by a sphygmomanometer. The following procedure was used to set up the patient-specific lumped-parameter model:

***1) Flow inputs***: The lumped-parameter model used only one reliably measured flow parameter as an input: forward left-ventricular outflow tract stroke volume (*Forward LVOT-SV*) (Equation 10). *Forward LVOT-SV* is defined as the volume of blood that passes through the LVOT every time the heart beats.

$$Forward\ LVOT\text{-}SV = A_{LVOT} \times VTI_{LVOT} = \frac{\pi \times (D_{LVOT})^2}{4} \times VTI_{LVOT} \quad (10)$$

where $D_{LVOT}$, $A_{LVOT}$, and $VTI_{LVOT}$ are the LVOT diameter, LVOT area, and LVOT velocity-time integral, respectively.

***2) Time inputs***: Cardiac cycle time (T) and ejection time ($T_{EJ}$) were measured using Doppler echocardiography.

***3) Aortic valve inputs***: $A_{AO}$ and $EOA|_{AV}$ were calculated using Equations 11 and 12, respectively.

$$\mathrm{A_{AO}} = \frac{\pi \times (D_{AO})^2}{4} \tag{11}$$

$$EOA|_{AV} = \frac{Forward\ LVOT\text{-}SV}{VTI_{AO}} \tag{12}$$

where $D_{AO}$ and $VTI_{AO}$ are the diameter of the ascending aorta and the velocity-time integral in the ascending aorta, respectively. To model the blood flow in the forward direction, $A_{AO}$ and $EOA|_{AV}$ were then substituted into Equation 5. Subsequently, Equation 4 was used to calculate the constant inductance ($\frac{2\pi\rho}{\sqrt{E_L Co|_{AV}}}$) and variable resistance ($\frac{\rho}{2E_L Co|_{AV}^2} Q(t)$) parameters.

***4) Aortic regurgitation inputs***: To model blood flow in the reverse direction (aortic valve insufficiency), $EOA_{AR}$ and $A_{LVOT}$ were substituted into Equation 6 to calculate the variable resistance ($\frac{\rho}{2E_L Co|_{AR}^2} Q(t)$) and constant inductance ($\frac{2\pi\rho}{\sqrt{E_L Co|_{AR}}}$) parameters. For patients with no insufficiency, the reverse branch was not included. $A_{LVOT}$ was quantified using Doppler echocardiography measurements.

***5) Mitral valve inputs***: To model the blood flow in the forward direction, the mitral valve area was substituted into Equation 7 to calculate the constant inductance ($\frac{M_{MV}}{EOA_{MV}}$) and variable resistance ($\frac{\rho}{2EOA|_{MV}^2} Q_{MV}(t)$) parameters. The mitral valve is approximately an ellipse, and its area was quantified using $A_{MV} = \frac{\pi * d_1 * d_2}{4}$, where $d_1$ and $d_2$ are mitral valve diameters measured in the apical two-chamber and apical four-chamber views, respectively.

***6) Mitral regurgitation inputs***: To model blood flow in the reverse direction (mitral valve insufficiency), $EOA_{MR}$ was substituted into Equation 8 to calculate the variable resistance ($\frac{\rho}{2EOA|_{MR}^2} Q(t)$) and constant inductance ($\frac{M_{MV}}{EOA_{MR}}$) parameters. For patients with no insufficiency, the reverse branch was not included.

***7) End systolic volume and end diastolic volume***: The end systolic volume (ESV) or end diastolic volume (EDV) measured using Doppler echocardiography were fed to the lumped-parameter model to adjust the starting and ending volumes in the P-V loop diagram.

***8) Left ventricle inputs:*** The cardiac cycle time (T) was substituted into $\tau_1$ , $\tau_2$ , $m_1$ and $m_2$ in Table 1, and then those values were substituted into Equation 3 to determine the elastance function.

***9) Left atrium inputs:*** The cardiac cycle time (T) was substituted into $\tau_1$ , $\tau_2$ , $m_1$ and $m_2$ in Table 1, and then those values were substituted into Equation 3 to determine the elastance function.

***10) Parameter estimation for systemic circulation****:* Parameters $R_{SA}$, $C_{SVC}$ and $C_{ao}$ were optimized so that the aortic pressure calculated using the model matched the patient's systolic and diastolic

brachial pressures measured using a sphygmomanometer (see computational algorithm section for details). The initial values of these parameters are given in Table 1.

***11) Simulation execution***: Please see the computational algorithm section.

*Computational algorithm*

The lumped-parameter model was analyzed numerically by forming and solving a system of ordinary differential equations in Matlab Simscape (MathWorks, Inc.), augmented by including additional functions written in Matlab and Simscape. Matlab's ode23t trapezoidal rule variable-step solver was used to solve the system of differential equations with an initial time step of 0.1 milliseconds. The convergence residual criterion was set to $10^{-6}$. Initial voltages and currents of the capacitors and inductors were set to zero. The model was run for several cycles to reach steady state before starting the response optimization process described below.

A double Hill function representation of a normalized elastance curve for human adults [35,36] was used to generate a signal to model LV elastance. It was shown that this elastance formulation can correctly represent the LV function independent of its healthy and/or pathological condition. Simulations began at the onset of isovolumic contraction. The instantaneous LV volume, V(t), was computed using the LV pressure, $P_{LV}$, and the time-varying elastance (Equation 1). The LV flow rate was subsequently calculated as the time derivative of the instantaneous LV volume. The same approach was used to obtain the left atrium volume, pressure and flow rate. $P_{LV}$ was first calculated using the initial values of the model input parameters from Table 1. The *Forward LVOT-SV* calculated using the lumped-parameter model was then fitted to the one measured (Equation 10) by optimizing $Q_{MPV}$ (as detailed below). Lastly, for each patient, $R_{SA}$, $C_{SVC}$ and $C_{ao}$ were optimized to fit the aortic pressure from the model to the patient systolic and diastolic pressures measured using a sphygmomanometer.

*Patient-specific response optimization*

The Simulink Design Optimization toolbox was used to optimize the response of the lumped-parameter model using the trust region reflective algorithm implemented in the Matlab fmincon function. The response optimization was performed in two sequential steps with tolerances of $10^{-6}$. In the first step, $Q_{MPV}$, the mean flow rate of the pulmonary valve, was optimized to minimize the error between the *Forward LVOT-SV* calculated by the lumped-parameter model and the one measured in each patient. In the second step, $R_{SA}$, $C_{SVC}$ and $C_{ao}$ were optimized so that the maximum and minimum values of the aortic pressure were respectively equal to the systolic and diastolic pressures measured using a sphygmomanometer in each patient.

### 3.3.3 Fluid-solid interaction simulation study

In this study, blood flow simulations rely on 3-D fluid-solid interaction (FSI) computational fluid dynamics using FOAM-Extend [37] in which the system of equations governing the FSI problem is formulated using the finite volume method.

*Governing equations for the fluid domain*

Blood flow was governed by the 3D incompressible Navier-Stokes equations [38,39] and was assumed to be a Newtonian and incompressible fluid with a dynamic viscosity of 0.004 Pa·s and a density of 1060 kg/m$^3$ [40]. The following continuity and momentum equations were used [41]:

$$\oint_s (n.v)ds = 0 \tag{13}$$

$$\int_\forall \frac{\partial V}{\partial t} d\forall + \oint_s v[n.v]ds = \frac{1}{\rho}\oint_s n.[\mu \nabla v]ds - \frac{1}{\rho}\int_\forall \nabla p d\forall \tag{14}$$

where $n$ is the normal vector to the surface $S$, $\forall$ is the volume, $V$ is the fluid velocity, $\mu$ is the fluid dynamic viscosity, $P$ is the blood pressure and $\rho$ is the fluid density. Due to the deformation of the fluid-solid interface, momentum Equation 14 was deemed in the Arbitrary Lagrangian-Eulerian (ALE) form as follows [41]:

$$\int_{\forall} \frac{\partial V}{\partial t} d\forall + \oint_s n.(V - V_s) v ds = \frac{1}{\rho} \oint_s n.[\mu \nabla V] ds - \frac{1}{\rho} \int_{\forall} \nabla p d\forall \tag{15}$$

$$\frac{d}{dt} \int_{\forall} d\forall = \oint_s n.V_s ds \tag{16}$$

where $V_s$ is the velocity of the surface. The relationship between the rates of change of the cell volume and the mesh motion flux was governed by conservation law [42]. Equation 16 indicates that the rates of change of the volume and the velocity of the surface are in equilibrium [42].

*Governing equations for the solid domain*

Because the LV is passive during diastole, its deformation depends on the tissue structure and the blood pressure inside the LV [43]. The endocardium, myocardium and epicardium are the three main layers that compose the wall of the heart. As the myocardium is located between the endocardium and epicardium and constitutes the majority of LV tissue thickness, it is primarily responsible for the mechanical behaviour of the LV wall [44]. Several empirical models have been designed to describe the passive behaviour of the myocardial layer [45–48], of which the most notable is the Holzapfel and Ogden model [48]. Although this model has proven to be reliable, it is based on experimental results from canine or porcine hearts, with significant structural differences from human hearts [49]. Models based on animal testing are limited by the animal's environment, morphology and physiology, which may not accurately simulate human physiology and pathophysiology in a clinical setting [50,51]. Recent studies have strived to obtain patient-specific

simulations of the LV tissue by optimizing the parameters of the Holzapfel and Ogden model using displacement fields obtained from human 3-D Magnetic Resonance Imaging (MRI) [52,53]. However, in those studies, the models and the parameters were developed for non-pulsatile blood flow of healthy LVs. Additionally, the direction of myocardial fibers is required to optimize such models, thus requiring additional imaging data such as tensor diffusive MRI [54–58]. Other studies have focused on pulsatile blood flow, but they did not optimize tissue parameters to be patient-specific [59–66]. All of these studies relied on high-resolution MRI data to simulate the moving boundary of the LV wall and usually excluded the thickness of the LV in their modeling. In addition, several recent studies have combined LPM with MRI data to obtain anisotropic material properties of the LV for electro-mechanical models [55–57,67,68]. However, MRI is costly, lengthy and not possible for many patients with implanted devices like TAVR [15,16].

In this study, we developed a method to adjust patient-specific passive material properties of the LV for patients who undergo TAVR, based on our patient-specific Doppler-based LPM algorithm [24]. *The algorithm decisively uses reliable non-invasive input parameters collected using DE. As opposed to MRI, DE is potentially the most versatile tool for hemodynamics and is low-cost and risk-free for all patients.* LV tissue was assumed to be isotropic by the Saint Venant-Kirchhoff solid model [66,69–74]. We adjusted the ventricular non-linear material properties during diastole using the results of our LPM algorithm as follows. The LPM algorithm provided the LV diastolic pressure as well as the LV pressure-volume (P-V) diagram. We applied the diastolic pressure as the boundary condition at the inner wall of the LV, and by assuming different values for material properties, we obtained a series of LV P-V diagrams. Material properties were then interpolated to find the best value that could match the LV P-V results obtained using solid modeling to those

acquired using the LPM. Young's modulus was then interpolated to match the LV P-V results to those obtained using our LPM algorithm.

According to the total Lagrangian form of the law of conservation of linear momentum, the deformation of elastic and compressible solid were considered as follows [75,76]:

$$\int_{V_0} \rho_0 \frac{\partial}{\partial t}(\frac{\partial u}{\partial t})dV = \oint_{s_0} n.(\Sigma.F^T)ds + \int_{V_0} \rho_0 b dV \quad (17)$$

where the subscript 0 describes the undeformed configuration and u is the displacement vector. F is the deformation gradient tensor and can be described as $F = I + (\nabla u)^T$; $I$ is the second order identity tensor.

Also, in Equation 17, Σ is the second Piola-Kirchhoff stress tensor and is described through the Cauchy stress tensor (σ) as follows:

$$\sigma = \frac{1}{\det F} F.\Sigma.F^T \quad (18)$$

Using the St. Venant-Kirchhoff constitutive material model, Σ is explained through isotropic Hooke's law:

$$\Sigma = \lambda tr(E)I + 2\mu E \quad (19)$$

where μ and λ are the Lame's constants (related to the Young's modulus and Poisson's ratio of material). E is the Green-Lagrangian strain tensor and is defined as follows:

$$E = \frac{1}{2}[\nabla u + (\nabla u)^T + \nabla u.(\nabla u)^T] \quad (20)$$

By substituting Equations 19 and 20 into Equation 17, the governing equation for the St. Venant-Kirchhoff hyperelastic solid in the total Lagrangian form can be obtained as follows [76]:

$$\int_{V_0} \rho_0 \frac{\partial}{\partial t}(\frac{\partial u}{\partial t})dV - \oint_{s_0} n.(2\mu + \lambda)\nabla u ds = \rho_0 \int_{V_0} b dV + \oint_{s_0} n.[\mu(\nabla u)^T + \lambda tr(\nabla u)I - (\mu + \lambda)\nabla u + \mu \nabla u.(\nabla u)^T + \frac{1}{2}\lambda tr[\nabla u.(\nabla u)^T]I + \sum.\nabla u]ds \quad (21)$$

*Fluid-structure interaction (FSI)*

The fluid and solid solvers were strongly coupled together to simulate the LV under pathophysiological flow and pressure conditions. We used the partitioned approach to separately solve the system of equations of the fluid and solid domains while the data were transferred at the interface. Both the solid and fluid were modeled using a finite-volume approach to reduce the cost of transferring information between the domains [77]. The fluid and solid solvers were coupled by the kinematic and dynamic conditions for the LV. To satisfy the kinematic condition, the velocity and displacement must be continuous across the interface [76].

$$u_{f,i} = u_{s,i} \quad (22)$$

$$V_{f,i} = V_{s,i} \quad (23)$$

where subscripts *i, s* and *f* indicate the interface, solid and fluid regions, respectively. To satisfy the dynamic condition, the forces at the interface must be in equilibrium:

$$n_i.\sigma_{f,i} = n_i.\sigma_{s,i} \quad (24)$$

The Dirichlet-Neumann procedure at the interface indicates that the fluid domain is solved for a given velocity/displacement while the solid domain is solved for a given traction [76].

*Grid Study*

Mesh for all models was generated using SALOME, an open-source mesh generation software [78]. Spatial mesh resolution had been examined to optimize the number of elements for FSI simulation. Mesh definition (with optimized non-orthogonality and skewness values) for both fluid and solid domains was considered acceptable when no significant difference (less than 2%) between successive meshes was noticed in velocity profiles. To maintain the initial quality of the cells, the fluid dynamic mesh was governed by Laplace mesh motion, which was controlled by variable diffusivity [41,79]. Mesh at the interface of the fluid and solid domains was not conformal, and consequently, interpolation was performed between the fluid and solid boundaries. The interpolation was performed based on the face-interpolation and vertex-interpolation procedures [41]. Moreover, time step independency had been studied for all models. The solution marched in time with a time step of 0.0001s, yielding a maximum Courant number of 0.2. To improve the accuracy of the numerical simulation and to reduce numerical dispersion, the Courant number was lower than 0.25 for all simulations investigated in this study. Convergence was obtained when all residuals reached a value lower than $10^{-6}$. Temporal discretization was performed with a second-order Euler backward scheme, and a second-order accurate scheme was used for the spatial discretization.

### 3.3.4 Boundary conditions & material properties

Imposing the correct boundary conditions to the flow model is critical because the local flow dynamics are influenced by downstream and upstream conditions. Boundary conditions were obtained from our patient-specific image-based lumped-parameter algorithm (Figure 1) [24]: (1) to provide the time-dependent trans-mitral blood flow rate with the physiologic E and A waveforms; (2) to calculate material properties; (3) to provide the reference pressure, set inside the LV. All

geometries were reconstructed based on images obtained at the beginning of diastole and, because LV diastolic dysfunction occurs in the left ventricular filling phase, all simulations were performed during diastole. Therefore, the TAVR was modeled to be rigidly closed and the mitral valve was modeled fully open during the diastolic phase. The effect of the chordae tendineae was not considered as the chordae tendineae do not play a significant role during mitral valve opening and do not influence the diastolic fluid dynamics [66]. A moving wall boundary condition was applied at the boundary surfaces between the fluid and solid inside the LV [65,66]. During diastole, there is an inflow from the atrium to the LV, but there is no outflow from the LV due to the closed aortic valve. Since the blood is incompressible [39], interactions between the solid and fluid domains should be considered to conserve mass by allowing the blood to expand and contract the LV wall. The no-slip boundary condition was applied to the fluid-solid interface. In order to solve the FSI problem inside the nonlinearly deforming LV, we used the Robin boundary condition for pressure based on the approach proposed by Tukovic et al [80]. The boundary condition for pressure was obtained from the following momentum equation [80]:

$$\frac{\partial V}{\partial t} + (V - V_s).\nabla V = \nabla.(v\nabla V) - \frac{1}{\rho}\nabla p \tag{25}$$

At the non-permeable moving LV wall, the following equation holds [80]:

$$n.\nabla p = -\rho \frac{\partial V_n}{\partial t} \tag{26}$$

where $V_n$ is the normal component of LV wall and fluid velocity.

Fluid pressure at the interface was estimated by solid inertia as follows:

$$p \approx \rho_s h_s \frac{\partial V_n}{\partial t} \tag{27}$$

where $\rho_s$ is the density of the LV structure and $h_s$ is the LV thickness calculated as [81]:

$$h_s = \Delta t \sqrt{\frac{\lambda + 2\mu}{\rho_s}} \tag{28}$$

where $\lambda$ and $\mu$ are Lame constants of the LV and $\Delta t$ is the time step size. Finally, combining Equations 26 and 27 gives the Robin boundary condition for pressure [80]:

$$p + \frac{\rho_s h_s}{\rho} \frac{\partial p}{\partial n} = 0 \tag{29}$$

Therefore, the coupled FSI problem employed the Robin-Neumann approach in which the fluid component used the Robin boundary condition for pressure, and subsequently, velocity was calculated based on that pressure.

### 3.3.5 FSI solution and strategy

Our FSI simulations relied on FOAM-Extend [37] in which the system of equations governing the FSI problem were formulated using the finite volume method (See Figure 2 for FSI algorithm flowchart). The system of equations governing the FSI problem was solved using a cell-centered finite volume method which is frequently used in CFD and is being increasingly used for solid modeling as well [82].

The fluid model was discretized in space using the second-order accurate cell-centered finite volume method. Numerical integration in time was performed using the second-order backward Euler scheme. The coupling between pressure and velocity was performed using the segregated

PISO algorithm [79,83]. The system of discretized equations was solved by a preconditioned Bi-Conjugate Gradient method [84].

In the solid model, the second-order derivative was discretized using a second-order accurate backward scheme, proven to stabilize the numerical model [85], to unify the discretization of the temporal terms between the fluid and solid discretization methods. The system of discretized equations was solved by a linear solver using a preconditioned Conjugate Gradient method [76].

The moving boundary (interface) of the LV was controlled using a dynamic mesh methodology which was updated with the movement of the solid boundary. This method, based on the Laplace equation, was used for updating the computational and geometric nodes of the fluid mesh and was discretized by the cell-centered finite-volume method [79]. The systems of discretized equations were solved by a geometric agglomerated algebraic multi-grid solver.

We used the interface Quasi-Newton-Implicit Jacobian Least-Squares (IQN-ILS) [86] algorithm to couple the discretized governing equations of the fluid and solid domains. The IQN-ILS method has been compared with the monolithic method and other partitioned methods such as Aitken's dynamic relaxation and has been proven to have better performance and stability [86,87]. In this partitioned approach, traction was calculated at the fluid side of the interface and was used as a traction boundary condition at the solid side of the interface.

The calculations of the 3-D flow fields were done on a discrete mesh and the data obtained from our calculations were discrete. Continuous contours for the 3-D flow fields were created in Paraview (an open-source visualization software) using linear interpolation.

## 3.4 Results

### 3.4.1 Validation: Non-invasive image-based diagnostic framework vs. clinical Doppler echocardiography data

***Trans-mitral velocity:*** Figures 3A to 3F and 4A to 4F compare the peak trans-mitral velocities for patients No. 1 to 3 between those simulated by our computational framework and those measured by DE (Figure 3: Pre-TAVR, Figure 4: Post-TAVR). There was a strong correlation between the simulated peak velocities and the ones measured by DE in all three patients, with a maximum relative error of: Pre-TAVR: 9.7% for E-waves and 8% for A-waves; Post-TAVR: 8.3% for E-waves and 8% for A-waves.

***Left ventricle flow (apical view):***

Depending on the direction of the flow, there are positive and negative values for DE velocity: red and blue colors represent blood flow towards and away from the transducer, respectively. As shown in Figures 3G to 3I and 4G to 4I, both the magnitude and direction of flow demonstrate good qualitative and quantitative agreements between our computational results and the DE measurements.

***Mitral valve flow (parasternal short axis & apical views):*** Figures 3J to 3L and 4J to 4L investigated mitral valve inflow measured by DE and calculated with our computational framework (4K: parasternal short axis; 3J, 3K, 3L, 4J and 4L: apical view). Our results show good agreements between the velocities calculated using the computational framework and the ones measured using DE.

### 3.4.2 Assessment of hemodynamics using current clinical routines

Changes of ventricular and valvular hemodynamic indices from baseline (prior to TAVR) to 90 days after TAVR are presented in Figure 5. All patients who received TAVR were diagnosed with moderate to severe aortic stenosis [88] (Severe AS is diagnosed based on a maximum aortic valve jet velocity > 4 m/s and a mean pressure gradient > 40 mmHg [88]). Clinical assessment of AS for intervention decision-making was performed based on the symptoms of aortic valve hemodynamic metrics. As expected, aortic valvular metrics improved significantly after TAVR by removing the aortic valve obstruction that was causing an excessive pressure gradient and LV afterload. Our DE data showed that for all patients, TAVR significantly reduced the maximum pressure gradient across the aortic valve to a normal range [88]. Indeed, the maximum velocity measured less than 2.5 m/s and the maximum pressure gradient measured less than 25 mmHg for all patients after TAVR. The aortic valve maximum pressure gradient reductions ranged between 42% (patient #1) and 67% (patient #6) (Figure 5A).

As an indicator of LV contractility, the ejection fraction (EF = (EDV-ESV)/EDV; EDV and ESV are end diastolic volume and end systolic volume, respectively) is considered to be abnormal once it is less than 41% [89]. Although the EF slightly increased for some patients after TAVR, with six patients demonstrating a 5-7% increase in EF, the EF still remained less than 41% for all patients from baseline to 90 days after intervention (Figure 5B).

As an indicator of heart failure symptoms, the New York Heart Association (NYHA) functional class was determined for each patient based on the level of limitation in their ordinary activities, from 1 (no limitation in daily activity) to 4 (severe limitations in daily activity). All the patients had symptoms of heart failure, defined as a NYHA functional class greater than 2, both at baseline

and at 90 days after TAVR. Post-TAVR, five patients' symptoms slightly improved (from NYHA 4 to NYHA 3), five patients remained unchanged, and one patient's symptoms worsened (from NYHA 3 to NYHA 4) (Figure 5C).

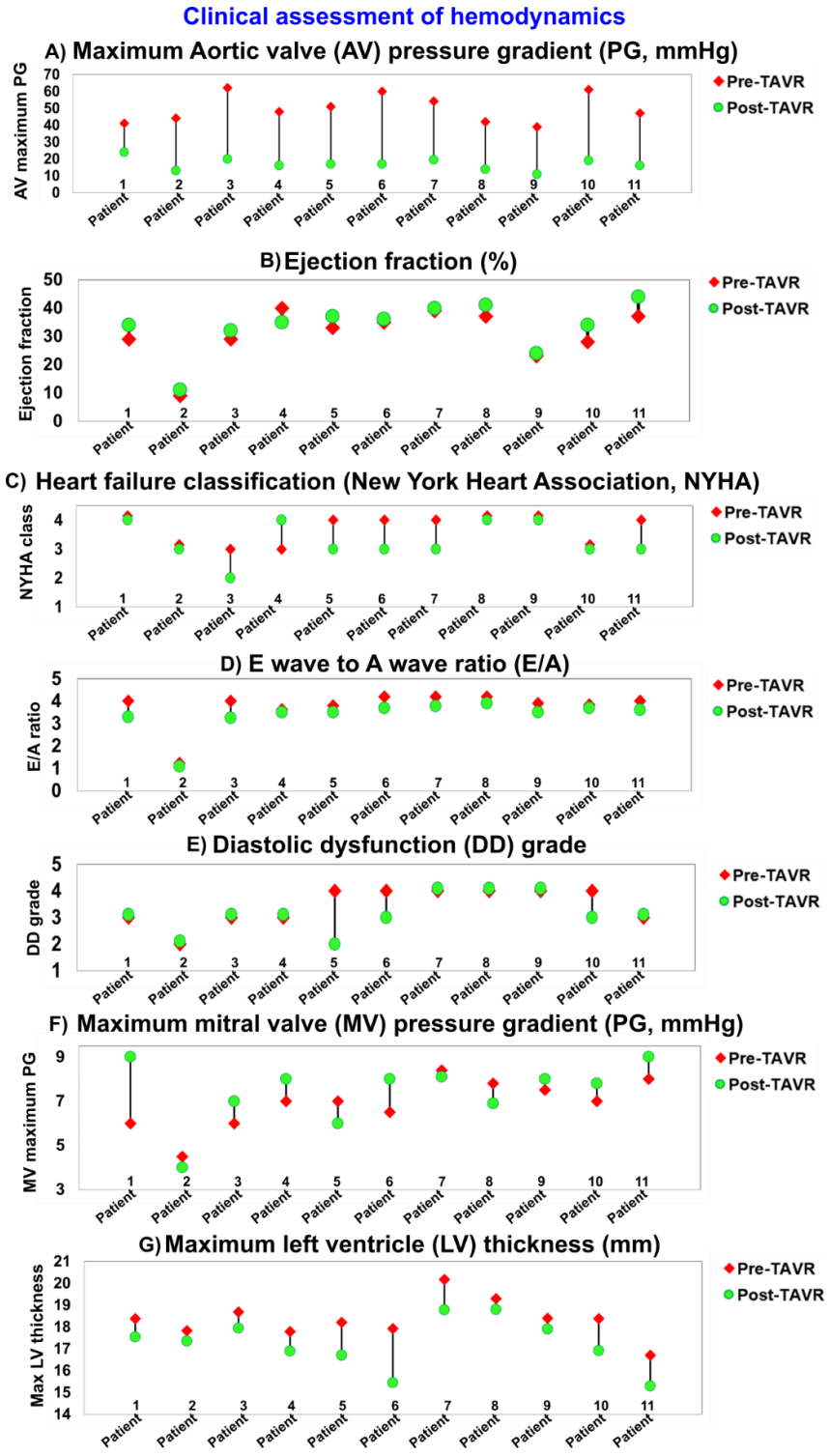


Figure 3-5. Changes in clinical assessment of hemodynamics in patients between baseline and 90-day post-TAVR (N=11). (a) Maximum aortic valve pressure gradient; (b) Ejection fraction; (c) Heart failure classification; (d) E wave to A wave ratio (E/A); (e) Diastolic dysfunction grade; (f) Maximum mitral valve pressure gradient; (g) Maximum left ventricle thickness.

Diastolic dysfunction refers to impaired LV relaxation with or without an increase in filling pressure [26]. The diastolic dysfunction grade was obtained according to the American Society of Echocardiography recommendations based on the mitral valve velocity ratio of early diastolic velocity (E) to atrial contraction velocity (A), defined as the E/A ratio, as well as the annulus velocity ($e^{'}$) as an index of LV diastolic filling efficiency [26] (Figure 5D). Diastolic dysfunction can be graded from 1 to 4; e.g. 1: Impaired relaxation, 2: Pseudo normal, 3: Reversible restrictive and 4: Fixed restrictive [90]. All patients had a diastolic dysfunction grade > 2 both at baseline and at 90 days after TAVR, meaning that they all had impaired filling at baseline, and no improvement was observed after TAVR (Figure 5E). While an E/A ratio of 0.8 to 2 is considered to be normal [26], most patients (85%) had an E/A > 2 both at baseline and at 90 days after TAVR; only one patient had E/A=1.1 for both pre and post-TAVR. While the unchanged diastolic dysfunction gradient correlated with the E/A gradient before and after TAVR, these results did not correlate with the maximum mitral valve pressure gradient (Figure 5F).

Maximum left ventricle thickness could be a potential indicator of mortality for patients with left ventricular hypertrophy (thickness > 15mm) [91–93]. Although a moderate reduction in the maximum LV wall thickness was observed for all patients after TAVR (between 2.6 % (patient # 2) and 14 % (patient # 6)), the maximum LV thickness remained greater than 15 mm for all patients even after TAVR (Figure 5G).

### 3.4.3 Non-invasive image-based diagnostic framework: computed global hemodynamics (metrics of circulatory function & metrics of cardiac function)

**Circulatory function**.

Systemic arterial compliance (SAC = stroke volume (SV)/pulse pressure (PP)) was obtained as an index of arterial hemodynamics. A low SAC (lower than 0.64 ml/m$^2$/mmHg) is associated with an increased risk of morbidity for patients with AS [94]. As shown in Figure 6A, SAC improved for the majority of patients after TAVR, with SAC increasing to > 1 (ml/mmHg) for all patients after intervention. For seven patients, the SAC increased between 16 % (patient #5) and 77% (patient #1), but for the other four patients, SAC variations were less than 10%. The increase in SAC was associated with a decrease in maximum LA pressure for all patients as shown in Figure 6B (from 14% (patient #4) to 31% (patient #1)). However, the maximum LA pressure was still greater than 18 mmHg for all patients even after TAVR (compared with normal LA pressure defined as < 15 mmHg [95]). The increased LA pressure was correlated with high velocity during the E wave and a high E/A ratio during diastole (Figure 5D) for both pre-TAVR and post-TAVR cases. Our results showed that the maximum LA pressure was universally reduced once the SAC increased after intervention. However, no improvement was observed in the E/A ratio (Figure 5D) or in diastolic dysfunction grade (Figure 5E).

**Global hemodynamics (metrics of circulatory function & metrics of cardiac function)**

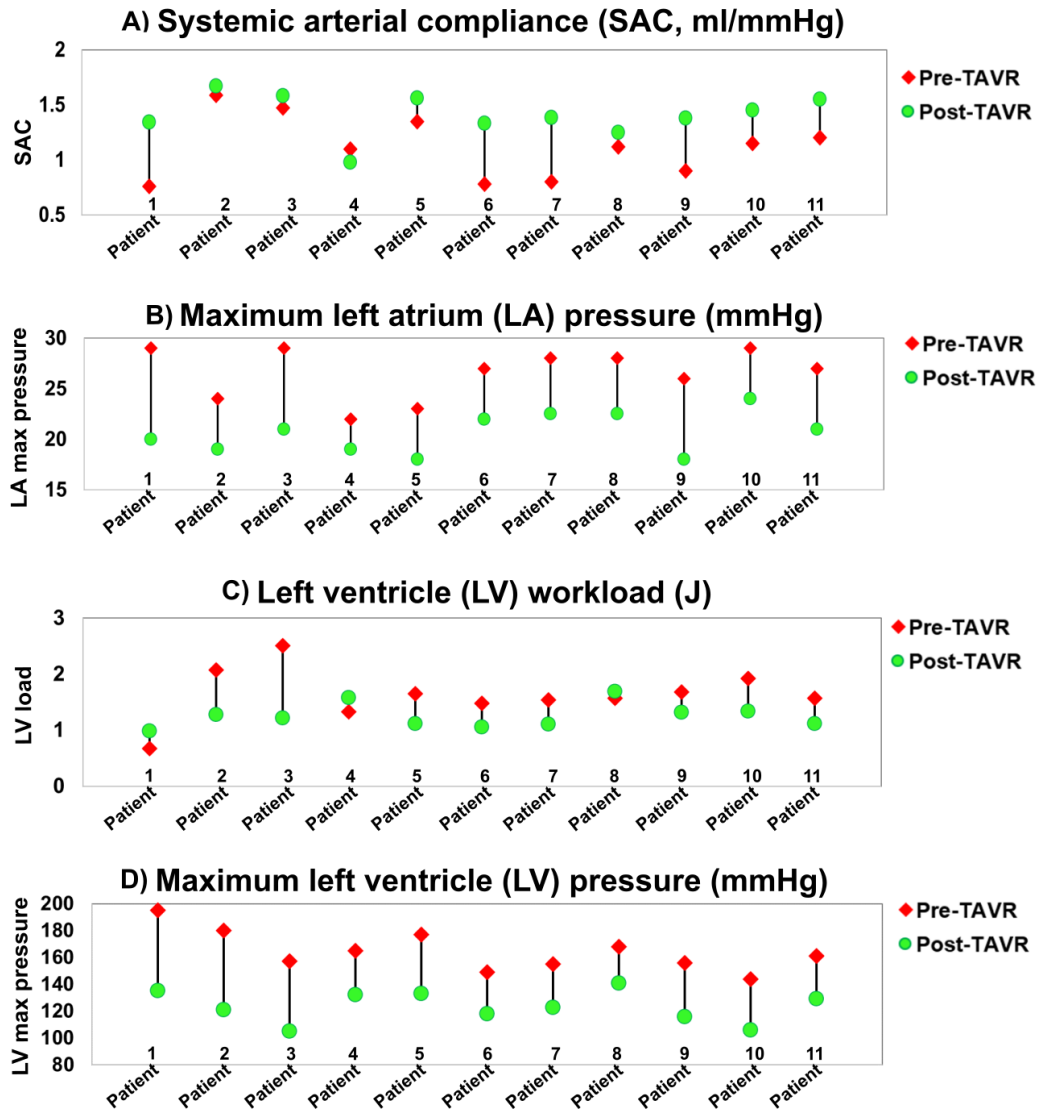


Figure 3-6. Changes in local hemodynamics (cardiac fluid dynamics) in patients between baseline and 90-day post-TAVR (N=11). (a) Systemic arterial compliance; (b) Maximum left atrium pressure; (c) Left ventricle workload; (d) Maximum left ventricle pressure. Local hemodynamics: cardiac fluid dynamics, e.g., details of the instantaneous 3-D flow and vortex formation.

**Cardiac function.** The LV workload is an effective metric of the LV load and clinical state [7,28], and represents the energy that the ventricle delivers to the blood during ejection plus the energy necessary to overcome the viscoelastic properties of the myocardium itself. The LV workload is the integral of LV pressure and its volume change and was calculated as the area encompassed by

the LV pressure–volume loop. Despite the universal reduction in the transvalvular pressure gradient, the LV workload did not improve (decrease) in all patients: TAVR reduced the LV workload in 70% of patients but increased the workload in 30% of patients (Figure 6C). Moreover, transvalvular pressure gradient reductions caused by TAVR did not always lead to an improvement in ejection fraction (Figure 5B) or heart failure symptoms as measured by the NYHA score (Figure 5C). Although TAVR did reduce the maximum LV pressure that was previously elevated by the increased LV burden from AS for all patients (Figure 6D), no improvement was observed in diastolic dysfunction grade for 73% of the patients (Figure 5E).

### 3.4.4 Non-invasive image-based diagnostic framework: computed local hemodynamics (cardiac fluid dynamics)

The flow vortical structure inside the LV depends on the atrioventricular pressure, LV geometry, LV wall stiffness and mitral valve geometry. LV dynamics during diastolic filling, in particular, could play a crucial role in overall cardiac health [96].

In order to explain the vortex morphology more precisely, the vortex sphericity index was calculated in the long axis view (2D plane) by dividing the vortex length (D2) by the vortex width ($D_1$) (Figures 7A, 8B, 9B & 10B) [97,98]. A normal vortex sphericity index (SI) is defined to be greater than 2, and a lower SI is associated with a higher risk of apex thrombosis or myocardial infarction [98]. For all patients in our study, the vortex sphericity index was lower than 2 both at baseline and 90 days after TAVR (maximum SI = 1.7), making the vortex more spherical and thus increasing the risk of thrombosis at the apex (Figure 7A). While 2/3 of patients experienced a slight increase in SI with improved filling function after TAVR, the rest (1/3 of patients) had a decrease in SI and a worsened filling pattern. Since the SI depends on upstream flow, metrics of circulatory and cardiac function, geometrical details of the mitral valve and LV, and LV relaxation, the SI can

either be improved or worsened depending on the interactions between these parameters. It is crucial to prevent the reduction of the SI following TAVR because this could lead to thrombus formation and adverse outcomes in the flow transferring mechanism from the atrium towards the left ventricular outflow tract [97,98]. This can be explained by the fact that when the elongated shape of vortex turns into a more circular shape, the apex of the LV is not exposed to a fast-moving blood flow, and thus, the flow separated from the vortex in the main stream could lead to the development of a thrombus (more prone at the apex or septum). This is an established complication in many cardiac conditions, with the highest rate detected in myocardial infarction and congestive heart failure.

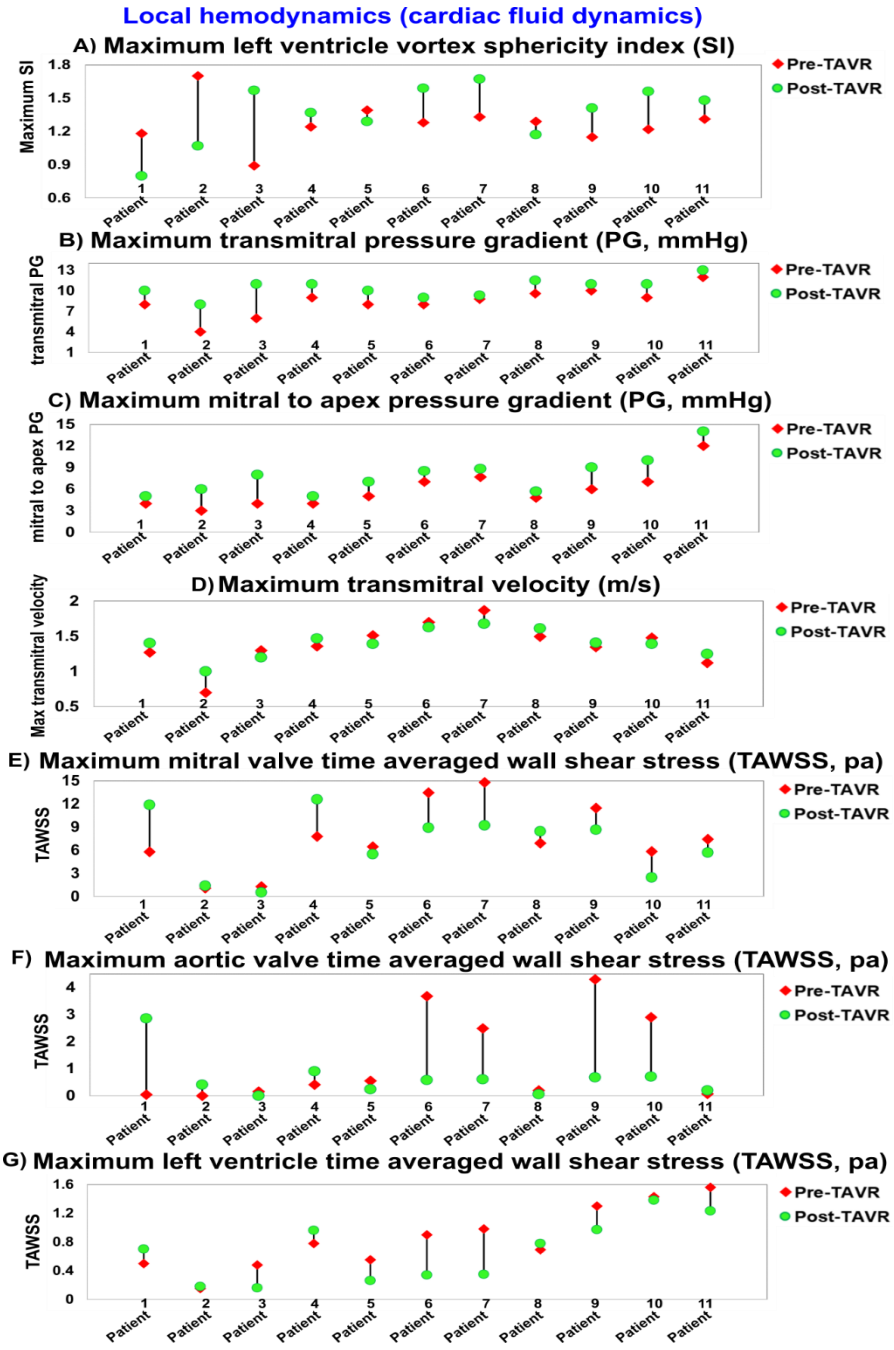


Figure 3-7. Changes in global hemodynamics (metrics of circulatory function & metrics of cardiac function) in patients between baseline and 90-day post-TAVR (N=11). (a) Maximum transmitral pressure gradient; (b) Maximum mitral to apex pressure gradient; (c) Maximum transmitral velocity; (d) Maximum mitral valve TAWSS; (e) Maximum aortic valve TAWSS; (f) Maximum left ventricle TAWSS; (g) Maximum left ventricle vortex sphericity index. Global hemodynamics: (1) Metrics of circulatory function, e.g., detailed information of the dynamics of the circulatory system, and (2) Metrics of cardiac function, e.g., heart workload and the breakdown of workload contributions from each cardiovascular disease component.

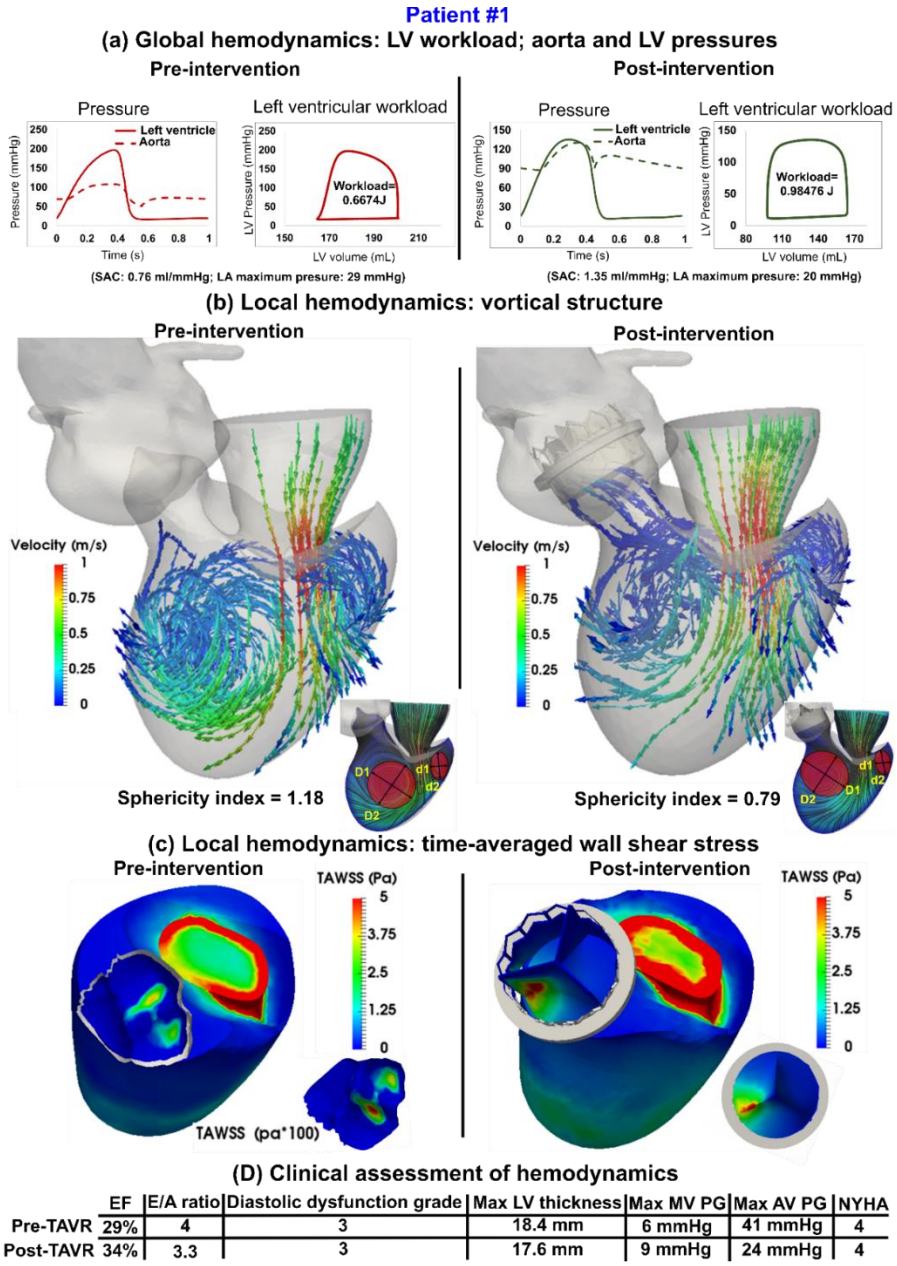


| | EF | E/A ratio | Diastolic dysfunction grade | Max LV thickness | Max MV PG | Max AV PG | NYHA |
|---|---|---|---|---|---|---|---|
| Pre-TAVR | 29% | 4 | 3 | 18.4 mm | 6 mmHg | 41 mmHg | 4 |
| Post-TAVR | 34% | 3.3 | 3 | 17.6 mm | 9 mmHg | 24 mmHg | 4 |

Figure 3-8. Changes in local and global hemodynamics in patient #1 between baseline and 90-day post-TAVR. (a) Global hemodynamics: LV workload, aorta and LV pressures; (b) Local hemodynamics: vortical structure; (c) Local hemodynamics: time-averaged wall shear stress; (d) Clinical assessment of hemodynamics. Local hemodynamics: cardiac fluid dynamics, e.g., details of the instantaneous 3-D flow and vortex formation. Global hemodynamics: (1) Metrics of circulatory function, e.g., detailed information of the dynamics of the circulatory system, and (2) Metrics of cardiac function, e.g., heart workload and the breakdown of workload contributions from each cardiovascular disease component.

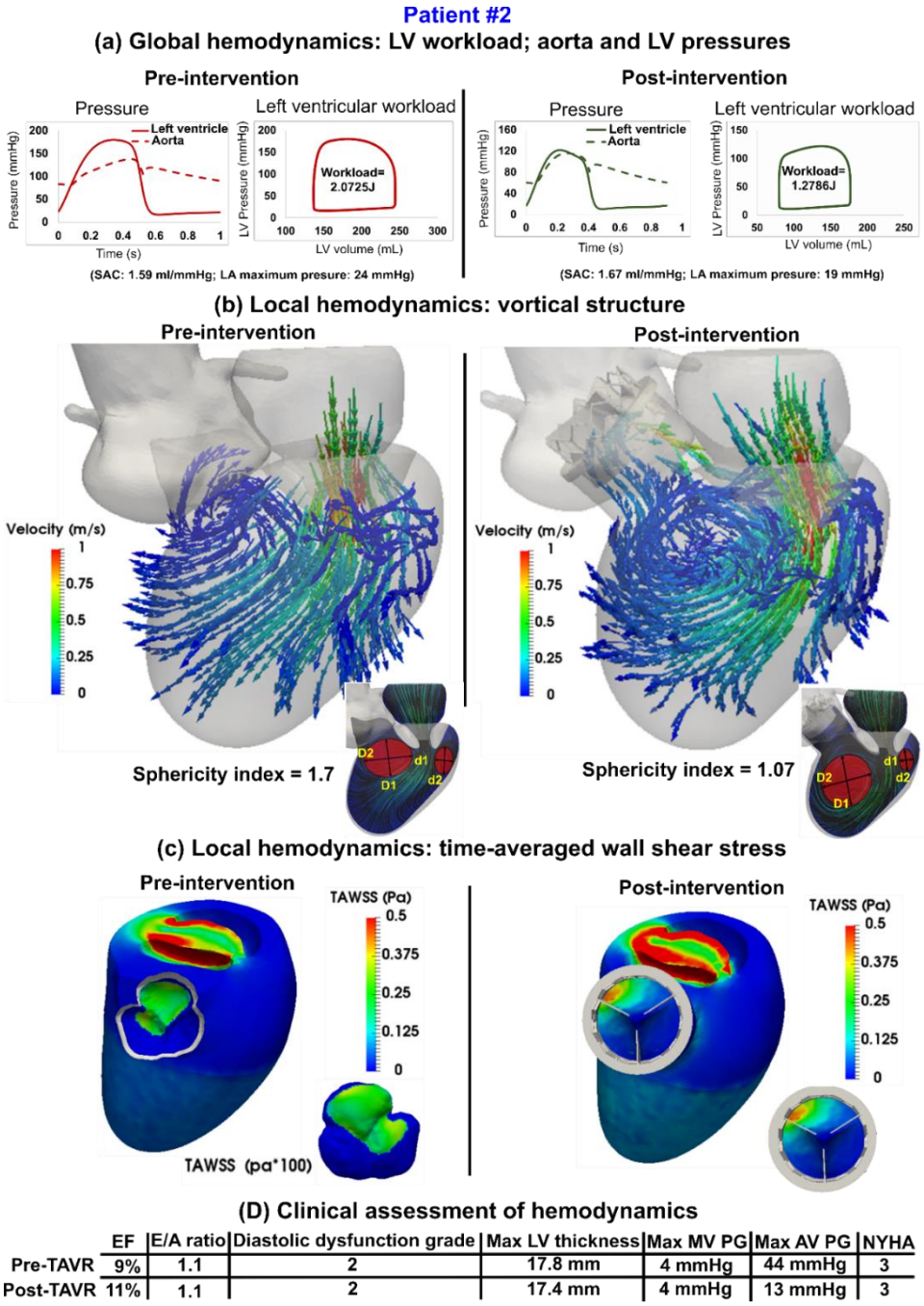


(D) Clinical assessment of hemodynamics

| | EF | E/A ratio | Diastolic dysfunction grade | Max LV thickness | Max MV PG | Max AV PG | NYHA |
|---|---|---|---|---|---|---|---|
| Pre-TAVR | 9% | 1.1 | 2 | 17.8 mm | 4 mmHg | 44 mmHg | 3 |
| Post-TAVR | 11% | 1.1 | 2 | 17.4 mm | 4 mmHg | 13 mmHg | 3 |

Figure 3-9. Changes in local and global hemodynamics in patient #2 between baseline and 90-day post-TAVR. (a) Global hemodynamics: LV workload, aorta and LV pressures; (b) Local hemodynamics: vortical structure; (c) Local hemodynamics: time-averaged wall shear stress; (d) Clinical assessment of hemodynamics.

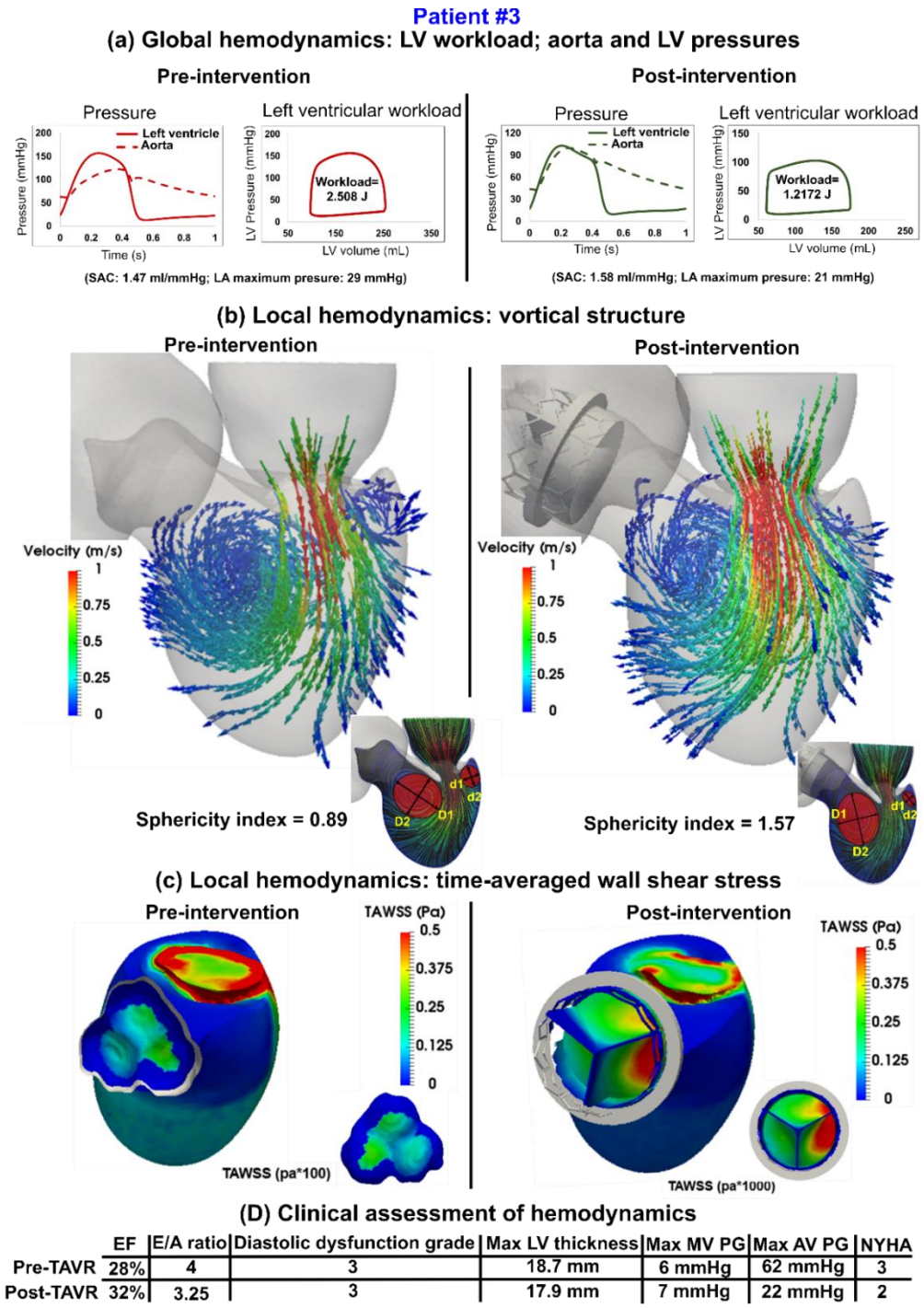


| | EF | E/A ratio | Diastolic dysfunction grade | Max LV thickness | Max MV PG | Max AV PG | NYHA |
|---|---|---|---|---|---|---|---|
| Pre-TAVR | 28% | 4 | 3 | 18.7 mm | 6 mmHg | 62 mmHg | 3 |
| Post-TAVR | 32% | 3.25 | 3 | 17.9 mm | 7 mmHg | 22 mmHg | 2 |

Figure 3-10. Changes in local and global hemodynamics in patient #3 between baseline and 90-day post-TAVR. (a) Global hemodynamics: LV workload, aorta and LV pressures; (b) Local hemodynamics: vortical structure; (c) Local hemodynamics: time-averaged wall shear stress; (d) Clinical assessment of hemodynamics.

As previously mentioned, our results showed that pressure reduced after TAVR both for the left ventricle and the left atrium (Figure 6, global hemodynamics). However, this does not always lead to an improved pressure gradient (PG) between the atrium and left ventricle after TAVR. Indeed, the maximum transmitral PG did not change for 36% of the patients, slightly increased for 45% of the patients and considerably increased for only 19% of the patients (Figure 7B). We also computed the PG from the atrium to apex to compare with the transmitral gradient. Although this diagram shares the same general trend as the transmitral PG, overall, the atrium to apex PG is lower than the transmitral PG (Figure 7C). Interestingly, this difference between the PGs (Figures 7B and 7C) is correlated with more spherical vortices (SI < 2) behind the anterior leaflet of the mitral valve, which causes less flow to be driven towards the apex and septum. In other words, a more spherical vortex leads to a reduced mitral-to-apex PG when compared to the transmitral PG. Moreover, no significant difference was observed in the maximum transmitral velocity (Figure 7D) for majority of the patients (82%), which is in agreement with the results of maximum transmitral PG (Figure 7B).

Wall shear stress, as a force induced by blood flow, has a major impact on regulating endothelial function [99]. In general, very high wall shear stress could damage the tissue and very low wall shear stress could lead to thrombus formation [99]. It has been reported that wall shear stress for a normal LV lies between 0.2 and 1.2 Pa [65,100] and increases slightly as a result of hypertrophy [100]. The total shear stress exerted on the wall throughout the cardiac cycle was evaluated using the time-averaged wall shear stress (TAWSS) which is obtained as $\mathrm{TAWSS} = \frac{1}{\mathrm{T}}\int_0^{\mathrm{T}} |\tau|\, \mathrm{dt}$ (T and $\tau$ are the cardiac cycle period and instantaneous wall shear stress, respectively). We calculated TAWSS during diastole for all cases in both pre and post TAVR states. The maximum local TAWSS was increased at both the mitral valve and aortic valve leaflets for 27% of the patients and at the LV for 20% of

the patients (Figures 7E, 7F and 7G) - Such high TAWSS could be a concern for patients who received TAVR. On the other hand, our findings showed that the aortic valve and LV could be at risk of thrombus formation for some patients as a result of very low TAWSS after TAVR (that is associated with a low velocity region around the ventricular side of the leaflets); the maximum TAWSS decreased significantly for 37% of the patients at the aortic valve (Figure 7F) and for 55% of patients at the LV (Figure 7G).

## 3.5 Discussion

*Quantification of the complex flow plays an essential role in accurate and early diagnosis of patients with C3VD* [101,102]. It can be used to effectively plan interventions and make critical clinical decisions with life-threatening risks. Once a C3VD patient develops symptoms, intervention becomes a class I recommendation [103,104]. However, at the time of diagnosis, symptoms are not reported by almost 40% of these patients [105]. Furthermore, there are often discrepancies found during clinical evaluation in one third of C3VD patients [105,106]. It is therefore essential to accurately diagnose individuals through careful hemodynamic evaluation to identify who may benefit from intervention (e.g., TAVR) and experience improved outcomes [106–108]. Overall, upon diagnosis, the results of anatomic and hemodynamic measures should agree [107]. Thus, accurate quantification of hemodynamic parameters is critical to resolve any inconsistencies and to identify the optimal course of treatment for each individual patient [106,107]. With an increasing appreciation for the hypothesis that valvular disease is complex and is also influenced by the principals of the LV and arterial system, quantitative investigations of hemodynamics that consider the interactive coupling of the valve, ventricle and arterial system have become extremely desirable [109–112]. **The following three requirements should be quantified by a clinically useful computational diagnostic**

**framework that evaluates both local and global hemodynamics for patients with C3VD and TAVR:**

**(1) Metrics of circulatory function (global hemodynamics).** The heart resides in a sophisticated vascular network whose loads impose boundary conditions on the heart function [7,25,28,102,113]. Furthermore, it is critical to replicate the correct flow and pressure conditions when developing a patient-specific cardiovascular simulator because the local flow dynamics are influenced by both downstream and upstream conditions. This ensures that patient-specific flow and pressure conditions are provided to the local flow while also enabling analysis of the effects of local hemodynamics on the global circulatory physiology. Complex valvular, ventricular and vascular diseases (C3VD) is the most fundamentally challenging cardiovascular pathology, in which several pathologies have mechanical interactions with one another wherein adverse physical phenomena associated with each pathology amplify the effects of others on the cardiovascular system [4–9,28]. TAVR often coexists with C3VD, thus making the investigation of flow and pressure details in the presence of TAVR very challenging. Although *cardiac catheterization* is currently the clinical gold standard for evaluating the global function of the heart and circulatory system using pressure and flow measurements, it is not practical for diagnosis in routine daily clinical practice or serial follow-up examinations, as it is invasive, expensive and high risk [14]. Furthermore, it is important to note that cardiac catheterization does not provide details of the physiological pulsatile flow and pressures throughout the heart and circulatory system, but instead, only enables access to blood pressure in very limited regions.

Effective diagnosis is critically dependent on quantifying details of the physiological pulsatile flow and pressures throughout the heart and circulatory system as well as the interactions within C3VD and how individual disease progressions may affect one another [114–120]. Indeed, due to these

interactions, several regions throughout the heart and surrounding system are often affected [118–120], and certain conditions of the circulatory system may prevent the accurate assessment of C3VD or affect the outcomes of TAVR [106]. For example, from a large registry of C3VD patients undergoing endovascular TAVR, almost one quarter suffered from coexisting peripheral artery disease, which was found to be associated with higher odds of vascular complications and major bleeding [121]. Moreover, regardless of the flow conditions, the presence of hypertension or reduced arterial compliance in patients with C3VD may reduce the transvalvular gradient and peak transvalvular velocity, thus causing an underestimation of aortic stenosis severity [106]. Hypertension is also a risk factor for cardiovascular events and may be associated with worse outcomes and faster progression of C3VD [106,116]. Overall, precise knowledge of these interactions and careful assessment of hemodynamics in a patient-specific manner helps optimize the diagnosis process to provide the best possible outcomes for patients [107,120], to decide upon the required course of treatment and determine if more than one intervention is required for the C3VD patients [106,117].

**(2) Metrics of cardiac function (global hemodynamics)**. In the presence of TAVR and/or C3VD, the heart is overloaded since the healthy instantaneous left-ventricle pressure and/or left-ventricle flow are altered [7,28]. In clinics, *cardiac catheterization* is the gold standard for evaluating heart function in terms of the heart workload obtained from the instantaneous left-ventricle pressure and/or left-ventricle flow. However, *there is no method to invasively or non-invasively quantify the heart workload (global function)* that can provide the contribution breakdown of each component of the cardiovascular system. This is especially crucial in C3VD and TAVR because quantification of the left-ventricle workload and its breakdown are vital to guide the prioritization of interventions and to sufficiently validate devices in regulatory testing machines. Moreover, there *is no non-invasive method for determining left-ventricular end-diastolic pressure,*

*instantaneous left-ventricular pressure, and contractility* – all of which provide valuable information about the patient's state of cardiac deterioration and heart recovery.

In patients with C3VD, the valves and left ventricle are diseased, thus altering the overall cardiac function [122,123]. Following TAVR, in many cases, there is improvement in the structure and function of the left ventricle, with regression of the myocardial cellular hypertrophy and diffuse fibrosis [122]. However, the development of focal fibrosis, which provides evidence of cardiomyocyte necrosis, is irreversible [122]. To optimize the intervention outcome before the ventricle is permanently damaged [114,124], to choose the optimal time of intervention [115,125], and to drastically reduce the risk of mortality [115], knowledge of the heart workload (cardiac function) and the contribution breakdown of each component in C3VD should be precisely quantified and evaluated at the time of diagnosis.

**(3) Cardiac fluid dynamics (local hemodynamics)**. The complex pulsatile flow in the left ventricle and its valves becomes even more complicated in C3VD. Chirality of the human heart causes this flow to be strongly three dimensional [10,96]. Moreover, as a result of TAVR, new interactions occur between the artificial implant and the native valve geometry, thus altering the fluid dynamics [126]. During filling of the normal heart, the blood entering the left ventricle through the mitral valve forms a vortex that minimizes energy dissipation, prevents blood stagnation and optimizes pumping efficiency [10,96]. C3VD and TAVR alter this optimized flow [7]: the vortex dynamics become less synchronized with the heart contraction, and vortices other than the healthy vortex ring may emerge and interact with one another. To predict the success of TAVR and plan the best deployment possible in each patient, it is crucial to know details of the instantaneous 3-D flow, vortex formation, growth, eventual shedding, and their effects on fluid transport and stirring inside the left ventricle and in the vicinity of the valves after deployment [10,96,127]. It is essential for

a diagnostic tool to carefully quantify and predict cardiac fluid dynamics in a patient-specific manner because there can be high inter-patient variability in the success of any given intervention [128]. Altered hemodynamics should be optimized with treatment, as they can lead to adverse outcomes such as an increased risk of thrombus formation [126]. One meta-analysis identified the risk of stroke being four times greater in TAVR patients with leaflet thrombosis [129].

A clinically-useful computational diagnostic framework should quantify both local and global hemodynamics. As examples: (1) Patient #1 (Figure 8); global hemodynamics: Circulatory function improved after TAVR; SAC increased from 0.76 ml/mmHg to 1.35 ml/mmHg and maximum atrium pressure decreased from 29 mmHg to 20 mmHg. However, circulatory function improvements were not associated with improvement of cardiac function. LV workload was adversely increased due to the paravalvular leakage after TAVR (Figure 8A: the workload increased from 0.67 J to 0.98 J). local hemodynamics: the increased workload led to early breakdown of the flow as a result of the interaction of paravalvular leakage with the mitral valve (Figure 8B); maximum SI decreased from 1.18 to 0.79, leading to the formation of a less intense spherical vortex behind the anterior leaflet that depicts worsening of the diastolic flow pattern after TAVR. Moreover, the maximum TAWSS increased significantly after TAVR, from 0.04 Pa to 3 Pa for the aortic valve leaflets and from 5.77 Pa to 11.86 Pa for the mitral valve leaflets. Such a significant increase in TAWSS resulted from a disturbed flow pattern around both valves. The spatial shift of the affected location following TAVR provides another critical factor while localizing the maximum TAWSS: the maximum TAWSS on the aortic valve shifted from the posterior and left coronary cusps to the right and left coronary cusps (Figure 8C). In summary, TAVR removed the aortic valve obstruction, reduced aortic valve pressure gradient and increased the ejection fraction in patient #1. However, considering cardiac function and local flow variations,

this patient is at a high risk of heart failure and did not fully benefit from TAVR; (2) Patient #2 (Figure 9); global hemodynamics: both the circulatory and cardiac functions improved after TAVR; SAC increased from 1.59 ml/mmHg to 1.67 ml/mmHg, maximum atrium pressure decreased from 24 mmHg to 19 mmHg and LV workload decreased from 2.07 J to 1.28 J (Figure 9A). local hemodynamics: the improvements of global hemodynamics were associated with an improved vortical structure; the reduced workload after TAVR was associated with slightly improved LV relaxation, which let the vortex moves forward and becomes closer to the apex prior to its interaction with the LV wall and its subsequent dissipation. Although the SI decreased for this patient, the isolated pre-TAVR vortex, located behind the anterior leaflet, shifted towards the center of the LV after TAVR (Figure 9B). This spatial shift of the vortex center facilitated the filling mechanism. Moreover, vortex alterations after TAVR led to a considerable increase of TAWSS at the aortic valve leaflets from 0.0015 Pa (with a high risk of thrombosis) to 0.4 Pa. TAVR improved the overall global and local hemodynamics, although no changes were observed in clinical hemodynamic assessment of diastolic function after TAVR (such as E/A ratio, max mitral valve PG or EF); (3) Patient #3 (Figure 10); global hemodynamics: both the circulatory and cardiac functions improved after TAVR; SAC increased from 1.47 ml/mmHg to 1.58 ml/mmHg, maximum atrium pressure decreased from 29 mmHg to 21 mmHg and LV workload decreased from 2.508 J to 1.22 J (Figure 10A). local hemodynamics: this global improvement of hemodynamics was associated with a vortex that was more elongated towards the apex with improved filling efficiency; the maximum SI increased from 0.89 to 1.57 after TAVR (Figure 10B). However, the maximum TAWSS at the aortic valve reduced significantly from 0.145 Pa (at the center of the aortic leaflets ) to 0.00052 Pa (on the left coronary cusp) after TAVR (Figure 10C), which is significantly lower than the minimum control value of 0.06 Pa [130]. Therefore,

although clinical assessments have shown improvements (increased EF, decreased aortic valve pressure gradient and decreased NYHA classification), geometrical alterations at the left ventricular outflow tract after TAVR could increase the risk of thrombus formation. Indeed, a recent study showed that left ventricular outflow tract calcification increases the risk of annular rupture and residual aortic regurgitation [131]. Therefore, despite the improvements of clinical parameters, our results depicting the details of local hemodynamics in this patient might partially explain how TAVR could adversely increase the risk of LVOT calcification and subsequent long-term complications.

A clinically-useful computational diagnostic framework that can quantify both local and global hemodynamics for patients with C3VD and TAVR should quantify the three requirements mentioned in the Introduction and Discussions. Several studies have used computational fluid dynamics (CFD) based on the discretization of the Navier-Stokes equations (finite volume method, finite element method, etc.) with a moving boundary in an attempt to quantify blood flow (local hemodynamics) inside the LV, but none of these studies considered LV tissue thickness or other tissue characteristics [40,59,62,64,66,132–136]. In addition, several researchers have recently used FSI as a promising tool for computational cardiology because it allows for the complete coupling of the heart wall and blood flow mechanics, thus demonstrating its worth as the most comprehensive tool for numerical modeling of the LV [60,137–155]. However, since: (1) patient-specific boundary conditions were not used; (2) normal valves and ventricles were modeled instead of those with C3VD; and (3) patient-specific geometries were not used, the models developed in these studies didn't satisfy the three requirements outlined in the Introduction [60,137–155] . While some models were partially validated using DE [146,153] or MRI [60], many were not validated. Five of the studies [60,74,137,143,148] did impose boundary conditions on the calculations by coupling fluid-structure

modeling calculations with lumped-parameter modeling, but the lumped-parameter models were either not patient-specific and/or they required information from MRI. MRI is not feasible in patients with implanted devices, and it is not available in all clinics, therefore restricting the collection of the necessary blood-flow and geometrical measurements. Additionally, idealized geometries were used in these studies, which could significantly affect the flow and vortex structure.

In this study, we developed an innovative computational diagnostic framework for complex diseases like C3VD and TAVR that dynamically couples the local hemodynamics (using a 3-D strongly-coupled fluid-solid interaction; FSI) with the global circulatory cardiovascular system (using the lumped-parameter algorithm) and satisfies the three requirements. This computational diagnostic framework is promising for future clinical adoption and can quantify: (1) metrics of circulatory function (global hemodynamics); (2) metrics of cardiac function (global hemodynamics) as well as (3) cardiac fluid dynamics (local hemodynamics) in patients with C3VD in both pre and post intervention states. Such information is vitally needed for effectively using advanced therapies to improve clinical outcomes and guide interventions in C3VD patients.

Due to the complex multiphysics nature of the left ventricle and heart valves, the overall estimation of cardiac parameters is very dependent on the outputs of the lumped-parameter model that are in-turn depend on the parameters used in the lumped-parameter model. Our patient-specific Doppler-based lumped-parameter algorithm, which provided boundary conditions, was validated against clinical catheterization data in forty-nine C3VD patients with a substantial inter- and intra-patient variability with a wide range of disease [24]. In the present study, we used the validated lumped-parameter model [24] to obtain time varying pressure and volume of the left ventricle as the inputs to the solid model of the LV. We modeled the LV as an isotropic Saint Venant-Kirchhoff solid

and found material parameters that could best reproduce the LV volume changes (obtained from the lumped-parameter model) while applying LV pressure (obtained from the lumped-parameter model) to the LV wall. Using this approach, in all patients that we have investigated in this study, we could always find material parameters that produce consistent results with the lumped-parameter model. Moreover, we performed a comprehensive parameter sensitivity analysis on the outputs of the lumped-parameter model that are used in the present study to find cardiac parameters. We found that the outputs from the lumped-parameter model were most sensitive to the forward left ventricular outflow tract stroke volume (Forward LVOT-SV, an input parameter to the lumped parameter algorithm): LV pressure: 27%, LV Volume 19% by a ±20% change in the Forward LVOT-SV. The other input parameters affected the output to a much lower degree. We should point out that Forward LVOT-SV is measured reliably using Doppler echocardiography with high accuracy and sensitivity of the model to this parameter does not jeopardize the results obtained from the model. In addition, sensitivity analysis revealed negligible effects of changes (±20%) in the free parameters on the model output variables. Indeed, as shown in Figures 3 and 4 in this study, the results obtained with fluid-structure interaction and lumped-parameter algorithm were validated against clinical Doppler echocardiography in patients. Our results show good agreements between velocity calculated using the computational framework and the ones measured using Doppler echocardiography in all investigated patients in both pre and post-TAVR intervention states.

## 3.6 Limitations

This study was performed and validated on 11 patients with C3VD and TAVR using a 3-D strongly-coupled fluid-solid interaction and lumped-parameter modeling framework in both pre and post intervention states (22 cases). Future studies must consider further validation of the

computational framework in a larger population of C3VD patients. However, our results in this study demonstrate the ability of the framework to track changes in both cardiac and vascular states. Our LPM algorithm allows analysis of any combination of complex valvular, vascular and ventricular diseases in both pre and post intervention conditions. It is important to note that this algorithm was validated against clinical catheterization data in forty-nine C3VD patients with a substantial inter- and intra-patient variability with a wide range of disease [24]. These observations made us more confident that the limitation in the number of patients in this study does not affect our conclusions.

*Acknowledgments*

This work was supported by NSERC Discovery Grant (RGPIN-2017-05349). Dr. Seller was supported by fellows from the Canadian Institutes of Health Research and the Michael Smith Foundation for Health Research. The funders had no role in study design, data collection and analysis, decision to publish, or preparation of the manuscript.

*Competing interests*

Drs. Blanke and Leipsic provide CT core lab services for makers of transcatheter heart valves (Edwards Lifesciences, Medtronic, Neovasc, Aegis and Tendyne Holdings), for which no direct compensation is received. Dr. Leipsic is a consultant to Edwards Lifesciences and has received institutional research support from Edwards Lifesciences.

*Author contributions*

S.K. Fluid-structure interaction and computational framework development, data collection and analysis, interpretation of data and manuscript writing; A.H. interpretation of data and manuscript writing; R.S., Data analysis and interpretation of data; S.S., P.B., and J.L. data collection and analysis; A.E. Data analysis, interpretation of data and critical revision of the manuscript; Z.K.M.

Conception and design, data analysis, algorithm development (LPM), interpretation of data, manuscript writing, critical revision, final approval of the manuscript and supervised this research. All authors read and approved the final manuscript.

*Data availability*

Upon acceptance all data will become available at https://dataverse.scholarsportal.info/.

## 3.7 References


1. Seferović, P. M. *et al.* The Heart Failure Association Atlas: rationale, objectives, and methods. *Eur. J. Heart Fail.* **22**, 638–645 (2020).
2. Jalava, M. P. *et al.* Transcatheter and Surgical Aortic Valve Replacement in Patients With Recent Acute Heart Failure. *Ann. Thorac. Surg.* **109**, 110–117 (2020).
3. Chen, S. *et al.* Impact of recent heart failure hospitalization on clinical outcomes in patients with severe aortic stenosis undergoing transcatheter aortic valve replacement: an analysis from the PARTNER 2 trial and registries. *Eur. J. Heart Fail.* (2020) doi:10.1002/ejhf.1841.
4. Généreux, P. *et al.* Paravalvular Leak After Transcatheter Aortic Valve Replacement: The New Achilles' Heel? A Comprehensive Review of the Literature. *J. Am. Coll. Cardiol.* **61**, 1125–1136 (2013).
5. Nombela-Franco, L. *et al.* Significant Mitral Regurgitation Left Untreated at the Time of Aortic Valve Replacement: A Comprehensive Review of a Frequent Entity in the Transcatheter Aortic Valve Replacement Era. *J. Am. Coll. Cardiol.* **63**, 2643–2658 (2014).
6. Blanke, P. *et al.* Predicting LVOT Obstruction in Transcatheter Mitral Valve Implantation: Concept of the Neo-LVOT. *JACC Cardiovasc. Imaging* **10**, 482–485 (2017).
7. Keshavarz-Motamed Zahra *et al.* Mixed Valvular Disease Following Transcatheter Aortic Valve Replacement: Quantification and Systematic Differentiation Using Clinical Measurements and Image-Based Patient-Specific In Silico Modeling. *J. Am. Heart Assoc.* **9**, e015063 (2020).
8. Elmariah Sammy *et al.* Outcomes of Transcatheter and Surgical Aortic Valve Replacement in High-Risk Patients With Aortic Stenosis and Left Ventricular Dysfunction. *Circ. Cardiovasc. Interv.* **6**, 604–614 (2013).
9. Sotiropoulos, F., Le, T. B. & Gilmanov, A. Fluid Mechanics of Heart Valves and Their Replacements. *Annu. Rev. Fluid Mech.* **48**, 259–283 (2016).
10. Pedrizzetti, G., La Canna, G., Alfieri, O. & Tonti, G. The vortex—an early predictor of cardiovascular outcome? *Nat. Rev. Cardiol.* **11**, 545–553 (2014).
11. Richter Yoram & Edelman Elazer R. Cardiology Is Flow. *Circulation* **113**, 2679–2682 (2006).
12. Vlachopoulos, C., O'Rourke, M. & Nichols, W. W. *McDonald's Blood Flow in Arteries: Theoretical, Experimental and Clinical Principles*. (CRC Press, 2011).
13. Kwon, S. & Gopal, A. Hemodynamic Classifications of Aortic Stenosis and Relevance to Prognosis. *Aortic Stenosis - Curr. Perspect.* (2019) doi:10.5772/intechopen.86707.
14. Omran, H. *et al.* Silent and apparent cerebral embolism after retrograde catheterisation of the aortic valve in valvular stenosis: a prospective, randomised study. *The Lancet* **361**, 1241–1246 (2003).
15. Elkins, C. J. & Alley, M. T. Magnetic resonance velocimetry: applications of magnetic resonance imaging in the measurement of fluid motion. *Exp. Fluids* **43**, 823–858 (2007).
16. Kilner, P. J., Gatehouse, P. D. & Firmin, D. N. Flow Measurement by Magnetic Resonance: A Unique Asset Worth Optimising. *J. Cardiovasc. Magn. Reson.* **9**, 723–728 (2007).
17. Eriksson, J. *et al.* Semi-automatic quantification of 4D left ventricular blood flow. *J. Cardiovasc. Magn. Reson.* **12**, 9 (2010).
18. Trahey, G. E., Allison, J. W. & von Ramm, O. T. Angle Independent Ultrasonic Detection of Blood Flow. *IEEE Trans. Biomed. Eng.* **BME-34**, 965–967 (1987).
19. Kim, H. B., Hertzberg, J. R. & Shandas, R. Development and validation of echo PIV. *Exp. Fluids* **36**, 455–462 (2004).

20. Poelma, C. *et al.* 3D Flow reconstruction using ultrasound PIV. *Exp. Fluids* **50**, 777–785 (2011).
21. Sengupta, P. P. *et al.* Left Ventricular Isovolumic Flow Sequence During Sinus and Paced Rhythms: New Insights From Use of High-Resolution Doppler and Ultrasonic Digital Particle Imaging Velocimetry. *J. Am. Coll. Cardiol.* **49**, 899–908 (2007).
22. Jensen, J. A., Nikolov, S. I., Yu, A. C. H. & Garcia, D. Ultrasound Vector Flow Imaging—Part I: Sequential Systems. *IEEE Trans. Ultrason. Ferroelectr. Freq. Control* **63**, 1704–1721 (2016).
23. Garcia, D. *et al.* Two-Dimensional Intraventricular Flow Mapping by Digital Processing Conventional Color-Doppler Echocardiography Images. *IEEE Trans. Med. Imaging* **29**, 1701–1713 (2010).
24. Keshavarz-Motamed, Z. A diagnostic, monitoring, and predictive tool for patients with complex valvular, vascular and ventricular diseases. *Sci. Rep.* **10**, 6905 (2020).
25. Keshavarz-Motamed, Z. *et al.* Elimination of transcoarctation pressure gradients has no impact on left ventricular function or aortic shear stress after intervention in patients with mild coarctation. *JACC Cardiovasc. Interv.* **9**, 1953–1965 (2016).
26. Nagueh, S. F. *et al.* Recommendations for the Evaluation of Left Ventricular Diastolic Function by Echocardiography: An Update from the American Society of Echocardiography and the European Association of Cardiovascular Imaging. *J. Am. Soc. Echocardiogr.* **29**, 277–314 (2016).
27. Yushkevich, P. A. *et al.* User-guided 3D active contour segmentation of anatomical structures: significantly improved efficiency and reliability. *Neuroimage* **31**, 1116–1128 (2006).
28. Ben-Assa, E. *et al.* Ventricular stroke work and vascular impedance refine the characterization of patients with aortic stenosis. *Sci. Transl. Med.* **11**, (2019).
29. Keshavarz-Motamed, Z., Garcia, J., Pibarot, P., Larose, E. & Kadem, L. Modeling the impact of concomitant aortic stenosis and coarctation of the aorta on left ventricular workload. *J. Biomech.* **44**, 2817–2825 (2011).
30. Keshavarz-Motamed, Z. *et al.* The role of aortic compliance in determination of coarctation severity: Lumped parameter modeling, in vitro study and clinical evaluation. *J. Biomech.* **48**, 4229–4237 (2015).
31. Keshavarz-Motamed, Z. *et al.* Effect of coarctation of the aorta and bicuspid aortic valve on flow dynamics and turbulence in the aorta using particle image velocimetry. *Exp. Fluids* **55**, 1696 (2014).
32. Keshavarz-Motamed, Z. *et al.* A new approach for the evaluation of the severity of coarctation of the aorta using Doppler velocity index and effective orifice area: In vitro validation and clinical implications. *J. Biomech.* **45**, 1239–1245 (2012).
33. Benevento, E., Djebbari, A., Keshavarz-Motamed, Z., Cecere, R. & Kadem, L. Hemodynamic Changes following Aortic Valve Bypass: A Mathematical Approach. *PLOS ONE* **10**, e0123000 (2015).
34. Keshavarz-Motamed, Z. *et al.* Non-Invasive Determination of Left Ventricular Workload in Patients with Aortic Stenosis Using Magnetic Resonance Imaging and Doppler Echocardiography. *PLOS ONE* **9**, e86793 (2014).
35. Mynard, J. P., Davidson, M. R., Penny, D. J. & Smolich, J. J. A simple, versatile valve model for use in lumped parameter and one-dimensional cardiovascular models. *Int. J. Numer. Methods Biomed. Eng.* **28**, 626–641 (2012).

36. Broomé, M., Maksuti, E., Bjällmark, A., Frenckner, B. & Janerot-Sjöberg, B. Closed-loop real-time simulation model of hemodynamics and oxygen transport in the cardiovascular system. *Biomed. Eng. OnLine* **12**, 69 (2013).
37. Weller, H. G., Tabor, G., Jasak, H. & Fureby, C. A tensorial approach to computational continuum mechanics using object-oriented techniques. *Comput. Phys.* **12**, 620–631 (1998).
38. Fung, Y. C. *Biomechanics: Circulation*. (Springer Science & Business Media, 2013).
39. Fung, Y. C. *Biomechanics: Circulation*. (Springer-Verlag, 1997).
40. Khodaei, S., Fatouraee, N. & Nabaei, M. Numerical simulation of mitral valve prolapse considering the effect of left ventricle. *Math. Biosci.* **285**, 75–80 (2017).
41. Jasak, H. & Tuković, Z. *Automatic Mesh Motion for the Unstructured Finite Volume Method*. (2004).
42. Demirdžić, I. & Perić, M. Space conservation law in finite volume calculations of fluid flow. *Int. J. Numer. Methods Fluids* **8**, 1037–1050 (1988).
43. Nikolić, S. *et al.* Passive properties of canine left ventricle: diastolic stiffness and restoring forces. *Circ. Res.* **62**, 1210–1222 (1988).
44. Sands, G. B. *et al.* Automated imaging of extended tissue volumes using confocal microscopy. *Microsc. Res. Tech.* **67**, 227–239 (2005).
45. Demiray, H. Stresses in Ventricular Wall. *J. Appl. Mech.* **43**, 194–197 (1976).
46. Humphrey, J. D., Strumpf, R. K. & Yin, F. C. P. Determination of a Constitutive Relation for Passive Myocardium: I. A New Functional Form. *J. Biomech. Eng.* **112**, 333–339 (1990).
47. Yin, F. C. P., Strumpf, R. K., Chew, P. H. & Zeger, S. L. Quantification of the mechanical properties of noncontracting canine myocardium under simultaneous biaxial loading. *J. Biomech.* **20**, 577–589 (1987).
48. Holzapfel, G. A. & Ogden, R. W. Constitutive modelling of passive myocardium: a structurally based framework for material characterization. *Philos. Trans. R. Soc. Math. Phys. Eng. Sci.* **367**, 3445–3475 (2009).
49. Lee J M & Boughner D R. Mechanical properties of human pericardium. Differences in viscoelastic response when compared with canine pericardium. *Circ. Res.* **57**, 475–481 (1985).
50. Kayvanpour, E. *et al.* Towards Personalized Cardiology: Multi-Scale Modeling of the Failing Heart. *PLOS ONE* **10**, e0134869 (2015).
51. Wang, V. Y. *et al.* Modelling passive diastolic mechanics with quantitative MRI of cardiac structure and function. *Med. Image Anal.* **13**, 773–784 (2009).
52. Palit, A., Bhudia, S. K., Arvanitis, T. N., Turley, G. A. & Williams, M. A. In vivo estimation of passive biomechanical properties of human myocardium. *Med. Biol. Eng. Comput.* **56**, 1615–1631 (2018).
53. Mojsejenko, D. *et al.* Estimating Passive Mechanical Properties in a Myocardial Infarction using MRI and Finite Element Simulations. *Biomech. Model. Mechanobiol.* **14**, 633–647 (2015).
54. Mekkaoui, C., Reese, T. G., Jackowski, M. P., Bhat, H. & Sosnovik, D. E. Diffusion MRI in the heart. *NMR Biomed.* **30**, e3426 (2017).
55. Hong, B. D., Moulton, M. J. & Secomb, T. W. Modeling left ventricular dynamics with characteristic deformation modes. *Biomech. Model. Mechanobiol.* **18**, 1683–1696 (2019).
56. Dabiri, Y. *et al.* Method for Calibration of Left Ventricle Material Properties Using Three-Dimensional Echocardiography Endocardial Strains. *J. Biomech. Eng.* **141**, (2019).

57. Dusturia, N., Choi, S. W., Song, K. S. & Lim, K. M. Effect of myocardial heterogeneity on ventricular electro-mechanical responses: a computational study. *Biomed. Eng. OnLine* **18**, 23 (2019).
58. Kim, Y. S. *et al.* Computational analysis of the effect of mitral and aortic regurgitation on the function of ventricular assist devices using 3D cardiac electromechanical model. *Med. Biol. Eng. Comput.* **56**, 889–898 (2018).
59. Khalafvand, S. S., Ng, E. Y.-K., Zhong, L. & Hung, T.-K. Three-dimensional diastolic blood flow in the left ventricle. *J. Biomech.* **50**, 71–76 (2017).
60. Gao, H. *et al.* A coupled mitral valve—left ventricle model with fluid–structure interaction. *Med. Eng. Phys.* **47**, 128–136 (2017).
61. Mangion, K., Gao, H., Husmeier, D., Luo, X. & Berry, C. Advances in computational modelling for personalised medicine after myocardial infarction. *Heart* **104**, 550–557 (2018).
62. Le, T. B., Elbaz, M. S. M., Van Der Geest, R. J. & Sotiropoulos, F. High Resolution Simulation of Diastolic Left Ventricular Hemodynamics Guided by Four-Dimensional Flow Magnetic Resonance Imaging Data. *Flow Turbul. Combust.* **102**, 3–26 (2019).
63. Miyauchi, S., Yamada, T., Hosoi, K., Hayase, T. & Funamoto, K. Numerical analysis of the blood flow in the left ventricle with internal structures: Effect of trabeculae carneae models and atrial fibrillation. *AIP Adv.* **9**, 105209 (2019).
64. Su, B. *et al.* Cardiac MRI based numerical modeling of left ventricular fluid dynamics with mitral valve incorporated. *J. Biomech.* **49**, 1199–1205 (2016).
65. Moosavi, M.-H. *et al.* Numerical simulation of blood flow in the left ventricle and aortic sinus using magnetic resonance imaging and computational fluid dynamics. *Comput. Methods Biomech. Biomed. Engin.* **17**, 740–749 (2014).
66. Govindarajan, V. *et al.* Synergy between Diastolic Mitral Valve Function and Left Ventricular Flow Aids in Valve Closure and Blood Transport during Systole. *Sci. Rep.* **8**, 1–14 (2018).
67. Kim, C.-H., Song, K.-S., Trayanova, N. A. & Lim, K. M. Computational prediction of the effects of the intra-aortic balloon pump on heart failure with valvular regurgitation using a 3D cardiac electromechanical model. *Med. Biol. Eng. Comput.* **56**, 853–863 (2018).
68. Garrett, A. S., Pham, T., Loiselle, D., Han, J.-C. & Taberner, A. Mechanical loading of isolated cardiac muscle with a real-time computed Windkessel model of the vasculature impedance. *Physiol. Rep.* **7**, e14184 (2019).
69. Bagnoli, P. *et al.* Computational Finite Element Model of Cardiac Torsion. *Int. J. Artif. Organs* **34**, 44–53 (2011).
70. Hassaballah, A. I., Hassan, M. A., Mardi, A. N. & Hamdi, M. An Inverse Finite Element Method for Determining the Tissue Compressibility of Human Left Ventricular Wall during the Cardiac Cycle. *PLOS ONE* **8**, e82703 (2013).
71. Hassan, M. A., Hamdi, M. & Noma, A. The nonlinear elastic and viscoelastic passive properties of left ventricular papillary muscle of a Guinea pig heart. *J. Mech. Behav. Biomed. Mater.* **5**, 99–109 (2012).
72. Quaini, A. *et al.* Validation of a 3D computational fluid–structure interaction model simulating flow through an elastic aperture. *J. Biomech.* **45**, 310–318 (2012).
73. Topnes, E. Computational modelling of cardiac mechanics - Efficient simulation of a heartbeat. (2016).

74. Lassila, T. *et al.* Simulation of left ventricle fluid dynamics with mitral regurgitation from magnetic resonance images with fictitious elastic structure regularization. *ArXiv170703998 Phys.* (2017).
75. Maneeratana, K. Development of the finite volume method for non-linear structural applications. (Imperial College London (University of London), 2000).
76. Tuković, Ž., Karač, A., Cardiff, P., Jasak, H. & Ivanković, A. OpenFOAM Finite Volume Solver for Fluid-Solid Interaction. *Trans. FAMENA* **42**, 1–31 (2018).
77. Rugonyi, S. & Bathe, K. J. On finite element analysis of fluid flows fully coupled with structural interactions. *CMES - Comput. Model. Eng. Sci.* **2**, 195–212 (2001).
78. Ribes, A. & Caremoli, C. Salome Platform Component Model for Numerical Simulation. in *Proceedings of the 31st Annual International Computer Software and Applications Conference - Volume 02* 553–564 (IEEE Computer Society, 2007). doi:10.1109/COMPSAC.2007.185.
79. Tuković, Ž. & Jasak, H. A moving mesh finite volume interface tracking method for surface tension dominated interfacial fluid flow. *Comput. Fluids* **55**, 70–84 (2012).
80. Tuković, Ž., Bukač, M., Cardiff, P., Jasak, H. & Ivanković, A. Added Mass Partitioned Fluid–Structure Interaction Solver Based on a Robin Boundary Condition for Pressure. in *OpenFOAM®* (eds. Nóbrega, J. M. & Jasak, H.) 1–22 (Springer International Publishing, 2019). doi:10.1007/978-3-319-60846-4_1.
81. Banks, J. W., Henshaw, W. D. & Schwendeman, D. W. An analysis of a new stable partitioned algorithm for FSI problems. Part I: Incompressible flow and elastic solids. *J. Comput. Phys.* **269**, 108–137 (2014).
82. Cardiff, P. & Demirdžić, I. Thirty years of the finite volume method for solid mechanics. *ArXiv Prepr. ArXiv181002105* (2018).
83. Issa, R. I. Solution of the implicitly discretised fluid flow equations by operator-splitting. *J. Comput. Phys.* **62**, 40–65 (1986).
84. Demmel, J. W. Matrix Computations (Gene H. Golub And Charles F. van Loan). *SIAM Rev.* **28**, 252–255 (1986).
85. Oliveira, I. L. *et al.* RUPTURE RISK PREDICTION OF INTRACRANIAL ANEURYSMS USING OPEN SOURCE CFD SOFTWARE. in (Begel House Inc., 2017). doi:10.1615/ICHMT.2017.CHT-7.400.
86. Degroote, J., Bathe, K.-J. & Vierendeels, J. Performance of a new partitioned procedure versus a monolithic procedure in fluid–structure interaction. *Comput. Struct.* **87**, 793–801 (2009).
87. Degroote, J., Bruggeman, P., Haelterman, R. & Vierendeels, J. Stability of a coupling technique for partitioned solvers in FSI applications. *Comput. Struct.* **86**, 2224–2234 (2008).
88. Baumgartner, H. *et al.* Recommendations on the echocardiographic assessment of aortic valve stenosis: a focused update from the European Association of Cardiovascular Imaging and the American Society of Echocardiography. *Eur. Heart J. Cardiovasc. Imaging* **18**, 254–275 (2017).
89. Lang, R. M. *et al.* Recommendations for cardiac chamber quantification by echocardiography in adults: an update from the American Society of Echocardiography and the European Association of Cardiovascular Imaging. *J. Am. Soc. Echocardiogr. Off. Publ. Am. Soc. Echocardiogr.* **28**, 1-39.e14 (2015).

90. Ha, J.-W. & Oh, J. K. Therapeutic Strategies for Diastolic Dysfunction: A Clinical Perspective. *J. Cardiovasc. Ultrasound* **17**, 86–95 (2009).
91. Spirito, P. *et al.* Magnitude of left ventricular hypertrophy and risk of sudden death in hypertrophic cardiomyopathy. *N. Engl. J. Med.* **342**, 1778–1785 (2000).
92. Orsinell, D. A., Aurigemma, G. P., Battista, S., Krendel, S. & Gaasch, W. H. Left ventricular hypertrophy and mortality after aortic valve replacement for aortic stenosis: A high risk subgroup identified by preoperative ralation wall thickness. *J. Am. Coll. Cardiol.* **22**, 1679–1683 (1993).
93. Gonzales, H. *et al.* Left Ventricular Hypertrophy and Clinical Outcomes Over 5 Years After TAVR: An Analysis of the PARTNER Trials and Registries. *JACC Cardiovasc. Interv.* **13**, 1329–1339 (2020).
94. Bahlmann, E. *et al.* Low systemic arterial compliance is associated with increased cardiovascular morbidity and mortality in aortic valve stenosis. *Heart* **105**, 1507–1514 (2019).
95. Braunwald Eugene, Brockenbrough Edwin C., Frahm Charles J., & Ross John. Left Atrial and Left Ventricular Pressures in Subjects without Cardiovascular Disease. *Circulation* **24**, 267–269 (1961).
96. Gharib, M., Rambod, E., Kheradvar, A., Sahn, D. J. & Dabiri, J. O. Optimal vortex formation as an index of cardiac health. *Proc. Natl. Acad. Sci.* **103**, 6305–6308 (2006).
97. Nucifora, G. *et al.* Left ventricular muscle and fluid mechanics in acute myocardial infarction. *Am. J. Cardiol.* **106**, 1404–1409 (2010).
98. Son, J.-W. *et al.* Abnormal Left Ventricular Vortex Flow Patterns in Association With Left Ventricular Apical Thrombus Formation in Patients With Anterior Myocardial Infarction. *Circ. J.* **76**, 2640–2646 (2012).
99. Gijsen, F. *et al.* Expert recommendations on the assessment of wall shear stress in human coronary arteries: existing methodologies, technical considerations, and clinical applications. *Eur. Heart J.* **40**, 3421–3433 (2019).
100. Ji, L. *et al.* Left ventricular energy loss and wall shear stress assessed by vector flow mapping in patients with hypertrophic cardiomyopathy. *Int. J. Cardiovasc. Imaging* **34**, 1383–1391 (2018).
101. Di Carli Marcelo F., Geva Tal, & Davidoff Ravin. The Future of Cardiovascular Imaging. *Circulation* **133**, 2640–2661 (2016).
102. Marsden, A. L. Simulation based planning of surgical interventions in pediatric cardiology. *Phys. Fluids* **25**, 101303 (2013).
103. Lancellotti, P. *et al.* Stress echocardiography in patients with native valvular heart disease. *Heart* **104**, 807–813 (2018).
104. Kanwar, A., Thaden, J. J. & Nkomo, V. T. Management of Patients With Aortic Valve Stenosis. *Mayo Clin. Proc.* **93**, 488–508 (2018).
105. Badiani, S., Waddingham, P., Lloyd, G. & Bhattacharyya, S. Stress echocardiography in valvular heart disease. *Expert Rev. Cardiovasc. Ther.* **16**, 795–804 (2018).
106. Côté Nancy *et al.* Impact of Vascular Hemodynamics on Aortic Stenosis Evaluation: New Insights Into the Pathophysiology of Normal Flow—Small Aortic Valve Area—Low Gradient Pattern. *J. Am. Heart Assoc.* **6**, e006276.
107. Abbas, A. E. & Pibarot, P. Hemodynamic characterization of aortic stenosis states. *Catheter. Cardiovasc. Interv.* **93**, 1002–1023 (2019).

108. Zakikhani, P., Ho, R., Wang, W. & Li, Z. Biomechanical assessment of aortic valve stenosis: Advantages and limitations. *Med. Nov. Technol. Devices* **2**, 100009 (2019).
109. Dweck, M. R., Boon, N. A. & Newby, D. E. Calcific Aortic Stenosis: A Disease of the Valve and the Myocardium. *J. Am. Coll. Cardiol.* **60**, 1854–1863 (2012).
110. Otto, C. M. Valvular Aortic Stenosis: Disease Severity and Timing of Intervention. *J. Am. Coll. Cardiol.* **47**, 2141–2151 (2006).
111. Pibarot, P. & Dumesnil, J. G. Improving Assessment of Aortic Stenosis. *J. Am. Coll. Cardiol.* **60**, 169–180 (2012).
112. Pibarot, P. & Dumesnil, J. G. Assessment of aortic stenosis severity: check the valve but don't forget the arteries! *Heart* **93**, 780–782 (2007).
113. Taylor, C. A. & Steinman, D. A. Image-Based Modeling of Blood Flow and Vessel Wall Dynamics: Applications, Methods and Future Directions. *Ann. Biomed. Eng.* **38**, 1188–1203 (2010).
114. Maeder, M. T. *et al.* Invasive Hemodynamic Staging Classification of Cardiac Damage in Patients With Aortic Stenosis Undergoing Valve Replacement. *Can. J. Cardiol.* (2020) doi:10.1016/j.cjca.2020.02.004.
115. Généreux, P. *et al.* Staging classification of aortic stenosis based on the extent of cardiac damage. *Eur. Heart J.* **38**, 3351–3358 (2017).
116. Katsi, V. *et al.* Aortic Stenosis, Aortic Regurgitation and Arterial Hypertension. *Curr. Vasc. Pharmacol.* **17**, 180–190 (2019).
117. Casas, B. *et al.* Bridging the gap between measurements and modelling: a cardiovascular functional avatar. *Sci. Rep.* **7**, 1–15 (2017).
118. Mohammadi, H., Cartier, R. & Mongrain, R. The impact of the aortic valve impairment on the distant coronary arteries hemodynamics: a fluid–structure interaction study. *Med. Biol. Eng. Comput.* **55**, 1859–1872 (2017).
119. Vendrik Jeroen *et al.* Long-Term Effects of Transcatheter Aortic Valve Implantation on Coronary Hemodynamics in Patients With Concomitant Coronary Artery Disease and Severe Aortic Stenosis. *J. Am. Heart Assoc.* **9**, e015133 (2020).
120. Ahmad, Y. *et al.* Coronary Hemodynamics in Patients With Severe Aortic Stenosis and Coronary Artery Disease Undergoing Transcatheter Aortic Valve Replacement: Implications for Clinical Indices of Coronary Stenosis Severity. *JACC Cardiovasc. Interv.* **11**, 2019–2031 (2018).
121. Mohananey, D. *et al.* Association of peripheral artery disease with in-hospital outcomes after endovascular transcatheter aortic valve replacement. *Catheter. Cardiovasc. Interv.* **94**, 249–255 (2019).
122. Treibel, T. A. *et al.* Reverse Myocardial Remodeling Following Valve Replacement in Patients With Aortic Stenosis. *J. Am. Coll. Cardiol.* **71**, 860–871 (2018).
123. Dahl, J. S., Magne, J., Pellikka, P. A., Donal, E. & Marwick, T. H. Assessment of Subclinical Left Ventricular Dysfunction in Aortic Stenosis. *JACC Cardiovasc. Imaging* **12**, 163–171 (2019).
124. Fukui, M. *et al.* Association of Structural and Functional Cardiac Changes With Transcatheter Aortic Valve Replacement Outcomes in Patients With Aortic Stenosis. *JAMA Cardiol.* **4**, 215–222 (2019).
125. Tastet, L., Vincent, F. & Pibarot, P. Cardiac Damage Staging in Aortic Stenosis: A Perspective From the Cardiac Catheterization Laboratory. *Can. J. Cardiol.* (2020) doi:10.1016/j.cjca.2020.03.033.

126. Shuhaiber, J. Transcatheter aortic valve replacement and thrombus formation. *Eur. J. Cardiothorac. Surg.* **56**, 495–496 (2019).
127. Shadden, S. C., Katija, K., Rosenfeld, M., Marsden, J. E. & Dabiri, J. O. Transport and stirring induced by vortex formation. *J. Fluid Mech.* **593**, 315–331 (2007).
128. Hellmeier, F. *et al.* Hemodynamic Evaluation of a Biological and Mechanical Aortic Valve Prosthesis Using Patient-Specific MRI-Based CFD. *Artif. Organs* **42**, 49–57 (2018).
129. D'Ascenzo, F. *et al.* Incidence, predictors and cerebrovascular consequences of leaflet thrombosis after transcatheter aortic valve implantation: a systematic review and meta-analysis. *Eur. J. Cardio-Thorac. Surg. Off. J. Eur. Assoc. Cardio-Thorac. Surg.* **56**, 488–494 (2019).
130. Sun, L., Rajamannan, N. M. & Sucosky, P. Design and Validation of a Novel Bioreactor to Subject Aortic Valve Leaflets to Side-Specific Shear Stress. *Ann. Biomed. Eng.* **39**, 2174–2185 (2011).
131. Okuno, T. *et al.* Impact of Left Ventricular Outflow Tract Calcification on Procedural Outcomes After Transcatheter Aortic Valve Replacement. *JACC Cardiovasc. Interv.* **13**, 1789–1799 (2020).
132. Seo, J. H. & Mittal, R. Effect of diastolic flow patterns on the function of the left ventricle. *Phys. Fluids* **25**, 110801 (2013).
133. Khalafvand, S. S., Ng, E. Y. K., Zhong, L. & Hung, T. K. Fluid-dynamics modelling of the human left ventricle with dynamic mesh for normal and myocardial infarction: Preliminary study. *Comput. Biol. Med.* **42**, 863–870 (2012).
134. Domenichini, F., Pedrizzetti, G. & Baccani, B. Three-dimensional filling flow into a model left ventricle. *J. Fluid Mech.* **539**, 179–198 (2005).
135. Jahanzamin, J., Fatouraee, N. & Nasiraei-Moghaddam, A. Effect of turbulent models on left ventricle diastolic flow patterns simulation. *Comput. Methods Biomech. Biomed. Engin.* **0**, 1–10 (2019).
136. Mao, W., Caballero, A., McKay, R., Primiano, C. & Sun, W. Fully-coupled fluid-structure interaction simulation of the aortic and mitral valves in a realistic 3D left ventricle model. *PLoS ONE* **12**, (2017).
137. Cheng, Y., Oertel, H. & Schenkel, T. Fluid-structure coupled CFD simulation of the left ventricular flow during filling phase. *Ann. Biomed. Eng.* **33**, 567–576 (2005).
138. Arefin, Md. S. & Morsi, Y. S. Fluid structure interaction (FSI) simulation of the left ventricle (LV) during the early filling wave (E-wave), diastasis and atrial contraction wave (A-wave). *Australas. Phys. Eng. Sci. Med.* **37**, 413–423 (2014).
139. Krittian, S., Janoske, U., Oertel, H. & Böhlke, T. Partitioned Fluid–Solid Coupling for Cardiovascular Blood Flow. *Ann. Biomed. Eng.* **38**, 1426–1441 (2010).
140. Tang, D., Yang, C., Geva, T. & del Nido, P. J. Image-based patient-specific ventricle models with fluid–structure interaction for cardiac function assessment and surgical design optimization. *Prog. Pediatr. Cardiol.* **30**, 51–62 (2010).
141. Le, T. B. & Sotiropoulos, F. Fluid–structure interaction of an aortic heart valve prosthesis driven by an animated anatomic left ventricle. *J. Comput. Phys.* **244**, 41–62 (2013).
142. Nordsletten, D. *et al.* Fluid–solid coupling for the investigation of diastolic and systolic human left ventricular function. *Int. J. Numer. Methods Biomed. Eng.* **27**, 1017–1039 (2011).
143. Chen, W. W., Gao, H., Luo, X. Y. & Hill, N. A. Study of cardiovascular function using a coupled left ventricle and systemic circulation model. *J. Biomech.* **49**, 2445–2454 (2016).

144. Chen, W. W., Gao, H., Luo, X. Y. & Hill, N. A. Study of cardiovascular function using a coupled left ventricle and systemic circulation model. *J. Biomech.* **49**, 2445–2454 (2016).
145. Quarteroni, A., Lassila, T., Rossi, S. & Ruiz-Baier, R. Integrated Heart—Coupling multiscale and multiphysics models for the simulation of the cardiac function. *Comput. Methods Appl. Mech. Eng.* **314**, 345–407 (2017).
146. Viola, F., Meschini, V. & Verzicco, R. Fluid–Structure-Electrophysiology interaction (FSEI) in the left-heart: A multi-way coupled computational model. *Eur. J. Mech. - BFluids* **79**, 212–232 (2020).
147. A, T. L. *et al. ventricle fluid dynamics with fictitious elastic*.
148. Watanabe, H., Sugiura, S., Kafuku, H. & Hisada, T. Multiphysics simulation of left ventricular filling dynamics using fluid-structure interaction finite element method. *Biophys. J.* **87**, 2074–2085 (2004).
149. Watanabe, H., Hisada, T., Sugiura, S., Okada, J. & Fukunari, H. Computer Simulation of Blood Flow, Left Ventricular Wall Motion and Their Interrelationship by Fluid-Structure Interaction Finite Element Method. *JSME Int. J. Ser. C Mech. Syst. Mach. Elem. Manuf.* **45**, 1003–1012 (2002).
150. Baillargeon, B., Rebelo, N., Fox, D. D., Taylor, R. L. & Kuhl, E. The Living Heart Project: A robust and integrative simulator for human heart function. *Eur. J. Mech. - ASolids* **48**, 38–47 (2014).
151. Caballero Andrés, Mao Wenbin, McKay Raymond, & Sun Wei. The impact of balloon-expandable transcatheter aortic valve replacement on concomitant mitral regurgitation: a comprehensive computational analysis. *J. R. Soc. Interface* **16**, 20190355 (2019).
152. Santiago, A. *et al.* Fully coupled fluid-electro-mechanical model of the human heart for supercomputers. *Int. J. Numer. Methods Biomed. Eng.* **34**, e3140 (2018).
153. Biffi, B. *et al.* A workflow for patient-specific fluid–structure interaction analysis of the mitral valve: A proof of concept on a mitral regurgitation case. *Med. Eng. Phys.* **74**, 153–161 (2019).
154. Gao, H., Carrick, D., Berry, C., Griffith, B. E. & Luo, X. Dynamic finite-strain modelling of the human left ventricle in health and disease using an immersed boundary-finite element method. *IMA J. Appl. Math.* **79**, 978–1010 (2014).
155. Nordsletten, D. A., Niederer, S. A., Nash, M. P., Hunter, P. J. & Smith, N. P. Coupling multi-physics models to cardiac mechanics. *Prog. Biophys. Mol. Biol.* **104**, 77–88 (2011).

# Chapter 4: Long-term prognostic impact of paravalvular leakage on coronary artery disease requires patient-specific quantification of hemodynamics

Seyedvahid Khodaei[1], Louis Garber[2], Julia Bauer[1], Ali Emadi [1,3], Zahra Keshavarz-Motamed*[1,2,4]

1. Department of Mechanical Engineering, McMaster University, Hamilton, ON, Canada
2. School of Biomedical Engineering, McMaster University, Hamilton, ON, Canada
3. Department of Electrical and Computer Engineering, McMaster University, Hamilton, ON, Canada
4. School of Computational Science and Engineering, McMaster University, Hamilton, ON, Canada

*This paper was submitted and is under review.*

* Correspondence author

## 4.1 Abstract

Transcatheter aortic valve replacement (TAVR) is a frequently used minimally invasive intervention for patient with aortic stenosis across a broad risk spectrum. While coronary artery disease (CAD) is present in approximately half of TAVR candidates, correlation of post-TAVR complications such as paravalvular leakage (PVL) or misalignment with CAD are not fully understood. For this purpose, we developed a multiscale computational framework based on a patient-specific lumped-parameter algorithm and a 3-D strongly-coupled fluid-solid interaction to quantify metrics of global circulatory function, metrics of global cardiac function and local cardiac fluid dynamics. Based on our findings, PVL limits the benefits of TAVR and restricts coronary perfusion due to the lack of sufficient coronary blood flow during diastole phase (e.g., maximum coronary flow rate reduced by 34% and 37% in the left anterior descending (LAD) and right coronary artery (RCA) respectively in patient #1). Moreover, PVL may increase the LV load (e.g., LV load increased by 35% for patient#1) and decrease the coronary wall shear stress (e.g., maximum wall shear stress reduced by 12.5% and 17% in the left anterior descending (LAD) and right coronary artery (RCA) respectively in patient #2), which could promote atherosclerosis development through loss of the physiological flow-oriented alignment of endothelial cells. This study demonstrated that a rigorously developed personalized image-based computational framework can provide vital insights into underlying mechanics of TAVR and CAD interactions and assist in treatment planning and patient risk stratification in patients.

## 4.2 Introduction

Transcatheter aortic valve replacement (TAVR) has become a standard minimally invasive alternative to the traditional surgical aortic valve replacement (SAVR) for patients with aortic valve stenosis (AS) who are at high risk of a complicated surgery. TAVR was recently approved

for low-risk patients [1], indicating that it may become the superior treatment modality for the whole risk spectrum [2].

However, there are drawbacks to TAVR arising from an improperly placed transcatheter heart valve: (1) *paravalvular leakage* (PVL), a back flow from the aorta to the left ventricle during diastole, is a major complication and an independent predictor of mortality following TAVR. PVL results in increased heart workload and leads to congestive heart failure [3]. It is estimated that 7.8% to 40.8% of PVL post-TAVR is mild, 5% to 37.9% is moderate, and 0.5% to 13.6% is severe [4]; (2) *coronary obstruction*: As the coronary ostia are located superior to the aortic valve, the presence of PVL jets may impede blood flow into the coronary arteries. The PVL most frequently occurs between the left and right coronary cusps (i.e., at the location of native valve commissures: 1 to 2 o'clock of the short axis view) [5]. Accessing one or both coronary arteries is challenging and would require the use of more aggressive methods, such as multiple catheter exchanges, in up to 46% of the patients after first TAVR [4]. The risk of coronary obstruction occurring with TAVR is potentially as high as 23% [6]. A patient suffering with coronary artery obstruction will typically present with severe hypertension and ventricular arrhythmias [7].

Development, progression, diagnosis, and treatment of cardiovascular disease is closely governed by fluid mechanics [8,9]. Indeed, the correlations between biological fluid mechanics and observed pathological events can be explained on the basis of adverse hemodynamics [9,10]. Detailed analysis of fluid mechanics within the cardiovascular system has led many researchers to conclude that valvular disease depends on the complex hemodynamics of both the ventricle and the vascular system [11–15].

Interactive coupling of ventricle, valve and vascular systems should be taken into consideration for accurate quantitative evaluation of hemodynamics in patients who receive TAVR to quantify

**global** flow environment (metrics of cardiac function and circulatory function, e.g., heart workload and its contribution breakdown of each component of the cardiovascular diseases) and the **local** microenvironment of flowing blood (coronary and valve fluid dynamics, e.g., details of the instantaneous 3-D flow) [11–15]. Despite the importance and advances in medical imaging, the current clinical diagnostic tools cannot sufficiently quantify flow conditions in patients with many cardiovascular diseases, including in-patient with valvular diseases who undergo TAVR [16–19]. More specifically, several imaging modalities exist for the coronary arteries, such as computed tomography coronary angiography (CTCA), cardiac magnetic resonance (CMR), echocardiography, ultrafast ultrasound, intravascular ultrasound (IVUS), and optical coherence tomography (OCT). However, all modalities, with the exception of CMR, are unable to quantify local and global hemodynamics [20,21]. CMR can only quantify local hemodynamics but has been limited to patients without a pacemaker, with the exception of MRI-compatible pacemakers [20]. In addition, coronary imaging with MRI is not routinely performed in clinical practice due to its limited spatial resolution [22].

In this study, the effect of TAVR complications such as PVL and misalignments on the coronary arteries and aortic root were assessed by means of a multiscale computational-mechanics framework in both pre and post TAVR states to quantify global and local hemodynamics. To this date, only lumped parameter models can quantify the global hemodynamics, thanks to their capability to overcome the prohibitive computational cost of 3-D models in the entire circulatory system [23]. Our computational framework used and image-based patient-specific lumped-parameter algorithm and a 3-D fluid structure interactions (FSI) model to quantify the global and local hemodynamics in 6 patients with sever AS who received TAVR in both pre and post intervention

states. The proposed framework could provide a platform for testing the intervention scenarios and evaluating their effects on the hemodynamics.

## 4.3 Materials and Methods

The innovative image-based computational fluid dynamics framework (Figures 1 to 5) was developed to quantify: (1) metrics of circulatory function (global hemodynamics); (2) metrics of cardiac function (global hemodynamics) as well as (3) cardiac fluid dynamics (local hemodynamics) in patients who underwent TAVR (Table 1: Baseline patient characteristics). This framework is based on our Doppler-based, patient-specific, lumped parameter modeling (Figure 1) as well as a 3-D strongly coupled FSI designed using FOAM-Extend [24] with additional supplements as explained below (Figures 2 to 5). Our Doppler-based, patient-specific lumped parameter model was further developed in this work to model any combination of mixed and complex valvular, vascular, mini-vascular, and ventricular diseases (Figure 1, Table 2). We used clinical cardiac catheterization data [19] and clinical Doppler echocardiographic (DE) measurements in 6 patients in post TAVR status to validate our proposed framework and to demonstrate its diagnostic abilities by providing novel analyses and interpretations of clinical data.

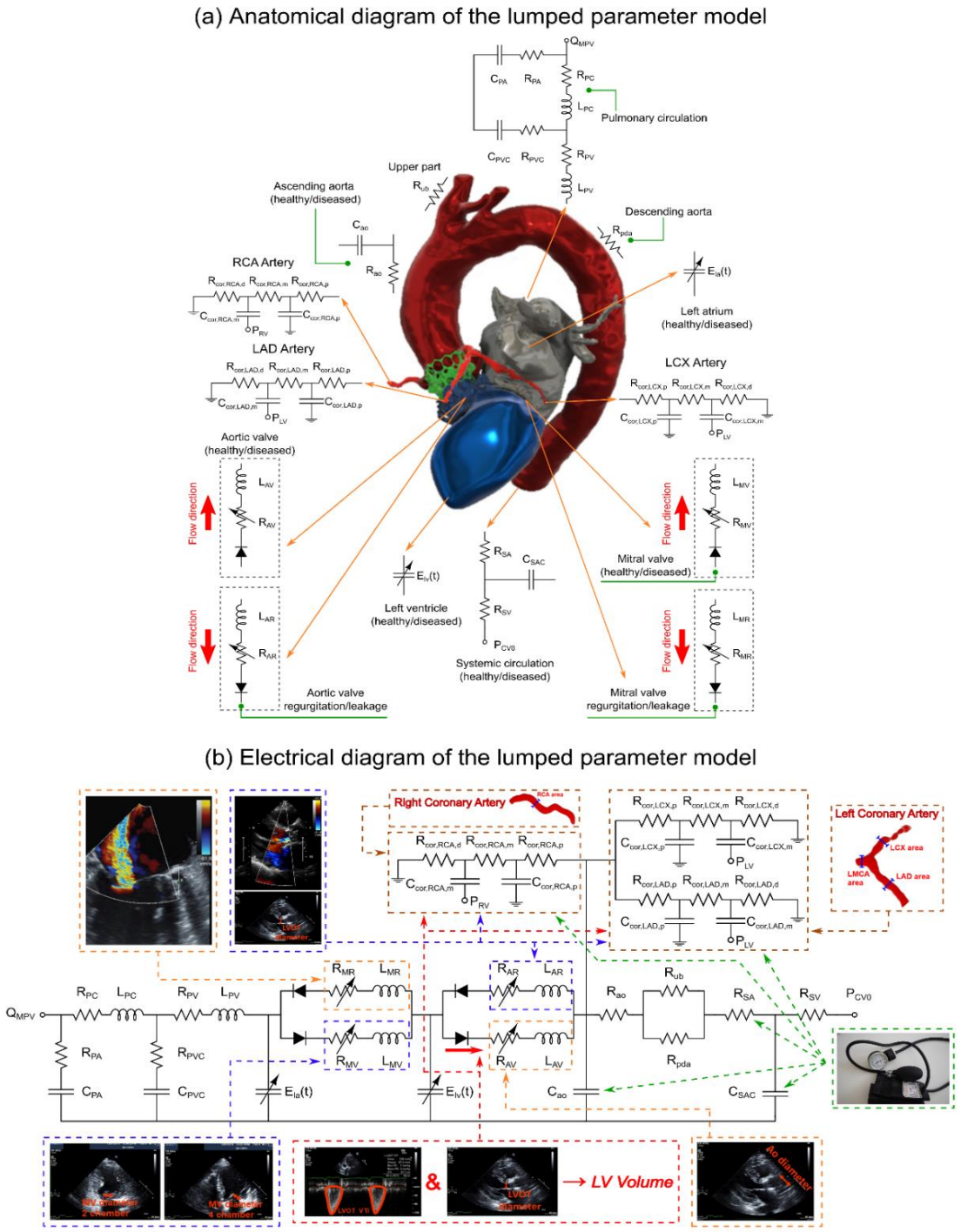


Figure 4-1. **Anatomical and electrical schematic diagrams of the lumped parameter modeling.** (a) Anatomical description; (b) Electrical representation. This model includes the following sub-models: left ventricle, left atrium, aortic valve, aortic valve regurgitation, mitral valve, mitral valve regurgitation, systemic circulation, pulmonary circulation, left main coronary artery, left anterior descending coronary artery, left circumflex coronary artery and right coronary artery. Abbreviations are the same as in Table 2.

Table 4-1. Baseline patient characteristics

| | **C3VD Patients (n=6, mean ± SD)** |
|---|---|
| **Patient description** | |
| Mean age (years) | 86 ± 3.55 |
| Gender | (Male: 5; Female: 1) |
| Mean weight (kg) | 75 ± 12.9 |
| Mean height (cm) | 169 ± 14.5 |
| NYHA classifications | |
| • Patient No. 1 | Pre-TAVR: Grade 4; Post-TAVR: Grade 4 |
| • Patient No. 2 | Pre-TAVR: Grade 3; Post-TAVR: Grade 3 |
| • Patient No. 3 | Pre-TAVR: Grade 3; Post-TAVR: Grade 3 |
| • Patient No. 4 | Pre-TAVR: Grade 4; Post-TAVR: Grade 4 |
| • Patient No. 5 | Pre-TAVR: Grade 4; Post-TAVR: Grade 4 |
| • Patient No. 6 | Pre-TAVR: Grade 2; Post-TAVR: Grade 2 |
| **Arterial hemodynamics** | |
| Systolic arterial pressure (mmHg) | Pre-TAVR: 124.5 ± 8.5; Post-TAVR: 137.3 ± 9.5 |
| Diastolic arterial pressure (mmHg) | Pre-TAVR: 64.5 ± 2; Post-TAVR: 65.75 ± 8 |
| Coronary artery disease (CAD) | n=6 |
| Hypertension (HTN) | n=6 |
| Dyslipidemia | n=6 |
| **Aortic valve hemodynamics** | |
| Stenotic aortic valve effective orifice area ($cm^2$) | 0.7 ± 0.14 |
| Stenotic aortic valve type | Tricuspid: 6; Bicuspid: 0 |
| Prosthetic size (mm) | 23 ± 1.7 |
| Prosthetic type | |
| • Edwards SAPIEN | n= 6 |
| Maximum aortic valve pressure gradient (mmHg) | Pre-TAVR: 43 ± 3.5; Post-TAVR: 21 ± 2.5 |
| Mean aortic valve pressure gradient (mmHg) | Pre-TAVR: 25 ± 4; Post-TAVR: 16.5 ± 5.5 |
| **Left ventricle hemodynamics** | |
| Ejection fraction (%) | |
| • Patient No. 1 | Pre-TAVR: 29; Post-TAVR: 34 |
| • Patient No. 2 | Pre-TAVR: 49; Post-TAVR: 57 |
| • Patient No. 3 | Pre-TAVR: 37; Post-TAVR: 58 |
| • Patient No. 4 | Pre-TAVR: 57; Post-TAVR: 59 |
| • Patient No. 5 | Pre-TAVR: 18; Post-TAVR: 22 |
| • Patient No. 6 | Pre-TAVR: 63; Post-TAVR: 73 |
| Heart rate (bpm) | Pre-TAVR: 53 ±9; Post-TAVR: 69 ± 13 |

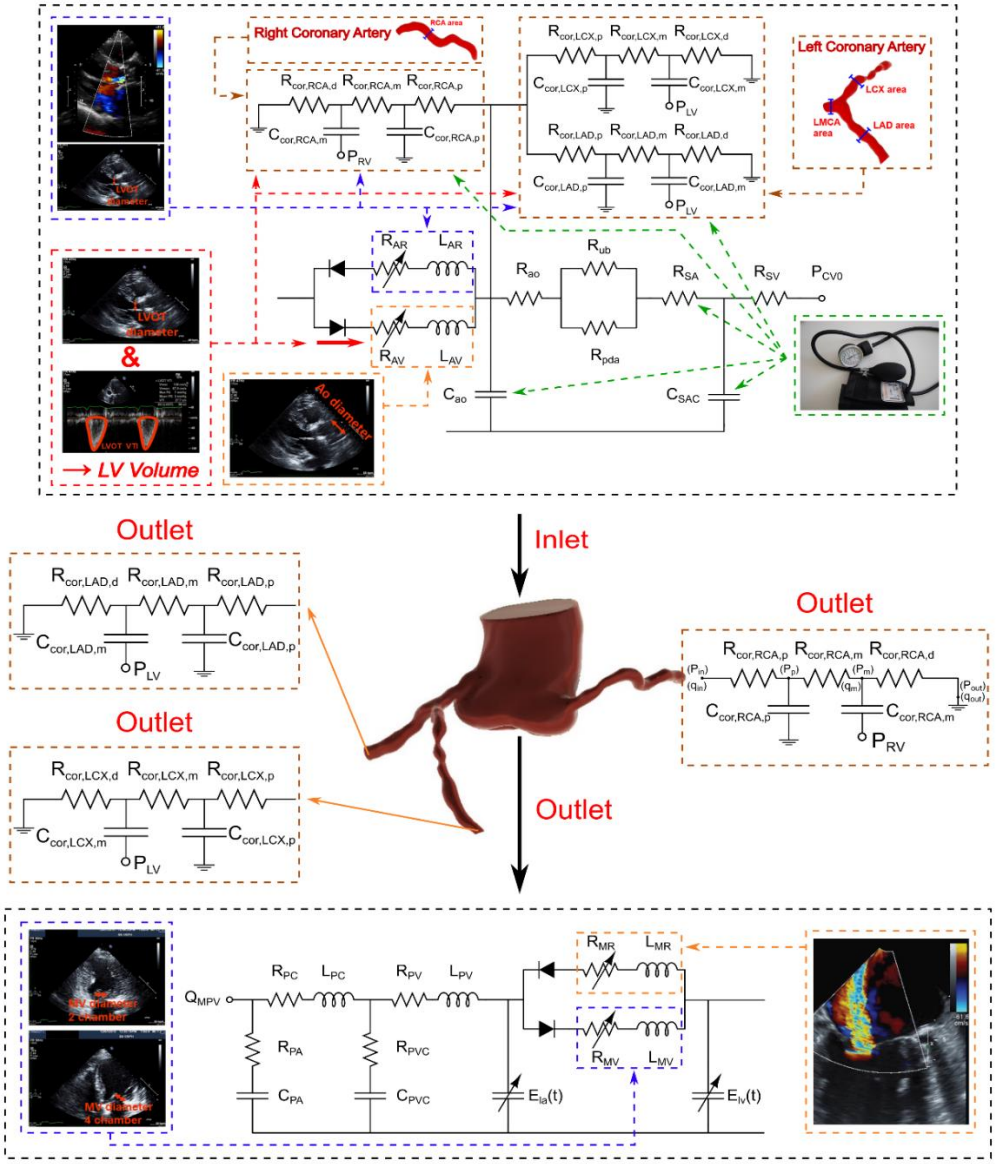


Figure 4-2. Schematic diagram of computational domain. Anatomical and electrical schematic diagrams of the lumped parameter modeling coupled to the fluid domain. This model includes the following sub-models. (1) ascending aorta, (2) left ventricle, (3) left anterior descending coronary artery, (4) left circumflex coronary artery, and (5) right coronary artery. Abbreviations are the same as in Table 2. Input parameters were measured using Doppler echocardiography and sphygmomanometer. Simulation domain and FSI modeling. Imposing correct boundary conditions to the flow model is critical because the local flow dynamics are influenced by downstream and upstream conditions. Patient-specific LPM simulating the function of the left side of the heart and coronary arteries was coupled to the inlet and outlets. This data was obtained from the patient-specific image-based lumped parameter model. Input parameters to the lumped parameter algorithm were reliable measured using OsiriX imaging software (OsiriX version 8.0.2; Pixmeo, Switzerland). We used ITK-SNAP (version 3.8.0-BETA) to segment and reconstruct the 3-D geometries of the complete aortic root and coronary arteries using CT images.

### 4.3.1 Clinical medical imaging

*Study population & Data acquisition*

The study population included six patients with severe aortic valve stenosis who received TAVR (Table 1; patients characteristics) in 2017 at St. Paul's Hospital (Vancouver, Canada; N=6). The protocols were reviewed and approved by the Clinical Research Ethics Board (CREB) and informed consents were collected from all participants. The data was anonymized and transferred from St. Paul's Hospital[11] and the approval was granted by the CREB. Measurements were performed according to all relevant guidelines and regulations including American Heart Association, American College of Cardiology and American Society of Echocardiography (ASE). Data were collected at two time points: pre-procedure and 90-days post-procedure. Results were expressed as mean ± standard deviations (SD) (Table 1: Baseline patient characteristics).

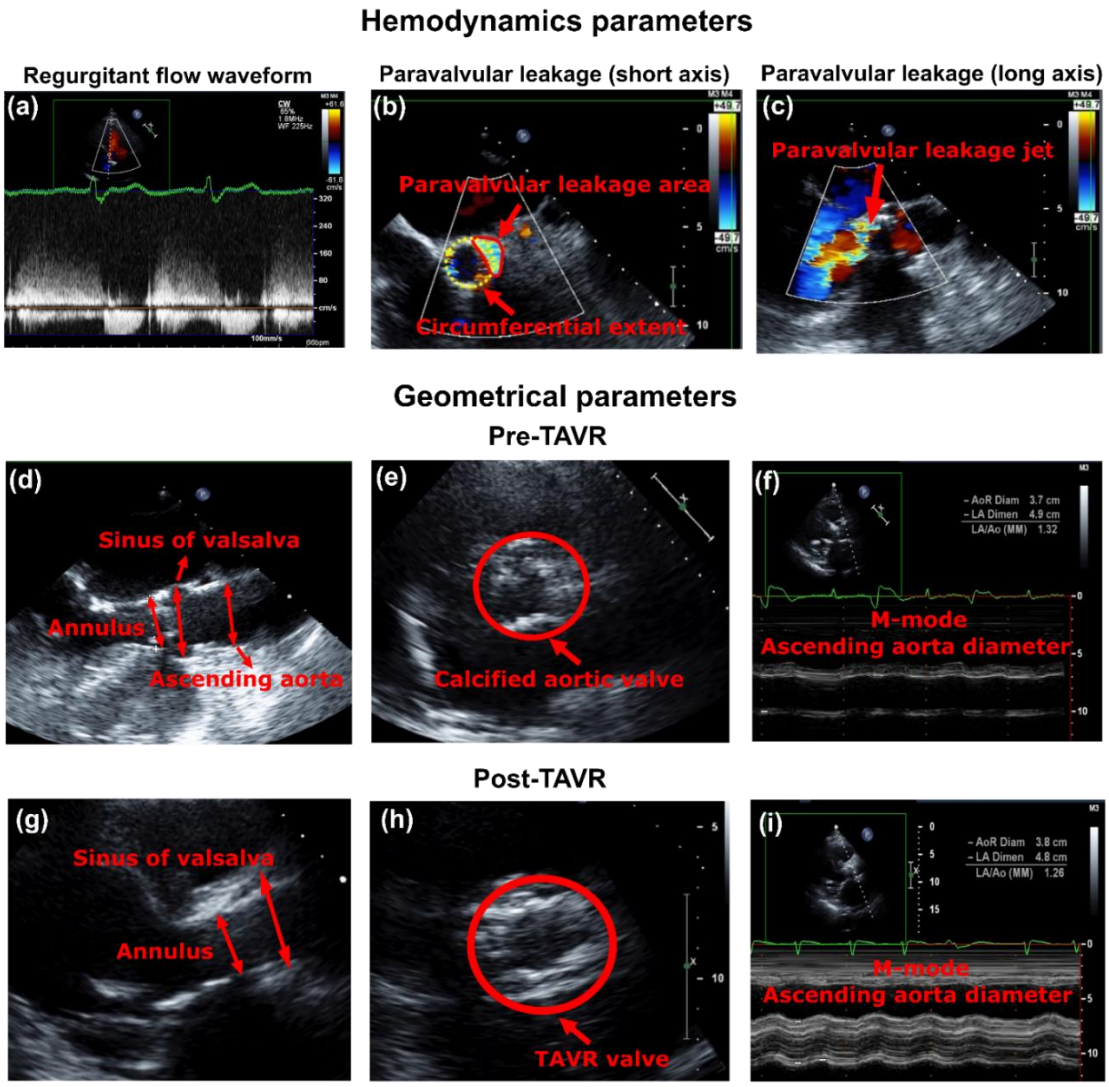


Figure 4-3. Hemodynamics parameter: (a) Regurgitant flow velocity waveform at the paravalvular leakage cite (5 chamber view); (b) Short axis color doppler view of the prosthetic valve and the paravalvular leakage area (Vena contracta area: 1.04 cm2) and its circumferential extent with respect to prosthetic valve diameter (35%); (c) Long axis color doppler view of paravalvular leakage jet interaction with diastolic flow behind the posterior mitral valve leaflet. Geometrical parameters: (d) Parasternal long-axis view associated with diff erent parts of the aortic root and ascending aorta before TAVR; (e) Parasternal short-axis view of aortic valve before TAVR; (f) M-Mode measurement of ascending aorta before TAVR; (g) Parasternal long-axis view associated with different parts of the aortic root, prosthetic frame, and ascending aorta after TAVR; (h) Parasternal short-axis view of TAVR; (i) M-Mode measurement of ascending aorta after TAVR.

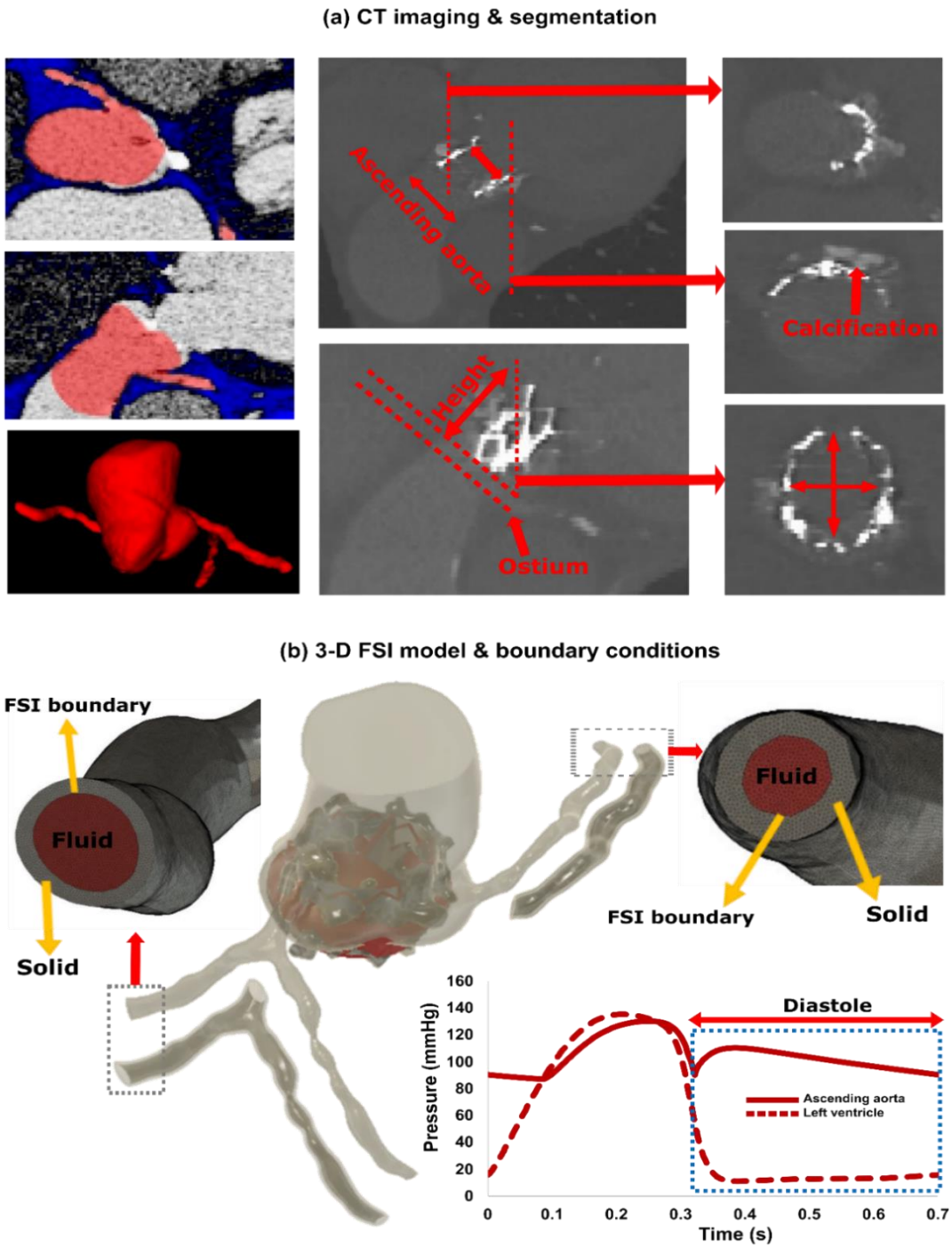


Figure 4-4. Reconstructed 3-dimensional geometry in a patient with AS who received TAVR using computed tomography, schematic diagram of LPM pressure boundary conditions and FSI. (a) CT views (coronal, sagittal and axial) of the ascending aorta, coronary branches, sinus of Valsalva and aortic valve for pre-TAVR (left column) and post-TAVR (middle and right column) as well as the segmentation process and geometry reconstruction; (b) computational domain and boundary condition. FSI simulations performed during diastole. Patient-specific LPM simulating the coronary perfusion pressure (ascending aorta pressure – LV diastolic pressure). This data was obtained from patient-specific imaged based lumped parameter model (Figure 4-1).

### 4.3.2 Patient-specific lumped parameter algorithm for complex valvular, vascular, mini-vascular, and ventricular diseases

We have previously developed a non-invasive diagnostic computational-mechanics framework for complex valvular, vascular and ventricular disease (called C3V-LPM for simplicity), described in detail elsewhere [19]. In this study, we further developed the C3V-LPM to enable the quantification of local and global hemodynamics in patients with mixed and complex valvular, vascular, mini-vascular and ventricular diseases (known as C3VM-LPM) (Figure 1, Table 2). The developed framework uses limited input parameters that can all be reliably measured non-invasively using DE, CT and a sphygmomanometer. Currently, none of the above metrics (global and local hemodynamics) can be obtained noninvasively in patients and when invasive procedures are undertaken, the collected metrics cannot be by any means as complete as the results that C3VM-LPM provides. The previously created model, C3V-LPM, was validated against clinical catheterization data in forty-nine AS patients with a substantial inter- and intra-patient variability with a wide range of disease [19]. In addition, some of the sub-models of the patient-specific lumped parameter algorithm have been used previously [11,13,25–29], with validation against *in vivo* cardiac catheterization (N=34) [30,31] in patients with vascular diseases, *in vivo* MRI data (N=57) [32] in patients with AS, and *in vivo* MRI data (N=23) [33,34] in patients with coarctation and mixed valvular diseases.

All details about modeling the left ventricle, left atrium, heart valves and patient specific optimization were presented elsewhere [16,17,19]. Here, we provide a detailed description about the new developments and algorithms related to the coronary arteries.

Table 4-2. **Cardiovascular parameters**. Summarized parameters used in the lumped parameter modeling to simulate all patient-specific cases

| Description | Abbreviation | Value |
|---|---|---|
| | | |
| **Valve parameters** | | |
| Effective orifice area | EOA | Measured using DE |
| Inertance (mitral valve) | $M_{MV}$ | Constant value: 0.53 $gcm^{-2}$ [31] |
| **Systematic circulation parameters** | | |
| Aortic resistance | $R_{ao}$ | Constant value: 0.05 $mmHg.s.mL^{-1}$ [17,22,27–29] |
| Aortic compliance | $C_{ao}$ | Initial value: 0.5 mL/mmHg<br>Optimized based on brachial pressures<br>*(Systolic and diastolic brachial pressures are optimization constraints)* |
| Systemic vein resistance | $R_{SV}$ | 0.05 $mmHg.s.mL^{-1}$ [17,22,27–29] |
| Systemic arteries and veins compliance | $C_{SAC}$ | Initial value: 2 mL/mmHg<br>Optimized based on brachial pressures<br>*(Systolic and diastolic brachial pressures are optimization constraints)* |
| systemic arteries resistance (including arteries, arterioles and capillaries) | $R_{SA}$ | Initial value: 0.8 $mmHg.s.mL^{-1}$<br>Optimized based on brachial pressures<br>*(Systolic and diastolic brachial pressures are optimization constraints)* |
| Upper body resistance | $R_{ub}$ | Adjusted to have 15% of total flow rate in healthy case [17,22,27–29] |
| Proximal descending aorta resistance | $R_{pda}$ | Constant value: 0.05 $mmHg.s.mL^{-1}$ [17,22,27–29] |
| **Elastance Function*** | | |
| Maximum Elastance | $E_{max}$ | 2.1 (LV)<br>0.17 (LA) [32,33] |
| Minimum Elastance | $E_{min}$ | 0.06 (LV, LA) [32,33] |
| Elastance ascending gradient | $m_1$ | 1.32 (LV, LA) [32,33] |
| Elastance descending gradient | $m_2$ | 27.4 (LV)<br>13.1 (LA) [32,33] |
| Elastance ascending time translation | $\tau_1$ | 0.269 T (LV)<br>0.110 T (LA) [32,33] |
| Elastance descending time translation | $\tau_2$ | 0.452 T (LV)<br>0.18 T (LA) [32,33] |
| **Pulmonary circulation parameters** | | |
| Pulmonary Vein Inertance | $L_{PV}$ | Constant value:0.0005 $mmHg{\cdot}s^2{\cdot}mL^{-1}$ [31] |
| Pulmonary Vein Resistance | $R_{PV}$ | Constant value: 0.002 $mmHg{\cdot}s{\cdot}mL^{-1}$ [31] |
| Pulmonary Vein and capillary Resistance | $R_{PVC}$ | Constant value: 0.001 $mmHg{\cdot}s{\cdot}mL^{-1}$ [31] |
| Pulmonary Vein and Capillary Compliance | $C_{PVC}$ | Constant value: 40 mL/mmHg [31] |
| Pulmonary Capillary Inertance | $L_{PC}$ | Constant value: 0.0003 $mmHg{\cdot}s^2{\cdot}mL^{-1}$ [31] |
| Pulmonary Capillary Resistance | $R_{PC}$ | Constant value: 0.21 $mmHg{\cdot}s{\cdot}mL^{-1}$ [31] |
| Pulmonary Arterial Resistance | $R_{PA}$ | Constant value: 0.01 $mmHg{\cdot}s{\cdot}mL^{-1}$ [31] |
| Pulmonary Arterial Compliance | $C_{PA}$ | Constant value: 4 mL/mmHg [31] |
| Mean Flow Rate of Pulmonary Valve | $Q_{MPV}$ | *Forward LVOT-SV* is the only input flow condition (measured using DE)<br>*$Q_{MPV}$ is a flow parameter that was optimized so that the lump-parameter model could reproduce the desirable DE-measured Forward LVOT-SV.* |
| **Input flow condition** | | |
| Forward left ventricular outflow tract stroke volume | Forward LVOT-SV | Measured using DE |
| **Output condition** | | |
| Central venous pressure | $P_{CV0}$ | Constant value: 4 mmHg [17,22,27–29] |
| **Coronary parameters** | | |
| Proximal Coronary Resistance | $R_{cor,p}$ | Adjusted based on MAP, CO and vessel cross sectional area [34–37] |
| Medial Coronary Resistance | $R_{cor,m}$ | Adjusted based on MAP, CO and vessel cross sectional area [34–37] |

| | | |
|---|---|---|
| Distal Coronary Resistance | $R_{cor,d}$ | Adjusted based on MAP, CO and vessel cross sectional area [34–37] |
| Proximal Coronary Compliance | $C_{cor,p}$ | Adjusted based on total vessel compliance and cross-sectional area [34,36,38] |
| Medial Coronary Compliance | $C_{cor,m}$ | Adjusted based on total vessel compliance and cross-sectional area [34,36,38] |
| **Other** | | |
| Constant blood density | $\rho$ | Constant value: 1050 kg/m$^3$ [17,22,27–29] |
| Heart rate | HR | Measured using DE |
| Duration of cardiac cycle | T | Measured using DE |
| Systolic End Ejection time | $T_{EJ}$ | Measured using DE |
| End diastolic volume | EDV | Measured using DE |
| End systolic volume | ESV | Measured using DE |

*Coronary arteries*

C3VM-LPM was developed to simulate blood flow rate at the outlets of the left anterior descending (LAD) artery, left circumflex (LCX) artery and right coronary artery (RCA), in addition to other regions of the heart and the cardiovascular system. The 5-element electrical circuit used to model each coronary branch was developed by Kim et al.[35] and has been used extensively to generate boundary conditions for higher order coronary models [36–42]. A 3D coronary computational fluid dynamic model which utilized the 5-element lumped model (based on the work of Kim et al.[35]) was clinically validated (N=103) by comparing the fractional flow reserve generated from the model with gold-standard invasive FFR measurements [43]. In a more recent study, Tajeddini et al. [42] used a similar 3D coronary model with the same 5-element lumped model as boundary conditions to compute a series of clinical coronary metrics. The model was applied to patients (N=7) and the resulting metrics were validated against results from other clinical studies. The circuits comprised of 3 resistors ($R_{cor,p}, R_{cor,m}, R_{cor,d}$), 2 capacitors ($C_{cor,p}, C_{cor,m}$) and an embedded pressure source ($P_{im}$) (Figures 1 and 2). While inductors are often included in the heart and circulatory models, they were not included in this coronary model since the inertial phenomena is not significant in the coronary artery branches [44]. By including an embedded pressure source, this layout has been shown to capture the bi-phasic nature of coronary flow, in which peak blood flow occurs during the diastole phase rather than during the systole phase [35,44].

The following ODEs are generated to model the coronary lumped parameter model [37]:

$$q_{in} = \frac{P_{in} - P_p}{R_{cor,p}} \quad (1)$$

$$q_{in} = C_{cor,p}\frac{dP_p}{dt} + q_m \quad (2)$$

$$P_p = q_m R_{cor,m} + P_m \quad (3)$$

$$q_m = q_{out} + C_{cor,m}\frac{dP_{im}}{dt} \quad (4)$$

$$P_m = q_{out} R_{cor,d} + P_{out} \quad (5)$$

where $q_{in}$, $P_{in}$, $q_{out}$ and $P_{out}$ are the blood flow and pressure into and out of the coronary branch. $R_{cor,p}, R_{cor,m}, R_{cor,d}$ are the proximal, medial, and distal resistors while $C_{cor,p}, C_{cor,m}$ are the proximal and medial capacitors. $P_p$, $P_m$ and $P_{im}$ are the proximal, medial and intramyocardial pressures.

$P_{im}$ is set to be either the left ventricle (LV) or right ventricle (RV) pressure, depending on the coronary artery that it is coupled to. In this study, we used the LV pressure for the left branches (LAD and LCX) and $0.5P_{LV}$ [35]to create the RV pressure for the right branch (RCA).

*Determining arterial resistance and compliance in coronaries*

Total coronary resistance The total coronary resistance was derived from a relationship between blood pressure and blood flow, where the mean flow rate to the coronary arteries was assumed to be 4.0% of the cardiac output [35], [36]:

$$R_{cor,total} = \frac{MAP}{Q_{cor,total}} = \frac{MAP}{(0.04) * CO} \quad (6)$$

where $R_{cor,total}$ is the total coronary resistance. Mean arterial pressure (MAP) is calculated based on systolic blood pressure (SBP), diastolic blood pressure (DBP) and heart rate (HR) [45]:

$$MAP = DBP + [\frac{1}{3} + (HR * 0.0012)](SBP - DBP) \quad (7)$$

***Left anterior descending (LAD) artery resistance.*** The total coronary resistance was divided between each of the branches based on a generalization of Murray's law [46], which relates resistance to vessel diameter:

$$R_{cor,LAD} = \frac{\sum_{i=1}^{n} \sqrt{A_i}^{2.6}}{\sqrt{A_{LAD}}^{2.6}} R_{cor,total} \quad (8)$$

where $R_{cor,LAD}$ is the total coronary resistance in the LAD and $A_i$ is the cross sectional area of each of the coronary vessels [35]. Further division of the total LAD resistance into the 3 resistive elements in the circuit was based on the work of Sankaran et al. [39]:

$$R_{cor,LAD,p} = (0.32)R_{cor,LAD} \quad R_{cor,LAD,m} = (0.52)R_{cor,LAD} \quad R_{cor,LAD,d} = (0.16)R_{cor,LAD} \quad (9)$$

where $R_{cor,LAD,p}$, $R_{cor,LAD,m}$, $R_{cor,LAD,d}$ are the proximal, medial, and distal resistors.

Similarly, the LAD compliance was computed by dividing the total left coronary compliance based on vessel diameter:

$$C_{cor,LAD} = \frac{A_{LAD}}{\sum_{i=1}^{n} A_i} C_{cor,total}^{L} \quad (10)$$

where $C_{cor,LAD}$ is the total LAD coronary compliance, $C^{L}_{cor,total}$ is the total left coronary compliance and $A_i$ is the cross sectional area of each of the left coronary branches [35]. A manual tuning process was utilized to determine total left coronary compliance value that lead to physiological coronary flow waveforms [40,47,48].

The LAD compliance was then divided across the 2 capacitors based on the following relationship [39]:

$$C_{cor,LAD,p} = (0.11)C_{cor,LAD} \qquad C_{cor,LAD,m} = (0.89)C_{cor,LAD} \tag{11}$$

where $C_{cor,LAD,p}$ and $C_{cor,LAD,m}$ are the proximal and medial capacitors.

***Left circumflex (LCX) artery*.** The LCX resistance and compliance were computed using the same methodology as the LAD artery.

***Right coronary artery (RCA) resistance***. The RCA resistance was computed using the same methodology as the LAD artery.

*Input parameters*

The following patient-specific parameters were inputs for the C3VM-LPM algorithm: forward left ventricular outflow tract stroke volume (Forward LVOT-SV), cardiac cycle time, ejection time, aortic valve effective orifice area (EOA), mitral valve EOA, ascending aorta cross sectional area, left ventricle outflow tract area, EOA during aortic regurgitation and EOA during mitral regurgitation measured by DE as well as brachial systolic and diastolic pressures measured by a sphygmomanometer. All the details about patient-specific parameter estimation were described in [19]. In addition, coronary geometry dimensions (left main coronary artery (LMCA) average diameter, LAD coronary artery average diameter, LCX coronary artery average diameter and right

coronary artery (RCA) average diameter), measured from the patient-specific reconstructed coronary artery geometry using CT data, are the input parameters for the C3VM-LPM algorithm.

*Computational algorithm*

MathWorks Simscape (MathWorks, Inc.) was used to formulate and solve the system of ordinary differential equations (ODEs) which govern the lumped parameter circuit. Additional functions were written in Matlab and Simscape to supplement and enhance the Simscape code. The ode23t trapezoid rule variable step solver with an initial time step of 0.1 ms was used to solve these ODEs. Initially the voltages and currents in the capacitors and inductors were set to zero and the model was run for ~150 cycles to reach a steady state. For the patient specific optimization, the residual criterion was set to $10^{-6}$.

### 4.3.3 Fluid solid interaction simulation study

The blood flow inside the coronary arteries was simulated using similar 3-D FSI set-up as described in our previous works[16,17] , using open-source FOAM-Extend library [24].

*Governing equations for fluid domain*

Blood flow was considered to be incompressible, Newtonian with a density of 1060 kg/m3 and dynamic viscosity of 0.004 Pa·s [49,50]. Since the Reynolds number is less than 500 inside the coronary arteries [51], the blood flow is assumed to be laminar [49,51]. Using 3-D incompressible Navier-Stokes equations in the form of Arbitrary Lagrangian-Eulerian (ALE), the continuity and momentum equations can be described as [16,17,52]:

$$\oint_s (n.V)ds = 0 \tag{12}$$

$$\int_{\forall} \frac{\partial V}{\partial t} d\forall + \oint_s n.(V - V_s)Vds = \frac{1}{\rho}\oint_s n.[\mu \nabla V]ds - \frac{1}{\rho}\int_{\forall} \nabla p d\forall \quad (13)$$

where n, ∀ , V, μ, P, ρ and Vs represent the normal vector to the surface S, the volume, fluid velocity, fluid dynamic viscosity, blood pressure ,fluid density, and velocity of the surface respectively.

*Governing equations for solid domain*

The coronary artery is comprised of three layers, intima, media, and adventitia, with the center layer, the media, constituting the majority of coronary tissue thickness [53]. Obtaining the human coronary tissue thickness and material properties are difficult due to the scarcity of human coronary tissue samples. In vivo quantification of material properties is even harder [54]. Creating an empirical model to describe the behavior of coronary artery has been of great interest with several previous designs [55–61]. Such in vitro studies, although proven to be reliable, were applied to the arteries after harvesting them from the body. Therefore, the properties and loading conditions in their studies do not accurately replicate the physiological conditions [62]. There are several studies on solid modelling of the coronary arteries based on clinical in vivo measurements, using IVUS and OCT [63–68]. However, both of these intracoronary imaging modalities introduce catheter based probes into the coronary artery and therefore, are invasive [62,66]. Using these techniques would be almost impossible for old patients with TAVR, for whom the coronary artery examination is limited to only non-invasive hemodynamic assessment using computed coronary angiography [69–71]. Due to these formidable challenges, there is no non-invasive method for obtaining patient specific material properties of coronary artery tissue to date [72].

Unlike previous FSI models with an idealized and simplified geometry for the coronary tissue [73–81], in this study, an average thickness of 1 mm was extruded from the patient specific fluid domain wall according to the previous clinical measured data for the tissue (solid domain) [82]. Moreover, we assumed an isotropic neo-Hookean solid model for the coronary tissue [83–86]. As shown in previous studies, the stiffness of coronary tissue increases significantly for older patients and with coronary artery disease due to complications such as collagen deposition or elastin fragmentation [61,87–89]. Since all patients in our study were elderly (average of 86 years old) and diagnosed with CAD, a Young's modulus of 4 MPa was assumed for all patients (Poisson's ratio for both patients: 0.49; density for both patients: 1000 kg/m$^3$) based on previous experiments to consider more realistic behavior of the tissue [61,87].

The governing momentum equation of solid domain in terms of initial undeformed configuration can be written as [90–92]:

$$\int_{\forall_0} \rho_0 \frac{\partial^2 u}{\partial t^2} d\forall_0 = \oint_{s_0} \sigma.(JF^{-T}.n_0) ds_0 + \int_{V_0} \rho_0 b dV_0 \tag{14}$$

where the subscript 0 denotes the undeformed configuration and u is the displacement vector. F is the deformation gradient tensor, described by $F = I + (\nabla u)^T$, where $I$ is the second order identity tensor and the Jacobian of the deformation gradient is $J=det[F]$.

For a neo-Hookean solid, σ can be expressed as [92,93]:

$$\sigma = \mu \,\mathrm{dev}[\bar{b}] + \frac{k}{2}\left(\frac{J^2-1}{J}\right) \tag{15}$$

$$\bar{b} = J^{-\frac{2}{3}} F.F^T \tag{16}$$

Where μ is the shear modulus and K is the bulk modulus (related to the Young's modulus and Poisson's ratio of material).

*Fluid-solid interaction (FSI)*

The coronary arteries were simulated under pathophysiological flow and pressure conditions with the strong coupling of the fluid and solid solvers. The fluid and solid domains system of equations were solved independently using the partitioned approach and the data was transferred at the FSI interface. Fluid and solid solvers were coupled by satisfying the kinematic and dynamic conditions. The kinematic and dynamic coupling conditions in the simulation process were [90]:

$$u_{f,i} = u_{s,i} \tag{17}$$

$$V_{f,i} = V_{s,i} \tag{18}$$

$$n_i . \sigma_{f,i} = n_i . \sigma_{s,i} \tag{19}$$

where subscripts *i*, *s*, and *f* indicate the interface, solid and fluid regions, respectively. Equation (19) indicates that the forces at the interface must be in equilibrium.

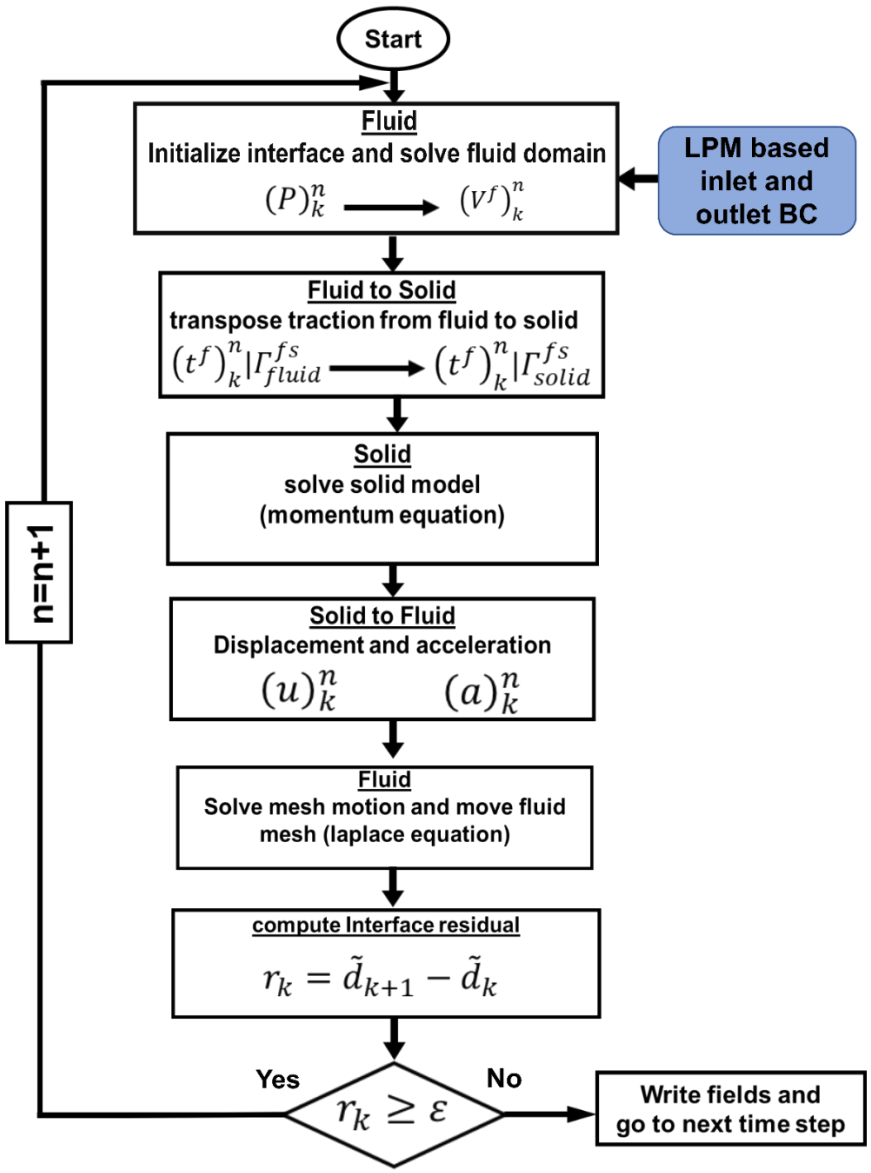


Figure 4-5. Patient-specific lumped parameter boundary conditions (BC) and strongly coupled FSI model flow chart.

*Grid Study*

For FSI simulations in the coronary arteries, different studies in the literature reported different acceptable error values between medium and refined mesh for the mesh independency. Several studies attained a reasonable accuracy once the variation of the peak velocity inside coronary was less than 5% [94–97]. Several other studies considered the flow results to be acceptable with variations of lower than 3% in the average of velocity [98], flow rate [42,99,100] or pressure [42,99,100] for mesh independency. In addition, regarding the mesh independency with respect to WSS, previous studies considered to be acceptable either less than 5% variation in peak (maximum) WSS [98,101] or less than 1% variation in the average WSS [97,102–104].

We used an open-source mesh generation software, SALOME, to produce the mesh for all models [105]. The number of elements for FSI simulation was optimized through the examination of spatial mesh resolution. We had performed a grid convergence analysis and the spatial resolution for our models ranged between 0.2 mm to 1 mm (unstructured tetrahedral elements with refined mesh near walls) (See Figure 6 for a sample of our grid convergence study). With optimized non-orthogonality and skewness values, the mesh definition for both the fluid and solid domains was considered acceptable when the velocity profiles in successive meshes showed a variation of less than 0.5%, such that this difference was not significant. The fluid dynamic mesh was controlled by Laplace mesh motion, which was subsequently influenced by variable diffusivity, to ensure the initial quality of the cells was maintained [52,106]. Mesh at the interface of the fluid and solid domains was not conformal. Consequently, following the face-interpolation and vertex-interpolation procedures, interpolation could be performed between the fluid and solid boundaries [52]. Indeed, we observed 0.5% variation as the maximum error in our mesh independency study in the entire velocity domain. At any other point in the domain and at any instance during diastole, the

maximum error was less than 0.5% and the variation of average velocity was less than 0.3%. In our study, the maximum WSS variations occurred at the PVL site and was less than 3% while the variation of the average WSS at the PVL site was less than 1%. In addition, the variation of the maximum value of the Von Mises stress for the coronary arteries (solid domain) was less than 2% [94,107].

Moreover, time step independency had been studied for all models. We found that a maximum Courant number of 0.5 was yielded as the solution marched in time with a time step of 0.00001s. For all simulations investigated in this study, the Courant number was lower than 0.5. This limit improved the accuracy of the numerical solution and reduced numerical dispersion. Convergence was obtained when all residuals reached a value lower than $10^{-6}$. Temporal discretization and spatial discretization were performed using a second-order Euler backward scheme and a second-order accurate scheme, respectively.

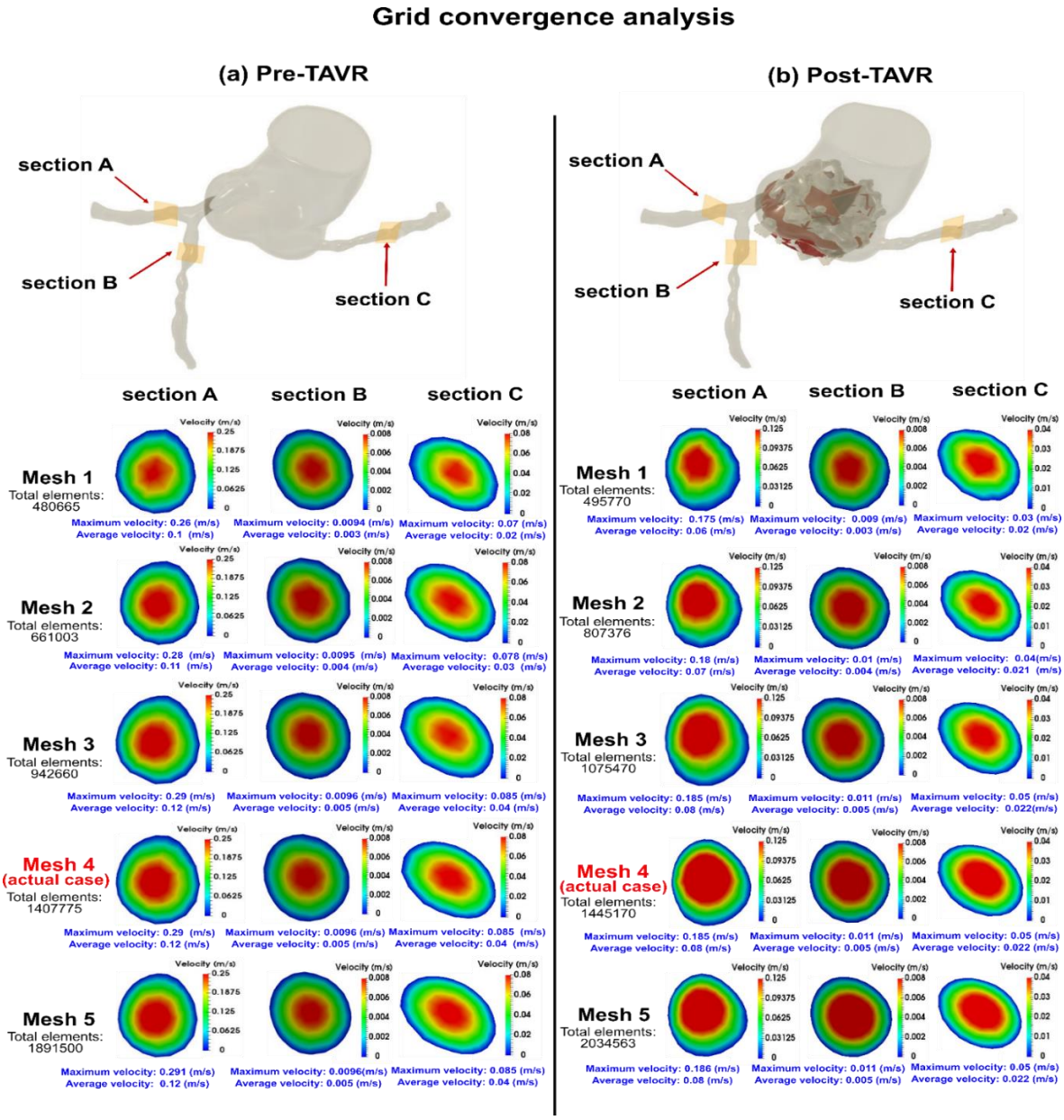


Figure 4-6. Grid convergence analysis. (a) Pre-TAVR: velocity comparisons for different mesh resolutions at the peak of filling phase for different coronary cross sections (sections A,B and C): difference in average velocity between mesh#3 and mesh#4 is less than 0.3% and between mesh#4 and #5 is less than 0.2% - difference in maximum velocity between mesh#3 and mesh#4 is less than 0.5% and between mesh#4 and mesh#5 is less than 0.3%; (b) Post-TAVR: velocity comparisons for different mesh resolutions at the peak of filling phase for different coronary cross sections (sections A,B and C): difference in average velocity between mesh#3 and mesh#4 is less than 0.3% and between mesh#4 and #5 is less than 0.2% - difference in maximum velocity between mesh#3 and mesh#4 is less than 0.5% and between mesh#4 and mesh#5 is less than 0.3%; In the aortic root and coronary arteries, the blood flow is laminar and does not experience turbulence during the diastolic phase. In this study, for all 3 patients, we considered the blood flow to be laminar.

*Model reconstruction*

We segmented and reconstructed the 3-D geometries of the ascending aorta, aortic root, sinotubular junction, sinus of Valsalva, aortic valve and main coronary arteries (proximal RCA, LMCA, proximal LCX and proximal LAD) in patients with aortic stenosis (Pre-TAVR) and Post-TAVR using CT images and ITK-SNAP (version 3.8.0-BETA) [108], a 3-D image processing and model generation software package (Figure 4). These 3-D reconstructions of the model were performed based on using images taken at the beginning of diastole. The reconstructed 3-D models were then used for FSI simulations during diastole. We used a smoothing procedure for the surfaces to overcome the challenges of computational convergence and stability. The change in the volume due to smoothing was less than 3% in all patients.

### 4.3.4 Boundary conditions & material properties

Our patients specific lumped parameter algorithm provided boundary conditions (Figures 1 and 2) non-invasively to provide [19]: (1) the time-dependent pressure waveform of ascending aorta during diastole which was applied as inlet boundary condition; (2) the time-dependent coronary flow waveforms which were applied as coronary outlet boundary condition; (3) for PVL, the ventricle pressure was applied as outlet at the leakage area location (leakage area was measured and located based on short axis DE, Figure 3b) to provide patient-specific PVL pressure gradient (pressure difference between ascending aorta and ventricle during diastole). All the simulations were performed during diastole and the aortic valve was therefore assumed to be rigidly closed.

### 4.3.5 FSI solution and strategy

The details of FSI simulation method is presented elsewhere [16,17]. Briefly, FOAM-Extend library[24] was used to discretize the governing equations of the FSI problem using the finite volume method

for fluid, solid and moving boundary [16,17,91,109] (See Figure 5 for FSI algorithm flowchart). Coupling of the discretized governing equations of the fluid and solid domains was performed using the interface Quasi-Newton-Implicit Jacobian Least-Squares (IQN-ILS) algorithm [110].

### 4.3.6 Validation: Doppler-based LPM and FSI framework vs. clinical Doppler echocardiography data

Figure 7(a) to 7(f) compares the peak PVL velocity simulated using our computational framework and DE data for two patients as a sample (7(a) and 7(d): regurgitant flow waveform 7(b): parasternal short axis view of PVL jet; 7(e): parasternal long axis view of PVL jet). The simulated peak velocities correlated well with the ones measured by DE in both patients with a maximum relative error of 8% for the peak velocity at the beginning of diastole phase (early filling). For the whole diastole phase, the results show good agreements between velocity calculated using the computational framework and the ones measured using DE in both cases investigated in this study.

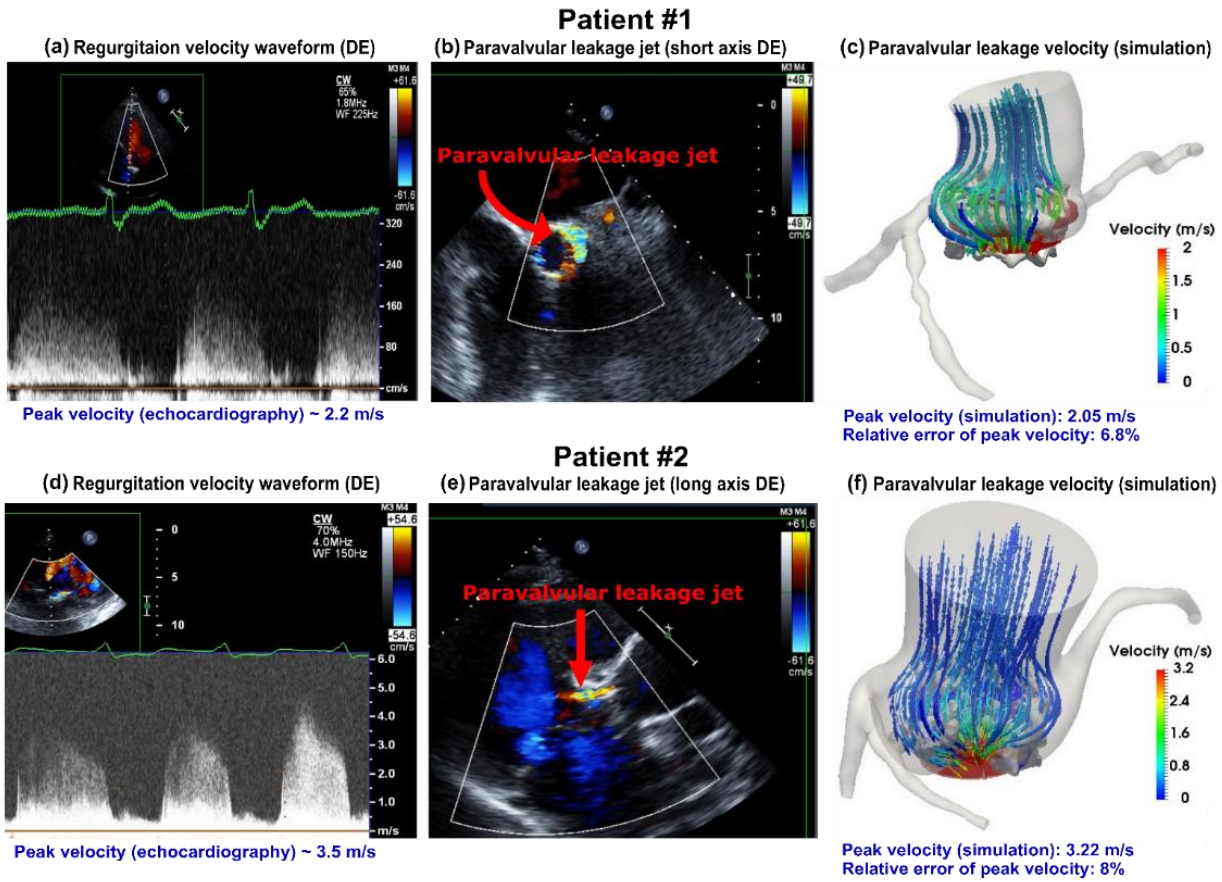


Figure 4-7. Validation: Doppler-based LPM and FSI framework vs. patients Doppler echocardiography data. (a) & (d) Regurgitant flow waveform during diastole in patients #1 and #2; (b) Parasternal short axis view of PVL during diastole in patient #1; (e) Parasternal long axis view of PVL during diastole in patient #2; (c) & (f) PVL flow velocity streamlines during diastole in patients #1 and #2.

## 4.4 Results

### 4.4.1 Effect of anatomic and deployment characteristics on aortic root and neo-sinus local hemodynamics (post-TAVR) computed by non-invasive image-based diagnostic framework

The blood flow vortical structure and stagnation in the aortic root, sinus of Valsalva and neo-sinus region depends on the ascending aorta and ventricular pressures, aortic root geometry, aortic valve

geometry, stent height, deployment angle and coronary ostium location. We investigated hemodynamic metrics computed by our computational framework (Figures 8 and 9) as follows:

#### 4.4.1.1 Vortical structure

In order to explore the washout mechanism of flow through vortex morphology, the mid planar velocity streamlines for all the leaflets (left coronary cusp (LCC), right coronary cusp (RCC) and non-coronary cusp (NCC)) is extracted at the peak and late phases of diastole. It has been shown that for a TAVR without PVL, the coronary flow influences the flow patterns of aortic root and neo-sinus and favors the transfer of blood flow towards ostium during diastole [111]. However, our results showed that in the presence of PVL, the aortic root vortices will not favor the transfer of blood flow towards ostium in the aortic root and neo-sinus region. As shown in Figures 8 (8a,8b and 8c) and 9 (9a,9b and 9c), for patients #1 and #2, the mainstream of PVL flow originates from ascending aorta towards the leakage orifice behind the stent and between LCC and RCC leaflets with a maximum of 2.05 m/s and 3.22 m/s for patients #1 and #2 respectively. However, the maximum velocity between left ostium and stent was 1.53 m/s and 0.42 m/s for patients #1 and #2 respectively. This can be explained by the fact that the size of the gap between the edge of stent frame and the ostium is smaller for patient #1 than patient #2, leading to higher divergent velocity towards the leakage area.

For both patients, a vortex forms in the neo-sinus region of all the leaflets (LCC, RCC and NCC) as shown in Figures 8 (8a, 8b and 8c) and 9 (9a, 9b and 9c). Our results showed this vortex is very different for LCC, RCC and NCC and for different patients. For patient #1, the vortex arises from the leaflet surface at early diastole and dominates the whole neo-sinus region at late diastole, leading to an efficient washout of blood flow from the LCC (Figure 8a). However, during the

whole diastole, the center of vortex remains close to the stent edge for RCC (Figure 8b), and for NCC (Figure 8c), the center of vortex remains close to the upper commissure and vanishes at late diastole. For both RCC and NCC (Figure 8b and 8c), the vortex does not move down to reach the leaflet surface, leading to a reduced washout of blood flow. For patient #2 though, the vortex center remains distant from the leaflets for LCC (Figure 9a) and NCC (Figure 9c) at early diastole and gets closer to the leaflets for RCC (Figure 9b). Although in mid diastole, the vortex size in LCC increases, and does not dominate the whole neo-sins similar to the vortex for patient #1. In other words, for patient #2, vortices aid the washout in RCC more than LCC and NCC.

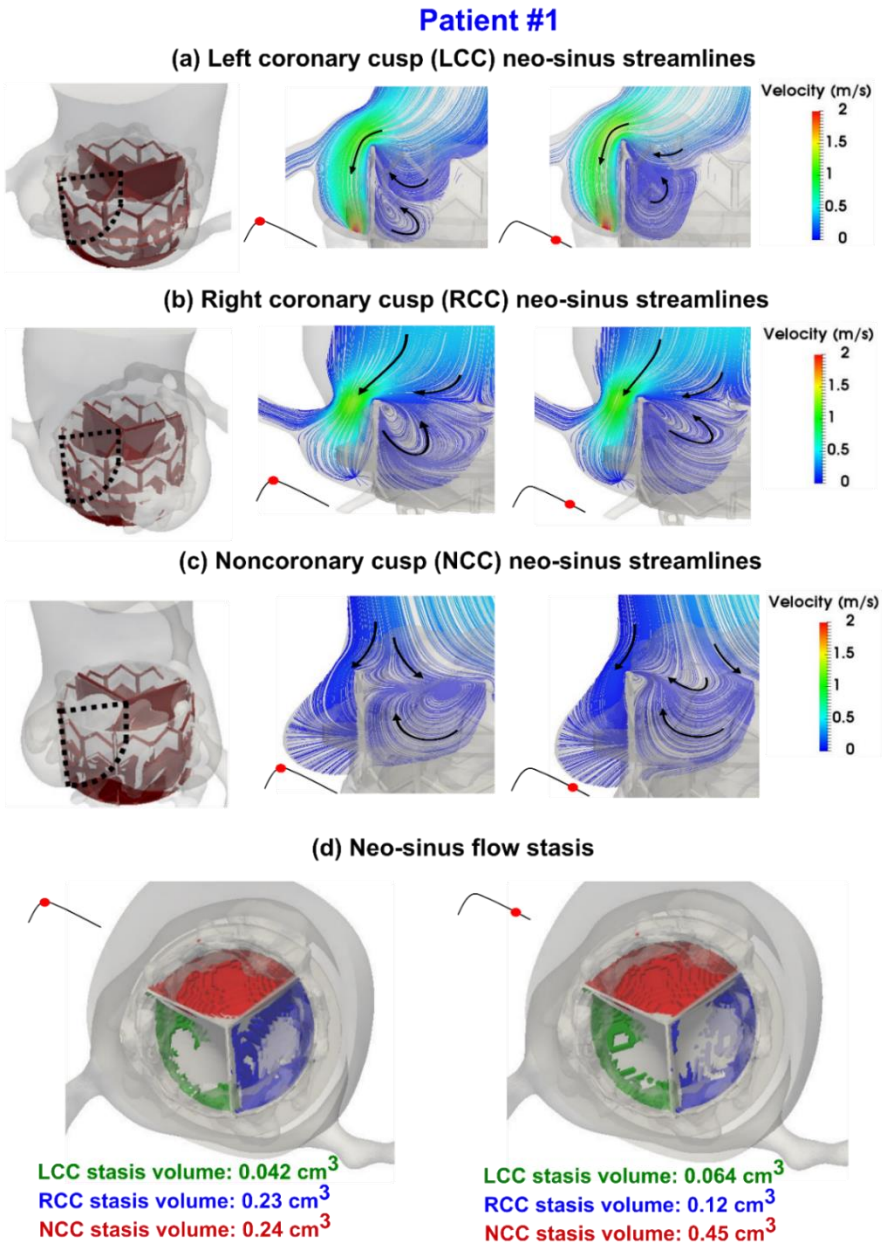


Figure 4-8. Evolution of vortical structure following TAVR in the aortic root and neo-sinus regions in patient #1 during diastole. (a) Mid-planar velocity of left coronary cusp neo-sinus; (b) Mid-planar velocity of right coronary cusp neo-sinus; (c) Mid-planar velocity of non-coronary cusp neo-sinus ; (d) Blood stasis volume. Pre-TAVR: severe aortic stenosis (EOA=0.6 cm2), coronary artery disease and hypertension, diastolic dysfunction, atrial fibrillation, ejection fraction: 29%, brachial pressures: 61 and 107 mmHg, forward LV stroke volume: 35 mL; Post-TAVR: aortic valve (EOA=1.7 cm2), hypertension, moderate mitral regurgitation, diastolic dysfunction, atrial fibrillation, ejection fraction: 34%, brachial pressures: 86 and 130 mmHg, forward LV stroke volume: 62 mL.

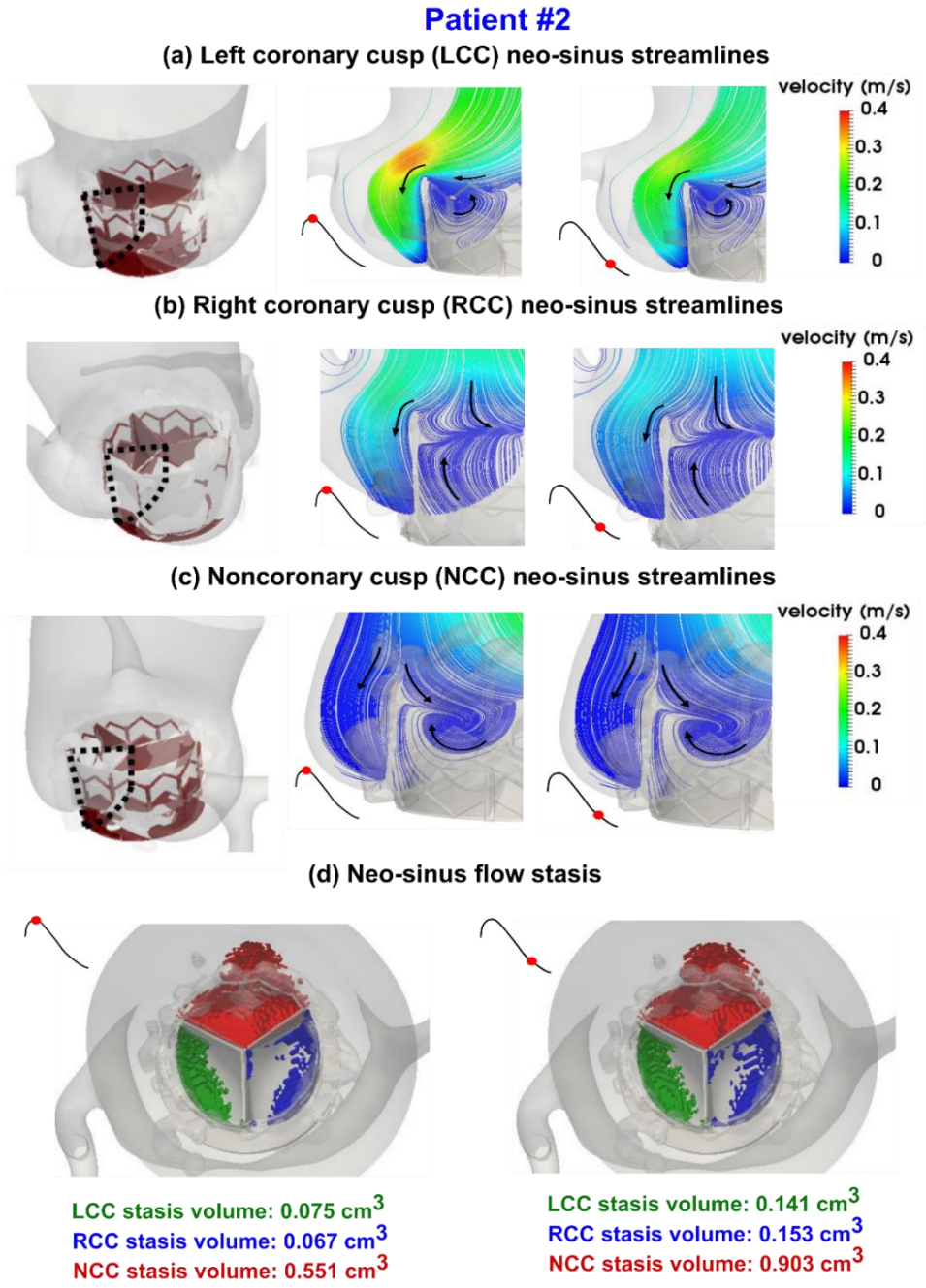


Figure 4-9. Evolution of vortical structure following TAVR in the aortic root and neo-sinus regions in patient #2 during diastole. (a) Mid-planar velocity of left coronary cusp neo-sinus; (b) Mid-planar velocity of right coronary cusp neo-sinus; (c) Mid-planar velocity of non-coronary cusp neo-sinus; (d) Blood stasis volume. Pre-TAVR: severe aortic stenosis (EOA=0.6 cm2), coronary artery disease and dyslipidemia, diastolic dysfunction, ejection fraction: 38%, brachial pressures: 54 and 107 mmHg, forward LV stroke volume: 74 mL; Post-TAVR: aortic valve (EOA=1.8 cm2), diastolic dysfunction, ejection fraction: 51%, brachial pressures: 59 and 120 mmHg, forward LV stroke volume: 92 mL.

#### 4.4.1.2 Stagnant and low-velocity flow

The volume of regions with velocity less than 0.001 m/s was obtained for all patients as a measure of blood stasis associated with high risk of thrombus formation [16,112,113]. For patients #1 and #2 as a sample, NCC neo-sinus had higher regions of stagnant flow than RCC and LCC neo-sinuses; 0.24 $cm^3$ at early diastole and 0.45$cm^3$ at late diastole for patient#1 (Figure 8d), and 0.55 $cm^3$ at early diastole and 0.903 $cm^3$ at late diastole for patient#2 (Figure 9d). For patient #1 the RCC had significantly higher stagnant flow than LCC for the whole diastole; 0.23 $cm^3$ and 0.042 $cm^3$ at early diastole and 0.12 $cm^3$ and 0.064 $cm^3$ at late diastole for RCC and LCC respectively. However, for patient #2, the LCC had slightly higher stagnant flow at early diastole and RCC had slightly higher stagnant flow at late diastole; 0.075 $cm^3$ and 0.067 $cm^3$ at early diastole and 0.141 $cm^3$ and 0.153 $cm^3$ at late diastole for LCC and RCC respectively. Interestingly, although patient #1 had more severe PVL than patient #2, the stagnant flow volume in the neo-sinus region was almost 2 folds larger for patient #2 than patient #1 (LCC and NCC). This can be explained by the fact that the blood stasis depends not only on the PVL severity, but also on the patient-specific aortic root geometry, ascending aorta and LV pressures and the deployment details of TAVR. In other words, our results showed that PVL severity alone cannot reveal the risk of thrombosis in the neo-sinus region.

#### 4.4.1.3 Aortic root wall shear stress

Wall shear stress, as a tangential force induced by blood flow, has a major influence on regulating endothelial function [114]. In general, very high wall shear stress (typically higher than 3 Pa) could

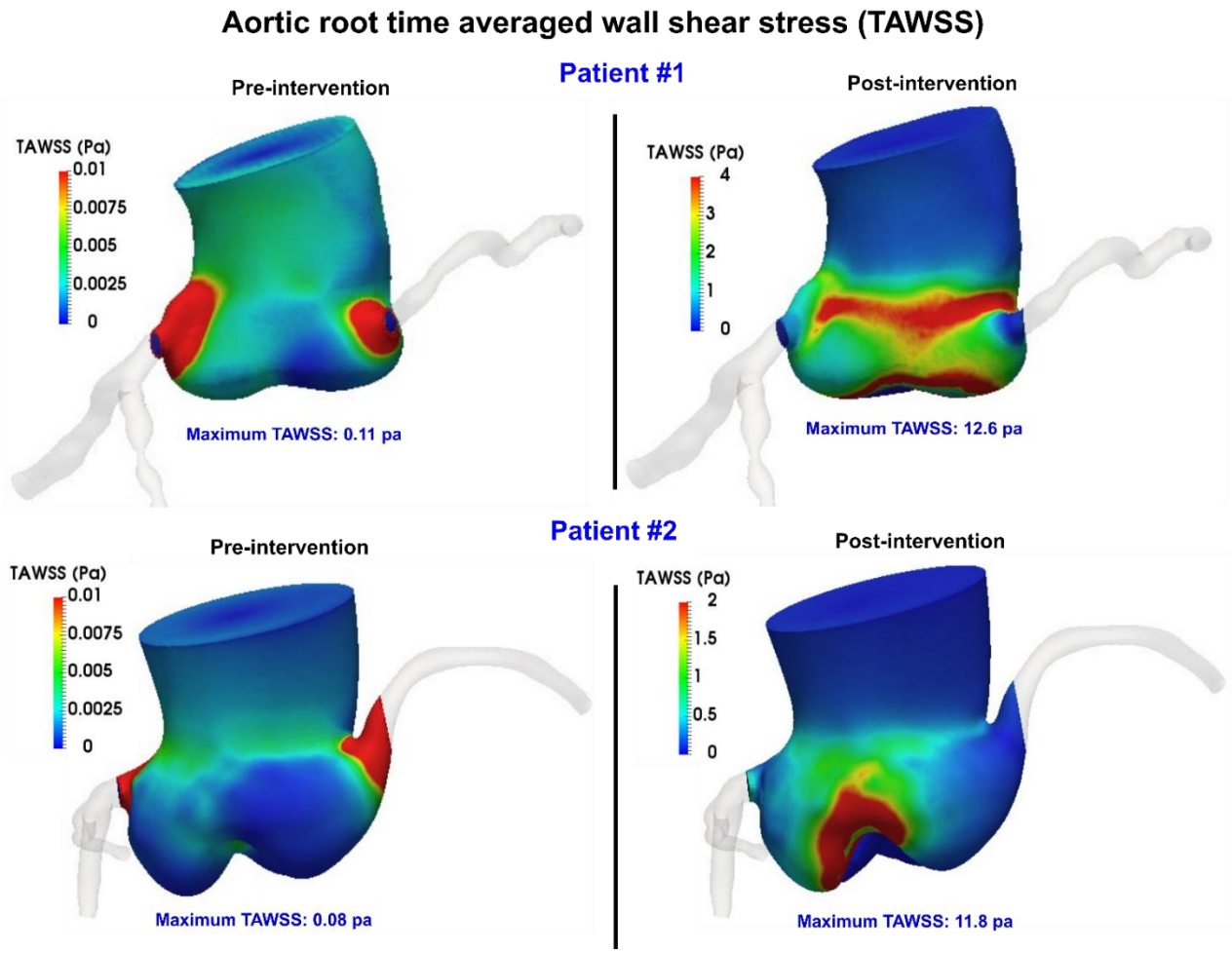


Figure 4-10. Time averaged wall shear stress of the aortic root during diastole for patients #1 and #2 in both pre and post intervention status

contribute to tissue rupture [115]. PVL could disturb the flow in the aortic root sinus after TAVR, leading to increased wall shear stress. We evaluated the total wall shear stress during diastole using the time-averaged wall shear stress (TAWSS) which is obtained with the formula $TAWSS = \frac{1}{T}\int_0^T |\tau| \mathrm{d}t$ (T and τ are the diastole duration time and instantaneous wall shear stress, respectively). TAWSS was calculated for all patients in both pre and post TAVR states. As an example, the maximum local TAWSS at the aortic root was increased drastically after TAVR for patients #1 and #2 (Figure 10); from 0.11 Pa and 0.08 Pa pre-TAVR to 12.6 Pa and 11.8 Pa post-

TAVR for patient #1 and patient #2 respectively. Such considerably high TAWSS might be a concern for patients who received TAVR. Moreover, our finding showed that the distribution of wall shear stress at the aortic root is very different for each patient, depending on the characteristics of TAVR deployment and aortic root geometry (Figure 10).

### 4.4.2 Coronary arteries fluid-structure interactions computed by non-invasive image-based diagnostic framework (pre-TAVR and post-TAVR)

In the presence of PVL after TAVR, the supplied blood flow through the coronary arteries is altered. We investigated the metrics of tissue (solid domain) and flow (fluid domain) computed by strongly coupled FSI algorithm as follows:

#### 4.4.2.1 Coronary arteries von-mises stress

Von-Mises stress of the tissue, induced by the transient blood flow pressure, is a critical parameter for assessment of tissue rupture and plaque burden [62,79,116,117]. The von-Mises stress can be obtained as:

$$\sigma_{VM} = \frac{1}{\sqrt{2}} \sqrt{(\sigma_{xx} - \sigma_{yy})^2 + (\sigma_{yy} - \sigma_{zz})^2 + (\sigma_{xx} - \sigma_{zz})^2 + 6\left(\sigma_{xy}^2 + \sigma_{yz}^2 + \sigma_{xz}^2\right)^2} \quad (34)$$

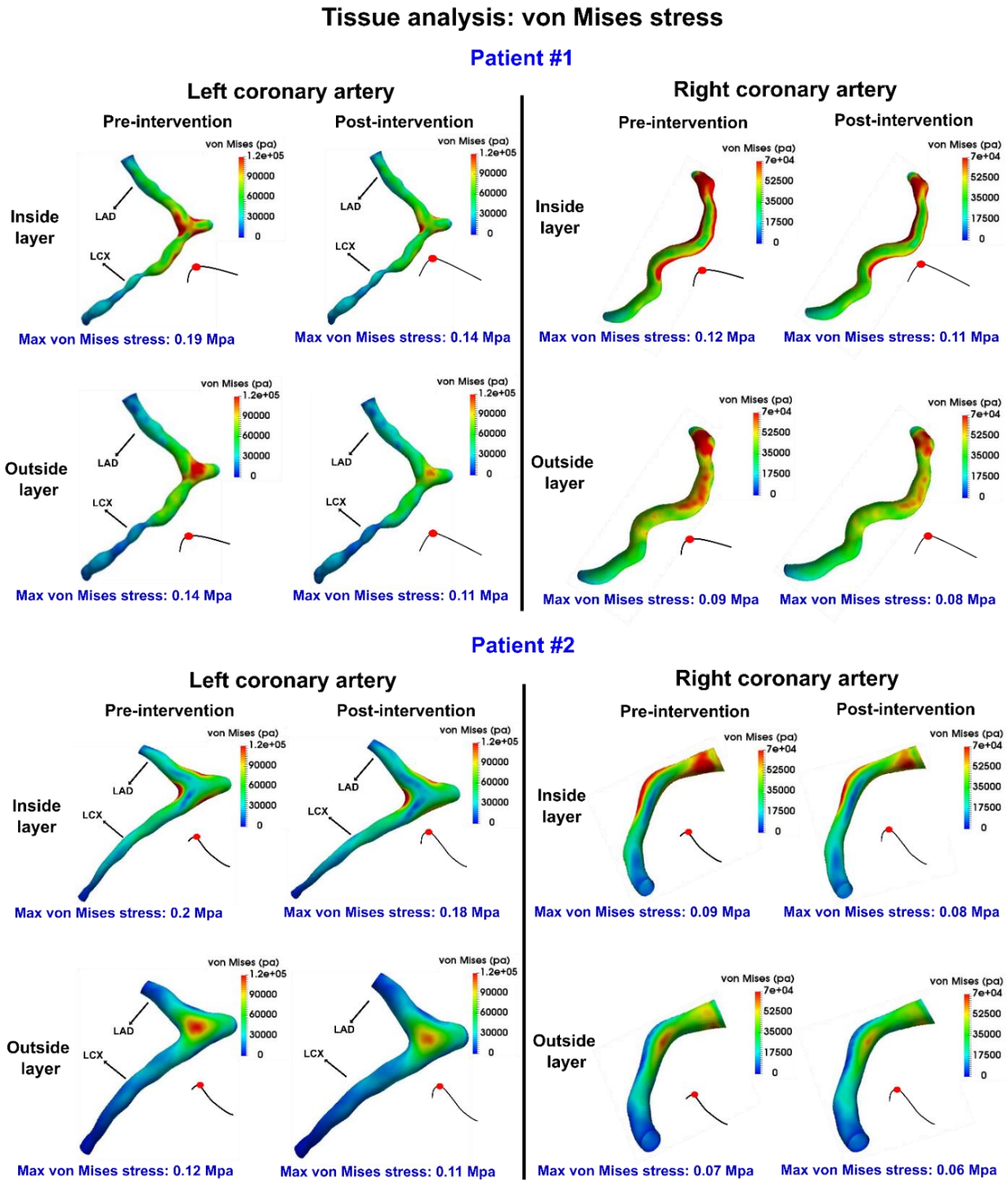


Figure 4-11. 3D distribution contours of Mises stress at peak diastole in patient#1 and patient#2 between baseline and 90-day post-TAVR

in which $\sigma_{xx}$, $\sigma_{yy}$ and $\sigma_{zz}$ are the normal stress components and $\sigma_{xy}$ , $\sigma_{yz}$ and $\sigma_{xz}$ are the shear stress components**.** Although there is no cut-off threshold available in the literature for the rupture of arterial wall von-Mises stress, an average stress of 0.3 MPa has been reported to initiate the first crack in the artery wall [116]. As shown in Figure 11, the distribution of von-Mises stress and its maximum, is different for inner and outer layers of tissue. The maximum von-Mises stress magnitude for all coronary branches in our study was less than 0.3 MPa during diastole for both pre-TAVR and post-TAVR. A universal reduction in maximum von-Mises stress was observed after TAVR for all coronary arteries; As an example, 26.3% reduction for left coronary branches and 11.11% reduction for right coronary in patient #1, and 10% reduction for left coronary branches and 14.3% reduction for right coronary in patient #2. Therefore, it can be concluded that PVL does not have any direct adverse effect on the tissue rupture. However, recent studies suggest that the decrease of structural stress in the regions of coronary artery with low wall shear stress is associated with exacerbated plaque burden [118,119].

#### 4.4.2.2 Coronary arteries wall shear stress

Endothelial cells which are exposed to low wall shear stress display a pro-inflammatory state, which is associated with plaque progression [114,118]. Although providing an exact cut-off value for low wall shear stress is still challenging, some studies suggested that wall shear stress lower than 1 Pa [114] or 1.2 Pa [118] is associated with higher plaque progression in a further serial study of coronary atherosclerosis. We calculated the wall shear stress over diastole for all patients in pre and post TAVR states. For patients#1 and #2 as examples, local and maximum wall shear stress were decreased for all coronary branches (LCX, LAD and RCA) as shown in Figure 12. For patient #2, the maximum wall shear stress slightly reduced for LAD and LCX branches; 8.5% and 12.5% for early and late diastole.

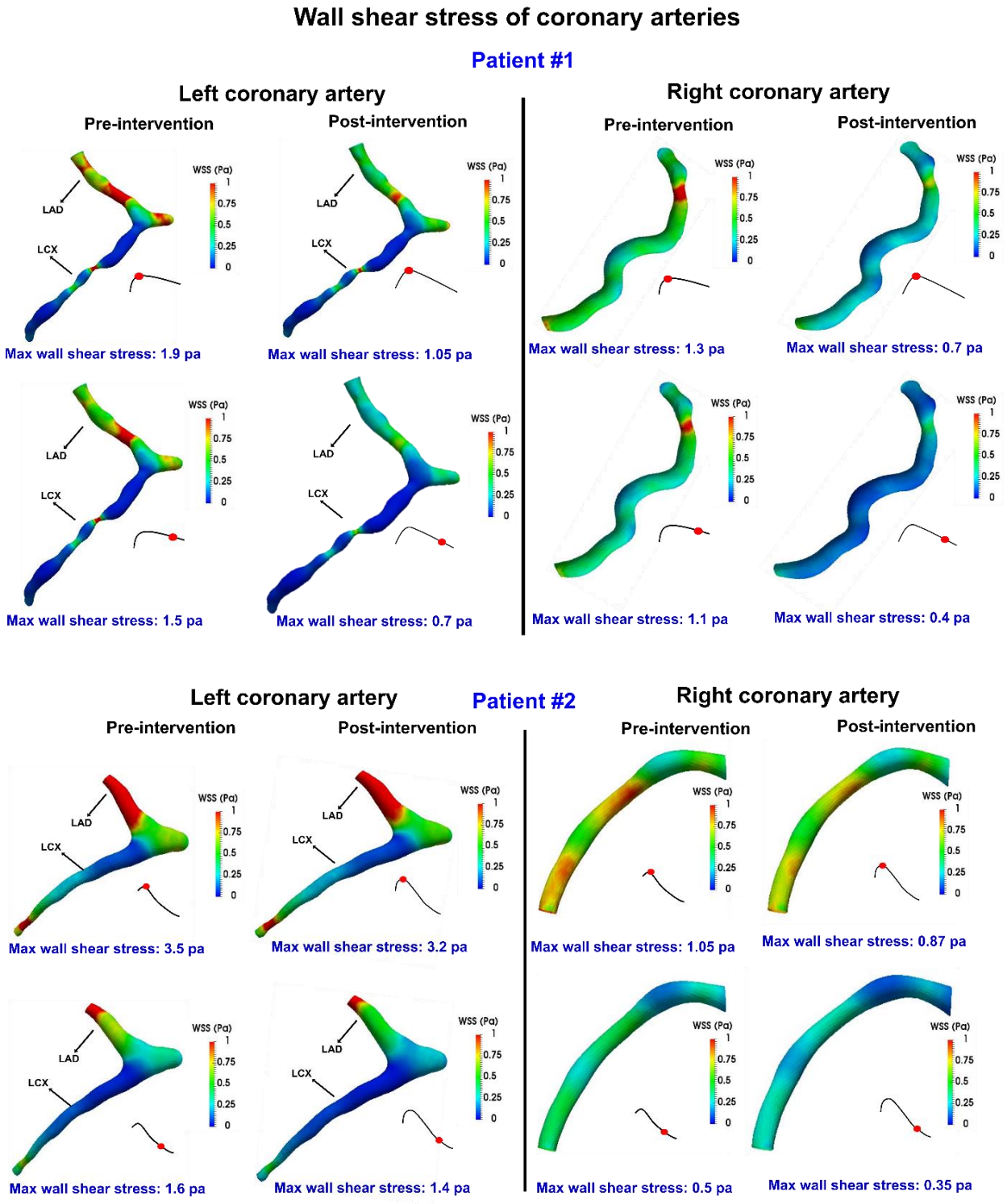


Figure 4-12. 3D distribution contours of wall shear stress at peak diastole in patient#1 and patient#2 between baseline and 90-day post-TAVR

However, for RCA, maximum wall shear stress decreased from 1.05 Pa to 0.87 Pa (17%) at the peak diastole and from 0.5 Pa to 0.35 Pa (30%) at late diastole. For patient #1, the maximum wall shear stress in the LAD and LCX branches reduced from 1.9 Pa to 1.05 Pa (44.7%) at the peak diastole and from 1.5 Pa to 0.7 Pa (53.3%) at late diastole. Also, for RCA, maximum wall shear stress decreased significantly from 1.3 Pa to 0.7 Pa (46.2%) at the peak diastole and from 1.1 Pa to 0.4 Pa (63.6%) at late diastole. Such considerable reduction in wall shear stress in a coronary artery (lower than 1.2 Pa) could promote plaque progression for patients who received TAVR treatment.

### 4.4.3 Non-invasive image-based diagnostic framework: computed global hemodynamics

#### 4.4.3.1 Cardiac function

LV workload represents the total energy required by the ventricle to eject blood, and is an effective metric of LV load and clinical state [11,13,16,17]. For patients #1 and #2 for example, despite the reduction of transvalvular pressure gradient, the LV workload increased after TAVR due to the presence of PVL (Figure 13a); 35% and 18.67% increase in workload after TAVR for patient #1 and #2 respectively. Although the LV pressure decreased post-TAVR, severe PVL contributed to a shift from ventricular pressure overload to a ventricular volume overload.

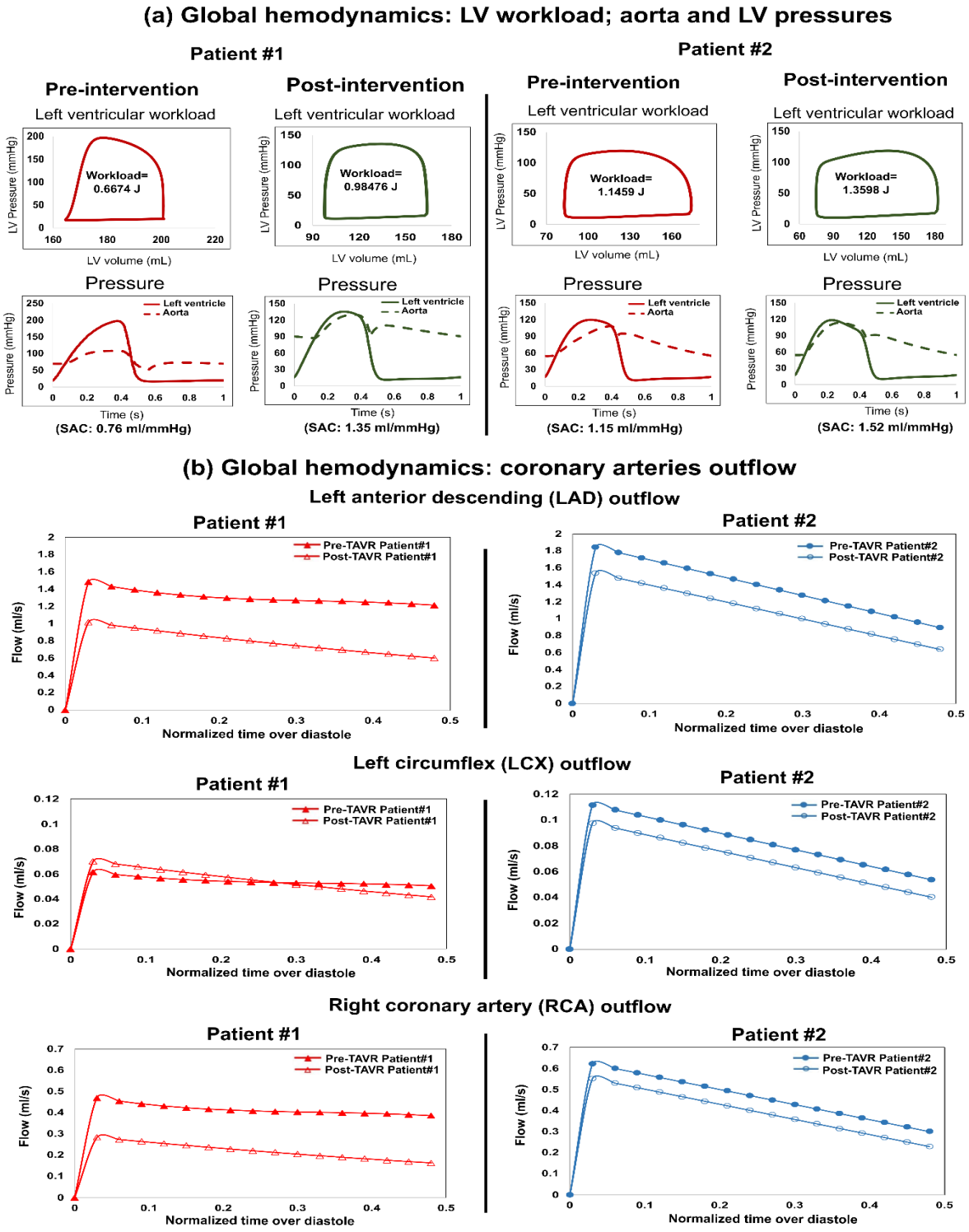


**Figure 4-13. Global hemodynamics.** Changes in predicted global hemodynamics before intervention and after TAVR for patients#1 and #2; (a) workload, left ventricle and ascending aorta pressure and systemic arterial compliance (SAC); (b) Changes in predicted coronary flowrate for LAD, LCX and RCA branches before intervention and after TAVR for both patients.

#### 4.4.3.2 Circulatory function

Systemic arterial compliance (SAC) is an index for predicting vascular disease states. For patients with AS, a low SAC (lower than 0.64 ml/m$^2$/mmHg) is associated with increased risk of morbidity [120]. As shown in Figure 13a, SAC improved for patients #1 and #2 after TAVR, with SAC increasing to > 1 (ml/mmHg) for both patients after intervention.

Increased aortic pressure is expected after TAVR as a result of the removal of AS obstruction [121,122]. As shown in Figure 13a, maximum aortic pressure increased 57% for patient #1 after TAVR. For patient #2, however, maximum aortic pressure increased only 5.1 %. Moreover, maximum left atrium pressure reduced by 39% for patient #1, while the change was almost negligible (less than 3% increase) for patient #2.

#### 4.4.3.3 Coronary circulatory function

Inadequate coronary flowrate and coronary hypoperfusion could lead to exacerbated heart failure [69]. It has been shown that the TAVR deployment characteristics (such as implant depth, angle and PVL) could affect the coronary flow [69,123–125]. As shown in Figure 13b, for all patients in our study, although the perfusion pressure has increased after TAVR, the PVL and flow disturbance in the aortic root significantly reduced the flowrate in almost all coronary branches. For example, maximum flowrate was reduced by 34% and 37% in LAD and RCA branches of patient #1 after TAVR. For LCX branch in patient#1, the flowrate remained almost unchanged, however, the flow in this branch was initial significantly reduced before TAVR because of the stenosis in the middle section of the artery (peak flow for LCX was 0.062 mL/s, while for LCA and RCA is 1.5 mL/s and 0.48 mL/s respectively). For patient #2, the maximum flowrate was reduced by 19% in LAD,

17% in LCX, and 14% in RCA branches. Even after the maximum flowrate at the peak diastole, the flow reduction persists for all coronary branches during the whole diastole for both patients after TAVR (Figure 13b). Such considerable reduction of flow could contribute to cases of ischemic lesions and promote thrombus formation.

## 4.5 Discussion

CAD is present in approximately 50% of the TAVR population, but this has decreased as the use of TAVR has migrated towards younger patients [69]. The question, however, of if CAD should be treated or reduced in severity prior to TAVR is still a topic for debate [69]. Patients suffering from CAD would typically undergo percutaneous coronary intervention (PCI) prior to TAVR, but some research suggests there may be less associated mortality if PCI is performed parallel to TAVR [69]. The benefits of performing both operations coincidentally are avoidance of several vascular punctures at different time periods as well as only having a single period where contrast agents are being injected [69]. The largest disadvantage is that large amounts of contrast agent would be required to perform both operations together, which can be dangerous to the kidney and result in contrast nephropathy [69].

Coronary arteries are supplied with blood mainly during diastole, and due to the disturbed flow associated with PVR [126], blood entering the coronary circulation may be disrupted. The complications resulting from this is relatively unknown, and more research is needed. Indeed, quantification of flow is important as it aids to correctly identify complications which exclusive anatomical examinations can overlook [71]. Based on hemodynamics, it was determined there was an increase in blood velocity and wall shear stress following TAVR, and blood flow was different with SAVR and TAVR [127]. These changes can lead to health complications in the future, and may

have gone undetected if a hemodynamic assessment was not done [127]. In the present work, there are several findings which should be individually discussed:

### 4.5.1 Improvements of coronary perfusion pressure and systemic arterial compliance after TAVR are poor indicators of coronary flow recovery in presence of paravalvular leak

AS disrupts coronary flow due to the low coronary perfusion pressure [121,128] and extravascular compressive forces [121,129], commonly associated with lower systemic arterial compliance and higher arterial resistance [121,130,131]. After TAVR, immediate increase in coronary flow is expected, as a result of increased aortic diastolic pressure (with increased forward pressure gradient at the coronary ostium) and decreased LV end diastolic pressure [121,122]. However, our findings revealed that for patients who undergo TAVR and suffer from PVL, despite the increase of aortic pressure and systemic arterial compliance, there is considerable decrease in coronary flow during diastole. We observed (Figures 8 and 9) that in the presence of PVL, a considerable portion of the forward flow towards coronary ostium diverges towards the left ventricle, leading to a decreased coronary flow. Furthermore, in agreement with recent studies [132–134], our results demonstrate the coronary flow is impeded if the distance between stent and coronary ostium is restricted after TAVR (Figure 8). Such decrease in coronary blood flow is associated with reduced capacity to augment myocardial oxygenation, leading to LV dysfunction, increased apoptosis (which is linked to myocardial fibrosis and is an independent indicator of mortality) and sudden death [121,135–137].

#### 4.5.1.1 In all patients with PVL following TAVR: No improvement of coronary flow post-TAVR

Although an increase in coronary flow is expected after AS removal and TAVR implantation, our results showed that for all patients who had PVL following TAVR, a universal reduction of flow occurs during diastole for all coronary branches (Figure 14). Recent studies suggest that despite the early improvements of systolic flow right after TAVR, coronary diastolic flow might not improve during the long-term (6-month) follow up. Our results show that the coronary diastolic flow recovery is even worse for patients with PVL following TAVR. Reduced flow in coronaries could affect the outcomes of revascularization and might play a role in the pathophysiological abnormalities leading to heart failure or increased risk of cardiovascular death.

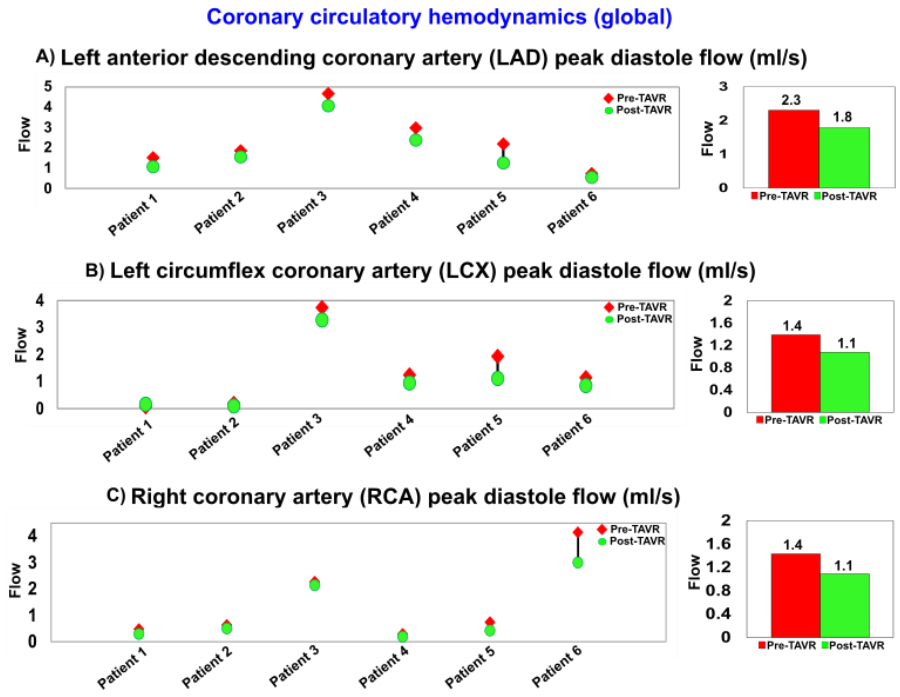


Figure 4-14. Changes in coronary circulatory hemodynamics in patients between baseline and 90-day post TAVR (N=6). (a) Left anterior descending coronary artery peak diastolic flow; (b) Left circumflex coronary artery peak diastolic flow; (c) Right coronary artery peak diastolic flow.

### 4.5.2 Sinus and neo-sinus washout after TAVR may be impaired in presence of paravalvular leak

TAVR can disturb the vortical structures inside the Valsalva sinuses, which are essential for the washout of sinus flow, assisting the smooth closure of the valve and providing flow to the coronary arteries during diastole [138–140]**.** While the sinus and neo-sinus washout efficacy of different transcatheter heart valves are still under debate [141]**,** our findings demonstrate that in addition to the TAVR influence on the aortic root morphology, PVL exacerbates the washout mechanism for the sinus and neo-sinus regions. We observed that the PVL jet substantially drains the flow from the sinus and neo-sinus regions, leading to pull the vortices out of the neo-sinus regions. Consequently, the vortices in the neo-sinus regions have less power to transfer the flow out of the leaflet roots. In addition, our results showed that NCC neo-sinus could be influenced the most by PVL, however, the LCC and RCC neo-sinuses irregular washout amplification depends on the severity of PVL and its location. The inefficient sinus and neo-sinus washout favors the thrombotic events after TAVR [125,138].

### 4.5.3 Subclinical leaflet thrombosis risk and hypo-attenuated leaflet thickening may be exacerbated in presence of paravalvular leak

The clinical understanding of leaflet thrombosis after TAVR is limited and little is known about the correlation of leaflet thrombosis with local hemodynamics [142,143]. Hypo-attenuating leaflet thickening (HALT) is a thin layer of thrombus covering the aortic side of the leaflets due to subclinical leaflet thrombosis [144]. Several risk factors have been reported for thrombosis after TAVR, including reduced valve durability, restricted leaflet motion and stroke [145–148]. In addition to the agreement between our findings and previous studies [143,147,149] regarding TAVR stent morphology effect on blood stasis, we found that the PVL exacerbates the blood stasis volume in the neo-sinus regions nonuniformly and asymmetrical with respect to the valve center. While it

has been reported that flow stasis risk is almost equal for LCC, RCC and NCC neo-sinuses [147], our results revealed that not only PVL increases the blood stasis and thrombus risk in neo-sinus regions globally, but also is different for each neo-sinus depending on the PVL severity and location. We observed that the NCC neo-sinus is more prone to be exposed to stagnant flow and is therefore at higher risk of leaflet thrombosis than LCC and RCC.

#### 4.5.3.1 PVL exacerbated aortic root and coronary arteries hemodynamics (local)

The jets emerging from the PVL orifice substantially alters the vortical structure in the aortic root, creating disturbed flow, leading to very high shear stress at the aortic root wall. Our results demonstrate that PVL amplifies non physiological flow patterns, and consequently increases TAWSS after TAVR, especially around the leakage location. The local abnormalities in WSS are thought to stimulate aneurysm formation or lead to progressive dilation of aortic root and ascending aorta [127,150].

On the other hand, our findings show that PVL leads to a significantly lower shear stress at the coronary walls due to the decreased blood supply during diastole after TAVR. This makes the coronary arteries susceptible to atherosclerosis, due to the low wall shear stress-induced inflammatory activation of endothelium mainly at the inner bend of curved arteries, ostia of branches and lateral walls of bifurcations [114,118]. Therefore, the decreased wall shear stress is associated with enlargement of plaque area, increased plaque eccentricity and reduced vessel area [114,151–153].

### 4.5.4 In all patients with PVL following TAVR: increased shear stress of aortic root and decreased shear stress of coronary arteries

For all patients in our study, PVL following TAVR exacerbated the shear stress during diastole (calculated through TAWSS) at aortic root and coronary arteries. TAWSS universally reduced in all branches of coronary arteries for all patients, and in contrast, significant increase of TAWSS was observed at the aortic root and around the leakage cite (Figure 15). While the correlation of decreased shear stress at the coronaries with increased risk of plaque progression has been shown previously [114,118], recent clinical studies also suggest that increased WSS at the aortic root could lead to ascending aorta dilation and rupture [154,155].

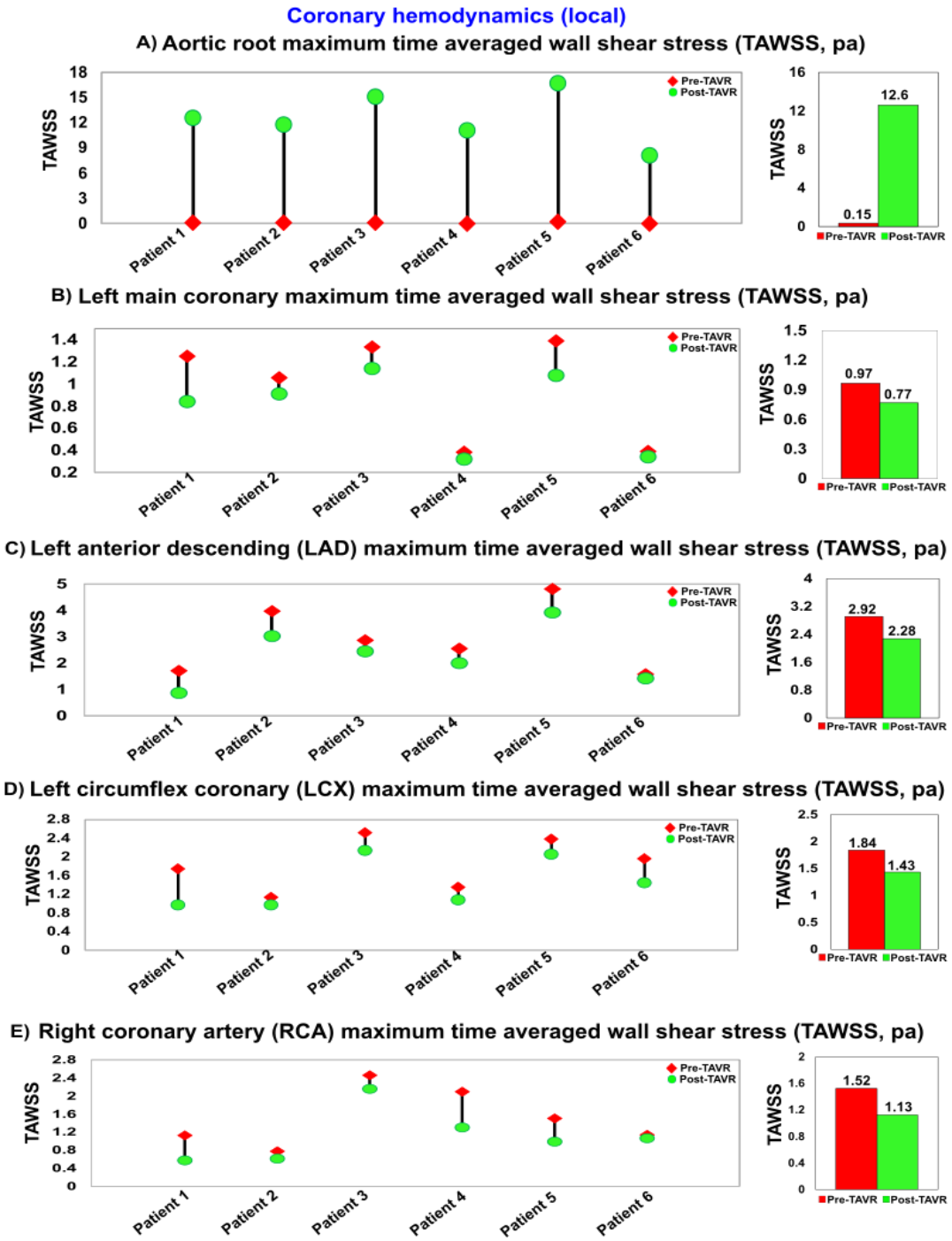


Figure 4-15. Changes in local hemodynamics in patients between baseline and 90-day post-TAVR (N=6). (a) Aortic root maximum TAWSS; (b) Left main coronary maximum TAWSS; (c) Left anterior descending coronary artery maximum TAWSS; (d) Left circumflex coronary artery maximum TAWSS; (e) Right coronary artery maximum TAWSS.

### 4.5.5 PVL exacerbated the left ventricular function and hemodynamics (global)

Our results showed that moderate to severe PVL increased the burden on the LV for all patients. Despite the LV pressure reduction and increase in aortic pressure post-TAVR, LV workload increased for all patients as a result of volume overload following PVL. Therefore, PVL following the malpositioning of TAVR causes an overloaded LV, resulting in faster cardiac tissue damage and LV dysfunction. In addition, an overloaded LV may lead to other valvular diseases such as mitral regurgitation or exacerbate the existed regurgitation for patients with mixed valvular disease who receive TAVR [11,17,19].

#### 4.5.5.1 PVL following TAVR is associated with increased LV workload post-TAVR despite the improvement of perfusion pressure and arterial compliance

As shown in Figure 16, our results showed that for all patients, the overall decrease in end diastolic pressure and increase of ascending aorta pressured lead to improved perfusion pressure. Moreover, systemic arterial compliance was improved for most of the patients (SAC recued only for one patient (figure 16)). However, PVL following TAVR lead to an increased workload for most patients (LV load reduced only for one patient (figure 16)). The increased workload contributes to progressive myocardial fibrosis and eventually myocardial dysfunction [156,157].

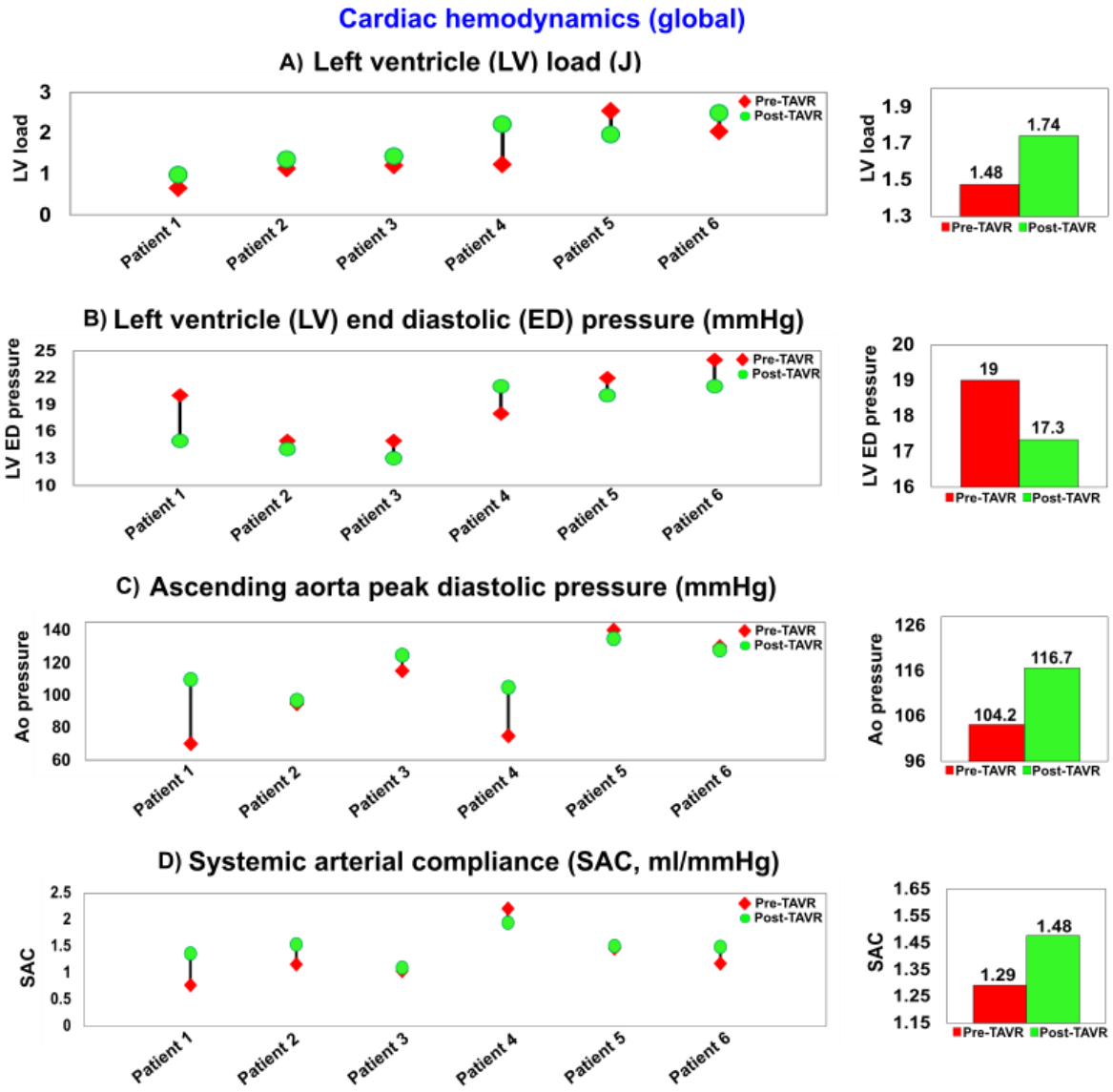


Figure 4-16. Changes in global hemodynamics (metrics of cardiac function & metrics of circulatory function) in patients between baseline and 90-day post TAVR (N=6). (a) Left ventricle workload; (b) Left ventricle end diastolic pressure; (c) Ascending aorta peak pressure in diastole; (d) Systemic arterial compliance.

### 4.5.6 Limitations of current clinical imaging modalities to capture coronary flow

Over the past decade, the use of medical imaging has drastically increased. In spite of amazing advancements in medical imaging, *medical imaging on its own cannot quantify local and global hemodynamics in coronaries*. As the need for patient-specific diagnostic methods continues to be studied, understanding the strengths and limitations of imaging modalities for coronaries is critical toward creating precise diagnostic tools:(1) *Computed tomography coronary angiography (CTCA)*: CTCA has a high spatial resolution allowing for visualization of coronary plaque and stenosis geometry [20,158]. However, CTCA suffers from temporal resolution challenges and requires the use of radiation, which is associated with health concerns especially in younger patients who need several scans throughout their lifetime [159]. CTCA does not provide any local and global hemodynamics measurements; (2) *4D flow magnetic resonance imaging (4D flow MRI):* 4D flow MRI is an emerging technology to allow local hemodynamic assessment in valvular, vascular and ventricular diseases. However, use of 4D flow MRI is limited in patients with implanted medical devices as they remain a major risk during the examination. Moreover, complete and thorough analysis of local hemodynamics in coronaries is not possible [20], due to the limited temporal resolution (4-D flow MRI has relatively high spatial resolution but lower temporal resolution (20 ms highest)). 4D flow MRI could not provide global hemodynamics; (3) *Doppler echocardiography (DE):* DE does not have the ability to quantify local hemodynamics through coronaries as well global hemodynamics [160] (4) *Ultrafast ultrasound:* Ultrafast ultrasound is an alternative option for DE, as it can image the heart at a rate of a thousand images per second [161]. Recently, ultrafast ultrasound has been combined with coronary Doppler imaging for quantification of local hemodynamics, which has aided in the diagnosis of PVR [161]. However, it has a limited imaging depth of 45 mm and cannot provide absolute quantification of flowrate for

adult patients with coronary disease [161] (5) *Intravascular Ultrasound (IVUS) & Optical Coherence Tomography (OCT):* IVUS and OCT provide information regarding severity of calcification, plaque morphology, and accurate vessel size [162,163]. However, none of them can provide local and global hemodynamics [164].

### 4.5.7 Limitations of current computational modeling to capture coronary flow

A clinically useful computational diagnostic framework should evaluate both global and local hemodynamics by quantifying three main requirements: (1) metrics of circulatory function (global hemodynamics), (2) metrics of cardiac function (global hemodynamics) and (3) Cardiac fluid dynamics (local hemodynamics) [16–19,31]. Few studies have been conducted to investigate the hemodynamic complexities after TAVR due to the presence of PVL using computational fluid dynamics (CFD) [165–170]. However, since: (1) patient-specific boundary conditions were not used; (2) hemodynamic validation was not performed; and (3) coronary arteries were excluded from the computational domain, the models developed in these studies did not satisfy the three requirements outlined in the Introduction [165–170]. In addition, several studies have recently used FSI as a promising tool for coronary arteries exclusively, since it allows consideration of the interactions of artery wall elastic behavior and blood flow mechanics, thus demonstrating its worth as a more realistic tool for numerical modelling of coronary arteries [42,50,63,68,78,79,107,171]. While only a few numbers of these studies [42] coupled lumped parameter model-based boundary conditions with FSI modelling, the lumped-parameter models were not patient-specific. Moreover, all of these studies have excluded the aortic root and sinus geometry from the computational domain [42,50,63,68,78,79,107,171], and most of these studies have used simplified and idealized geometries of

coronaries [73,76,78,79]. Exclusion of the aortic sinus at the upstream or using idealized geometry for coronaries could significantly affect the flow structure.

In this study, the requirements mentioned in the Introduction and Discussions have been examined in our study to evaluate the influence of TAVR on coronary arteries and the aortic root, when complications such as PVL or misalignment exist. In summary, our study showed that TAVR removed the aortic valve obstruction during ejection, reduced aortic valve pressure gradient and increased ejection fraction for all patients. However, considering the local flow parameters and cardiac function, all patients had adverse events after TAVR and are at high risk of heart failure. Therefore, despite the improvements of global circulatory function and clinical parameters, our results illustrating the details of local hemodynamics in these patients could partially explain how complications of TAVR could adversely increase the risk of thrombosis at aortic root and neo-sinus region of the valve leaflets, as well as plaque progression inside coronary arteries and subsequent long-term complications.

## 4.6 Limitations

This study was performed and validated on 6 patients who underwent TAVR in both pre- and post-intervention states (12 cases). Future studies must consider further validation of the computational framework in a large population of AS patients in both pre- and post-intervention states, however, our results in this study demonstrate the ability of the framework to track changes in both cardiac, and vascular states.

*Acknowledgments*

This work was supported by NSERC Discovery Grant (RGPIN-2017-05349). The funders had no role in study design, data collection and analysis, decision to publish, or preparation of the manuscript.

*Author contributions*

S.K. Conception and design, FSI development, data collection and analysis (FSI), interpretation of data and manuscript writing; L.G. Data analysis, algorithm development (LPM), manuscript writing; J.B. Interpretation of data and manuscript writing; A.M. Data analysis, interpretation of data, and supervision; Z.K.M. Conception and design, data analysis, algorithm development (LPM), interpretation of data, manuscript writing, critical revision, final approval of the manuscript and supervised this research. All authors read and approved the final manuscript.

*Data availability*

The codes and the optimization algorithm are available from the author upon request

## 4.7 References

1. Coylewright, M., Forrest, J. K., McCabe, J. M. & Nazif, T. M. TAVR in Low-Risk Patients. *J. Am. Coll. Cardiol.* **75**, 1208–1211 (2020).
2. Waksman, R. *et al.* Transcatheter Aortic Valve Replacement in Low-Risk Patients With Symptomatic Severe Aortic Stenosis. *J. Am. Coll. Cardiol.* **72**, 2095–2105 (2018).
3. Shah, S. *et al.* Characteristics and longer-term outcomes of paravalvular leak after aortic and mitral valve surgery. *J. Thorac. Cardiovasc. Surg.* **157**, 1785-1792.e1 (2019).
4. Fanous, E. J. *et al.* Paravalvular Leak Assessment: Challenges in Assessing Severity and Interventional Approaches. *Curr. Cardiol. Rep.* **22**, 166 (2020).
5. Pibarot, P., Hahn, R. T., Weissman, N. J. & Monaghan, M. J. Assessment of Paravalvular Regurgitation Following TAVR: A Proposal of Unifying Grading Scheme. *JACC Cardiovasc. Imaging* **8**, 340–360 (2015).
6. Forrestal, B. J. *et al.* Risk of Coronary Obstruction and Feasibility of Coronary Access After Repeat Transcatheter Aortic Valve Replacement With the Self-Expanding Evolut Valve. *Circ. Cardiovasc. Interv.* **13**, e009496 (2020).

7. Valvo, R., Costa, G. & Barbanti, M. How to Avoid Coronary Occlusion During TAVR Valve-in-Valve Procedures. *Front. Cardiovasc. Med.* **6**, 168 (2019).
8. Taylor, C. A. & Steinman, D. A. Image-Based Modeling of Blood Flow and Vessel Wall Dynamics: Applications, Methods and Future Directions. *Ann. Biomed. Eng.* **38**, 1188–1203 (2010).
9. Siebes, M. & Ventikos, Y. The Role of Biofluid Mechanics in the Assessment of Clinical and Pathological Observations. *Ann. Biomed. Eng.* **38**, 1216–1224 (2010).
10. Lieber, B. B., Siebes, M. & Yamaguchi, T. Correlation of Hemodynamic Events with Clinical and Pathological Observations. *Ann. Biomed. Eng.* **33**, 1695–1703 (2005).
11. Keshavarz-Motamed Zahra *et al.* Mixed Valvular Disease Following Transcatheter Aortic Valve Replacement: Quantification and Systematic Differentiation Using Clinical Measurements and Image-Based Patient-Specific In Silico Modeling. *J. Am. Heart Assoc.* **9**, e015063 (2020).
12. Pibarot, P. & Dumesnil, J. G. Assessment of aortic stenosis severity: check the valve but don't forget the arteries! *Heart* **93**, 780–782 (2007).
13. Ben-Assa, E. *et al.* Ventricular stroke work and vascular impedance refine the characterization of patients with aortic stenosis. *Sci. Transl. Med.* **11**, (2019).
14. Antonini-Canterin, F. *et al.* The Ventricular-Arterial Coupling: From Basic Pathophysiology to Clinical Application in the Echocardiography Laboratory. *J. Cardiovasc. Echography* **23**, 91–95 (2013).
15. Ikonomidis, I. *et al.* The role of ventricular–arterial coupling in cardiac disease and heart failure: assessment, clinical implications and therapeutic interventions. A consensus document of the European Society of Cardiology Working Group on Aorta & Peripheral Vascular Diseases, European Association of Cardiovascular Imaging, and Heart Failure Association. *Eur. J. Heart Fail.* **21**, 402–424 (2019).
16. Khodaei, S. *et al.* Towards a non-invasive computational diagnostic framework for personalized cardiology of transcatheter aortic valve replacement in interactions with complex valvular, ventricular and vascular disease. *Int. J. Mech. Sci.* **202–203**, 106506 (2021).
17. Khodaei, S. *et al.* Personalized intervention cardiology with transcatheter aortic valve replacement made possible with a non-invasive monitoring and diagnostic framework. *Sci. Rep.* **11**, 10888 (2021).
18. Baiocchi, M. *et al.* Effects of Choice of Medical Imaging Modalities on a Non-invasive Diagnostic and Monitoring Computational Framework for Patients With Complex Valvular, Vascular, and Ventricular Diseases Who Undergo Transcatheter Aortic Valve Replacement. *Front. Bioeng. Biotechnol.* **9**, 389 (2021).
19. Keshavarz-Motamed, Z. A diagnostic, monitoring, and predictive tool for patients with complex valvular, vascular and ventricular diseases. *Sci. Rep.* **10**, 6905 (2020).
20. Dewey, M. *et al.* Clinical quantitative cardiac imaging for the assessment of myocardial ischaemia. *Nat. Rev. Cardiol.* **17**, 427–450 (2020).
21. Johnston, C. M., Krafft, A. J., Russe, M. F. & Rog-Zielinska, E. A. A new look at the heart—novel imaging techniques. *Herzschrittmachertherapie Elektrophysiologie* **29**, 14–23 (2018).
22. Adamson, P. D. & Newby, D. E. Non-invasive imaging of the coronary arteries. *Eur. Heart J.* **40**, 2444–2454 (2019).

23. Garber, L., Khodaei, S. & Keshavarz-Motamed, Z. The Critical Role of Lumped Parameter Models in Patient-Specific Cardiovascular Simulations. *Arch. Comput. Methods Eng.* (2021) doi:10.1007/s11831-021-09685-5.
24. Weller, H. G., Tabor, G., Jasak, H. & Fureby, C. A tensorial approach to computational continuum mechanics using object-oriented techniques. *Comput. Phys.* **12**, 620–631 (1998).
25. Keshavarz-Motamed, Z., Garcia, J., Pibarot, P., Larose, E. & Kadem, L. Modeling the impact of concomitant aortic stenosis and coarctation of the aorta on left ventricular workload. *J. Biomech.* **44**, 2817–2825 (2011).
26. Keshavarz-Motamed, Z. *et al.* The role of aortic compliance in determination of coarctation severity: Lumped parameter modeling, in vitro study and clinical evaluation. *J. Biomech.* **48**, 4229–4237 (2015).
27. Keshavarz-Motamed, Z. *et al.* Effect of coarctation of the aorta and bicuspid aortic valve on flow dynamics and turbulence in the aorta using particle image velocimetry. *Exp. Fluids* **55**, 1696 (2014).
28. Keshavarz-Motamed, Z. *et al.* A new approach for the evaluation of the severity of coarctation of the aorta using Doppler velocity index and effective orifice area: In vitro validation and clinical implications. *J. Biomech.* **45**, 1239–1245 (2012).
29. Benevento, E., Djebbari, A., Keshavarz-Motamed, Z., Cecere, R. & Kadem, L. Hemodynamic Changes following Aortic Valve Bypass: A Mathematical Approach. *PLOS ONE* **10**, e0123000 (2015).
30. Keshavarz-Motamed, Z. *et al.* Elimination of transcoarctation pressure gradients has no impact on left ventricular function or aortic shear stress after intervention in patients with mild coarctation. *JACC Cardiovasc. Interv.* **9**, 1953–1965 (2016).
31. Sadeghi, R., Khodaei, S., Ganame, J. & Keshavarz-Motamed, Z. Towards non-invasive computational-mechanics and imaging-based diagnostic framework for personalized cardiology for coarctation. *Sci. Rep.* **10**, 9048 (2020).
32. Keshavarz-Motamed, Z. *et al.* Non-Invasive Determination of Left Ventricular Workload in Patients with Aortic Stenosis Using Magnetic Resonance Imaging and Doppler Echocardiography. *PLOS ONE* **9**, e86793 (2014).
33. Sadeghi, R., Gasner, N., Khodaei, S., Garcia, J. & Keshavarz-Motamed, Z. Impact of mixed valvular disease on coarctation hemodynamics using patient-specific lumped parameter and Lattice Boltzmann modeling. *Int. J. Mech. Sci.* **217**, 107038 (2022).
34. Sadeghi, R. *et al.* Reducing morbidity and mortality in patients with coarctation requires systematic differentiation of impacts of mixed valvular disease on coarctation hemodynamics. *J. Am. Heart Assoc.* **in press**,.
35. Kim, H. J. *et al.* Patient-Specific Modeling of Blood Flow and Pressure in Human Coronary Arteries. *Ann. Biomed. Eng.* **38**, 3195–3209 (2010).
36. Taylor, C. A., Fonte, T. A. & Min, J. K. Computational Fluid Dynamics Applied to Cardiac Computed Tomography for Noninvasive Quantification of Fractional Flow Reserve: Scientific Basis. *J. Am. Coll. Cardiol.* **61**, 2233–2241 (2013).
37. Yin, M., Yazdani, A. & Karniadakis, G. E. One-dimensional modeling of fractional flow reserve in coronary artery disease: Uncertainty quantification and Bayesian optimization. *Comput. Methods Appl. Mech. Eng.* **353**, 66–85 (2019).
38. Li, B., Wang, W., Mao, B. & Liu, Y. A Method to Personalize the Lumped Parameter Model of Coronary Artery. *Int. J. Comput. Methods* **16**, 1842004 (2019).

39. Sankaran, S. *et al.* Patient-Specific Multiscale Modeling of Blood Flow for Coronary Artery Bypass Graft Surgery. *Ann. Biomed. Eng.* **40**, 2228–2242 (2012).
40. Coogan, J. S., Humphrey, J. D. & Figueroa, C. A. Computational simulations of hemodynamic changes within thoracic, coronary, and cerebral arteries following early wall remodeling in response to distal aortic coarctation. *Biomech. Model. Mechanobiol.* **12**, 79–93 (2013).
41. Fossan, F. E. *et al.* Uncertainty Quantification and Sensitivity Analysis for Computational FFR Estimation in Stable Coronary Artery Disease. *Cardiovasc. Eng. Technol.* **9**, 597–622 (2018).
42. Tajeddini, F. *et al.* High precision invasive FFR, low-cost invasive iFR, or non-invasive CFR?: optimum assessment of coronary artery stenosis based on the patient-specific computational models. *Int. J. Numer. Methods Biomed. Eng.* **36**, e3382 (2020).
43. Koo, B.-K. *et al.* Diagnosis of ischemia-causing coronary stenoses by noninvasive fractional flow reserve computed from coronary computed tomographic angiograms. Results from the prospective multicenter DISCOVER-FLOW (Diagnosis of Ischemia-Causing Stenoses Obtained Via Noninvasive Fractional Flow Reserve) study. *J. Am. Coll. Cardiol.* **58**, 1989–1997 (2011).
44. Mantero, S., Pietrabissa, R. & Fumero, R. The coronary bed and its role in the cardiovascular system: a review and an introductory single-branch model. *J. Biomed. Eng.* **14**, 109–116 (1992).
45. Razminia, M. *et al.* Validation of a new formula for mean arterial pressure calculation: The new formula is superior to the standard formula. *Catheter. Cardiovasc. Interv.* **63**, 419–425 (2004).
46. Zhou, Y., Kassab, G. S. & Molloi, S. On the design of the coronary arterial tree: a generalization of Murray's law. *Phys. Med. Biol.* **44**, 2929–2945 (1999).
47. Garcia, D. *et al.* Impairment of coronary flow reserve in aortic stenosis. *J. Appl. Physiol.* **106**, 113–121 (2009).
48. Ofili, E. O. *et al.* Differential characterization of blood flow, velocity, and vascular resistance between proximal and distal normal epicardial human coronary arteries: analysis by intracoronary Doppler spectral flow velocity. *Am. Heart J.* **130**, 37–46 (1995).
49. Khodaei, S., Fatouraee, N. & Nabaei, M. Numerical simulation of mitral valve prolapse considering the effect of left ventricle. *Math. Biosci.* **285**, 75–80 (2017).
50. Pakravan, H. A., Saidi, M. S. & Firoozabadi, B. A multiscale approach for determining the morphology of endothelial cells at a coronary artery. *Int. J. Numer. Methods Biomed. Eng.* **33**, e2891 (2017).
51. Pandey, R., Kumar, M., Majdoubi, J., Rahimi-Gorji, M. & Srivastav, V. K. A review study on blood in human coronary artery: Numerical approach. *Comput. Methods Programs Biomed.* **187**, 105243 (2020).
52. Jasak, H. & Tuković, Z. *Automatic Mesh Motion for the Unstructured Finite Volume Method*. (2004).
53. Taki, A., Kermani, A., Ranjbarnavazi, S. M. & Pourmodheji, A. Chapter 4 - Overview of Different Medical Imaging Techniques for the Identification of Coronary Atherosclerotic Plaques. in *Computing and Visualization for Intravascular Imaging and Computer-Assisted Stenting* (eds. Balocco, S., Zuluaga, M. A., Zahnd, G., Lee, S.-L. & Demirci, S.) 79–106 (Academic Press, 2017). doi:10.1016/B978-0-12-811018-8.00004-7.

54. Guo, X. *et al.* Quantify patient-specific coronary material property and its impact on stress/strain calculations using in vivo IVUS data and 3D FSI models: a pilot study. *Biomech. Model. Mechanobiol.* **16**, 333–344 (2017).
55. Kural, M. H. *et al.* Planar biaxial characterization of diseased human coronary and carotid arteries for computational modeling. *J. Biomech.* **45**, 790–798 (2012).
56. Teng, Z., Tang, D., Zheng, J., Woodard, P. K. & Hoffman, A. H. An experimental study on the ultimate strength of the adventitia and media of human atherosclerotic carotid arteries in circumferential and axial directions. *J. Biomech.* **42**, 2535–2539 (2009).
57. Barrett, S. R. H., Sutcliffe, M. P. F., Howarth, S., Li, Z.-Y. & Gillard, J. H. Experimental measurement of the mechanical properties of carotid atherothrombotic plaque fibrous cap. *J. Biomech.* **42**, 1650–1655 (2009).
58. Pandit, A., Lu, X., Wang, C. & Kassab, G. S. Biaxial elastic material properties of porcine coronary media and adventitia. *Am. J. Physiol. Heart Circ. Physiol.* **288**, H2581-2587 (2005).
59. Holzapfel, G. A., Sommer, G. & Regitnig, P. Anisotropic mechanical properties of tissue components in human atherosclerotic plaques. *J. Biomech. Eng.* **126**, 657–665 (2004).
60. Holzapfel, G. A., Stadler, M. & Schulze-Bauer, C. A. J. A Layer-Specific Three-Dimensional Model for the Simulation of Balloon Angioplasty using Magnetic Resonance Imaging and Mechanical Testing. *Ann. Biomed. Eng.* **30**, 753–767 (2002).
61. Karimi, A., Navidbakhsh, M., Shojaei, A. & Faghihi, S. Measurement of the uniaxial mechanical properties of healthy and atherosclerotic human coronary arteries. *Mater. Sci. Eng. C* **33**, 2550–2554 (2013).
62. Carpenter, H. J., Gholipour, A., Ghayesh, M. H., Zander, A. C. & Psaltis, P. J. A review on the biomechanics of coronary arteries. *Int. J. Eng. Sci.* **147**, 103201 (2020).
63. Guo, X. *et al.* Combining IVUS and Optical Coherence Tomography for More Accurate Coronary Cap Thickness Quantification and Stress/Strain Calculations: A Patient-Specific Three-Dimensional Fluid-Structure Interaction Modeling Approach. *J. Biomech. Eng.* **140**, (2018).
64. Wang, L. *et al.* Fluid-structure interaction models based on patient-specific IVUS at baseline and follow-up for prediction of coronary plaque progression by morphological and biomechanical factors: A preliminary study. *J. Biomech.* **68**, 43–50 (2018).
65. Fan, R. *et al.* Human coronary plaque wall thickness correlated positively with flow shear stress and negatively with plaque wall stress: an IVUS-based fluid-structure interaction multi-patient study. *Biomed. Eng. OnLine* **13**, 32 (2014).
66. Gholipour, A., Ghayesh, M. H., Zander, A. C. & Psaltis, P. J. In vivo based biomechanics of right and left coronary arteries. *Int. J. Eng. Sci.* **154**, 103281 (2020).
67. Gholipour, A., Ghayesh, M. H., Zander, A. C. & Psaltis, P. J. In vivo based biomechanics of right and left coronary arteries. *Int. J. Eng. Sci.* **154**, 103281 (2020).
68. Guo, X. *et al.* Quantify patient-specific coronary material property and its impact on stress/strain calculations using in vivo IVUS data and 3D FSI models: a pilot study. *Biomech. Model. Mechanobiol.* **16**, 333–344 (2017).
69. Faroux, L. *et al.* Coronary Artery Disease and Transcatheter Aortic Valve Replacement: JACC State-of-the-Art Review. *J. Am. Coll. Cardiol.* **74**, 362–372 (2019).
70. Chieffo, A. *et al.* Routine Screening of Coronary Artery Disease With Computed Tomographic Coronary Angiography in Place of Invasive Coronary Angiography in

Patients Undergoing Transcatheter Aortic Valve Replacement. *Circ. Cardiovasc. Interv.* **8**, e002025 (2015).
71. Ahmad, Y. *et al.* Coronary Hemodynamics in Patients With Severe Aortic Stenosis and Coronary Artery Disease Undergoing Transcatheter Aortic Valve Replacement: Implications for Clinical Indices of Coronary Stenosis Severity. *JACC Cardiovasc. Interv.* **11**, 2019–2031 (2018).
72. Zhong, L. *et al.* Application of Patient-Specific Computational Fluid Dynamics in Coronary and Intra-Cardiac Flow Simulations: Challenges and Opportunities. *Front. Physiol.* **9**, (2018).
73. Pakravan, H. A., Saidi, M. S. & Firoozabadi, B. A multiscale approach for determining the morphology of endothelial cells at a coronary artery. *Int. J. Numer. Methods Biomed. Eng.* **33**, e2891 (2017).
74. Ahmadi, M. & Ansari, R. Computational simulation of an artery narrowed by plaque using 3D FSI method: influence of the plaque angle, non-Newtonian properties of the blood flow and the hyperelastic artery models. *Biomed. Phys. Eng. Express* **5**, 045037 (2019).
75. He, F., Hua, L. & Guo, T. Fluid–structure interaction analysis of hemodynamics in different degrees of stenoses considering microcirculation function. *Adv. Mech. Eng.* **13**, 1687814021989012 (2021).
76. Gholipour, A., Ghayesh, M. H. & Zander, A. Nonlinear biomechanics of bifurcated atherosclerotic coronary arteries. *Int. J. Eng. Sci.* **133**, 60–83 (2018).
77. Rotman, O. M., Zaretsky, U., Shitzer, A. & Einav, S. Pressure drop and arterial compliance – Two arterial parameters in one measurement. *J. Biomech.* **50**, 130–137 (2017).
78. Jahromi, R., Pakravan, H. A., Saidi, M. S. & Firoozabadi, B. Primary stenosis progression versus secondary stenosis formation in the left coronary bifurcation: A mechanical point of view. *Biocybern. Biomed. Eng.* **39**, 188–198 (2019).
79. Gholipour, A., Ghayesh, M. H., Zander, A. & Mahajan, R. Three-dimensional biomechanics of coronary arteries. *Int. J. Eng. Sci.* **130**, 93–114 (2018).
80. Kabinejadian, F. & Ghista, D. N. Compliant model of a coupled sequential coronary arterial bypass graft: Effects of vessel wall elasticity and non-Newtonian rheology on blood flow regime and hemodynamic parameters distribution. *Med. Eng. Phys.* **34**, 860–872 (2012).
81. Nejad, A. A., Talebi, Z., Cheraghali, D., Shahbani-Zahiri, A. & Norouzi, M. Pulsatile flow of non-Newtonian blood fluid inside stenosed arteries: Investigating the effects of viscoelastic and elastic walls, arteriosclerosis, and polycythemia diseases. *Comput. Methods Programs Biomed.* **154**, 109–122 (2018).
82. Gradus-Pizlo, I. *et al.* Left anterior descending coronary artery wall thickness measured by high-frequency transthoracic and epicardial echocardiography includes adventitia. *Am. J. Cardiol.* **91**, 27–32 (2003).
83. Maldonado, N. *et al.* A mechanistic analysis of the role of microcalcifications in atherosclerotic plaque stability: potential implications for plaque rupture. *Am. J. Physiol.-Heart Circ. Physiol.* **303**, H619–H628 (2012).
84. Cardoso, L., Kelly-Arnold, A., Maldonado, N., Laudier, D. & Weinbaum, S. Effect of tissue properties, shape and orientation of microcalcifications on vulnerable cap stability using different hyperelastic constitutive models. *J. Biomech.* **47**, 870–877 (2014).
85. Akyildiz, A. C. *et al.* Effects of intima stiffness and plaque morphology on peak cap stress. *Biomed. Eng. OnLine* **10**, 25 (2011).

86. Maldonado, N., Kelly-Arnold, A., Cardoso, L. & Weinbaum, S. The explosive growth of small voids in vulnerable cap rupture; cavitation and interfacial debonding. *J. Biomech.* **46**, 396–401 (2013).
87. Kohn, J. C., Lampi, M. C. & Reinhart-King, C. A. Age-related vascular stiffening: causes and consequences. *Front. Genet.* **6**, (2015).
88. Morović, S. & Demarin, V. Arterial Stiffness and Aging. in *Mind and Brain: Bridging Neurology and Psychiatry* (ed. Demarin, V.) 129–135 (Springer International Publishing, 2020). doi:10.1007/978-3-030-38606-1_11.
89. Wu Shouling *et al.* Aging, Arterial Stiffness, and Blood Pressure Association in Chinese Adults. *Hypertension* **73**, 893–899 (2019).
90. Tuković, Ž., Karač, A., Cardiff, P., Jasak, H. & Ivanković, A. OpenFOAM Finite Volume Solver for Fluid-Solid Interaction. *Trans. FAMENA* **42**, 1–31 (2018).
91. Cardiff, P. & Demirdžić, I. Thirty years of the finite volume method for solid mechanics. *ArXiv Prepr. ArXiv181002105* (2018).
92. Cardiff, P. *et al.* An open-source finite volume toolbox for solid mechanics and fluid-solid interaction simulations. *ArXiv180810736 Phys.* (2018).
93. Simo, J. C. & Hughes, T. J. R. *Computational Inelasticity*. (Springer Science & Business Media, 2006).
94. Lee, W., Cho, S. W., Allahwala, U. K. & Bhindi, R. Numerical study to identify the effect of fluid presence on the mechanical behavior of the stents during coronary stent expansion. *Comput. Methods Biomech. Biomed. Engin.* **23**, 744–754 (2020).
95. Frattolin, J., Zarandi, M. M., Pagiatakis, C., Bertrand, O. F. & Mongrain, R. Numerical study of stenotic side branch hemodynamics in true bifurcation lesions. *Comput. Biol. Med.* **57**, 130–138 (2015).
96. Rezaeimoghaddam, M. *et al.* Patient-Specific Hemodynamics of New Coronary Artery Bypass Configurations. *Cardiovasc. Eng. Technol.* **11**, 663–678 (2020).
97. Pinto, S. I. S., Romano, E., António, C. C., Sousa, L. C. & Castro, C. F. The impact of non-linear viscoelastic property of blood in right coronary arteries hemodynamics — A numerical implementation. *Int. J. Non-Linear Mech.* **123**, 103477 (2020).
98. Wellnhofer, E. *et al.* Flow simulation studies in coronary arteries—Impact of side-branches. *Atherosclerosis* **213**, 475–481 (2010).
99. Ghorbanniahassankiadeh, A., Marks, D. S. & LaDisa, J. F., Jr. Correlation of Computational Instantaneous Wave-Free Ratio With Fractional Flow Reserve for Intermediate Multivessel Coronary Disease. *J. Biomech. Eng.* **143**, (2021).
100. Wang, L. *et al.* IVUS-Based FSI Models for Human Coronary Plaque Progression Study: Components, Correlation and Predictive Analysis. *Ann. Biomed. Eng.* **43**, 107–121 (2015).
101. Chen, X., Zhuang, J., Huang, H. & Wu, Y. Fluid–structure interactions ( FSI ) based study of low-density lipoproteins ( LDL ) uptake in the left coronary artery. *Sci. Rep.* **11**, 4803 (2021).
102. Bahrami, S. & Norouzi, M. A numerical study on hemodynamics in the left coronary bifurcation with normal and hypertension conditions. *Biomech. Model. Mechanobiol.* **17**, 1785–1796 (2018).
103. Buradi, A. & Mahalingam, A. Impact of coronary tortuosity on the artery hemodynamics. *Biocybern. Biomed. Eng.* **40**, 126–147 (2020).

104. Eslami, P. *et al.* Validation of Wall Shear Stress Assessment in Non-invasive Coronary CTA versus Invasive Imaging: A Patient-Specific Computational Study. *Ann. Biomed. Eng.* **49**, 1151–1168 (2021).
105. Ribes, A. & Caremoli, C. Salomé platform component model for numerical simulation. in *31st Annual International Computer Software and Applications Conference (COMPSAC 2007)* vol. 2 553–564 (2007).
106. Tuković, Ž. & Jasak, H. A moving mesh finite volume interface tracking method for surface tension dominated interfacial fluid flow. *Comput. Fluids* **55**, 70–84 (2012).
107. Bukač, M., Čanić, S., Tambača, J. & Wang, Y. Fluid–structure interaction between pulsatile blood flow and a curved stented coronary artery on a beating heart: A four stent computational study. *Comput. Methods Appl. Mech. Eng.* **350**, 679–700 (2019).
108. Yushkevich, P. A. *et al.* User-guided 3D active contour segmentation of anatomical structures: significantly improved efficiency and reliability. *Neuroimage* **31**, 1116–1128 (2006).
109. Cardiff, P. & Demirdžić, I. Thirty Years of the Finite Volume Method for Solid Mechanics. *Arch. Comput. Methods Eng.* (2021) doi:10.1007/s11831-020-09523-0.
110. Degroote, J., Bathe, K.-J. & Vierendeels, J. Performance of a new partitioned procedure versus a monolithic procedure in fluid–structure interaction. *Comput. Struct.* **87**, 793–801 (2009).
111. Madukauwa-David, I. D. *et al.* An Evaluation of the Influence of Coronary Flow on Transcatheter Heart Valve Neo-Sinus Flow Stasis. *Ann. Biomed. Eng.* **48**, 169–180 (2020).
112. Singh-Gryzbon, S. *et al.* Influence of Patient-Specific Characteristics on Transcatheter Heart Valve Neo-Sinus Flow: An In Silico Study. *Ann. Biomed. Eng.* **48**, 2400–2411 (2020).
113. Raghav, V. *et al.* Three-dimensional extent of flow stagnation in transcatheter heart valves. *J. R. Soc. Interface* **16**, 20190063 (2019).
114. Gijsen, F. *et al.* Expert recommendations on the assessment of wall shear stress in human coronary arteries: existing methodologies, technical considerations, and clinical applications. *Eur. Heart J.* **40**, 3421–3433 (2019).
115. Dolan, J. M., Kolega, J. & Meng, H. High wall shear stress and spatial gradients in vascular pathology: a review. *Ann. Biomed. Eng.* **41**, 1411–1427 (2013).
116. Ferrara, A. & Pandolfi, A. Numerical modelling of fracture in human arteries. *Comput. Methods Biomech. Biomed. Engin.* **11**, 553–567 (2008).
117. Liu, X. *et al.* Prediction of coronary plaque progression using biomechanical factors and vascular characteristics based on computed tomography angiography. *Comput. Assist. Surg.* **22**, 286–294 (2017).
118. Cameron, J. N. *et al.* Exploring the relationship between biomechanical stresses and coronary atherosclerosis. *Atherosclerosis* **302**, 43–51 (2020).
119. Costopoulos, C. *et al.* Impact of combined plaque structural stress and wall shear stress on coronary plaque progression, regression, and changes in composition. *Eur. Heart J.* **40**, 1411–1422 (2019).
120. Bahlmann, E. *et al.* Low systemic arterial compliance is associated with increased cardiovascular morbidity and mortality in aortic valve stenosis. *Heart* **105**, 1507–1514 (2019).
121. McConkey, H. Z. R. *et al.* Coronary Microcirculation in Aortic Stenosis. *Circ. Cardiovasc. Interv.* **12**, e007547.

122. Ben-Dor, I. *et al.* Coronary blood flow in patients with severe aortic stenosis before and after transcatheter aortic valve implantation. *Am. J. Cardiol.* **114**, 1264–1268 (2014).
123. Scarsini, R. *et al.* Long-term variations of FFR and iFR after transcatheter aortic valve implantation. *Int. J. Cardiol.* **317**, 37–41 (2020).
124. Calderan, J., Mao, W., Sirois, E. & Sun, W. Development of an In Vitro Model to Characterize the Effects of Transcatheter Aortic Valve on Coronary Artery Flow. *Artif. Organs* **40**, 612–619 (2016).
125. Pott, D. *et al.* Hemodynamics inside the neo- and native sinus after TAVR: Effects of implant depth and cardiac output on flow field and coronary flow. *Artif. Organs* **45**, 68–78 (2021).
126. Iwata, S., Inano, C. & Ozaki, M. Perpendicular and turbulent flow after aortic valve replacement: paravalvular or transvalvular leakage? – a case report. *J. Cardiothorac. Surg.* **15**, 19 (2020).
127. Farag, E. S. *et al.* Transcatheter aortic valve replacement alters ascending aortic blood flow and wall shear stress patterns: A 4D flow MRI comparison with age-matched, elderly controls. *Eur. Radiol.* **29**, 1444–1451 (2019).
128. Crea, F., Camici, P. G. & Bairey Merz, C. N. Coronary microvascular dysfunction: an update. *Eur. Heart J.* **35**, 1101–1111 (2014).
129. Dunn, R. B. & Griggs, D. M. Ventricular filling pressure as a determinant of coronary blood flow during ischemia. *Am. J. Physiol.* **244**, H429-436 (1983).
130. Pibarot, P. & Dumesnil, J. G. Low-flow, low-gradient aortic stenosis with normal and depressed left ventricular ejection fraction. *J. Am. Coll. Cardiol.* **60**, 1845–1853 (2012).
131. Tiwari, N. & Madan, N. Hypertension and transcatheter aortic valve replacement: parallel or series? *Integr. Blood Press. Control* **11**, 81–91 (2018).
132. Nai Fovino, L. *et al.* Coronary Angiography After Transcatheter Aortic Valve Replacement (TAVR) to Evaluate the Risk of Coronary Access Impairment After TAVR-in-TAVR. *J. Am. Heart Assoc.* **9**, e016446 (2020).
133. Oh, J.-H. *et al.* Distance between valvular leaflet and coronary ostium predicting risk of coronary obstruction during TAVR. *IJC Heart Vasc.* **37**, 100917 (2021).
134. Heitkemper, M. *et al.* Simple 2-dimensional anatomic model to predict the risk of coronary obstruction during transcatheter aortic valve replacement. *J. Thorac. Cardiovasc. Surg.* **162**, 1075-1083.e1 (2021).
135. Lester, S. J., Heilbron, B., Gin, K., Dodek, A. & Jue, J. The natural history and rate of progression of aortic stenosis. *Chest* **113**, 1109–1114 (1998).
136. Vesey, A. T., Esson, G., Chin, C., Dweck, M. & Newby, D. Detection of cardiac fibrosis and cell death in patients with aortic stenosis. *J. Am. Coll. Cardiol.* **65**, A1190–A1190 (2015).
137. Dweck, M. R. *et al.* Midwall fibrosis is an independent predictor of mortality in patients with aortic stenosis. *J. Am. Coll. Cardiol.* **58**, 1271–1279 (2011).
138. Toninato, R., Salmon, J., Susin, F. M., Ducci, A. & Burriesci, G. Physiological vortices in the sinuses of Valsalva: An in vitro approach for bio-prosthetic valves. *J. Biomech.* **49**, 2635–2643 (2016).
139. Moore, B. L. Influence of anatomic valve conditions and coronary flow on aortic sinus hemodynamics. (2014).
140. Kaneko, T. Flow in the Aortic Sinus After Valve-in-Valve TAVR. *JACC Cardiovasc. Interv.* **14**, 2667–2669 (2021).

141. Hatoum, H. *et al.* Neosinus and Sinus Flow After Self-Expanding and Balloon-Expandable Transcatheter Aortic Valve Replacement. *JACC Cardiovasc. Interv.* **14**, 2657–2666 (2021).
142. Yanagisawa Ryo *et al.* Early and Late Leaflet Thrombosis After Transcatheter Aortic Valve Replacement. *Circ. Cardiovasc. Interv.* **12**, e007349 (2019).
143. Midha, P. A. *et al.* The Fluid Mechanics of Transcatheter Heart Valve Leaflet Thrombosis in the Neosinus. *Circulation* **136**, 1598–1609 (2017).
144. Rosseel, L., De Backer, O. & Søndergaard, L. Clinical valve thrombosis and subclinical leaflet thrombosis in transcatheter aortic heart valves: clinical manifestations, diagnosis, and treatment. *Precis. Clin. Med.* **1**, 111–117 (2018).
145. Jose, J. *et al.* Clinical Bioprosthetic Heart Valve Thrombosis After Transcatheter Aortic Valve Replacement. *JACC Cardiovasc. Interv.* **10**, 686–697 (2017).
146. Sellers, S. L. *et al.* Transcatheter Aortic Heart Valves. *JACC Cardiovasc. Imaging* **12**, 135–145 (2019).
147. Trusty, P. M. *et al.* The role of flow stasis in transcatheter aortic valve leaflet thrombosis. *J. Thorac. Cardiovasc. Surg.* (2020) doi:10.1016/j.jtcvs.2020.10.139.
148. Brown, R. A. *et al.* Subclinical Leaflet Thrombosis Post Transcatheter Aortic Valve Replacement – An Update for 2020. *Struct. Heart* **4**, 369–381 (2020).
149. Raghav, V. *et al.* Three-dimensional extent of flow stagnation in transcatheter heart valves. *J. R. Soc. Interface* **16**, 20190063 (2019).
150. Trauzeddel, R. F. *et al.* Blood flow characteristics in the ascending aorta after TAVI compared to surgical aortic valve replacement. *Int. J. Cardiovasc. Imaging* **32**, 461–467 (2016).
151. Samady, H. *et al.* Coronary Artery Wall Shear Stress Is Associated With Progression and Transformation of Atherosclerotic Plaque and Arterial Remodeling in Patients With Coronary Artery Disease. *Circulation* **124**, 779–788 (2011).
152. Eshtehardi, P. *et al.* Association of Coronary Wall Shear Stress With Atherosclerotic Plaque Burden, Composition, and Distribution in Patients With Coronary Artery Disease. *J. Am. Heart Assoc.* **1**, e002543.
153. Papafaklis, M. I. *et al.* Effect of the local hemodynamic environment on the de novo development and progression of eccentric coronary atherosclerosis in humans: Insights from PREDICTION. *Atherosclerosis* **240**, 205–211 (2015).
154. Soulat, G. *et al.* Association of Regional Wall Shear Stress and Progressive Ascending Aorta Dilation in Bicuspid Aortic Valve. *JACC Cardiovasc. Imaging* **15**, 33–42 (2022).
155. Guala, A. *et al.* Wall Shear Stress Predicts Aortic Dilation in Patients With Bicuspid Aortic Valve. *JACC Cardiovasc. Imaging* **15**, 46–56 (2022).
156. Rader, F., Sachdev, E., Arsanjani, R. & Siegel, R. J. Left Ventricular Hypertrophy in Valvular Aortic Stenosis: Mechanisms and Clinical Implications. *Am. J. Med.* **128**, 344–352 (2015).
157. Kampaktsis, P. N. *et al.* Impact of paravalvular leak on left ventricular remodeling and global longitudinal strain 1 year after transcatheter aortic valve replacement. *Future Cardiol.* **17**, 337–345 (2021).
158. Fairbairn, T. A. *et al.* Sex Differences in Coronary Computed Tomography Angiography–Derived Fractional Flow Reserve. *JACC Cardiovasc. Imaging* **13**, 2576–2587 (2020).
159. Henein, M. Y., Vancheri, S., Bajraktari, G. & Vancheri, F. Coronary Atherosclerosis Imaging. *Diagnostics* **10**, 65 (2020).

160. Zagatina, A. *et al.* Role of Coronary Flow Velocity in Predicting Adverse Outcome in Clinical Practice. *Ultrasound Med. Biol.* **44**, 1402–1410 (2018).
161. Maresca, D. *et al.* Noninvasive Imaging of the Coronary Vasculature Using Ultrafast Ultrasound. *JACC Cardiovasc. Imaging* **11**, 798–808 (2018).
162. Shammas, N. W. *et al.* The role of precise imaging with intravascular ultrasound in coronary and peripheral interventions. *Vasc. Health Risk Manag.* **15**, 283–290 (2019).
163. Lee, C. H. & Hur, S.-H. Optimization of Percutaneous Coronary Intervention Using Optical Coherence Tomography. *Korean Circ. J.* **49**, 771–793 (2019).
164. Darmoch, F. *et al.* Intravascular Ultrasound Imaging–Guided Versus Coronary Angiography–Guided Percutaneous Coronary Intervention: A Systematic Review and Meta-Analysis. *J. Am. Heart Assoc.* **9**, e013678 (2020).
165. Mao, W., Wang, Q., Kodali, S. & Sun, W. Numerical Parametric Study of Paravalvular Leak Following a Transcatheter Aortic Valve Deployment Into a Patient-Specific Aortic Root. *J. Biomech. Eng.* **140**, 1010071–10100711 (2018).
166. Rocatello, G. *et al.* The Impact of Size and Position of a Mechanical Expandable Transcatheter Aortic Valve: Novel Insights Through Computational Modelling and Simulation. *J Cardiovasc. Transl. Res.* **12**, 435–446 (2019).
167. Luraghi, G. *et al.* On the Modeling of Patient-Specific Transcatheter Aortic Valve Replacement: A Fluid–Structure Interaction Approach. *Cardiovasc. Eng. Technol.* **10**, 437–455 (2019).
168. Lavon, K. *et al.* Biomechanical modeling of transcatheter aortic valve replacement in a stenotic bicuspid aortic valve: deployments and paravalvular leakage. *Med. Biol. Eng. Comput.* **57**, 2129–2143 (2019).
169. de Jaegere, P. *et al.* Patient-Specific Computer Modeling to Predict Aortic Regurgitation After Transcatheter Aortic Valve Replacement. *JACC Cardiovasc. Interv.* **9**, 508–512 (2016).
170. Schultz, C. *et al.* Patient-specific image-based computer simulation for theprediction of valve morphology and calcium displacement after TAVI with the Medtronic CoreValve and the Edwards SAPIEN valve. *EuroIntervention J. Eur. Collab. Work. Group Interv. Cardiol. Eur. Soc. Cardiol.* **11**, 1044–1052 (2016).
171. Wang, L. *et al.* Optical Coherence Tomography-Based Patient-Specific Residual Multi-Thrombus Coronary Plaque Models With Fluid–Structure Interaction for Better Treatment Decisions: A Biomechanical Modeling Case Study. *J. Biomech. Eng.* **143**, (2021).
172. Tanné, D., Kadem, L., Rieu, R. & Pibarot, P. Hemodynamic impact of mitral prosthesis-patient mismatch on pulmonary hypertension: an in silico study. *J. Appl. Physiol. Bethesda Md 1985* **105**, 1916–1926 (2008).
173. Stergiopulos, N., Meister, J. J. & Westerhof, N. Determinants of stroke volume and systolic and diastolic aortic pressure. *Am. J. Physiol.-Heart Circ. Physiol.* **270**, H2050–H2059 (1996).
174. Mynard, J. P., Davidson, M. R., Penny, D. J. & Smolich, J. J. A simple, versatile valve model for use in lumped parameter and one-dimensional cardiovascular models. *Int. J. Numer. Methods Biomed. Eng.* **28**, 626–641 (2012).

# Chapter 5: Reducing long-term mortality post-TAVR requires systemic differentiation of patient-specific coronary hemodynamics

Seyedvahid Khodaei[1], Louis Garber[2], Mohamed Adbelkhalek[2], Ali Emadi [1,3], Zahra Keshavarz-Motamed*[1,2,4]

1. Department of Mechanical Engineering, McMaster University, Hamilton, ON, Canada
2. School of Biomedical Engineering, McMaster University, Hamilton, ON, Canada
3. Department of Electrical and Computer Engineering, McMaster University, Hamilton, ON, Canada
4. School of Computational Science and Engineering, McMaster University, Hamilton, ON, Canada

*This paper was submitted and is under review.*

* Correspondence author

## 5.1 Abstract

**Background**: Despite the proven benefits of transcatheter aortic valve replacement (TAVR) and its recent expansion towards the whole risk spectrum, coronary artery disease (CAD) is present in more than half of TAVR candidates. Many previous studies do not focus on the longer-term impact of TAVR on coronary arteries and hemodynamic changes to the circulatory system in response to the anatomical changes caused by TAVR are not fully understood.

**Objectives**: We used computational modelling to examine TAVR effect on coronary hemodynamics non-invasively.

**Method**: We developed a multiscale computational framework based on a patient-specific lumped-parameter algorithm and a 3-D fluid-solid interaction model to quantify metrics of global circulatory function, metrics of global cardiac function and local cardiac fluid dynamics of aortic root and coronary arteries.

**Results**: Based on our findings, TAVR might have adverse impact on coronary hemodynamics due to the lack of sufficient coronary blood flow during diastole phase (e.g., maximum coronary flow rate reduced by 8.98%, 16.83% and 22.73% in the left anterior descending (LAD), left circumflex coronary artery and right coronary artery (RCA) respectively (N=31)). Moreover, TAVR may increase the left ventricle (LV) load (e.g., LV load increased by 2.52 % (N=31)) and decrease the coronary wall shear stress (e.g., maximum time averaged wall shear stress reduced by 9.47%, 7.75%, 6.94%, 8.07% and 6.28% for bifurcation, LMCA, LAD, LCX and RCA branches respectively).

**Conclusion**: This study demonstrated that a personalized image-based computational framework can provide crucial insights into underlying mechanics of TAVR and CAD interactions and assist in treatment planning and longer-term patient risk stratification in TAVR population.

**Keywords:** Transcatheter aortic valve replacement, Coronary hemodynamics, Local fluid dynamics, Global hemodynamics, Cardiac fluid dynamics, Patient-specific lumped parameter model

## Abbreviations

| | |
|---|---|
| AS | Aortic stenosis |
| TAVR | Transcatheter aortic valve replacement |
| CT | Computed tomography |
| LCC | Left coronary cusp |
| RCC | Right coronary cusp |
| LMCA | Left main coronary artery |
| LAD | Left anterior descending |
| LCX | Left circumflex |
| RCA | Right coronary artery |
| LPM | Lumped parameter model |
| FSI | Fluid-solid interaction |

## 5.2 Introduction

Transcatheter aortic valve replacement (TAVR) is becoming popular for patients who are of a high, intermediate, or low risk, indicating that it may become the superior treatment modality for aortic stenosis (AS) for the whole risk spectrum and younger populations [1–4]. While coronary artery disease (CAD) is present in up to two third of the TAVR population [5], CAD severity assessment is challenging and the decision for coronary lesion revascularization is currently mainly based on invasive procedures [6,7]. However, invasive coronary access is limited in significant proportion of patients who undergo TAVR, due to anatomical restrictions such as overlap between transcatheter heart valve and the coronary ostia [8]. Consequently, this presents a dilemma among patients with post-TAVR complications, regarding the relative contribution of CAD versus the valve insufficiencies on long term symptoms and prognosis, and more studies are needed on how TAVR affect coronary hemodynamics [5].

After TAVR, immediate increase in coronary flow is expected as a result of reduced afterload and subendocardial compression. However, there is uncertainty regarding coronary flow reserve (CFR) post-TAVR, with some studies suggesting flow recovery instantly after TAVR [9] and others suggesting that it is a long-term event [10,11]. Currently, the decision for revascularisation of CAD after TAVR is being made readily through methods that solely focus on obstructed coronary arteries, such as angiography assessment, fractional flow reserve (FFR) and instantaneous wave free ratio (iFR)[5]. However, the optimal method and timing of the intervention remain undefined especially in patients with multivessel CAD and some studies suggest that incomplete revascularization is associated with increased cardiovascular events [12–14]. In addition, areas of contention and uncertainty remain for the patients with signs of ischemic heart disease because of reduced coronary flow and with no obstructed coronary arteries [15,16]. Therefore, due to the

complexity of dual pathology (AS and CAD) and the effect of the TAVR procedure on coronary hemodynamics, it is recommended that the decision for revascularization must be made on a case-by-case basis until further trial data [5].

Computational simulations are a powerful tool for accurate and early diagnosis of long-term hemodynamic complications that are difficult or impossible to infer in clinical practice. Some technical challenges and concerns of the effect of TAVR on both short term and long term coronary hemodynamics can be predicted through numerical simulation [5,16]. However, such simulations should be personalized for each patient and be able to capture the effect of global and local hemodynamics on a case-by-case basis to provide a clinically meaningful tool based on critical patient anatomy and valve implantation parameters [17,18].

In this study, we propose a novel strategy to quantitatively investigate the impact of TAVR on coronary artery hemodynamics. We developed a personalized lumped parameter model and computational fluid dynamics framework based on patient-specific hemodynamic and anatomical parameters to examine the effect of factors such as valve to coronary distance, aortic root diameter, coronary ostium height and commissural misalignment on coronary artery hemodynamics. We showed that coronary flow improvement depends on post-TAVR aortic root remodeling and ventricular-vascular coupling hemodynamics. We quantified the effect of TAVR on coronary flow and cardiac function and investigated the correlation of hemodynamic parameters with the metrics currently used in clinical practice. We used the clinically measured hemodynamic metrics of 31 patients in both pre and post TAVR conditions to provide novel hemodynamic analysis and interpretations of clinical data.

## 5.3 Methods

### 5.3.1 Study Population

31 patients with severe AS who received TAVR (Table 1: patients characteristics) were retrospectively selected from anonymized databases between 2020 and 2022 at the Hamilton General Hospital in Hamilton, Ontario, Canada. Patients' selections were done by operators blinded to the study objectives. The protocols were reviewed and approved by the Hamilton Integrated Research Ethics Board (HiREB) and informed consents were collected from all participants. Measurements were obtained according to guidelines including American Heart Association, American College of Cardiology and American Society of Echocardiography. Data was collected at both pre-procedure and post procedure time points. Results were expressed as mean ± standard deviations (SD).

### 5.3.2 Doppler echocardiography

Doppler echocardiography data included the measurements and reports that were collected pre-procedure and at post-procedure. Echocardiograms and reports were reviewed and analyzed in a blinded fashion by senior cardiologists using OsiriX imaging software (OsiriX version 8.0.2; Pixmeo, Bernex, Switzerland).

Table 5-1

| | **C3VD Patients (n=31, mean ± SD)** |
|---|---|
| **Patient description** | |
| Mean age (years) | 77.8± 7.78 |
| Gender | (Male: 17; Female: 14) |
| Mean weight (kg) | 88± 29.8 |
| Mean height (cm) | 167.4 ± 11.11 |
| STS score (%) | 2.8 ± 1.84 |
| Body surface area (BSA) | 1.91 ± 0.27 |

| | |
|---|---|
| Smoker | n=6 |
| Prior atrial fibrillation (AF) | n=4 |
| Previous stroke | n=3 |
| **Arterial hemodynamics** | |
| Systolic arterial pressure (mmHg) | Pre-TAVR: 131 ± 21.35; Post-TAVR: 138.7 ± 23.5 |
| Diastolic arterial pressure (mmHg) | Pre-TAVR: 69.7 ± 9.8; Post-TAVR: 72 ± 16.48 |
| Coronary artery disease (CAD) | n=14 |
| Hypertension (HTN) | n=24 |
| Dyslipidemia | n=14 |
| Prior coronary angiogram | n=5 |
| Coronary angiogram during TAVR | n=13 |
| Prior percutaneous coronary intervention (PCI) | n=4 |
| Hb level (g/dL) (Day of procedure) | 132 ± 17 |
| Creatinine (mg/dL) (Day of procedure) | 82.71 ± 19.25 |
| Chronic kidney disease (CKD) | n=4 |
| Chronic obstructive pulmonary disease (COPD) | n=4 |
| Anticoagulation | n=5 |
| **Aortic valve hemodynamics** | |
| Stenotic aortic valve area ($cm^2$) | 0.81 ± 0.19 |
| Stenotic aortic valve area index | 0.425 ± 0.09 |
| Stenotic aortic valve type | Tricuspid: 25; Bicuspid: 6 |
| Prosthetic size (mm) | 25.1 ± 2.4 |
| Prosthetic type | |
| • Edwards SAPIEN 3 | n= 31 |
| Maximum aortic valve pressure gradient (mmHg) | Pre-TAVR: 81.37 ± 21.85; Post-TAVR: 28.9 ± 14.9 |
| Mean aortic valve pressure gradient (mmHg) | Pre-TAVR: 46 ± 13.2; Post-TAVR: 16.6 ± 8.18 |
| Maximum aortic valve velocity (m/s) | Pre-TAVR: 4.47± 0.59; Post-TAVR: 2.62 ± 0.65 |
| Doppler velocity index (DVI) | Pre-TAVR: 0.25 ± 0.05; Post-TAVR: 0.48 ± 0.11 |
| Pre-dilation | n= 5 |
| Post-dilation | n= 4 |
| **Left ventricle and atrial hemodynamics** | |
| Ejection fraction (%) | Pre-TAVR: 56.8 ± 13; Post-TAVR: 59.8± 13 |
| Heart rate (bpm) | Pre-TAVR: 71 ±14; Post-TAVR: 72 ± 13 |
| LV mass index | Pre-TAVR: 94.9 ± 18.55; Post-TAVR: 93.4 ± 26.2 |
| New onset atrial fibrillation (AF) | n= 4 |
| New Left bundle branch block (LBBB) | n= 6 |
| | |
| | |

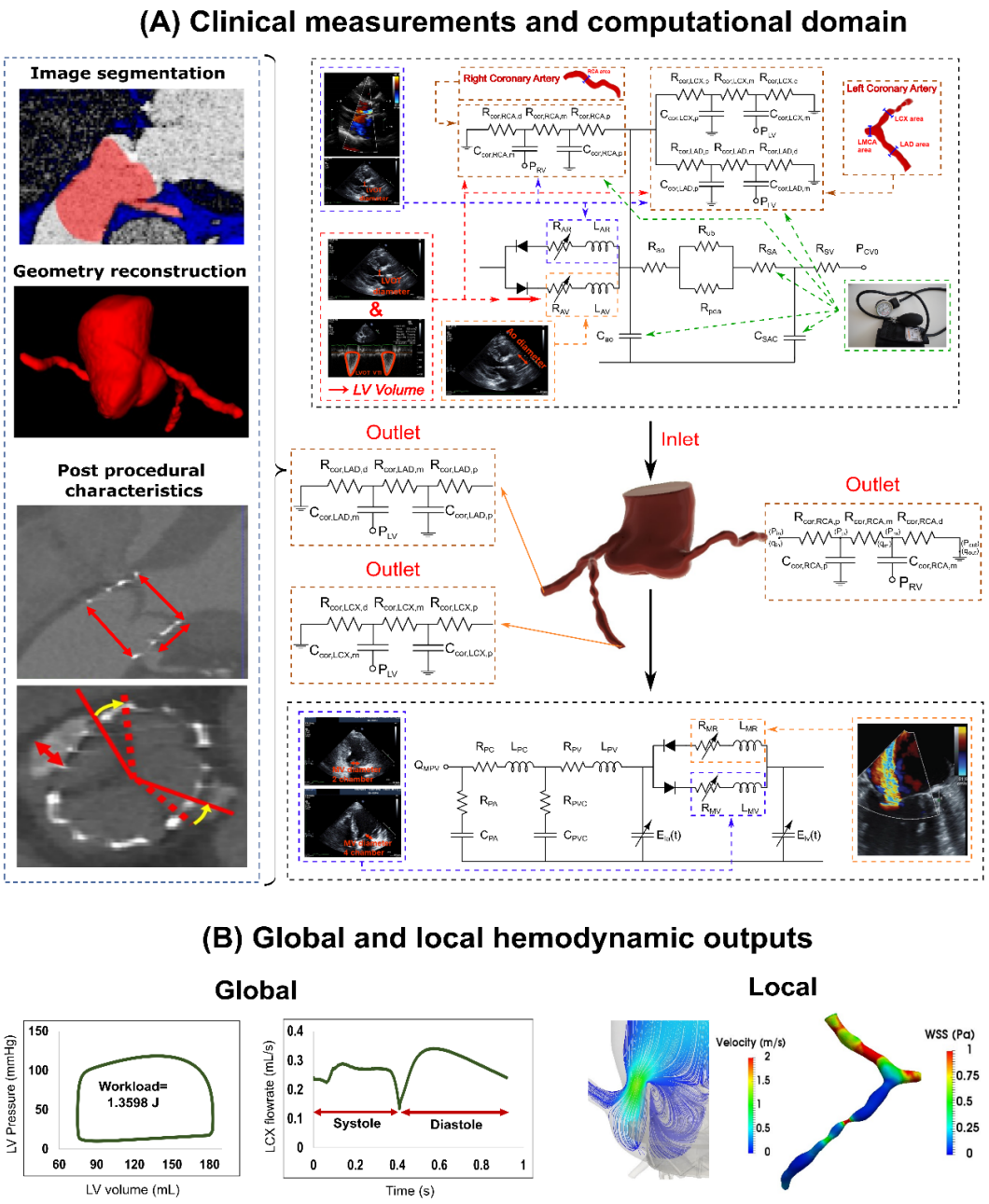


Figure 5-1. (A) Schematic of computational domain. Electrical and anatomical schematic diagrams of the lumped parameter modeling coupled to the fluid domain. This model includes the following sub-models. (1) ascending aorta, (2) left ventricle, (3) left anterior descending coronary artery, (4) left circumflex coronary artery, and (5) right coronary artery. Abbreviations are the same as in Table 2. Simulation domain and FSI modeling. Patient-specific LPM simulating the function of the left side of the heart and coronary arteries was coupled to the inlet and outlets. Reconstructed Geometries in Patients with AS and TAVR. (B) Sample results of local and global hemodynamic outputs generated with the non-invasive computational framework

### 5.3.3 Geometry reconstruction

3D geometries of the aortic root and coronary arteries including annulus, sinotubular junction, ascending aorta, sinus of Valsalva, aortic valve, proximal left main coronary artery, left circumflex coronary artery, left anterior descending coronary artery and right coronary artery were reconstructed in both pre- and post-TAVR from segmented computed tomography images of patients using ITK-SNAP (version 3.8.0-BETA) (Figure 1). The reconstructed models were based on CT images during diastole (75% cardiac cycle). A smoothing procedure was used for the surfaces to overcome the computational challenges. The volume difference due to smoothing was less than 3% in all patients.

### 5.3.4 Statistical analysis

Appropriate statistical tests were performed using Jamovi (v.1.8.1.0). For the variables presented in performed (Fig. 7; Table. 1) Continuous variables were expressed as mean±SD, categorical variables were expressed as counts. Correlations, and comparisons between the variables was performed using Pearson's r, Spearman's rho. Paired samples t-tests were performed on pre-post TAVR variables using Mann-Whitney U or Wilcoxon W depending on normality. Statistical significance was considered when the p-value was less than 0.05. Detailed information regarding normalization of relevant parameters is outlined in supplemental results.

### 5.3.5 Numerical study

The innovative imaged-based computational fluid dynamics framework was developed (Figure 1) using the 3D FSI and lumped parameter modeling to quantify both the local and global hemodynamics in patients with AS and TAVR (pre-TAVR and post-TAVR). This framework uses limited non-invasive input parameters from DE, CT, and sphygmomanometer.

### 5.3.6 Global hemodynamics

We have previously developed a non-invasive diagnostic computational-mechanics framework for complex valvular, vascular and ventricular disease (C3V-LPM), described in detail elsewhere [19]. In this study, the C3V-LPM was developed (appendix) to a greater extent to compute local and global hemodynamics in patients with mixed valvular, vascular, mini-vascular and ventricle diseases (called C3VM-LPM for simplicity) (Figure 1, Table 2). The precedingly developed framework (C3V-LPM) was validated against cardiac catheterization data with a considerable inter- and intra-patient variability with a broad range of disease in a population of forty-nine patients (with AS) [19]. Moreover, some of the sub-models of the patient-specific lumped parameter algorithm have been used previously [20–26] , with validation against in vivo cardiac catheterization (N=34) [27,28] in patients with vascular diseases, in vivo MRI data (N=57) [29] in patients with AS, and in vivo MRI data (N=23) [30,31] in patients with mixed valvular diseases and coarctation.

### 5.3.7 Local hemodynamics (blood flow dynamics)

A computational fluid dynamics and lumped parameter modeling framework was developed to compute 3D blood flow dynamics in all main coronary artery branches (proximal left main coronary artery, left circumflex coronary artery, left anterior descending coronary artery and right coronary artery), aortic root, ascending aorta, sinus, and neo-sinus regions for both pre- and post-TAVR (Figure 1). This framework is based on lumped parameter modelling and 3D FSI modelling as implemented in open-source foam-extend library and validated against in-vivo DE data as explained in Khodaei et al [18,32]. Please refer to appendix for details related to numerical study.

Table 5-2

| Description | Abbreviation | Value |
|---|---|---|
| **Valve parameters** | | |
| Effective orifice area | EOA | Measured using DE |
| Inertance (mitral valve) | $M_{MV}$ | Constant value: 0.53 $gcm^{-2}$ [33] |
| **Systematic circulation parameters** | | |
| Aortic resistance | $R_{ao}$ | Constant value: 0.05 $mmHg.s.mL^{-1}$ [19,22,27–29] |
| Aortic compliance | $C_{ao}$ | Initial value: 0.5 mL/mmHg<br>Optimized based on brachial pressures<br>*(Systolic and diastolic brachial pressures are optimization constraints)* |
| Systemic vein resistance | $R_{SV}$ | 0.05 $mmHg.s.mL^{-1}$ [19,22,27–29] |
| Systemic arteries and veins compliance | $C_{SAC}$ | Initial value: 2 mL/mmHg<br>Optimized based on brachial pressures<br>*(Systolic and diastolic brachial pressures are optimization constraints)* |
| systemic arteries resistance (including arteries, arterioles and capillaries) | $R_{SA}$ | Initial value: 0.8 $mmHg.s.mL^{-1}$<br>Optimized based on brachial pressures<br>*(Systolic and diastolic brachial pressures are optimization constraints)* |
| Upper body resistance | $R_{ub}$ | Adjusted to have 15% of total flow rate in healthy case [19,22,27–29] |
| Proximal descending aorta resistance | $R_{pda}$ | Constant value: 0.05 $mmHg.s.mL^{-1}$ [19,22,27–29] |
| **Elastance Function*** | | |
| Maximum Elastance | $E_{max}$ | 2.1 (LV)<br>0.17 (LA) [34,35] |
| Minimum Elastance | $E_{min}$ | 0.06 (LV, LA) [34,35] |
| Elastance ascending gradient | $m_1$ | 1.32 (LV, LA) [34,35] |
| Elastance descending gradient | $m_2$ | 27.4 (LV)<br>13.1 (LA) [34,35] |
| Elastance ascending time translation | $\tau_1$ | 0.269 T (LV)<br>0.110 T (LA) [34,35] |
| Elastance descending time translation | $\tau_2$ | 0.452 T (LV)<br>0.18 T (LA) [34,35] |
| **Pulmonary circulation parameters** | | |
| Pulmonary Vein Inertance | $L_{PV}$ | Constant value:0.0005 $mmHg{\cdot}s^2{\cdot}mL^{-1}$ [33] |
| Pulmonary Vein Resistance | $R_{PV}$ | Constant value: 0.002 $mmHg{\cdot}s{\cdot}mL^{-1}$ [33] |
| Pulmonary Vein and capillary Resistance | $R_{PVC}$ | Constant value: 0.001 $mmHg{\cdot}s{\cdot}mL^{-1}$ [33] |
| Pulmonary Vein and Capillary Compliance | $C_{PVC}$ | Constant value: 40 mL/mmHg [33] |
| Pulmonary Capillary Inertance | $L_{PC}$ | Constant value: 0.0003 $mmHg{\cdot}s^2{\cdot}mL^{-1}$ [33] |
| Pulmonary Capillary Resistance | $R_{PC}$ | Constant value: 0.21 $mmHg{\cdot}s{\cdot}mL^{-1}$ [33] |
| Pulmonary Arterial Resistance | $R_{PA}$ | Constant value: 0.01 $mmHg{\cdot}s{\cdot}mL^{-1}$ [33] |
| Pulmonary Arterial Compliance | $C_{PA}$ | Constant value: 4 mL/mmHg [33] |
| Mean Flow Rate of Pulmonary Valve | $Q_{MPV}$ | *Forward LVOT-SV* is the only input flow condition (measured using DE)<br>*$Q_{MPV}$ is a flow parameter that was optimized so that the lump-parameter model could reproduce the desirable DE-measured Forward LVOT-SV*. |
| **Input flow condition** | | |
| Forward left ventricular outflow tract stroke volume | Forward LVOT-SV | Measured using DE |
| **Output condition** | | |
| Central venous pressure | $P_{CV0}$ | Constant value: 4 mmHg [19,22,27–29] |
| **Coronary parameters** | | |

| | | |
|---|---|---|
| Proximal Coronary Resistance | $R_{cor,p}$ | Adjusted based on MAP, CO and vessel cross sectional area [36–39] |
| Medial Coronary Resistance | $R_{cor,m}$ | Adjusted based on MAP, CO and vessel cross sectional area [36–39] |
| Distal Coronary Resistance | $R_{cor,d}$ | Adjusted based on MAP, CO and vessel cross sectional area [36–39] |
| Proximal Coronary Compliance | $C_{cor,p}$ | Adjusted based on total vessel compliance and cross-sectional area [36,38,40] |
| Medial Coronary Compliance | $C_{cor,m}$ | Adjusted based on total vessel compliance and cross-sectional area [36,38,40] |
| **Other** | | |
| Constant blood density | $\rho$ | Constant value: 1050 kg/m$^3$ [19,22,27–29] |
| Heart rate | HR | Measured using DE |
| Duration of cardiac cycle | T | Measured using DE |
| Systolic End Ejection time | $T_{EJ}$ | Measured using DE |
| End diastolic volume | EDV | Measured using DE |
| End systolic volume | ESV | Measured using DE |

## 5.4 Results

The efficacy of supplied oxygenated blood flow for myocardium through coronary arteries depends on both global and local hemodynamics. The coronary hemodynamics alterations after TAVR depend on the ascending aorta and ventricular pressures changes (global) as well as TAVR deployment characteristics such as aortic root geometry, valve size, aorta angle, coronary ostium height and valve to coronary distance (local). We investigated hemodynamic metrics computed by our computational framework (Figures 2 to 6) and their correlations with geometrical parameters (Figure 7) as follows:

### 5.4.1 Coronary blood flow

Although an increase in coronary flow is expected after AS removal and TAVR implantation, our results showed that despite the improvement of systolic flow, a universal reduction of flow occurs during diastole for different coronary branches in most of the patients. As shown in figure 4, on average, the peak systole flow increased 12.8%, 4.39 % and 25.67% for LAD, LCX and RCA respectively, while the peak diastole flow decreased by 8.98%, 16.83% and 22.73% for LAD, LCX and RCA respectively. Reduced flow in coronaries is a crucial factor for TAVR success that could affect the outcomes of revascularization and might play a role in the pathophysiological abnormalities leading to heart failure or increased risk of cardiovascular death [41–44].

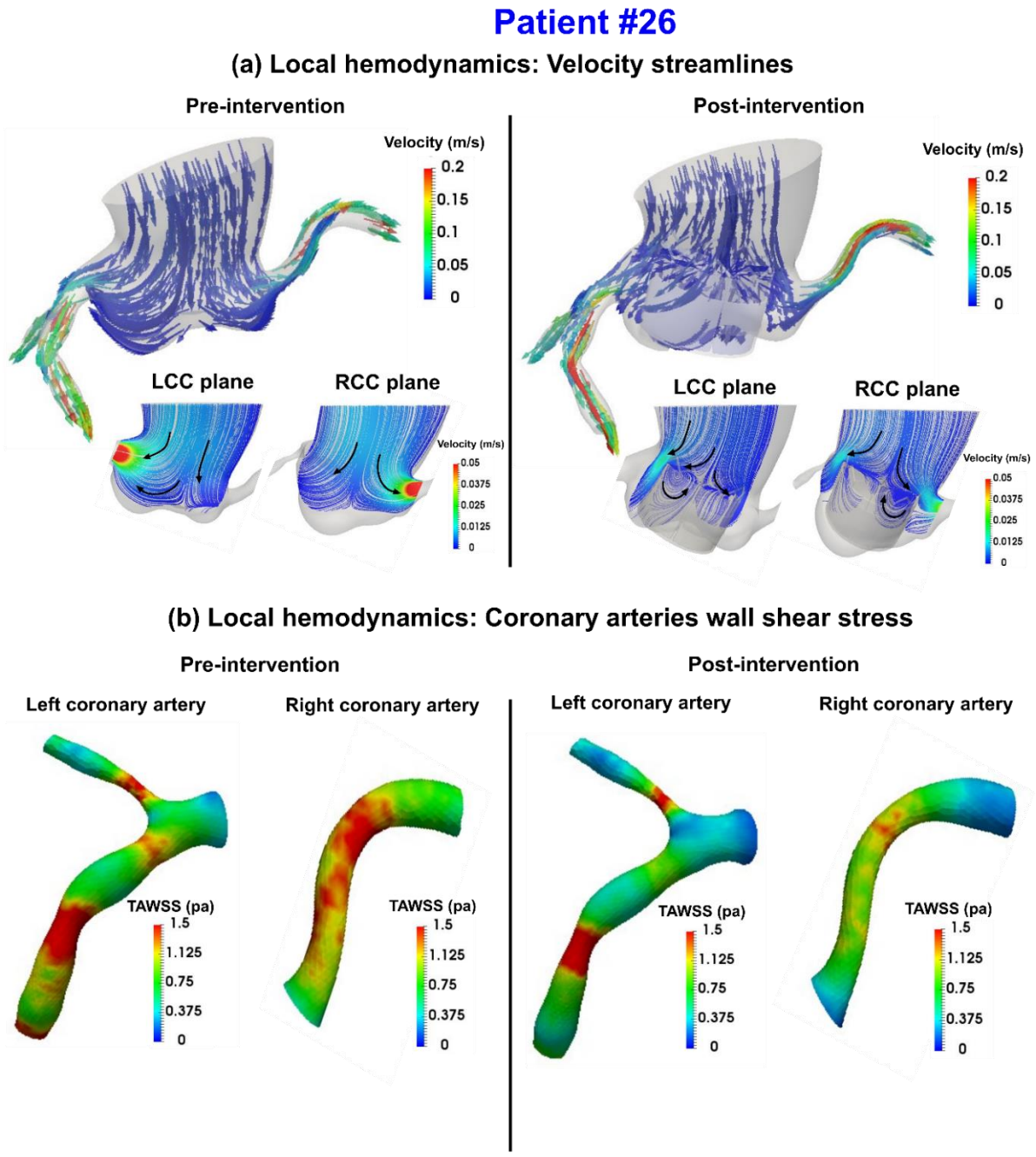


Figure 5-2. Flow modelling in patient #26 (a) Velocity streamlines and the vortical structure in the sinus and coronary ostium during diastole in pre and post TAVR states (b) Left and right coronary branches TAWSS during diastole. In patient #26, the restricted gap between stent and the coronary ostium as well as anatomical alterations of aortic root impede the flow reaching coronary arteries, leading to reduced flow and wall shear stress. LCC indicated the left coronary cusp; RCC indicated the right coronary cusp.

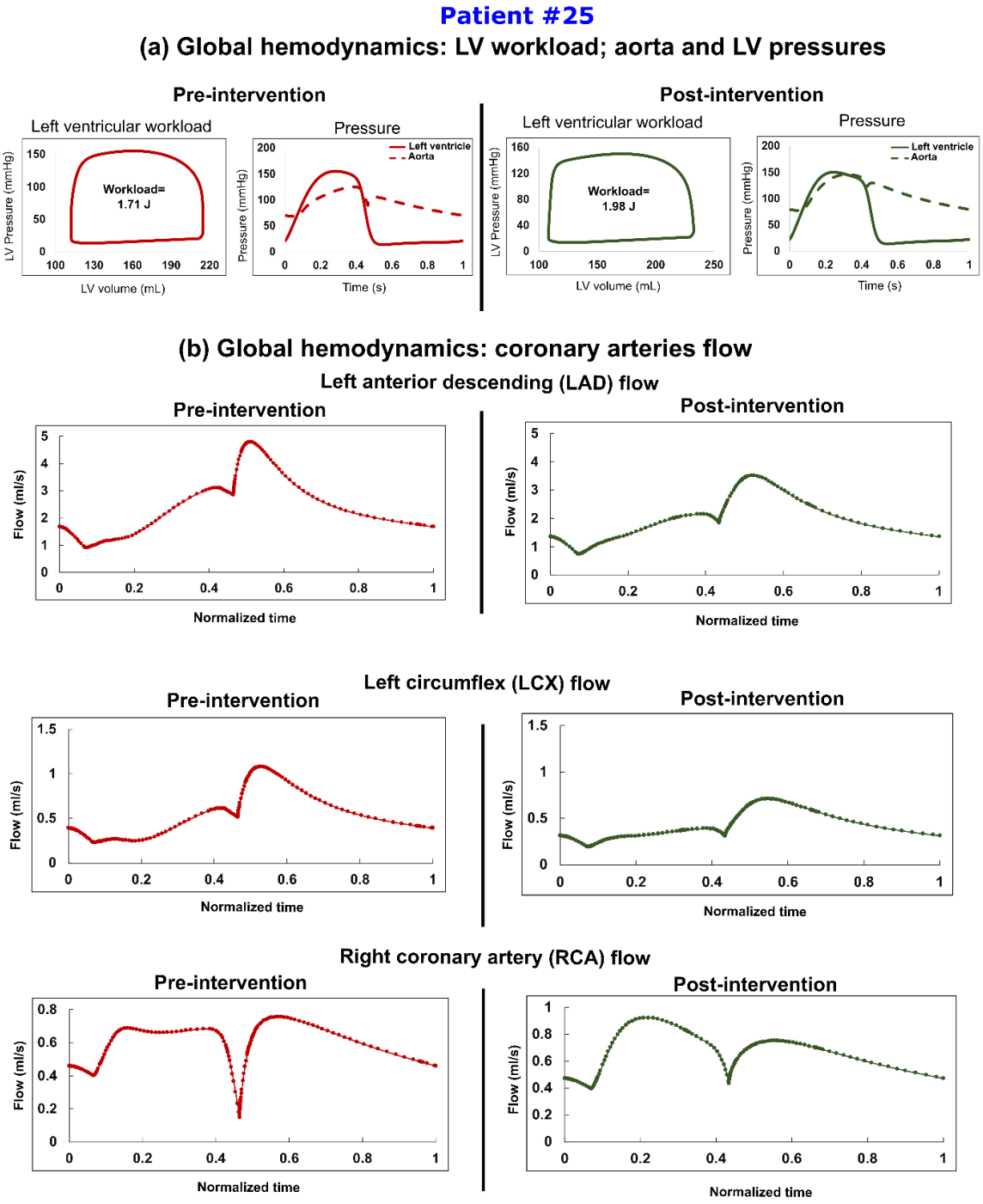


Figure 5-3. Example of changes in predicted global hemodynamics before intervention and after TAVR in patients #25. (a) LV workload left ventricle and ascending aorta pressure (b) Changes in predicted coronary flowrate for LAD, LCX and RCA branches before intervention and after TAVR for both patients.

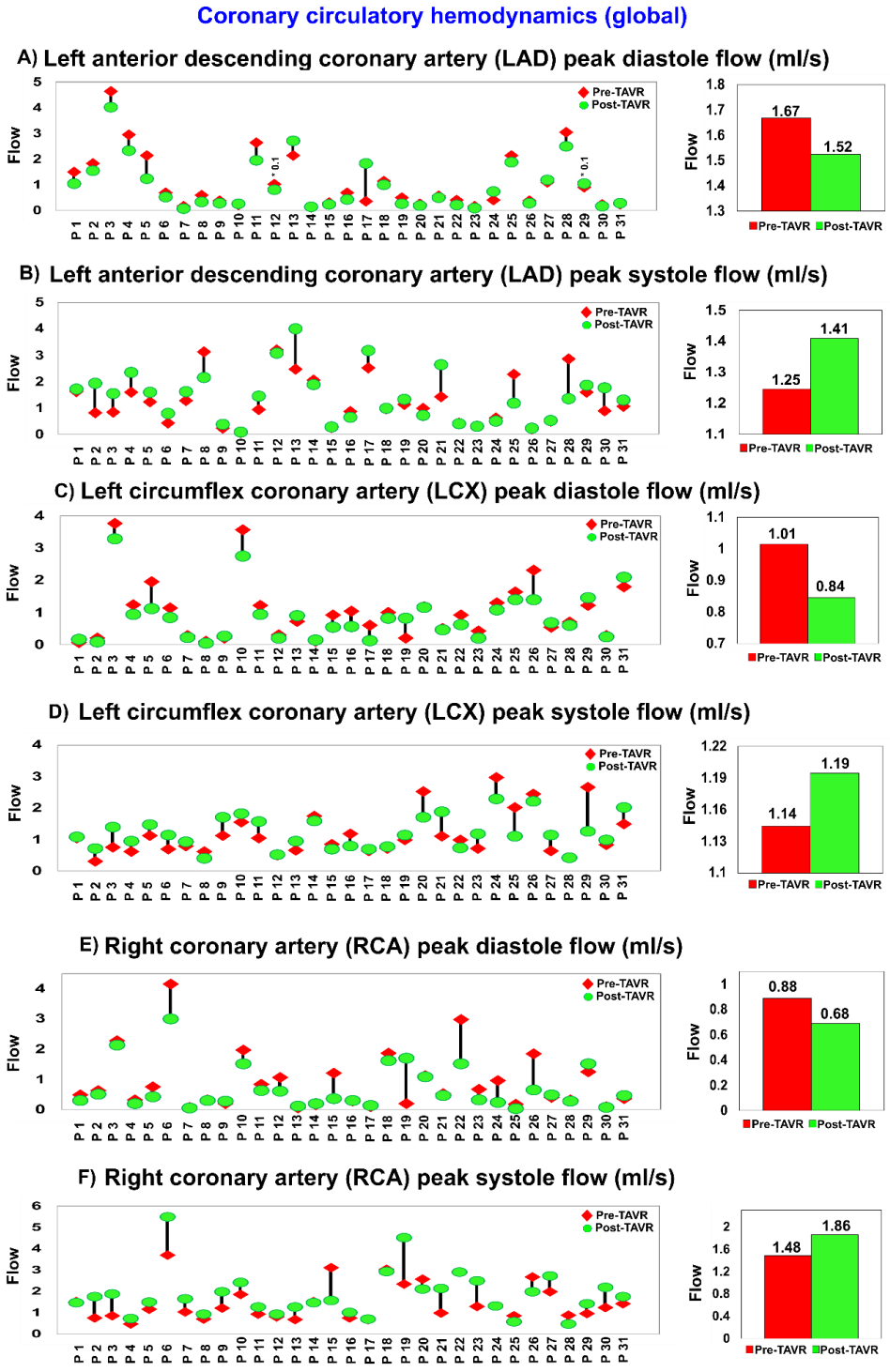


Figure 5-4. Changes in coronary circulatory hemodynamics in patients between pre and post TAVR (N=31). (a) Left anterior descending coronary artery peak diastolic flow; (b) Left anterior descending coronary artery peak systolic flow; (c) Left circumflex coronary artery peak diastolic flow; (d) Left circumflex coronary artery peak systolic flow; (e) Right coronary artery peak diastolic flow; (f) Right coronary artery peak systolic flow

### 5.4.2 Coronary Wall shear stress

Endothelial cells show a pro-inflammatory state in presence of low wall shear stress microenvironment, which is linked to plaque progression [45,46]. While there have been efforts to come up with a cut-off value for low wall shear stress, allometric arguments show that this is not a universal property [47]. We calculated the time averaged wall shear stress over diastole for all patients in pre and post TAVR states. On average, TAWSS decreased for 84% of the patients for different coronary branches. As shown in figures 5 and 7g, maximum TAWSS decreased (n=31) 9.47%, 7.75%, 6.94%, 8.07% and 6.28% for bifurcation ($t = 2.3$; $p < .05$), LMCA ($W = 343$; $p = 0.06$), LAD ($t = 1.7$; $p = 0.1$), LCX ($t = 1.7$; $p = 0.1$) and RCA ($t = 1.5$; $p = 0.2$) branches respectively.

We also observed that the distribution of TAWSS and its maximum is very different for each patient and is highly dependent to the geometrical characterization of the coronary walls. For patient #26 as a sample (Figure 2b), the TAWSS ranges from 0.12 pa to 1.5 pa across the coronary arteries with considerable reduction (to a range of 0.1pa to 1.2 pa) followed by TAVR.

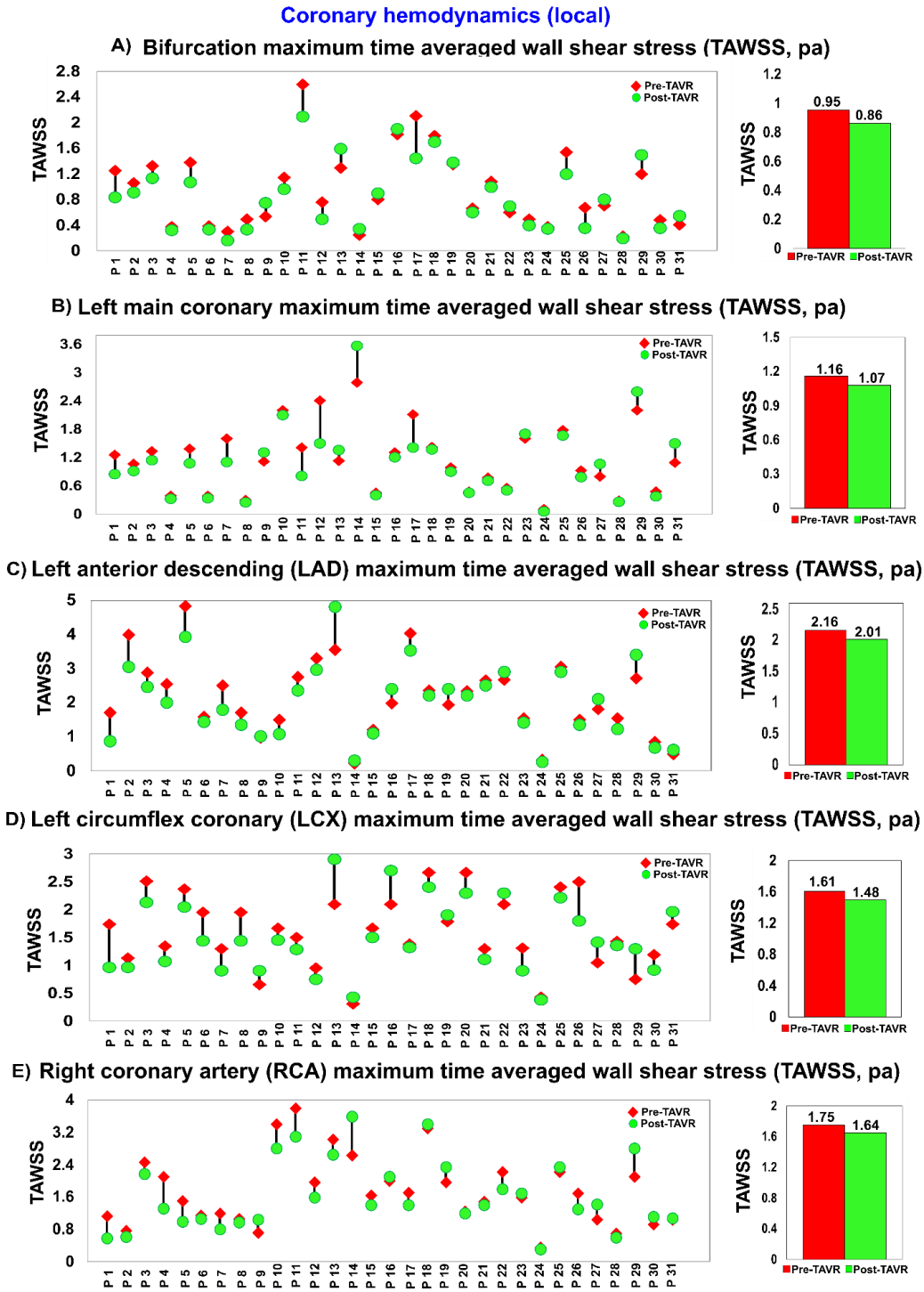


Figure 5-5. Changes in local hemodynamics in patients between pre- and post-TAVR (N=31). (a) Bifurcation maximum TAWSS; (b) Left main coronary maximum TAWSS; (c) Left anterior descending coronary artery maximum TAWSS; (d) Left circumflex coronary artery maximum TAWSS; (e) Right coronary artery maximum TAWSS.

### 5.4.3 Left ventricle load

LV workload represents the total energy required by the ventricle to eject blood, and is an effective metric of LV load and clinical state [18,20,21,32]. The workload was computed through the integral of the left ventricle pressure-volume loop generated by the lumped model. Despite the significant decrease in aortic valve pressure gradient for all patients after TAVR (Figure 6) as a results of AS removal, the ventricular workload did not improve for 54.84% of the patients. As shown in figure 6, while on average, the aortic valve mean pressure gradient dropped by 64% ($t = 12.4$; $p < .001$) after TAVR, the workload burden was not removed (2.52% increase in workload) after TAVR. In addition, in 24 patients (77.42%) the workload remained above 1J after TAVR, which is an indicator of overload ventricle.

### 5.4.4 Correlation analysis

We examined the correlation between coronary flow and other hemodynamics and geometrical parameters (please see the appendix for the comprehensive statistical analysis and correlation matrix). As shown in figure 7a and 7b, we observed strong correlation between left ventricle workload and mean coronary flow for both pre- and post-TAVR cases ($r = 0.75$; $p < .001$ pre-TAVR and $r = 0.52$; $p < .003$ post-TAVR). This is an interesting finding, as LV load could be an effective non-invasive metric to predict the oxygen demand of myocardium after TAVR without a need to perform invasive coronary hemodynamic measurements.

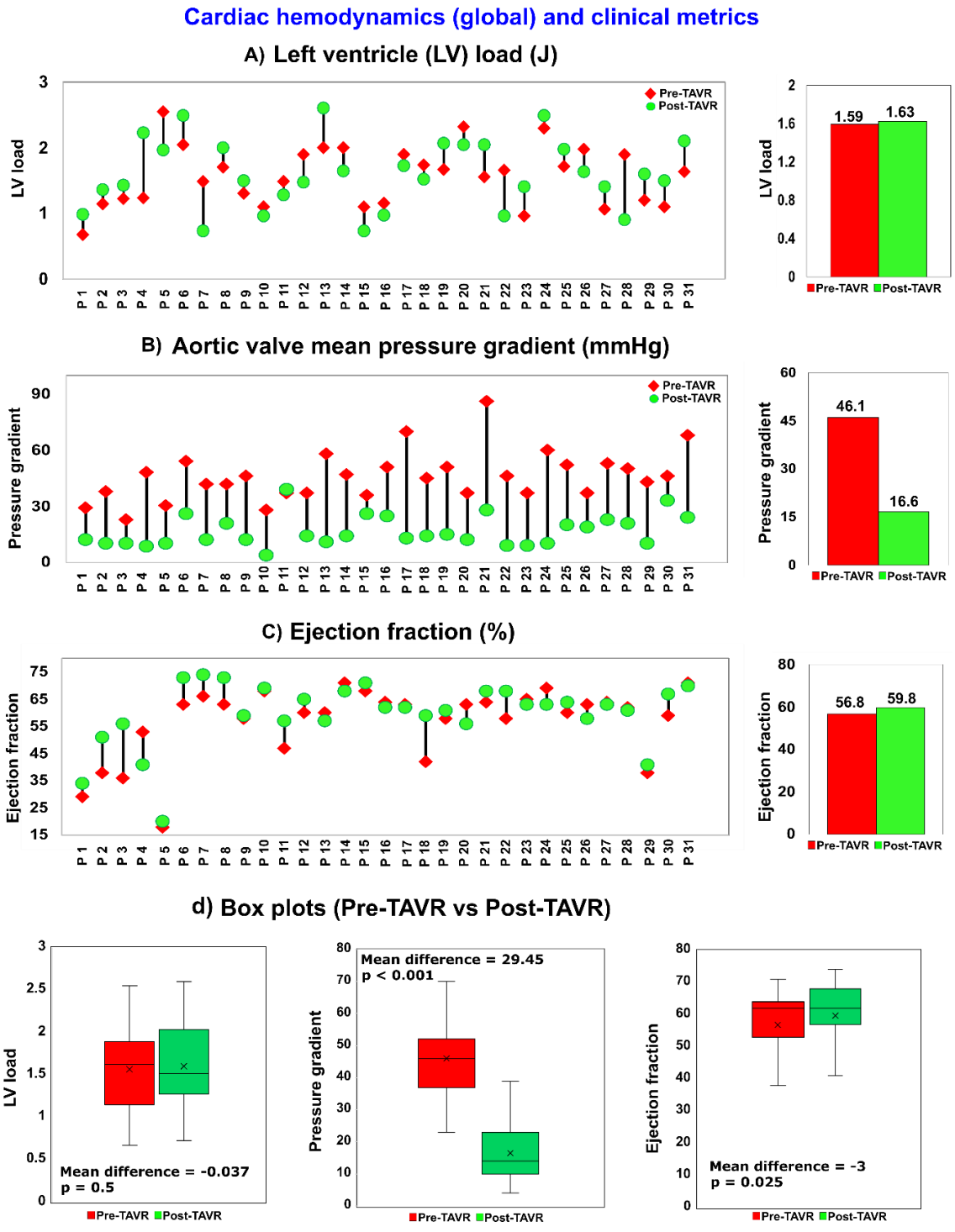


Figure 5-6. Changes in LV workload and clinical assessments of LV in patients between baseline and post TAVR (N=31). (a) Left ventricle workload; (b) Aortic valve mean pressure gradient; (c) Ejection fraction; (d) Box plots comparing LV workload and clinical parameters pre- and post-TAVR

Additionally, among all the geometrical parameters, strong correlation was observed between mean coronary flow and valve to coronary distance (left and right ostium), left coronary ostium height and aortic root diameter with mean coronary flow. As shown in figure 7e and 7f, mean coronary flow was strongly correlated with coronary ostium height ($r = 0.79$; $p < .001$) and aortic root diameter ($r = 0.58$; $p < .001$). Moreover, strong correlation was observed between mean coronary flow and valve to left coronary distance (figure 7c) ($r = 0.78$; $p < .001$). This correlation was less significant for valve to right coronary distance (figure 7d) ($r= 0.5$; $p=0.004$). In summary, our findings showed that the restricted gap between the expanded valve and coronary inlet might impeded the coronary blood flow. We also found that patients with lower coronary ostium height are at higher risk of reduced coronary flow after TAVR.

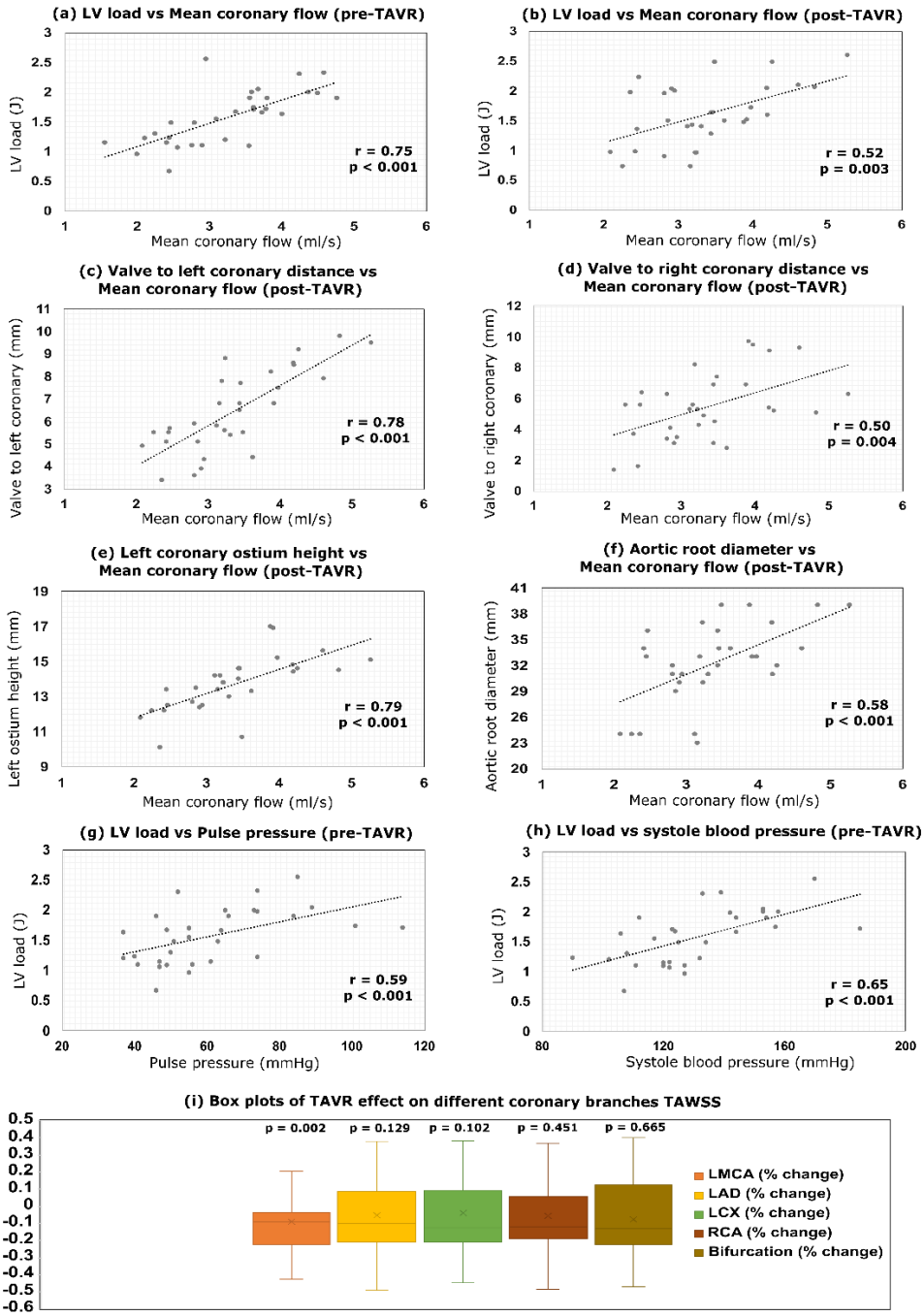


Figure 5-7. Statistics and data plots for parameters (N=31). (a) Scatter plot of LV load vs mean coronary flow (pre-TAVR); (b) Scatter plot of LV load vs mean coronary flow (post-TAVR); (c) Scatter plot of valve to left coronary distance vs mean coronary flow (post-TAVR); (d) Scatter plot of valve to right coronary distance vs mean coronary flow (post-TAVR); (e) Scatter plot of left coronary ostium height vs mean coronary flow (post-TAVR); (f) Scatter plot of aortic root diameter vs mean coronary flow (post-TAVR); (g) Scatter plot of LV load vs pulse pressure; (h) Scatter plot of LV load vs Systole pressure ; (i) Box plots comparing coronary branches TAWSS changes after TAVR for all patients.

## 5.5 Discussion

CAD is present in more than 50% of the patients who undergo TAVR and the question of if CAD should be treated in severity before TAVR procedure is still up for debate [48]. After TAVR, the risk of death is closely related to the complications and severity of CAD with significant increase in all-cause mortality at 1 year [49,50]. However, there is still no clear evidence based recommendation for the risk-benefit ratio of PCI in TAVR population [49]. Moreover, the variability in definition of CAD or CAD severity with syntax score across studies makes the clinical endpoint very subjective [48]. Also, most of the studies in literature had less than 2 years follow up and therefore, longer term effect of CAD on clinical outcomes of TAVR remains unknown [48].

Coronary arteries are supplied with blood mainly during diastole and recent studies have shown that coronary flow does not change during the wave-free period of diastole after TAVR [48,51]. The coronary flow has direct impact on plaque progression and the majority of coronary events post-TAVR are related to atherosclerotic plaque formation and CAD progression [48]. TAVR prosthetic and its influence on natural flow pathways in the sinus of Valsalva attributes to disturbance of the blood entering the coronary circulation [52]. The complications resulting from this is relatively unknown, and more research is needed. Indeed, quantification of global and local flow is important as it aids to correctly identify complications which exclusive anatomical examinations can overlook [53]. These changes can lead to ischemia in the future, and may have gone undetected if a hemodynamic assessment was not done [54]. In the present work, there are several findings which should be individually discussed.

### 5.5.1 Coronary diastolic flow might not recover after TAVR

Induced extravascular compressive forces caused by AS reduces the coronary perfusion pressure which is associated with reduced systemic arterial compliance [41,55]. After TAVR, immediate increase of pressure and flow downstream of aortic valve (ascending aorta) is expected as results of AS removal [41,56]. Our results confirm that the expected enhancement in pressure and coronary flow occurs during systole. However, the diastolic flow in coronaries might not improve or even decrease for many patients. Such decrease in coronary blood flow is associated with reduced capacity to augment myocardial oxygenation, leading to LV dysfunction, increased apoptosis (which is linked to myocardial fibrosis and is an independent indicator of mortality) and sudden death [41–44,57].

### 5.5.2 Patients with lower valve to coronary distance are at higher risk of reduced coronary flow after TAVR

We observed that (Fig 7) in addition to the global hemodynamics and aorta pressure, the geometrical details including the valve to aorta distance, valve to coronary distance, implantation depth and aortic root shape drastically affects the local hemodynamics before reaching coronary ostium. While the focus of recent studies has been on the risk assessment for coronary obstruction [58–60], our findings suggest that if the distance between stent and aorta wall is restricted (even if not fully obstructed) after TAVR , the coronary flow will be impeded. In other words, the coronary obstruction should not be the only concern as the coronary flow also depends on the available gap between valve and aorta. On the other hand, while the number of patients who need a second TAVR is increasing as TAVR expands toward younger patients [61], the true risk of coronary

obstruction is not known yet [62]. This means, the proper coronary filling mechanism will be more complicated in these population with higher risk of mortality [41–44].

### 5.5.3 Coronary arteries might be at higher risk of plaque progression after TAVR

Another interesting finding of this study was that TAVR might reduce the wall shear stress for the coronary arteries during diastole due to the reduced blood flow. This makes the coronary arteries more susceptible to atherosclerosis, due to the low wall shear stress-induced inflammatory activation of endothelium mainly at the inner bend of curved arteries, ostia of branches and lateral walls of bifurcations [45,46].

The progression mechanism of AS is very similar to that of atherosclerosis in coronary artery disease (CAD) and there is a high coincidence of both disease in the same patient [63]. AS and CAD share several important cellular mechanisms including lipid deposition, inflammatory cell infiltration, cytokine release, and calcification [64] and that explains why CAD is present in approximately 50% of the AS patients [48]. Our study revealed that the reduction of TAWSS for majority of patients during diastole might increase the current existing risk of CAD through enlargement of plaque area, increased plaque eccentricity and reduced vessel area [46,65–67].

### 5.5.4 Left coronary bifurcation could be at higher risk of plaque progression after TAVR

Coronary artery bifurcation has a unique local flow and wall shear stress condition because of patient-specific anatomy of main and side branches [68,69]. The unfavorable hemodynamic alterations at the branch points of bifurcation followed by reduced shear stress could promote endothelial cell dysfunction which attributes to the progression of atherosclerosis[69]. Interestingly, our results showed that for all patients, regardless of flow alterations after TAVR, coronary

bifurcation is exposed to a considerably low wall shear stress region with higher risk of plaque formation. This is a critical concern for TAVR patients as there is a high risk of restenosis for bifurcation lesions after PCI [70,71].

### 5.5.5 In Some Patients: No Improvement in Left Ventricular Hemodynamics Post-TAVR

LV workload is an effective metric for LV functional assessment, which is closely dependent to the coronary perfusion and the coronary flow [72,73]. Increased workload promoted cardiac remodeling with an increase in myocardial oxygen demand which makes myocardium vulnerable to ischemia [74,75]. AS increases the LV workload in order compensate the reduced ejected flow and after TAVR, a reduced workload is expected[75]. However, our results showed that the reduction in aortic valve pressure gradient post-TAVR was not associated with reduced workload for a large number of patients.

Another interesting finding of our study was that that the coronary flow was correlated with LV workload for both pre- and post-TAVR states. While we have previously shown the usefulness of LV load metric for TAVR patients [75], this study demonstrated the significance of the interplay between LV load and coronary flow. Our findings are indeed in line with the critical role of effective coronary circulation for cardioprotection, as the reduction in coronary blood flow will lead to myocardial infarction over time [76].

## 5.6 Conclusions

An optimal TAVR procedure strategy is subject-specific, and there are several factors that affect the coronary hemodynamics including the global hemodynamic and circulatory system alterations, aortic root and aortic valve anatomical specifications, coronary height, valve to coronary distance

and prosthetic overexpansion. The confined space between the valve stent and coronary ostium could obstruct the optimal flow movement towards coronary arteries and is associated with increased myocardium workload. The findings of this study suggests that special consideration should be paid during TAVR to the patients with lower coronary height or smaller aortic root, as these patients are at higher risk of reduced coronary flow and long-term CAD. Personalized computational simulations can provide virtual experiments to guide the interventional cardiologist for optimal decision planning. The developed framework in this work is just such a tool to improve the clinical outcomes and guiding interventions for patients who receive TAVR and might be at risk of CAD over the course of time.

## *Acknowledgments*

This work was supported by NSERC Discovery Grant (RGPIN-2017-05349). The funders had no role in study design, data collection and analysis, decision to publish, or preparation of the manuscript.

## References


1. Smith, C. R. *et al.* Transcatheter versus surgical aortic-valve replacement in high-risk patients. *N. Engl. J. Med.* **364**, 2187–2198 (2011).
2. Leon, M. B. *et al.* Transcatheter or surgical aortic-valve replacement in intermediate-risk patients. *N. Engl. J. Med.* **374**, 1609–1620 (2016).
3. Reardon, M. J. *et al.* Surgical or Transcatheter Aortic-Valve Replacement in Intermediate-Risk Patients. *N. Engl. J. Med.* **376**, 1321–1331 (2017).
4. Popma, J. J. *et al.* Transcatheter Aortic-Valve Replacement with a Self-Expanding Valve in Low-Risk Patients. *N. Engl. J. Med.* **380**, 1706–1715 (2019).
5. Patel, K. P. *et al.* Coronary Revascularization in Patients Undergoing Aortic Valve Replacement for Severe Aortic Stenosis. *JACC Cardiovasc. Interv.* **14**, 2083–2096 (2021).
6. Authors/Task Force Members *et al.* Guidelines on the management of valvular heart disease (version 2012): The Joint Task Force on the Management of Valvular Heart Disease of the European Society of Cardiology (ESC) and the European Association for Cardio-Thoracic Surgery (EACTS). *Eur. Heart J.* **33**, 2451–2496 (2012).
7. Vendrik, J. *et al.* Long-Term Effects of Transcatheter Aortic Valve Implantation on Coronary Hemodynamics in Patients With Concomitant Coronary Artery Disease and Severe Aortic Stenosis. *J. Am. Heart Assoc.* **9**, e015133 (2020).
8. Ochiai, T. *et al.* Coronary Access After TAVR. *JACC Cardiovasc. Interv.* **13**, 693–705 (2020).
9. Wiegerinck, E. M. A. *et al.* Impact of Aortic Valve Stenosis on Coronary Hemodynamics and the Instantaneous Effect of Transcatheter Aortic Valve Implantation. *Circ. Cardiovasc. Interv.* **8**, e002443 (2015).
10. Camuglia, A. C. *et al.* Invasively Assessed Coronary Flow Dynamics Improve Following Relief of Aortic Stenosis With Transcatheter Aortic Valve Implantation. *J. Am. Coll. Cardiol.* **63**, 1808–1809 (2014).
11. Rolandi, M. C. *et al.* Transcatheter Replacement of Stenotic Aortic Valve Normalizes Cardiac–Coronary Interaction by Restoration of Systolic Coronary Flow Dynamics as Assessed by Wave Intensity Analysis. *Circ. Cardiovasc. Interv.* **9**, e002356 (2016).
12. Faroux, L. *et al.* Procedural Characteristics and Late Outcomes of Percutaneous Coronary Intervention in the Workup Pre-TAVR. *JACC Cardiovasc. Interv.* **13**, 2601–2613 (2020).
13. Landt, M. *et al.* Impact of Revascularization Completeness on Outcomes of Patients with Coronary Artery Disease Undergoing Transcatheter Aortic Valve Replacement. *Struct. Heart* **3**, 393–400 (2019).
14. Stefanini, G. G. *et al.* Coronary artery disease severity and aortic stenosis: clinical outcomes according to SYNTAX score in patients undergoing transcatheter aortic valve implantation. *Eur. Heart J.* **35**, 2530–2540 (2014).
15. Bairey Merz, C. N. *et al.* Ischemia and No Obstructive Coronary Artery Disease (INOCA). *Circulation* **135**, 1075–1092 (2017).
16. Loureiro Garcia, M. *et al.* P6224Hemodynamics of the left coronary artery after TAVI procedure: a numerical simulation analysis. *Eur. Heart J.* **39**, ehy566.P6224 (2018).

17. Keshavarz-Motamed, Z. A diagnostic, monitoring, and predictive tool for patients with complex valvular, vascular and ventricular diseases. *Sci. Rep.* **10**, 1–19 (2020).
18. Khodaei, S. *et al.* Personalized intervention cardiology with transcatheter aortic valve replacement made possible with a non-invasive monitoring and diagnostic framework. *Sci. Rep.* **11**, 10888 (2021).
19. Keshavarz-Motamed, Z. A diagnostic, monitoring, and predictive tool for patients with complex valvular, vascular and ventricular diseases. *Sci. Rep.* **10**, 6905 (2020).
20. Keshavarz-Motamed Zahra *et al.* Mixed Valvular Disease Following Transcatheter Aortic Valve Replacement: Quantification and Systematic Differentiation Using Clinical Measurements and Image-Based Patient-Specific In Silico Modeling. *J. Am. Heart Assoc.* **9**, e015063 (2020).
21. Ben-Assa, E. *et al.* Ventricular stroke work and vascular impedance refine the characterization of patients with aortic stenosis. *Sci. Transl. Med.* **11**, (2019).
22. Keshavarz-Motamed, Z., Garcia, J., Pibarot, P., Larose, E. & Kadem, L. Modeling the impact of concomitant aortic stenosis and coarctation of the aorta on left ventricular workload. *J. Biomech.* **44**, 2817–2825 (2011).
23. Keshavarz-Motamed, Z. *et al.* The role of aortic compliance in determination of coarctation severity: Lumped parameter modeling, in vitro study and clinical evaluation. *J. Biomech.* **48**, 4229–4237 (2015).
24. Keshavarz-Motamed, Z. *et al.* Effect of coarctation of the aorta and bicuspid aortic valve on flow dynamics and turbulence in the aorta using particle image velocimetry. *Exp. Fluids* **55**, 1696 (2014).
25. Keshavarz-Motamed, Z. *et al.* A new approach for the evaluation of the severity of coarctation of the aorta using Doppler velocity index and effective orifice area: In vitro validation and clinical implications. *J. Biomech.* **45**, 1239–1245 (2012).
26. Benevento, E., Djebbari, A., Keshavarz-Motamed, Z., Cecere, R. & Kadem, L. Hemodynamic Changes following Aortic Valve Bypass: A Mathematical Approach. *PLOS ONE* **10**, e0123000 (2015).
27. Keshavarz-Motamed, Z. *et al.* Elimination of transcoarctation pressure gradients has no impact on left ventricular function or aortic shear stress after intervention in patients with mild coarctation. *JACC Cardiovasc. Interv.* **9**, 1953–1965 (2016).
28. Sadeghi, R., Khodaei, S., Ganame, J. & Keshavarz-Motamed, Z. Towards non-invasive computational-mechanics and imaging-based diagnostic framework for personalized cardiology for coarctation. *Sci. Rep.* **10**, 9048 (2020).
29. Keshavarz-Motamed, Z. *et al.* Non-Invasive Determination of Left Ventricular Workload in Patients with Aortic Stenosis Using Magnetic Resonance Imaging and Doppler Echocardiography. *PLOS ONE* **9**, e86793 (2014).
30. Sadeghi, R., Gasner, N., Khodaei, S., Garcia, J. & Keshavarz-Motamed, Z. Impact of mixed valvular disease on coarctation hemodynamics using patient-specific lumped parameter and Lattice Boltzmann modeling. *Int. J. Mech. Sci.* **217**, 107038 (2022).
31. Sadeghi, R. *et al.* Reducing morbidity and mortality in patients with coarctation requires systematic differentiation of impacts of mixed valvular disease on coarctation hemodynamics. *J. Am. Heart Assoc.* **in press**,.
32. Khodaei, S. *et al.* Towards a non-invasive computational diagnostic framework for personalized cardiology of transcatheter aortic valve replacement in interactions with

complex valvular, ventricular and vascular disease. *Int. J. Mech. Sci.* **202–203**, 106506 (2021).
33. Tanné, D., Kadem, L., Rieu, R. & Pibarot, P. Hemodynamic impact of mitral prosthesis-patient mismatch on pulmonary hypertension: an in silico study. *J. Appl. Physiol. Bethesda Md 1985* **105**, 1916–1926 (2008).
34. Stergiopulos, N., Meister, J. J. & Westerhof, N. Determinants of stroke volume and systolic and diastolic aortic pressure. *Am. J. Physiol.-Heart Circ. Physiol.* **270**, H2050–H2059 (1996).
35. Mynard, J. P., Davidson, M. R., Penny, D. J. & Smolich, J. J. A simple, versatile valve model for use in lumped parameter and one-dimensional cardiovascular models. *Int. J. Numer. Methods Biomed. Eng.* **28**, 626–641 (2012).
36. Kim, H. J. *et al.* Patient-Specific Modeling of Blood Flow and Pressure in Human Coronary Arteries. *Ann. Biomed. Eng.* **38**, 3195–3209 (2010).
37. Taylor, C. A., Fonte, T. A. & Min, J. K. Computational Fluid Dynamics Applied to Cardiac Computed Tomography for Noninvasive Quantification of Fractional Flow Reserve: Scientific Basis. *J. Am. Coll. Cardiol.* **61**, 2233–2241 (2013).
38. Sankaran, S. *et al.* Patient-Specific Multiscale Modeling of Blood Flow for Coronary Artery Bypass Graft Surgery. *Ann. Biomed. Eng.* **40**, 2228–2242 (2012).
39. Zhou, Y., Kassab, G. S. & Molloi, S. On the design of the coronary arterial tree: a generalization of Murray's law. *Phys. Med. Biol.* **44**, 2929–2945 (1999).
40. Coogan, J. S., Humphrey, J. D. & Figueroa, C. A. Computational simulations of hemodynamic changes within thoracic, coronary, and cerebral arteries following early wall remodeling in response to distal aortic coarctation. *Biomech. Model. Mechanobiol.* **12**, 79–93 (2013).
41. McConkey, H. Z. R. *et al.* Coronary Microcirculation in Aortic Stenosis. *Circ. Cardiovasc. Interv.* **12**, e007547.
42. Lester, S. J., Heilbron, B., Gin, K., Dodek, A. & Jue, J. The natural history and rate of progression of aortic stenosis. *Chest* **113**, 1109–1114 (1998).
43. Vesey, A. T., Esson, G., Chin, C., Dweck, M. & Newby, D. Detection of cardiac fibrosis and cell death in patients with aortic stenosis. *J. Am. Coll. Cardiol.* **65**, A1190–A1190 (2015).
44. Dweck, M. R. *et al.* Midwall fibrosis is an independent predictor of mortality in patients with aortic stenosis. *J. Am. Coll. Cardiol.* **58**, 1271–1279 (2011).
45. Cameron, J. N. *et al.* Exploring the relationship between biomechanical stresses and coronary atherosclerosis. *Atherosclerosis* **302**, 43–51 (2020).
46. Gijsen, F. *et al.* Expert recommendations on the assessment of wall shear stress in human coronary arteries: existing methodologies, technical considerations, and clinical applications. *Eur. Heart J.* **40**, 3421–3433 (2019).
47. Peiffer, V., Sherwin, S. J. & Weinberg, P. D. Does low and oscillatory wall shear stress correlate spatially with early atherosclerosis? A systematic review. *Cardiovasc. Res.* **99**, 242–250 (2013).
48. Faroux, L. *et al.* Coronary Artery Disease and Transcatheter Aortic Valve Replacement: JACC State-of-the-Art Review. *J. Am. Coll. Cardiol.* **74**, 362–372 (2019).
49. D'Ascenzo, F. *et al.* Independent impact of extent of coronary artery disease and percutaneous revascularisation on 30-day and one-year mortality after TAVI: a meta-

analysis of adjusted observational results. *EuroIntervention J. Eur. Collab. Work. Group Interv. Cardiol. Eur. Soc. Cardiol.* **14**, e1169–e1177 (2018).
50. Sankaramangalam, K. *et al.* Impact of Coronary Artery Disease on 30-Day and 1-Year Mortality in Patients Undergoing Transcatheter Aortic Valve Replacement: A Meta-Analysis. *J. Am. Heart Assoc.* **6**, e006092.
51. Vendrik, J. *et al.* Long-Term Effects of Transcatheter Aortic Valve Implantation on Coronary Hemodynamics in Patients With Concomitant Coronary Artery Disease and Severe Aortic Stenosis. *J. Am. Heart Assoc.* **9**, e015133 (2020).
52. Ducci, A., Pirisi, F., Tzamtzis, S. & Burriesci, G. Transcatheter aortic valves produce unphysiological flows which may contribute to thromboembolic events: An in-vitro study. *J. Biomech.* **49**, 4080–4089 (2016).
53. Ahmad, Y. *et al.* Coronary Hemodynamics in Patients With Severe Aortic Stenosis and Coronary Artery Disease Undergoing Transcatheter Aortic Valve Replacement: Implications for Clinical Indices of Coronary Stenosis Severity. *JACC Cardiovasc. Interv.* **11**, 2019–2031 (2018).
54. Farag, E. S. *et al.* Transcatheter aortic valve replacement alters ascending aortic blood flow and wall shear stress patterns: A 4D flow MRI comparison with age-matched, elderly controls. *Eur. Radiol.* **29**, 1444–1451 (2019).
55. Crea, F., Camici, P. G. & Bairey Merz, C. N. Coronary microvascular dysfunction: an update. *Eur. Heart J.* **35**, 1101–1111 (2014).
56. Ben-Dor, I. *et al.* Coronary blood flow in patients with severe aortic stenosis before and after transcatheter aortic valve implantation. *Am. J. Cardiol.* **114**, 1264–1268 (2014).
57. Heusch, G. Myocardial ischemia: lack of coronary blood flow, myocardial oxygen supply-demand imbalance, or what? *Am. J. Physiol.-Heart Circ. Physiol.* **316**, H1439–H1446 (2019).
58. Nai Fovino, L. *et al.* Coronary Angiography After Transcatheter Aortic Valve Replacement (TAVR) to Evaluate the Risk of Coronary Access Impairment After TAVR-in-TAVR. *J. Am. Heart Assoc.* **9**, e016446 (2020).
59. Oh, J.-H. *et al.* Distance between valvular leaflet and coronary ostium predicting risk of coronary obstruction during TAVR. *IJC Heart Vasc.* **37**, 100917 (2021).
60. Heitkemper, M. *et al.* Simple 2-dimensional anatomic model to predict the risk of coronary obstruction during transcatheter aortic valve replacement. *J. Thorac. Cardiovasc. Surg.* **162**, 1075-1083.e1 (2021).
61. Bapat, V. N. *et al.* Surgical Explantation After TAVR Failure: Mid-Term Outcomes From the EXPLANT-TAVR International Registry. *JACC Cardiovasc. Interv.* **14**, 1978–1991 (2021).
62. Okuno, T. Risk of "Future" Coronary Obstruction. *JACC Cardiovasc. Interv.* **15**, 725–727 (2022).
63. Carabello, B. A. & Paulus, W. J. Aortic stenosis. *The Lancet* **373**, 956–966 (2009).
64. Milin, A. C., Vorobiof, G., Aksoy, O. & Ardehali, R. Insights Into Aortic Sclerosis and Its Relationship With Coronary Artery Disease. *J. Am. Heart Assoc.* **3**, e001111.
65. Samady, H. *et al.* Coronary Artery Wall Shear Stress Is Associated With Progression and Transformation of Atherosclerotic Plaque and Arterial Remodeling in Patients With Coronary Artery Disease. *Circulation* **124**, 779–788 (2011).

66. Eshtehardi, P. *et al.* Association of Coronary Wall Shear Stress With Atherosclerotic Plaque Burden, Composition, and Distribution in Patients With Coronary Artery Disease. *J. Am. Heart Assoc.* **1**, e002543.
67. Papafaklis, M. I. *et al.* Effect of the local hemodynamic environment on the de novo development and progression of eccentric coronary atherosclerosis in humans: Insights from PREDICTION. *Atherosclerosis* **240**, 205–211 (2015).
68. Antoniadis, A. P. *et al.* Impact of local flow haemodynamics on atherosclerosis in coronary artery bifurcations. *EuroIntervention J. Eur. Collab. Work. Group Interv. Cardiol. Eur. Soc. Cardiol.* **11 Suppl V**, V18-22 (2015).
69. Nakazawa, G. *et al.* Pathological Findings at Bifurcation Lesions: The Impact of Flow Distribution on Atherosclerosis and Arterial Healing After Stent Implantation. *J. Am. Coll. Cardiol.* **55**, 1679–1687 (2010).
70. Al Suwaidi, J. *et al.* Immediate and long-term outcome of intracoronary stent implantation for true bifurcation lesions. *J. Am. Coll. Cardiol.* **35**, 929–936 (2000).
71. Yamashita, T. *et al.* Bifurcation lesions: two stents versus one stent—immediate and follow-up results. *J. Am. Coll. Cardiol.* **35**, 1145–1151 (2000).
72. Keshavarz-Motamed, Z. A diagnostic, monitoring, and predictive tool for patients with complex valvular, vascular and ventricular diseases. *Sci. Rep.* **10**, 1–19 (2020).
73. Heward, S. J. & Widrich, J. Coronary Perfusion Pressure. in *StatPearls* (StatPearls Publishing, 2021).
74. Banerjee, P. Heart failure: a story of damage, fatigue and injury? *Open Heart* **4**, e000684 (2017).
75. Keshavarz-Motamed Zahra *et al.* Mixed Valvular Disease Following Transcatheter Aortic Valve Replacement: Quantification and Systematic Differentiation Using Clinical Measurements and Image-Based Patient-Specific In Silico Modeling. *J. Am. Heart Assoc.* **9**, e015063 (2020).
76. Heusch, G. The Coronary Circulation as a Target of Cardioprotection. *Circ. Res.* **118**, 1643–1658 (2016).

# Chapter 6: Conclusion and future directions

## 1.1 Conclusion

Flow patterns inside the left ventricle plays an important role in assessment of TAVR success, and it may help the clinician optimize the plan treatment. However, diagnostic tools or reliable hemodynamic metrics in clinical routine are not well developed yet. Currently, the final decisions for valve interventions are largely made based on the anatomy and structural heart assessment. In addition, the gold standard technique to evaluate basic hemodynamic parameters (such as pressure) is the cardiac catheterization, which is invasive, high risk, expensive and not feasible for majority of the patients who undergo TAVR. Also, current imaging modalities capable of flow assessment including Echo-PIV, phase contrast MRI and Echocardiography suffer from low temporal and spatial resolution. In this study, we developed a non-invasive method for assessing the TAVR, using fluid-structure interactions method, lumped parameter modelling and personalized medical images modalities, that can numerically compute the blood flow fields. The diagnostic and predictive information, that framework can provide, is crucial for improve clinical outcomes, to examine patient risk and to plan intervention optimally. This framework was validated against clinical Doppler echocardiography measurements.

The other line of current study was to investigate the interplay between PVL and coronary arteries and aortic root for the patients who undergo TAVR. A complicating factor of PVL after TAVR which has been underestimated is its impact on coronary flow shortage during diastole as well as the increased risk of blood stagnation at the neo-sinus region. Although PVL is prevalent in TAVR patients and unavoidable to a certain extent, argument and uncertainty persist when PVL coexists with CAD. The optimal course of intervention for a patient with coexisting PVL and CAD is an area of contention and uncertainty. Our observations can be summarized as follows:

- *Coronary perfusion pressure improvement is a poor indicator of coronary flow recovery in presence of PVL:* Our results show that despite the increase in aortic pressure and improvement of coronary perfusion pressure, there is a considerable decrease in coronary flow during diastole in presence of PVL. A portion of the overall flow volume that is meant to be carried forward towards the coronary arteries diverges towards the left ventricle which leads to coronary flow shortage after TAVR. This is critical issue in the longer term since reduced coronary blood flow after TAVR is associated with reduced capacity to augment myocardial oxygenation, leading to LV dysfunction, increased apoptosis, and sudden death.
- *PVL impairs the sinus and neo-sinus washout mechanism:* TAVR alters the original configuration of aortic sinus, and efficient vortical flow is essential for effective washout of neo-sinus and sinus flow. Our findings revealed that PVL amplifies irregular washout mechanism for the sinus and neo-sinus region. PVL jet alters the flow topology of these regions by pulling the vortices out of neo-sinus. As a results, the vortices in the neo-sinus regions have less power to transfer the flow out of the leaflet roots.

- *PVL might exacerbate the risk of subclinical leaflet thrombosis and hypo-attenuated leaflet thickening:* While there is limited knowledge about the causes of leaflet thrombosis after TAVR, we found that PVL exacerbated the blood stasis volume in the neo-sinus regions. The blood stasis volume was nonuniform and asymmetrical with respect to valve centerline, and NCC neo-sinus is exposed to the most stagnant flow and therefore, at higher risk of leaflet thrombosis.

- *PVL following TAVR could increase the risk of tissue damage at the aortic root and plaque progression in coronaries:* The disturbed flow at the aortic root and around the PVL area leads to abnormal increased wall shear stress which could stimulate aneurysm or cause progressive dilation of aortic root and ascending aorta. On the other hand, we found that PVL reduces the shear stress at the coronary walls. Given that low wall shear stress could induce inflammatory activation of endothelium, PVL might promote plaque promotion or increase plaque eccentricity for a vessel with stable stenosis.

The other intention of current study was investigation of coronary hemodynamics alterations after TAVR and its correlation with the ascending aorta and ventricular pressures changes (global) as well as TAVR deployment characteristics such as aortic root geometry, valve size, aorta angle, coronary ostium height and valve to coronary distance (local). We investigated hemodynamic metrics computed by our computational framework. Our results can provide unique insights about the possible reasons for longer term CAD and heart failure after TAVR as follows:

- *Coronary flow might not improve after TAVR.* While coronary flow improvement is expected immediately after TAVR, our results show that although systolic flow increases after TAVR, the diastolic flow in coronary arteries might not improve or even worsen for many patients.
- *Coronary arteries might be higher risk of plaque progression after TAVR:* Our findings suggest that for majority of patients, TAVR might reduce the wall shear stress for the coronary branches during diastole due to the flow reduction. This makes the coronary arteries more susceptible to atherosclerosis and plaque growth.
- *Anatomical alteration after TAVR could have direct impact on coronary flow:* In addition to the perfusion alterations after TAVR, the anatomical and prosthesis implantation details

including the valve to aorta distance, valve to coronary distance, implantation depth and aortic root shape significantly impacts the local hemodynamics before reaching coronary ostium. Our findings suggest that if the gap between the prosthesis and aorta wall is restricted or if the coronary ostium is closer to the aortic root, the chance of flow obstruction increases. While TAVR is expanding towards younger patients, the improper filling of coronary will lead to heart failure in the course of time.

In summary, our personalized image-based framework may serve as a valuable tool to non-invasively investigate the flow dynamics of TAVR before and after the intervention, and in coexistence of coronary artery disease or other forms of ventricular, vascular, or valvular diseases. The diagnostic information, that the framework can provide, is vitally needed to improve clinical outcomes, to assess patient risk and to plan optimized intervention with long term benefits.

## 1.2 Future directions

- We developed a computational fluid dynamics framework using 3-D fluid-structure interactions method (FSI) and lumped parameter model to simulate both the local and global hemodynamics in patients with aortic stenosis who received TAVR. One limitation of our simulations is the small number of patients. Future studies must consider further validation of the computational framework in a large population of C3VD patients in both pre and post intervention states.
- Our computational framework focused on only diastole phase, due to higher spatial resolution of CT images for accurate geometry and the numerical complications of active electromechanical function of left ventricle during systole. Another limitation that may be

associated with our simulations is modeling the transcatheter aortic valve leaflets to be rigidly close and mitral valve leaflets to be rigidly open throughout the diastolic phase. Future numerical studies should consider the interactions between the fluid and deforming valve-leaflet structure during the entire cardiac cycle and should investigate the effects of dynamical opening and closing of the aortic and mitral valve leaflets on vortex dynamics in the LV.

- Although the focus of this study was the left side of the heart, the developed computational framework can be easily adjusted for simulation of right heart and right ventricle and for the simulation of different tricuspid and pulmonary valves interventions. In addition, the data from this research could be used to develop either low-order flow models or machine learning models to be used as predictive tools.

## References

(Used in Chapter 1 and Chapter 6)


1. Levine, G. N. *Cardiology Secrets*. (Elsevier Health Sciences, 2021).
2. Rouleau, S. G., Brady, W. J., Koyfman, A. & Long, B. Transcatheter aortic valve replacement complications: A narrative review for emergency clinicians. *The American Journal of Emergency Medicine* **56**, 77–86 (2022).
3. Carabello, B. A. & Paulus, W. J. Aortic stenosis. *The Lancet* **373**, 956–966 (2009).
4. Jalava, M. P. *et al.* Transcatheter and Surgical Aortic Valve Replacement in Patients With Recent Acute Heart Failure. *The Annals of Thoracic Surgery* **109**, 110–117 (2020).
5. Shah, A. S. V. *et al.* Left Ventricular Hypertrophy With Strain and Aortic Stenosis. *Circulation* **130**, 1607–1616 (2014).
6. Klein, A. L., Ramchand, J. & Nagueh, S. F. Aortic Stenosis and Diastolic Dysfunction. *Journal of the American College of Cardiology* **76**, 2952–2955 (2020).
7. El Sabbagh, A. & Nishimura, R. A. Clinical Conundrum of Coronary Artery Disease and Aortic Valve Stenosis. *Journal of the American Heart Association* **6**, e005593.
8. Urena, M. *et al.* Arrhythmia Burden in Elderly Patients With Severe Aortic Stenosis as Determined by Continuous Electrocardiographic Recording. *Circulation* **131**, 469–477 (2015).
9. Stortecky, S. *et al.* Atrial Fibrillation and Aortic Stenosis. *Circulation: Cardiovascular Interventions* **6**, 77–84 (2013).
10. Andreasen, C. *et al.* Incidence of Ischemic Stroke in Individuals With and Without Aortic Valve Stenosis. *Stroke* **51**, 1364–1371 (2020).
11. Coffey, S. *et al.* Global epidemiology of valvular heart disease. *Nat Rev Cardiol* **18**, 853–864 (2021).
12. Généreux, P. *et al.* Paravalvular Leak After Transcatheter Aortic Valve Replacement: The New Achilles' Heel? A Comprehensive Review of the Literature. *Journal of the American College of Cardiology* **61**, 1125–1136 (2013).
13. Nombela-Franco, L. *et al.* Significant Mitral Regurgitation Left Untreated at the Time of Aortic Valve Replacement: A Comprehensive Review of a Frequent Entity in the Transcatheter Aortic Valve Replacement Era. *Journal of the American College of Cardiology* **63**, 2643–2658 (2014).
14. Blanke, P. *et al.* Predicting LVOT Obstruction in Transcatheter Mitral Valve Implantation: Concept of the Neo-LVOT. *J Am Coll Cardiol Img* **10**, 482–485 (2017).
15. Elmariah Sammy *et al.* Outcomes of Transcatheter and Surgical Aortic Valve Replacement in High-Risk Patients With Aortic Stenosis and Left Ventricular Dysfunction. *Circulation: Cardiovascular Interventions* **6**, 604–614 (2013).
16. Rosenhek, R. *et al.* Predictors of Outcome in Severe, Asymptomatic Aortic Stenosis. *New England Journal of Medicine* **343**, 611–617 (2000).
17. Ross, J. & Braunwald, E. Aortic Stenosis. *Circulation* **38**, V–61 (1968).
18. Aldrugh, S., Valle, J. E., Parker, M. W., Harrington, C. M. & Aurigemma, G. P. Prevalence of Left Ventricular Hypertrophy Caused by Systemic Hypertension Preceding the Development of Severe Aortic Stenosis. *The American Journal of Cardiology* **150**, 89–94 (2021).

19. Hein, S. *et al.* Progression From Compensated Hypertrophy to Failure in the Pressure-Overloaded Human Heart. *Circulation* **107**, 984–991 (2003).
20. Kampaktsis, P. N. *et al.* The role and clinical implications of diastolic dysfunction in aortic stenosis. *Heart* **103**, 1481–1487 (2017).
21. Nagueh, S. F. *et al.* Recommendations for the Evaluation of Left Ventricular Diastolic Function by Echocardiography: An Update from the American Society of Echocardiography and the European Association of Cardiovascular Imaging. *J Am Soc Echocardiogr* **29**, 277–314 (2016).
22. Fukui, M., Généreux, P. & Cavalcante, J. L. Assessment of Cardiac Damage in Aortic Stenosis. *Cardiology Clinics* **38**, 23–31 (2020).
23. Anantha-Narayanan, M. *et al.* Impact of diastolic dysfunction on long-term mortality and quality of life after transcatheter aortic valve replacement. *Catheterization and Cardiovascular Interventions* **95**, 1034–1041 (2020).
24. Asami, M. *et al.* The Impact of Left Ventricular Diastolic Dysfunction on Clinical Outcomes After Transcatheter Aortic Valve Replacement. *JACC: Cardiovascular Interventions* **11**, 593–601 (2018).
25. Sanfilippo, F., Scolletta, S., Morelli, A. & Vieillard-Baron, A. Practical approach to diastolic dysfunction in light of the new guidelines and clinical applications in the operating room and in the intensive care. *Ann. Intensive Care* **8**, 1–12 (2018).
26. Gillebert, T. C., Pauw, M. D. & Timmermans, F. Echo-Doppler assessment of diastole: flow, function and haemodynamics. *Heart* **99**, 55–64 (2013).
27. Milin, A. C., Vorobiof, G., Aksoy, O. & Ardehali, R. Insights Into Aortic Sclerosis and Its Relationship With Coronary Artery Disease. *Journal of the American Heart Association* **3**, e001111.
28. Faroux, L. *et al.* Coronary Artery Disease and Transcatheter Aortic Valve Replacement: JACC State-of-the-Art Review. *Journal of the American College of Cardiology* **74**, 362–372 (2019).
29. Lévy, S. *et al.* Atrial fibrillation: current knowledge and recommendations for management. *European Heart Journal* **19**, 1294–1320 (1998).
30. Benjamin, E. J. *et al.* Impact of Atrial Fibrillation on the Risk of Death. *Circulation* **98**, 946–952 (1998).
31. Saikrishnan, N., Kumar, G., Sawaya, F. J., Lerakis, S. & Yoganathan, A. P. Accurate Assessment of Aortic Stenosis. *Circulation* **129**, 244–253 (2014).
32. Baumgartner, H. *et al.* Recommendations on the echocardiographic assessment of aortic valve stenosis: a focused update from the European Association of Cardiovascular Imaging and the American Society of Echocardiography. *Eur Heart J Cardiovasc Imaging* **18**, 254–275 (2017).
33. Chong, A., Senior, R. & Wahi, S. Contemporary Imaging of Aortic Stenosis. *Heart, Lung and Circulation* **28**, 1310–1319 (2019).
34. Donati, F. *et al.* Beyond Bernoulli. *Circulation: Cardiovascular Imaging* **10**, e005207 (2017).
35. Pawade, T., Sheth, T., Guzzetti, E., Dweck, M. R. & Clavel, M.-A. Why and How to Measure Aortic Valve Calcification in Patients With Aortic Stenosis. *JACC: Cardiovascular Imaging* **12**, 1835–1848 (2019).
36. Manda, Y. R. & Baradhi, K. M. Cardiac Catheterization Risks and Complications. in *StatPearls* (StatPearls Publishing, 2022).

37. Pflederer, T. & Achenbach, S. Aortic valve stenosis: CT contributions to diagnosis and therapy. *Journal of Cardiovascular Computed Tomography* **4**, 355–364 (2010).
38. Schultz, C. H., Fairley, R., Murphy, L. S.-L. & Doss, M. The Risk of Cancer from CT Scans and Other Sources of Low-Dose Radiation: A Critical Appraisal of Methodologic Quality. *Prehospital and Disaster Medicine* **35**, 3–16 (2020).
39. Baiocchi, M. *et al.* Effects of Choice of Medical Imaging Modalities on a Non-invasive Diagnostic and Monitoring Computational Framework for Patients With Complex Valvular, Vascular, and Ventricular Diseases Who Undergo Transcatheter Aortic Valve Replacement. *Frontiers in Bioengineering and Biotechnology* **9**, 389 (2021).
40. Bohbot, Y. *et al.* Usefulness of Cardiac Magnetic Resonance Imaging in Aortic Stenosis. *Circulation: Cardiovascular Imaging* **13**, e010356 (2020).
41. Dewey, M. *et al.* Clinical quantitative cardiac imaging for the assessment of myocardial ischaemia. *Nat Rev Cardiol* **17**, 427–450 (2020).
42. Barker, C. M. Clinical Practice Update: Who Should Be Referred for Transcatheter Aortic Valve Replacement in 2017? (2017).
43. Waksman, R. *et al.* Transcatheter Aortic Valve Replacement in Low-Risk Patients With Symptomatic Severe Aortic Stenosis. *Journal of the American College of Cardiology* **72**, 2095–2105 (2018).
44. Coylewright, M., Forrest, J. K., McCabe, J. M. & Nazif, T. M. TAVR in Low-Risk Patients. *Journal of the American College of Cardiology* **75**, 1208–1211 (2020).
45. Leon, M. B. *et al.* Transcatheter or surgical aortic-valve replacement in intermediate-risk patients. *New England Journal of Medicine* **374**, 1609–1620 (2016).
46. Suri, R. M. & Schaff, H. V. Selection of Aortic Valve Prostheses: Contemporary Reappraisal of Mechanical Versus Biologic Valve Substitutes. *Circulation* **128**, 1372–1380 (2013).
47. Vy, P. *et al.* Review of patient-specific simulations of transcatheter aortic valve implantation. *International Journal of Advances in Engineering Sciences and Applied Mathematics* **8**, 2–24 (2016).
48. Cheung, A. & Ree, R. Transcatheter Aortic Valve Replacement. *Anesthesiology Clinics* **26**, 465–479 (2008).
49. Leon, M. B. *et al.* Transcatheter or Surgical Aortic-Valve Replacement in Intermediate-Risk Patients. *New England Journal of Medicine* **374**, 1609–1620 (2016).
50. De Backer, O., Wong, I., Wilkins, B., Carranza, C. L. & Søndergaard, L. Patient-Tailored Aortic Valve Replacement. *Frontiers in Cardiovascular Medicine* **8**, (2021).
51. Kolkailah, A. A. *et al.* Transcatheter aortic valve implantation versus surgical aortic valve replacement for severe aortic stenosis in people with low surgical risk. *Cochrane Database Syst Rev* **2019**, CD013319 (2019).
52. Arora, S., Misenheimer, J. A. & Ramaraj, R. Transcatheter Aortic Valve Replacement: Comprehensive Review and Present Status. *Tex Heart Inst J* **44**, 29–38 (2017).
53. Shannon, J. *et al.* Recognition and management of complications during transcatheter aortic valve implantation. *Expert Rev Cardiovasc Ther* **9**, 913–926 (2011).
54. Stähli, B. E. *et al.* Aortic regurgitation after transcatheter aortic valve implantation: mechanisms and implications. *Cardiovascular Diagnosis and Therapy* **3**, 15-22–22 (2013).
55. Pislaru, S. V., Nkomo, V. T. & Sandhu, G. S. Assessment of Prosthetic Valve Function After TAVR. *JACC: Cardiovascular Imaging* **9**, 193–206 (2016).

56. Gotzmann, M., Lindstaedt, M. & Mügge, A. From pressure overload to volume overload: Aortic regurgitation after transcatheter aortic valve implantation. *American Heart Journal* **163**, 903–911 (2012).
57. Manoharan, G. *et al.* Treatment of Symptomatic Severe Aortic Stenosis With a Novel Resheathable Supra-Annular Self-Expanding Transcatheter Aortic Valve System. *JACC: Cardiovascular Interventions* **8**, 1359–1367 (2015).
58. Rahimtoola, S. H. The problem of valve prosthesis-patient mismatch. *Circulation* **58**, 20–24 (1978).
59. Daneshvar, S. A. & Rahimtoola, S. H. Valve Prosthesis–Patient Mismatch (VP–PM): A Long-Term Perspective. *Journal of the American College of Cardiology* **60**, 1123–1135 (2012).
60. Astudillo, L. M. *et al.* Clinical predictors of prosthesis-patient mismatch after aortic valve replacement for aortic stenosis. *Clinics (Sao Paulo)* **67**, 55–60 (2012).
61. Hatoum, H. Fluid Mechanics of Transcatheter Aortic Valve Replacement. (The Ohio State University, 2018).
62. Abdul-Jawad Altisent, O. *et al.* Neurological damage after transcatheter aortic valve implantation compared with surgical aortic valve replacement in intermediate risk patients. *Clin Res Cardiol* **105**, 508–517 (2016).
63. Athappan, G. *et al.* Influence of Transcatheter Aortic Valve Replacement Strategy and Valve Design on Stroke After Transcatheter Aortic Valve Replacement: A Meta-Analysis and Systematic Review of Literature. *Journal of the American College of Cardiology* **63**, 2101–2110 (2014).
64. Arora, S., Ramm, C. J., Misenheimer, J. A. & Vavalle, J. P. Early transcatheter valve prosthesis degeneration and future ramifications. *Cardiovascular Diagnosis and Therapy* **7**, 1–3 (2017).
65. Bogyi, M. *et al.* Subclinical Leaflet Thrombosis After Transcatheter Aortic Valve Replacement. *JACC: Cardiovascular Interventions* **14**, 2643–2656 (2021).
66. Karády, J. *et al.* Quantification of hypo-attenuated leaflet thickening after transcatheter aortic valve implantation: clinical relevance of hypo-attenuated leaflet thickening volume. *European Heart Journal - Cardiovascular Imaging* **21**, 1395–1404 (2020).
67. Garcia, S. *et al.* Clinical Impact of Hypoattenuating Leaflet Thickening After Transcatheter Aortic Valve Replacement. *Circulation: Cardiovascular Interventions* **0**, CIRCINTERVENTIONS.121.011480.
68. Makkar, R. R. *et al.* Subclinical Leaflet Thrombosis in Transcatheter and Surgical Bioprosthetic Valves: PARTNER 3 Cardiac Computed Tomography Substudy. *Journal of the American College of Cardiology* **75**, 3003–3015 (2020).
69. Blanke, P. *et al.* Bioprosthetic Aortic Valve Leaflet Thickening in the Evolut Low Risk Sub-Study. *Journal of the American College of Cardiology* **75**, 2430–2442 (2020).
70. Nakatani, S. Subclinical leaflet thrombosis after transcatheter aortic valve implantation. *Heart* **103**, 1942–1946 (2017).
71. Mylotte, D. *et al.* Transcatheter heart valve failure: a systematic review. *European Heart Journal* **36**, 1306–1327 (2015).
72. Hatoum, H. *et al.* Predictive Model for Thrombus Formation After Transcatheter Valve Replacement. *Cardiovasc Eng Tech* **12**, 576–588 (2021).
73. Lederman, R. J. *et al.* Preventing Coronary Obstruction During Transcatheter Aortic Valve Replacement. *JACC Cardiovasc Interv* **12**, 1197–1216 (2019).

74. Khan, J. M. *et al.* Preventing Coronary Obstruction During Transcatheter Aortic Valve Replacement. *JACC: Cardiovascular Interventions* **14**, 941–948 (2021).
75. Valvo, R., Costa, G. & Barbanti, M. How to Avoid Coronary Occlusion During TAVR Valve-in-Valve Procedures. *Frontiers in Cardiovascular Medicine* **6**, 168 (2019).
76. Taylor, C. A., Fonte, T. A. & Min, J. K. Computational Fluid Dynamics Applied to Cardiac Computed Tomography for Noninvasive Quantification of Fractional Flow Reserve: Scientific Basis. *Journal of the American College of Cardiology* **61**, 2233–2241 (2013).
77. Randles, A., Frakes, D. H. & Leopold, J. A. Computational Fluid Dynamics and Additive Manufacturing to Diagnose and Treat Cardiovascular Disease. *Trends in Biotechnology* **35**, 1049–1061 (2017).
78. Taylor, C. A. & Draney, M. T. Experimental and Computational Methods in Cardiovascular Fluid Mechanics. *Annual Review of Fluid Mechanics* **36**, 197–231 (2004).
79. Soudah, E. *et al.* Estimation of wall shear stress using 4d flow cardiovascular mri and computational fluid dynamics. *J. Mech. Med. Biol.* **17**, 1750046 (2017).
80. Martinez, -Legazpi Pablo *et al.* Stasis Mapping Using Ultrasound. *JACC: Cardiovascular Imaging* **11**, 514–515 (2018).
81. Postigo, A. *et al.* Assessment of Blood Flow Transport in the Left Ventricle Using Ultrasound. Validation Against 4-D Flow Cardiac Magnetic Resonance. *Ultrasound in Medicine & Biology* **48**, 1822–1832 (2022).
82. Vu, V. *et al.* Mitral Valve Prosthesis Design Affects Hemodynamic Stasis and Shear In The Dilated Left Ventricle. *Ann Biomed Eng* **47**, 1265–1280 (2019).
83. Dwyer, H. A. *et al.* Computational fluid dynamics simulation of transcatheter aortic valve degeneration. *Interact CardioVasc Thorac Surg* **9**, 301–308 (2009).
84. Sirois, E., Wang, Q. & Sun, W. Fluid Simulation of a Transcatheter Aortic Valve Deployment into a Patient-Specific Aortic Root. *Cardiovasc Eng Tech* **2**, 186–195 (2011).
85. Sun, W. (proxy), Sirois, E., Mao, W., Li, K. & Calderan, J. Simulated Transcatheter Aortic Valve Flow: Implications of Elliptical Deployment and Under-Expansion at the Aortic Annulus. *Artif Organs* **42**, E141–E152 (2018).
86. Wang, Q., Sirois, E. & Sun, W. Patient-Specific Modeling of Biomechanical Interaction in Transcatheter Aortic Valve Deployment. *J Biomech* **45**, 1965–1971 (2012).
87. Morganti, S. *et al.* Simulation of transcatheter aortic valve implantation through patient-specific finite element analysis: Two clinical cases. *J BIOMECH* **47**, 2547–2555 (2014).
88. Sotiropoulos, F., Le, T. B. & Gilmanov, A. Fluid Mechanics of Heart Valves and Their Replacements. *Annual Review of Fluid Mechanics* **48**, 259–283 (2016).
89. Le, T. B., Sotiropoulos, F., Coffey, D. & Keefe, D. Vortex formation and instability in the left ventricle. *Physics of Fluids* **24**, 091110 (2012).
90. Le, T. B., Elbaz, M. S. M., Van Der Geest, R. J. & Sotiropoulos, F. High Resolution Simulation of Diastolic Left Ventricular Hemodynamics Guided by Four-Dimensional Flow Magnetic Resonance Imaging Data. *Flow Turbulence Combust* **102**, 3–26 (2019).
91. Mao, W., Caballero, A., McKay, R., Primiano, C. & Sun, W. Fully-coupled fluid-structure interaction simulation of the aortic and mitral valves in a realistic 3D left ventricle model. *PLoS One* **12**, (2017).
92. Catalano, C. & Pasta, S. On the Modeling of Transcatheter Therapies for the Aortic and Mitral Valves: A Review. *Prosthesis* **4**, 102–112 (2022).

93. Bavo, A. M. *et al.* Fluid-Structure Interaction Simulation of Prosthetic Aortic Valves: Comparison between Immersed Boundary and Arbitrary Lagrangian-Eulerian Techniques for the Mesh Representation. *PLOS ONE* **11**, e0154517 (2016).
94. Lee, J. H. *et al.* Fluid–Structure Interaction Models of Bioprosthetic Heart Valve Dynamics in an Experimental Pulse Duplicator. *Ann Biomed Eng* (2020) doi:10.1007/s10439-020-02466-4.
95. Pasta, S. *et al.* Simulation study of transcatheter heart valve implantation in patients with stenotic bicuspid aortic valve. *Med Biol Eng Comput* **58**, 815–829 (2020).
96. Saikali, E., Bilotta, G., Hérault, A. & Zago, V. Accuracy Improvements for Single Precision Implementations of the SPH Method. *International Journal of Computational Fluid Dynamics* **34**, 774–787 (2020).
97. Holzapfel, G. A. & Ogden, R. W. Constitutive modelling of passive myocardium: a structurally based framework for material characterization. *Philosophical Transactions of the Royal Society A: Mathematical, Physical and Engineering Sciences* **367**, 3445–3475 (2009).
98. Demiray, H. Stresses in Ventricular Wall. *J. Appl. Mech* **43**, 194–197 (1976).
99. Humphrey, J. D., Strumpf, R. K. & Yin, F. C. P. Determination of a Constitutive Relation for Passive Myocardium: I. A New Functional Form. *J Biomech Eng* **112**, 333–339 (1990).
100. Yin, F. C. P., Strumpf, R. K., Chew, P. H. & Zeger, S. L. Quantification of the mechanical properties of noncontracting canine myocardium under simultaneous biaxial loading. *Journal of Biomechanics* **20**, 577–589 (1987).
101. Lee J M & Boughner D R. Mechanical properties of human pericardium. Differences in viscoelastic response when compared with canine pericardium. *Circulation Research* **57**, 475–481 (1985).
102. Khalafvand, S. S., Ng, E. Y.-K., Zhong, L. & Hung, T.-K. Three-dimensional diastolic blood flow in the left ventricle. *Journal of Biomechanics* **50**, 71–76 (2017).
103. Khalafvand, S. S., Ng, E. Y. K., Zhong, L. & Hung, T. K. Fluid-dynamics modelling of the human left ventricle with dynamic mesh for normal and myocardial infarction: Preliminary study. *Computers in Biology and Medicine* **42**, 863–870 (2012).
104. Khodaei, S., Fatouraee, N. & Nabaei, M. Numerical simulation of mitral valve prolapse considering the effect of left ventricle. *Mathematical biosciences* **285**, 75–80 (2017).
105. Palit, A., Bhudia, S. K., Arvanitis, T. N., Turley, G. A. & Williams, M. A. In vivo estimation of passive biomechanical properties of human myocardium. *Med Biol Eng Comput* **56**, 1615–1631 (2018).
106. Mojsejenko, D. *et al.* Estimating Passive Mechanical Properties in a Myocardial Infarction using MRI and Finite Element Simulations. *Biomech Model Mechanobiol* **14**, 633–647 (2015).
107. Mekkaoui, C., Reese, T. G., Jackowski, M. P., Bhat, H. & Sosnovik, D. E. Diffusion MRI in the heart. *NMR in Biomedicine* **30**, e3426 (2017).
108. Hong, B. D., Moulton, M. J. & Secomb, T. W. Modeling left ventricular dynamics with characteristic deformation modes. *Biomech Model Mechanobiol* **18**, 1683–1696 (2019).
109. Dabiri, Y. *et al.* Method for Calibration of Left Ventricle Material Properties Using Three-Dimensional Echocardiography Endocardial Strains. *J Biomech Eng* **141**, (2019).
110. Elkins, C. J. & Alley, M. T. Magnetic resonance velocimetry: applications of magnetic resonance imaging in the measurement of fluid motion. *Exp Fluids* **43**, 823–858 (2007).

111. Kilner, P. J., Gatehouse, P. D. & Firmin, D. N. Flow Measurement by Magnetic Resonance: A Unique Asset Worth Optimising. *Journal of Cardiovascular Magnetic Resonance* **9**, 723–728 (2007).
112. Le, T. B., Usta, M., Aidun, C., Yoganathan, A. & Sotiropoulos, F. Computational Methods for Fluid-Structure Interaction Simulation of Heart Valves in Patient-Specific Left Heart Anatomies. *Fluids* **7**, 94 (2022).
113. Viola, F., Meschini, V. & Verzicco, R. Fluid–Structure-Electrophysiology interaction (FSEI) in the left-heart: A multi-way coupled computational model. *European Journal of Mechanics - B/Fluids* **79**, 212–232 (2020).
114. Caballero Andrés, Mao Wenbin, McKay Raymond, & Sun Wei. The impact of balloon-expandable transcatheter aortic valve replacement on concomitant mitral regurgitation: a comprehensive computational analysis. *Journal of The Royal Society Interface* **16**, 20190355 (2019).
115. Santiago, A. *et al.* Fully coupled fluid-electro-mechanical model of the human heart for supercomputers. *International Journal for Numerical Methods in Biomedical Engineering* **34**, e3140 (2018).
116. Garber, L., Khodaei, S. & Keshavarz-Motamed, Z. The Critical Role of Lumped Parameter Models in Patient-Specific Cardiovascular Simulations. *Arch Computat Methods Eng* (2021) doi:10.1007/s11831-021-09685-5.
117. Keshavarz-Motamed, Z. A diagnostic, monitoring, and predictive tool for patients with complex valvular, vascular and ventricular diseases. *Sci Rep* **10**, 6905 (2020).
118. Sadeghi, R., Khodaei, S., Ganame, J. & Keshavarz-Motamed, Z. Towards non-invasive computational-mechanics and imaging-based diagnostic framework for personalized cardiology for coarctation. *Scientific Reports* **10**, 9048 (2020).
119. Khodaei, S. *et al.* Personalized intervention cardiology with transcatheter aortic valve replacement made possible with a non-invasive monitoring and diagnostic framework. *Sci Rep* **11**, 10888 (2021).
120. Cai, L. *et al.* The Comparison of Different Constitutive Laws and Fiber Architectures for the Aortic Valve on Fluid–Structure Interaction Simulation. *Frontiers in Physiology* **12**, (2021).
121. Mirramezani, M., Diamond, S. L., Litt, H. I. & Shadden, S. C. Reduced Order Models for Transstenotic Pressure Drop in the Coronary Arteries. *J Biomech Eng* **141**, 0310051–03100511 (2019).
122. Keshavarz-Motamed, Z. A diagnostic, monitoring, and predictive tool for patients with complex valvular, vascular and ventricular diseases. *Scientific Reports* **10**, 1–19 (2020).